EIGENVALUE ANALYSIS OF IDEAL FLUIDS' SLOSHING MOVEMENT IN CONTAINERS USING VIRTUAL MASS METHOD

by

Burak Tonga

B.S., Civil Engineering, Istanbul Bilgi University, 2016

Submitted to the Institute for Graduate Studies in
Science and Engineering in partial fulfillment of
the requirements for the degree of
Master of Science

Graduate Program in Structural Engineering

Boğaziçi University

2019

EIGENVALUE ANALYSIS OF IDEAL FLUIDS' SLOSHING MOVEMENT IN CONTAINERS USING VIRTUAL MASS METHOD

APPROVED BY:

Assoc. Prof. Sami And Kılıç .....
(Thesis Supervisor)

Assoc. Prof. Emre Otay .....

Assist. Prof. Gökhan Yazıcı .....

DATE OF APPROVAL: 09.09.2019

ACKNOWLEDGEMENTS

I would like to acknowledge my thesis supervisor Assoc. Prof. Sami And Kılıç for his guidance and support throughout my studies in Boğaziçi University. In addition, I would like to express my gratitude to Assoc. Prof. Emre Otay for his great interest and help during my thesis period.

I would like to thank all the members of my thesis defense jury, Assoc. Prof. Sami And Kılıç, Assoc. Prof. Emre Otay, and Assist. Prof. Gökhan Yazıcı for their interest and valuable comments.

I also express my deepest gratitude to my mother, Tülay Tonga, and to my father, Güven Tonga for their endless support during my all education life; I could not accomplish anything without their help.

Lastly, I am very thankful to Research Assistant Gökçen Özalp from Gebze Technical University for her great support and understanding throughout my studies.

ABSTRACT

EIGENVALUE ANALYSIS OF IDEAL FLUIDS' SLOSHING MOVEMENT IN CONTAINERS USING VIRTUAL MASS METHOD

The sloshing motion of fluids in rectangular and cylindrical containers which have different sizes and materials are investigated. 2 different analytical methods, the methods of Abramson [1] and Housner [2] are utilized. With Abramson's method the sloshing motion of ideal fluid which has the properties of being inviscid, irrotational and incompressible with its governing Laplace equation in rigid rectangular and cylindrical tanks is examined. The boundary conditions are defined through tank bottom and tank wall whereas its kinematic boundary condition comes from its free surface. With Housner's analytical method, first natural frequencies of the sloshing motion in rectangular and cylindrical tanks assumed in 2D are found. In addition to analytical methods, a numerical method, virtual mass method of Nastran is used to obtain natural frequencies and modeshapes of the sloshing motion by eigenvalue analysis. The parameters of tank thickness, tank material, tank mesh resolution, phantom surface mesh resolution and phantom surface mesh topology are investigated with the aim of finding an optimum model in analyses that uses virtual mass method. The success of numerical model is tested by comparing frequencies with analytical ones. In terms of sizes of numerical models, small scale, and large scale models that can be seen in real life applications are analyzed. This study is enriched with laboratory experiment results of Erginbas [3]. In order to make the modelling easier for eigenvalue analyses over rectangular and cylindrical tanks, 2 Matlab scripts are developed. With these scripts, the time to create tanks and implement eigenvalue analyses are reduced.

ÖZET

KONTEYNERLERDEKİ İDEAL AKIŞKANLARIN ÇALKALANMA HAREKETİNİN SANAL KÜTLE METODU KULLANILARAK YAPILAN ÖZGÜN DEĞER ANALİZİ

Farklı ölçülere ve materyallere sahip dikdörtgen prizma ve silindir tanklardaki akışkanların çalkalanma davranışı incelenmiştir. 2 farklı analitik metod -Abramson'un [1] ve Housner'ın [2] metodları- kullanılmıştır. Abramson'ın metoduyla rijit dikdörtgen prizma ve silindir tanklardaki viskoz olmayan, sıkıştırılamıyan, çevrimsiz ve Laplace korunum denklemine sahip ideal akışkanların çalkalanma davranışı incelenmiştir. Sınır koşulları tank tabanı ve tank duvarı ile tanımlanıren kinematik sınır koşulları serbest yüzeyden gelmektedir. Housner'ın analitik metoduyla 2 boyutlu olduğu varsayılan dikdörtgen prizma ve silindir tanklardaki çalkalanma hareketinin ilk doğal frekansı bulunmuştur. Analitik metodlara ek olarak, bir sayısal metod, Nastran'ın sanal kütle metodu doğal frekansları ve mod şekillerini elde etmek için özgün değer (eigenvalue) analiziyle kullanılmıştır. Tank kalınlığı, tank materyali, tank elek (mesh) çözünürlüğü, fantom yüzey elek çözünürlüğü ve fantom yüzey elek topolojisi parametreleri sanal kütle metodu kullanılan analizlerde bir optimum model bulma amacıyla incelenmiştir. Numerik modellerin başarısı analitik sonuçlarla kıyaslanarak ölçülmüştür. Sayısal modellerin ölçüleri bağlamında küçük ölçekli, ve gerçek hayat uygulamalarında görülen büyük ölçekli modeller analiz edilmiştir. Bu çalışma Erginbaş'ın [3] laboratuvar deneyi sonuçlarıyla zenginleştirilmiştir. Özgün değer(eigen value) analizinin yapıldığı dikdörtgen prizma ve silindir modellerinin oluşturulmasını kolaylaştırmak için 2 bilgisayar komut dizisi geliştirilmiştir. Bu komut dizileriyle tankı oluşturma ve özgün değer analizi oluşturma süresi azaltılmıştır.

TABLE OF CONTENTS

ACKNOWLEDGEMENTS . . . iii
ABSTRACT . . . iv
ÖZET . . . v
LIST OF FIGURES . . . ix
LIST OF TABLES . . . xx
LIST OF SYMBOLS . . . xxx
LIST OF ACRONYMS/ABBREVIATIONS . . . xxxi
1. INTRODUCTION . . . 1
2. LITERATURE REVIEW . . . 4
3. NUMERICAL IMPLEMENTATION OF VIRTUAL MASS METHOD . . . 8
4. NUMERICAL ANALYSIS OF MODES AND COMPARISON OF ANALYTICAL, NUMERICAL AND EXPERIMENTAL RESULTS . . . 35
4.1. Rectangular Tanks . . . 35
4.1.1. Small Scale Tank . . . 35
4.1.2. Analytical Methods . . . 36
4.1.3. Numerical Analyses . . . 37
4.1.4. Laboratory Experiments . . . 45
4.1.5. Results . . . 54
4.1.6. Large Scale Tank . . . 80
4.1.7. Numerical Analyses . . . 81
4.1.8. Results . . . 82
4.2. Cylindrical Tanks . . . 87
4.2.1. Small Scale Tank . . . 87
4.2.2. Analytical Method . . . 88
4.2.3. Numerical Analyses . . . 89
4.2.4. Laboratory Experiments . . . 99
4.2.5. Results . . . 105
4.2.6. Large Scale Tank . . . 159
4.2.7. Numerical Analyses . . . 159

4.2.8. Results 159
5. CONCLUSION 172
REFERENCES 175
APPENDIX A: MATHEMATICAL DERIVATION OF NATURAL FREQUENCY FROM HOUSNER'S ANALYTICAL METHOD STUDY . . . 180
A.1. Impulsive Pressures 180
A.2. Convective Pressures 185
APPENDIX B: MATHEMATICAL DERIVATION OF SLOSHING MOTION FOR RECTANGULAR AND CYLINDRICAL TANKS STUDY . . 193
B.1. Sloshing Motion in Rectangular Tank 193
B.1.1. Governing equation 193
B.1.2. Boundary Conditions 198
B.1.3. Solving the Differential Equation 202
B.2. Sloshing Motion in Cylindrical Tank 211
B.2.1. Governing Equation 211
B.2.2. Boundary Conditions 212
B.2.3. Solving the Differential Equation 213
APPENDIX C: MATHEMATICAL DERIVATION OF SLOSHING MOTION FOR MSC NASTRAN 227
C.1. Assumptions 227
C.1.1. Incompressibility 227
C.1.2. Small Displacements 227
C.1.3. Inviscid Flow 228
C.1.4. Irrotational Flow 228
C.1.5. Free surface 228
C.1.6. Surface Waves and Gravitational Effects 228
C.2. Mathematical Derivation of Virtual Mass Method 228
C.2.1. The concept of Virtual Mass 229
C.2.2. Mass Conservation 231
C.2.3. Element Pressures 251
C.2.4. Element Displacements 254

C.2.5. Displacements, Forces and Virtual Mass Values at Grid Points . 260
C.2.6. Displacements, Forces and Virtual Mass Values in Analysis Set Coordinates 262
APPENDIX D: COMPUTER SCRIPTS FOR CREATING RECTANGULAR AND CYLINDRICAL TANK MODELS AND IMPLEMENTING SOL 103 ANALYSES IN NASTRAN 264

LIST OF FIGURES

Figure 3.1. Representation of phantom surface of a rectangular tank during sloshing motion 11

Figure 3.2. Sloshing motion of aluminum phantom surface 13

Figure 3.3. Sloshing motion of phantom surface that has material with 1000 GPa Young Modulus 14

Figure 3.4. Representation of sloshing motion of free surface during laboratory experiment of plexiglass rectangular tank [3]. 15

Figure 3.5. Representation of gap distance between phantom surface and tank wall from the top of the rectangular tank 16

Figure 3.6. Representation of gap distance between phantom surface and tank wall from the top of the cylindrical tank 17

Figure 3.7. Area distribution over the nodes at corner, edge and interior of the phantom surface. Adapted from [4] 19

Figure 3.8. Right Hand Rule representation for deciding positive side of the CTRIA3 or CQUAD4 elements. Adapted from [4] 24

Figure 3.9. ZFS and free surface heights [5] 25

Figure 3.10. Representation of a rectangular tank model of Nastran 26

Figure 3.11. Representation of a cylindrical tank model of Nastran 27

Figure 4.1. Representation of gap ratio, and gap distance between tank wall and phantom surface for rectangular tank 39

Figure 4.2. 1st modeshape of sloshing motion in Patran - Modeshape (1,0) . . 40

Figure 4.3. 2nd modeshape of sloshing motion in Patran - Modeshape (0,1) . . 41

Figure 4.4. 3rd modeshape of sloshing motion in Patran - Modeshape (1,1) . . 41

Figure 4.5. 4th modeshape of sloshing motion in Patran - Modeshape (2,0) . . 42

Figure 4.6. 5th modeshape of sloshing motion in Patran - Modeshape (2,1) . . 42

Figure 4.7. 6th modeshape of sloshing motion in Patran - Modeshape (3,0) . . 43

Figure 4.8. 9th modeshape of sloshing motion in Patran - Modeshape (3,1) . . 43

Figure 4.9. 16th modeshape of sloshing motion in Patran - Modeshape (5,0) . 44

Figure 4.10. 19th modeshape of sloshing motion in Patran - Modeshape (5,1) . 44

Figure 4.11. 21th modeshape of sloshing motion in Patran - Modeshape (5,2) . 45

Figure 4.12. Demonstration of the excitation axis of the rectangular tank. Adapted from [5]. 46

Figure 4.13. Representation of modeshape (1,0) during laboratory experiment of plexiglass rectangular tank [3]. 47

Figure 4.14. Representation of modeshape (2,0) during laboratory experiment of plexiglass rectangular tank [3]. 48

Figure 4.15. Representation of modeshape (3,0) during laboratory experiment of plexiglass rectangular tank [3]. 49

Figure 4.16. Representation of modeshape (3,1) during laboratory experiment of plexiglass rectangular tank [3]. 50

Figure 4.17. Representation of modeshape (5,0) during laboratory experiment of plexiglass rectangular tank [3]. 51

Figure 4.18. Representation of modeshape (5,1) during laboratory experiment of plexiglass rectangular tank [3]. 52

Figure 4.19. Representation of modeshape (5,2) during laboratory experiment of plexiglass rectangular tank [3]. 53

Figure 4.20. Representation of partially-filled steel rectangular tank's error rates for its first 5 modes with respect to changing tank thickness 57

Figure 4.21. Representation of partially-filled plexiglass rectangular tank's error rates for its first 5 modes with respect to changing tank thickness 59

Figure 4.22. Representation of partially-filled plexiglass rectangular tank's error rates for its first 5 modes with respect to changing tank mesh resolution 61

Figure 4.23. Representation of partially-filled plexiglass rectangular tank's error rates for its first 5 modes with respect to changing element length-gap distance ratio 65

Figure 4.24. Representation of partially-filled plexiglass rectangular tank's error rates for its first 5 modes with respect to changing element length-gap distance ratio 68

Figure 4.25. Representation of comparison of analytical, numerical and laboratory experiment frequencies for plexiglass rectangular tank 73

Figure 4.26. Representation of comparison of numerical and experimental error rates for plexiglass rectangular tank 75

Figure 4.27. Error rates table representation of partially-filled small scale rectangular tank with high rigidity for its first 5 modes with respect to tank thickness, tank mesh resolution, element length-gap distance ratio and phantom mesh resolution 79

Figure 4.28. Large scale partially filled rectangular tank representation 83

Figure 4.29. Representation of partially-filled steel large scale rectangular tank's error rates for its first 5 modes with respect to tank thickness, tank mesh resolution, element length-gap distance ratio and phantom mesh resolution 86

Figure 4.30. Unstructured mesh used for phantom surface. 90

Figure 4.31. Butterfly mesh used for phantom surface. 90

Figure 4.32. Radial mesh used for phantom surface. 91

Figure 4.33. Demonstration of gap ratio between phantom surface element size and gap distance for phantom surface with unstructured mesh . . 92

Figure 4.34. Demonstration of gap ratio between phantom surface element size and gap distance for phantom surface with butterfly mesh 93

Figure 4.35. Demonstration of gap ratio between phantom surface element size and gap distance for phantom surface with radial mesh 94

Figure 4.36. Modeshape (1,1) for cylindrical tank with unstructured mesh. . . . 96

Figure 4.37. Modeshape (2,1) for cylindrical tank with unstructured mesh. . . . 96

Figure 4.38. Modeshape (3,1) for cylindrical tank with unstructured mesh. . . . 97

Figure 4.39. Modeshape (1,2) for cylindrical tank with unstructured mesh. . . . 97

Figure 4.40. Modeshape (4,1) for cylindrical tank with unstructured mesh. . . . 98

Figure 4.41. Modeshape (2,2) for cylindrical tank with unstructured mesh. . . . 98

Figure 4.42. Demonstration of the excitation axis of the cylindrical tank. Adapted from [5]. 99

Figure 4.43. Representation of modeshape (1,1) during laboratory experiment of plexiglass cylindrical tank [3]. 100

Figure 4.44. Representation of modeshape (2,1) during laboratory experiment of plexiglass cylindrical tank [3]. 101

Figure 4.45. Representation of modeshape (1,2) during laboratory experiment of plexiglass cylindrical tank [3]. 102

Figure 4.46. Representation of modeshape (4,1) during laboratory experiment of plexiglass cylindrical tank [3]. 103

Figure 4.47. Representation of modeshape (1,3) during laboratory experiment of plexiglass cylindrical tank [3]. 104

Figure 4.48. Error rates representation of partially-filled steel cylindrical tank with phantom surface of unstructured mesh for its first 5 modes with respect to changing tank thickness 107

Figure 4.49. Error rates representation of partially-filled steel cylindrical tank with butterfly phantom surface for its first 5 modes with respect to changing tank thickness 109

Figure 4.50. Error rates representation of partially-filled steel cylindrical tank with phantom surface of radial mesh for its first 5 modes with respect to changing tank thickness 111

Figure 4.51. Error rates representation of partially-filled plexiglass cylindrical tank with phantom surface of unstructured mesh for its first 5 modes with respect to changing tank thickness 113

Figure 4.52. Error rates representation of partially-filled plexiglass cylindrical tank with phantom surface of butterfly mesh for its first 5 modes with respect to changing tank thickness 115

Figure 4.53. Error rates representation of partially-filled plexiglass cylindrical tank with phantom surface of radial mesh for its first 5 modes with respect to changing tank thickness 117

Figure 4.54. Error rates representation of partially-filled plexiglass cylindrical tank with phantom surface of unstructured mesh for its first 5 modes with respect to changing tank mesh resolution 119

Figure 4.55. Error rates representation of partially-filled plexiglass cylindrical tank with phantom surface of butterfly mesh for its first 5 modes with respect to changing tank mesh resolution 121

Figure 4.56. Error rates representation of partially-filled plexiglass cylindrical tank with phantom surface of radial mesh for its first 5 modes with respect to changing tank mesh resolution 123

Figure 4.57. Error rates representation of partially-filled plexiglass cylindrical tank with phantom surface of unstructured mesh for its first 5 modes with respect to changing gap 126

Figure 4.58. Error rates representation of partially-filled plexiglass cylindrical tank with phantom surface of butterfly mesh for its first 5 modes with respect to gap 128

Figure 4.59. Error rates representation of partially-filled plexiglass cylindrical tank with phantom surface of radial mesh for its first 5 modes with respect to gap 130

Figure 4.60. Representation of partially-filled plexiglass cylindrical tank's error rates for its first 5 modes with respect to changing phantom surface mesh topology 132

Figure 4.61. Representation of comparison of analytical, numerical and laboratory experiment frequencies with each other for several modeshapes in cylindrical tank 142

Figure 4.62. Representation of comparison of numerical and laboratory experiment error rates with each other for several modeshapes in cylindrical tank. 144

Figure 4.63. Modeshape (2,1) in cylindrical tank with unstructured mesh . . . 145

Figure 4.64. Modeshape (2,1) in cylindrical tank with butterfly mesh 145

Figure 4.65. Modeshape (2,1) in cylindrical tank with radial mesh 146

Figure 4.66. Modeshape (2,1) in cylindrical tank from laboratory experiment . 146

Figure 4.67. Modeshape (4,1) in cylindrical tank with unstructured mesh . . . 147

Figure 4.68. Modeshape (4,1) in cylindrical tank with butterfly mesh 147

Figure 4.69. Modeshape (4,1) in cylindrical tank with radial mesh 148

Figure 4.70. Modeshape (4,1) in cylindrical tank from laboratory experiment . 148

Figure 4.71. Representation of error rates of partially-filled highly rigid cylindrical tank with phantom surface of unstructured mesh for its first 5 modes with respect to changing tank thickness, tank mesh resolution, phantom surface gap ratio and phantom surface mesh topology 152

Figure 4.72. Representation of error rates of partially-filled highly rigid cylindrical tank with phantom surface of butterfly mesh for its first 5 modes with respect to changing tank thickness,tank mesh resolution, phantom surface gap ratio and phantom surface mesh topology 155

Figure 4.73. Representation of error rates of partially-filled highly rigid cylindrical tank with phantom surface of unstructured mesh for its first 5 modes with respect to changing tank thickness, tank mesh resolution, phantom surface gap ratio and phantom surface mesh topology 158

Figure 4.74. Representation of large scale cylindrical tank with phantom surface of unstructured mesh 161

Figure 4.75. Representation of error rates of partially-filled steel large scale cylindrical tank with phantom surface of unstructured mesh for its first 5 modes with respect to changing tank thickness,tank mesh resolution, phantom surface gap ratio and phantom surface mesh topology 164

Figure 4.76. Representation of error rates of partially-filled large scale cylindrical tank with phantom surface of butterfly mesh for its first 5 modes with respect to changing tank thickness, tank mesh resolution, phantom surface gap ratio and phantom surface mesh topology 167

Figure 4.77. Representation of error rates of partially-filled steel large scalecylindrical tank with phantom surface of radial mesh for its first 5 modes withrespect to changing tank thickness,tank mesh resolution, phantom surface gap ratioand phantom surface mesh topology 170

Figure A.1. Laminas of fluid with unit thickness in 2 dimensional tank. Adapted from [2] 181

Figure A.2. Vertical velocity of fluid when it is constrained between two adjacent membranes. Adapted from [2] 182

Figure A.3. 2 dimensional tank with horizontal, rigid membranes that are free to rotate. Adapted from [2] 186

Figure B.1. Representation of infinitesimal parallelpiped fluid particle. Adapted from [6]. 194

Figure B.2. Simple representation of a rectangular tank. Adapted from [6]. . . 198

Figure B.3. Side view of the rectangular tank during sloshing. Adapted from [6].200

Figure C.1. An accelerated cylinder in a fluid under the effect of additional force230

Figure C.2. Representation of the fluid volume V surrounded by surface S. Adapted from [4] 232

Figure C.3. Cartesian and Spherical Coordinates. Adapted from [4] 238

Figure C.4. Sphere of radius r for solid angle method. Adapted from [4] 244

Figure C.5. A triangle with angles of a_1, a_2, a_3. Adapted from [4]. 245

Figure C.6. A triangle projected onto a sphere with angles of $\alpha_1, \alpha_2, \alpha_3$. Adapted from [4]. 246

Figure C.7. A sphere crossed with 3 great circles which form 2 triangles on sphere's surface. Adapted from [4] 247

Figure C.8. The angle α between 2 great circles over the sphere. Adapted from [4].248

Figure C.9. 3 2-gons with the angles of α_1, α_2, and α_3. Adapted from [4]. . . . 249

Figure C.10. 2 partially immersed triangle finite elements. Adapted from [4]. . . 250

Figure C.11. 3 partially immersed quadrilateral finite elements. Adapted from [4] 251

Figure C.12. Representation of vortex along boundary of the surface. Adapted from [4]. 255

LIST OF TABLES

Table 3.1. Sections of Nastran input text file 9

Table 3.2. Partitioning steps of sets in static analysis. Adapted from [7] . . . 20

Table 4.1. Analytical frequencies of smaii scale rectangular tank by using Abramson's method 54

Table 4.2. First 5 frequencies of partially-filled steel rectangular tank with respect to changing tank thickness 55

Table 4.3. Partially-filled steel rectangular tank's error rates for its first 5 modes with respect to changing tank thickness 56

Table 4.4. First 5 frequencies of partially-filled plexiglass rectangular tank with respect to changing tank thickness 58

Table 4.5. Partially-filled plexiglass rectangular tank's error rates for its first 5 modes with respect to changing tank thickness 58

Table 4.6. First 5 frequencies of partially-filled plexiglass rectangular tank with respect to changing tank mesh resolution 60

Table 4.7. Partially-filled plexiglass rectangular tank's error rates for its first 5 modes with respect to changing tank mesh resolution 61

Table 4.8. First 5 frequencies of plexiglass rectangular tank with respect to changing element length-gap distance ratio (NR stands for "No results") 63

Table 4.9. Partially-filled plexiglass rectangular tank's error rates for its first 5 modes with respect to changing element length-gap distance ratio (NR stands for "No results") 64

Table 4.10. First 5 frequencies of plexiglass rectangular tank with respect to changing phantom mesh resolution 67

Table 4.11. Partially-filled plexiglass rectangular tank's error rates for its first 5 modes with respect to changing phantom mesh resolution 67

Table 4.12. First 5 frequencies of plexiglass rectangular tank with respect to changing tank thickness, tank mesh resolution, element length-gap distance ratio and phantom mesh resolution 69

Table 4.13. Partially-filled plexiglass rectangular tank's error rates for its first 5 modes with respect to changing tank thickness, tank mesh resolution, element length-gap distance ratio and phantom mesh resolution 70

Table 4.14. Comparison of analytical, numerical and laboratory experiment frequencies for plexiglass rectangular tank 72

Table 4.15. Comparison of numerical and experimental error rates for plexiglass rectangular tank 74

Table 4.16. First 5 frequencies of small scale rectangular tank with high rigidity with respect to tank thickness, tank mesh resolution, element length-gap distance ratio and phantom mesh resolution 77

Table 4.17. Error rates of partially-filled small scale rectangular tank with high rigidity for its first 5 modes with respect to tank thickness, tank mesh resolution, element length-gap distance ratio and phantom mesh resolution 78

Table 4.18. Analytical frequencies of large scale partially filled rectangular tanks by using Abramson's method 82

Table 4.19. First 5 frequencies of large scale rectangular tank with high rigidity with respect to tank thickness, tank mesh resolution, element length-gap distance ratio and phantom mesh resolution 84

Table 4.20. Partially-filled steel large scale rectangular tank[Pleaseinsertintopreamble]s error rates for its first 5 modes with respect to tank thickness, tank mesh resolution, element length-gap distance ratio and phantom mesh resolution 85

Table 4.21. Analytical frequencies of small scale partially filled cylindrical tanks by using Abramson's method 105

Table 4.22. First 5 frequencies of partially-filled steel cylindrical tank with phantom surface of unstructured mesh with respect to changing tank thickness 106

Table 4.23. Error rates of partially-filled steel cylindrical tank with phantom surface of unstructured mesh for its first 5 modes with respect to changing tank thickness 106

Table 4.24. First 5 frequencies of partially-filled steel cylindrical tank with phantom surface of butterfly mesh with respect to changing tank thickness 108

Table 4.25. Error rates of partially-filled steel cylindrical tank with phantom surface of butterfly mesh for its first 5 modes with respect to changing tank thickness 108

Table 4.26. First 5 frequencies of partially-filled steel cylindrical tank with phantom surface of radial mesh with respect to changing tank thickness 110

Table 4.27. Error rates of partially-filled steel cylindrical tank with phantom surface of radial mesh for its first 5 modes with respect to changing tank thickness 110

Table 4.28. First 5 frequencies of partially-filled plexiglass cylindrical tank with phantom surface of unstructured mesh respect to changing tank thickness 112

Table 4.29. Error rates of partially-filled plexiglass cylindrical tank with phantom surface of unstructured mesh for its first 5 modes with respect to changing tank thickness 112

Table 4.30. First 5 frequencies of partially-filled plexiglass cylindrical tank with phantom surface of radial mesh with respect to changing tank thickness 114

Table 4.31. Error rates of partially-filled plexiglass cylindrical tank with butterfly phantom surface for its first 5 modes with respect to changing tank thickness 114

Table 4.32. First 5 frequencies of partially-filled plexiglass cylindrical tank with phantom surface of radial mesh with respect to changing tank thickness 116

Table 4.33. Error rates of partially-filled plexiglass cylindrical tank with phantom surface of radial mesh for its first 5 modes with respect to changing tank thickness 116

Table 4.34. First 5 frequencies of partially-filled plexiglass cylindrical tank with phantom surface of unstructured mesh with respect to changing tank mesh resolution 118

Table 4.35. Error rates of partially-filled plexiglass cylindrical tank with phantom surface of unstructured mesh for its first 5 modes with respect to changing tank mesh resolution 119

Table 4.36. First 5 frequencies of partially-filled plexiglass cylindrical tank with phantom surface of butterfly mesh with respect to changing tank mesh resolution 120

Table 4.37. Error rates of partially-filled plexiglass cylindrical tank with phantom surface of butterfly mesh for its first 5 modes with respect to changing tank mesh resolution 120

Table 4.38. First 5 frequencies of partially-filled plexiglass cylindrical tank with phantom surface of radial mesh with respect to changing tank mesh resolution 122

Table 4.39. Error rates of partially-filled plexiglass cylindrical tank with phantom surface of radial mesh for its first 5 modes with respect to changing tank mesh resolution 122

Table 4.40. First 5 frequencies of partially-filled plexiglass cylindrical tank with phantom surface of unstructured mesh with respect to changing gap (NR stands for “No results”). 124

Table 4.41. Error rates of partially-filled plexiglass cylindrical tank with phantom surface of unstructured mesh for its first 5 modes with respect to changing gap 125

Table 4.42. First 5 frequencies of partially-filled plexiglass cylindrical tank with phantom surface of butterfly mesh with respect to changing gap (NR stands for "No results"). 127

Table 4.43. Error rates of partially-filled plexiglass cylindrical tank with phantom surface of butterfly mesh for its first 5 modes with respect to changing gap 127

Table 4.44. First 5 frequencies of partially-filled plexiglass cylindrical tank with phantom surface of radial mesh with respect to changing gap (NR stands for "No results"). 129

Table 4.45. Error rates of partially-filled plexiglass cylindrical tank with phantom surface of radial mesh for its first 5 modes with respect to changing gap 129

Table 4.46. First 5 frequencies of partially-filled plexiglass cylindrical tank with respect to changing phantom surface mesh topology 131

Table 4.47. Partially-filled plexiglass cylindrical tank's error rates for its first 5 modes with respect to changing phantom surface mesh topology resolution 132

Table 4.48. First 5 frequencies of partially-filled plexiglass cylindrical tank with phantom surface of unstructured mesh with respect to changing tank thickness, tank mesh resolution, phantom surface gap ratio and phantom surface mesh topology 134

Table 4.49. Error rates of partially-filled plexiglass cylindrical tank with unstructured mesh for its first 5 modes with respect to changing tank thickness, tank mesh resolution, phantom surface gap ratio and phantom surface mesh topology 135

Table 4.50. First 5 frequencies of partially-filled plexiglass cylindrical tank with butterfly mesh with respect to changing tank thickness, tank mesh resolution, phantom surface gap ratio and phantom surface mesh topology 136

Table 4.51. Error rates of partially-filled plexiglass cylindrical tank with phantom surface of butterfly mesh for its first 5 modes with respect to changing tank thickness, tank mesh resolution, phantom surface gap ratio and phantom surface mesh topology 137

Table 4.52. First 5 frequencies of partially-filled plexiglass cylindrical tank with radial mesh with respect to changing tank thickness, tank mesh resolution, phantom surface gap ratio and phantom surface mesh topology 138

Table 4.53. Error rates of partially-filled plexiglass cylindrical tank with phantom surface of radial mesh for its first 5 modes with respect to changing tank thickness, tank mesh resolution, phantom surface gap ratio and phantom surface mesh topology 139

Table 4.54. Comparison of analytical, numerical and laboratory experiment frequencies with each other for several modeshapes in cylindrical tank. 141

Table 4.55. Comparison of numerical and laboratory experiment error rates with each other for several modeshapes in cylindrical tank. 143

Table 4.56. First 5 frequencies of partially-filled highly rigid cylindrical tank with phantom surface of unstructured mesh with respect to changing tank thickness, tank mesh resolution, phantom surface gap ratio and phantom surface mesh topology 150

Table 4.57. Error rates of partially-filled highly rigid cylindrical tank with phantom surface of unstructured mesh for its first 5 modes with respect to changing tank thickness, tank mesh resolution, phantom surface gap ratio and phantom surface mesh topology 151

Table 4.58. First 5 frequencies of partially-filled highly rigid cylindrical tank with phantom surface of butterfly mesh with respect to changing tank thickness, tank mesh resolution, phantom surface gap ratio and phantom surface mesh topology 153

Table 4.59. Error rates of partially-filled highly rigid cylindrical tank with phantom surface of butterfly mesh for its first 5 modes with respect to changing tank thickness,tank mesh resolution, phantom surface gap ratio and phantom surface mesh topology 154

Table 4.60. First 5 frequencies of partially-filled highly rigid cylindrical tank with phantom surface of radial mesh with respect to changing tank thickness, tank mesh resolution, phantom surface gap ratio and phantom surface mesh topology 156

Table 4.61. Error rates of partially-filled highly rigid cylindrical tank with phantom surface of radial mesh for its first 5 modes with respect to changing tank thickness,tank mesh resolution, phantom surface gap ratio and phantom surface mesh topology 157

Table 4.62. Analytical frequencies of large scale partially filled cylindrical tanks by using Abramson's method 160

Table 4.63. First 5 frequencies of partially-filled steel large scale cylindrical tank with phantom surface of unstructured mesh with respect to changing tank thickness, tank mesh resolution, phantom surface gap ratio and phantom surface mesh topology 162

Table 4.64. Error rates of partially-filled steel large scale cylindrical tank with phantom surface of unstructured mesh for its first 5 modes with respect to changing tank thickness,tank mesh resolution, phantom surface gap ratio and phantom surface mesh topology 163

Table 4.65. First 5 frequencies of partially-filled steel large scale cylindrical tank with phantom surface of butterfly mesh with respect to changing tank thickness, tank mesh resolution, phantom surface gap ratio and phantom surface mesh topology 165

Table 4.66. Error rates of partially-filled large scale cylindrical tank with phantom surface of butterfly mesh for its first 5 modes with respect to changing tank thickness, tank mesh resolution, phantom surface gap ratio and phantom surface mesh topology 166

Table 4.67. First 5 frequencies of partially-filled steel large scale cylindrical tank with phantom surface of radial mesh with respect to changing tank thickness, tank mesh resolution, phantom surface gap ratio and phantom surface mesh topology 168

Table 4.68. Error rates of partially-filled large scale cylindrical tank with phantom surface of radial mesh for its first 5 modes with respect to changing tank thickness, tank mesh resolution, phantom surface gap ratio and phantom surface mesh topology 169

LIST OF SYMBOLS

$\vec{F}$	Force
g	Gravitational acceleration
p	Gage pressure
m_a	Virtual mass
P	Pressure
J_n	Bessel function
ω	Angular frequency
Φ	Velocity potential
ρ	Density
η	The wave height of free surface during sloshing

LIST OF ACRONYMS/ABBREVIATIONS

DOF	Degree of Freedom
MAC	Marker and Cell
MSC	MacNeal-Schwendler Corporation
NASA	National Aeronautics and Space Administration
NR	No Results
PS	Phantom Surface
VOF	Volume of Fluid
ZFS	Zero Free Surface

1. INTRODUCTION

Hydrodynamic loads that occur due to earthquake in partially-filled tanks can cause severe deformations on the structure. These deformations can affect both the society and the environment. If it is considered that the tanks mostly contain petrochemicals, it is vital to investigate this important phenomenon. In addition, these deformations can affect the corporations economically, as well. For instance, a fire, or an explosion in a refinery due to sloshing related deformation, besides to its danger to people, economically can demolish a corporation if it is noticed that millions of dollars are invested to these businesses.

Sloshing motion can be seen in many different places. The vessels under the effect of wave loads, the cars' fuel tanks under acceleration change can be exposed to sloshing motion. In 1960s the sloshing motion in the fuel tanks of spacecrafts are studied a lot by NASA. The study of Abramson as a NASA engineer during these studies became one of the backbones of steel tank design [1]. Nowadays, the gas tankers are used for transportation, frequently. Preventing tilt over motion of the tankers needs a focus on this important subject.

The earthquake of Marmara in 1999 caused a fire in petrochemical refinery of Tüpraş by deforming the tanks. The time of the earthquake of Marmara saved hundreds of employees from a disaster and only caused economical and environmental problems. The motivation of this study was born from preventing this kind of deformations by understanding the sloshing behaviour in a better way.

In this study, the optimum model in Nastran which is a structural analysis program in order to reach most accurate natural frequencies of sloshing motion as a result of eigenvalue analysis for given partially filled three dimensional rectangular and cylindrical tanks with different sizes is proposed. The accuracy of results are validated by comparing them with analytical values of natural frequencies. Obtaining the optimum model can give an opinion to other researchers who will use Nastran about how they

can enhance the accuracy of their results. Nastran is a program that was developed by NASA engineers and it uses virtual mass method. In this method, free surface is formed with very thin finite elements and linear spring elements are attached from free surface nodes to the ground for representing fluid behaviour instead of using fluid elements. The variables of tank thickness, tank material, tank mesh resolution, phantom surface mesh resolution, phantom surface mesh topology and its sizes are tested and the values that give most accurate natural frequencies are reached for given tanks. Also, for solving the problem of time consumption during modelling of the tanks, a computer script that helps to create the tank model and to implement eigenvalue analysis in Nastran is proposed as a part of this study. A reduction in time consumption is achieved.

To create a background knowledge to this study, the frequencies of sloshing motion in rectangular and cylindrical tanks are derived. Afterwards, the numerical method that is developed, virtual mass method, is investigated by using Nastran structural analysis program. Mathematical and physical background of this method can be found in this thesis. In order to use the method in most efficient way, to have an idea about what is going on the background of this method is considered as a good idea for this study. With this method, the fluid volume can be modelled without using any fluid elements. Instead of fluid elements, by using the sources and doublets that are located on the fluid structure boundaries the fluid is modelled.

In Chapter 3, numerical implementation of virtual mass method in Nastran is defined. Every step in order to create the numerical models and implementing analyses in Nastran are described.

In Chapter 4, numerical analyses are done for reaching frequencies of rectangular and cylindrical tanks by using Nastran. There are many studies in the literature about Nastran, however, when a literature survey is done for finding a study that works on the question of "how we can reach the optimum model in Nastran", we could not find anything. That is why, parametric studies that are about finding the effect on tank material, tank thickness, tank mesh resolution, phantom surface gap size and phantom surface mesh topology are completed in this study for different tank sizes. The results are compared with experimental study of Erginbas [3].

For our study, 2 Matlab scripts that are created with the aim of creating fast and efficient tool that can be used in Nastran eigenvalue analyses for rectangular and cylindrical tanks can be found.

2. LITERATURE REVIEW

Tanks have been used for a long time in several fields, such as storing the petroleum in a refinery, in order to keep the liquids in safe. As a result of external disturbances to the tank, the free surface of the fluid changes its position with respect time and this situation is called sloshing. Raouf Ibrahim also describes sloshing as "any motion of the free liquid surface inside its container", and this situation can be caused by any type disturbance for partially-filled container [8]. Since the sloshing motion can deform tanks due to the stresses formed on the tank, it is accepted as so crucial in the design context.

Many scientists have worked to understand this important phenomenon. In 1831, Faraday studied over fluids which have interaction with vibrating elastic surfaces [9]. In 1879, in his well-known book, Hydrodynamics, Sir Horace Lamb examined the theory of the sloshing motion [10]. In addition to tanks, effects of dynamic excitations over the dams, the fluid pressures over the walls, were studied in history, as well. Westergaard worked on the fluid pressures of a vertical and rectangular dam due to horizontal loads [11]. In 1949, Jacobsen calculated hydrodynamic masses of a fluid in a cylindrical tank under horizontal motion [12]. The convective and impulsive pressures of a rectangular tank were calculated by Graham and Rodriguez [13] and the convective and impulsive part of the fluid were modelled with equivalent fixed and spring mounted masses, respectively, by Housner in 1957 [2].

The researches about the sloshing intensified during the development of rocket and spacecraft designs in the 1960s. In evaluation report of a NASA vehicle's flight, Saturn I, the stability problem of the vehicle during its flight due to sloshing motion of the fuel was investigated in detail [14]. In another study, in 1966 for the space vehicle studies of NASA, Abramson pointed out that one of the problems of space vehicles was the coupling of control system frequencies, elastic body frequencies and fuel sloshing frequencies with each other [1]. In his same study, he analyzed the sloshing motion of liquids in moving containers by employing analytical and experimental methods.

In 1968, the effect of propellant slosh loads due to sloshing motion were explained for NASA Space Vehicle Design Criteria [15]. The study of Abramson in 1969 for suppressing the sloshing motion with several types of baffles, such as rigid-ring baffles and flexible fat ring baffles, became the part of the design criteria of NASA's space vehicles for sloshing [16].

In some situations, the differential equations can not be solved by using analytical methods. This problem can be seen for the sloshing motions in a container, as well. In these times, numerical methods can be an answer. The development of more advanced computers and computational methods let the researchers to use numerical methods easily and more frequently. One of numerical methods that is developed is Marker and Cell (MAC) method. In 1965, Harlow and Welch improved the method of MAC in order to solve problems that arise from defining the free surface boundary conditions by using velocity and pressure for the first time as the main variables [17]. In this method, Navier-Stokes equation for incompressible fluid are solved by using explicit finite difference scheme. In 1975, Von Kerczek compiled the studies that use numerical techniques for solving differential equation of free-surface problems [18]. Faltinsen investigated the two dimensional flow of a fluid with a numerical method in 1978 and by this method exact nonlinear free surface conditions were reached [19]. Another method is developed by Nakayama and Washizu in 1980 where pitch excitations with big amplitudes was implemented to rigid, open tank in a reference coordinate system fixed to the tank for the first time [20]. In 1981, Hirt and Nichols created the method of Volume of Fluid (VOF) where the free boundary movements could be represented more efficient than other methods at that time [21]. In 1996, Chen created a method for simulating nonlinear sloshing motion of free surface due to seismic excitation [22]. The method used a curvilinear mesh system and mapped nonlinear sloshing motion from non-rectangular physical domain to rectangular computational domain. In 2004, the work of Nakayama and Washizu were followed by Cho and Lee. Cho and Lee examined the large amplitudes of sloshing movement modelled with non-linear finite elements in two dimensional tank under horizontal sinusoidal excitation [23]. In 2009, Liu and Lin utilized virtual boundary force method for examining the effect of vertical baffles on the tank [24].

In the literature, the researches by employing Nastran which is adopted by us for our study, as well, can be found. In 1997, Kim and Lee examined the natural sloshing modes and hydroelastic modes of a rectangular tank and compared them with analytical values by using free surface matrix formulation in Nastran [25]. Another research was done by Hatanaka and Yoshida in 1998 for understanding the dynamic stresses over a fuel tank of a vehicle where the fuel was modelled by using virtual mass method [26]. In 2012, Wu *et al.* completed a dynamic analyses of a satellite structure with liquid propellant consuming [27] by using virtual mass and other methods, such as beam modeling method, and as a result of this analysis it was seen that as the liquid propellant was consumed the frequencies of the main modeshapes were increasing. Yazici *et al.* used the Nastran virtual mass method to study the sloshing modes of rectangular and cylindrical tanks containing water [28].

As a general fact, the modelling of the geometries and finite elements has high significance in terms of reaching accurate results in numerical modelling. When the literature is examined, it is seen that there are many studies which utilize Nastran and its virtual mass method. However, there are no any study which can recommend an optimum modelling way by investigating modelling parameters for virtual mass method in Nastran. For contributing to this area, in our study, the optimum model for eigenvalue analysis of fluids in partially filled rectangular and cylindrical tanks using virtual mass method in Nastran is going to be investigated.

In this study, after examining the literature, the works of Abramson [1] and Housner [2] are used as the analytical method which will be used as a benchmark of natural frequencies. In his work, Abramson had the assumption of incompressible, inviscid and irrotational fluid for reaching the natural frequencies of partially filled rectangular and cylindrical tanks and he solved the Laplace's equation as the governing equation by using potential flow theory. According to his study, it was found out that the natural frequencies of the partially filled rectangular and cylindrical tank depends on gravitational acceleration, length and width of the rectangular tank and radius of the cylindrical tank, height of fluid, and modeshape of the free surface.

For our study, another method used from the literature is virtual mass method of Nastran. This method is created in 1977 by Nastran engineers [29] and like in the case of Abramson's work in 1966, the assumption of incompressible, inviscid and irrotational fluid were made. In addition, as the result of linear finite element theory, it was assumed that the fluid displacements are small and with this situation nonlinear terms could be neglected during calculations. Laplace's equation was employed as the governing equation like in Abramson's study whereas also the potential flow theory was used. The fluid volume was created with sources located at the center of finite elements which have interaction with fluid instead of fluid elements. Sloshing of free surface was envisioned with triangular or quadrilateral thin finite elements that was connected to ground with linear spring elements. These linear spring elements were used to simulate gravitational pull of the fluid.

3. NUMERICAL IMPLEMENTATION OF VIRTUAL MASS METHOD

As a part of the research, the numerical models are created and analyzed by using MSC Nastran structural analysis program. In Nastran, many analyses, such as eigenvalue, linear buckling, linear static analyses and more, can be implemented [30]. Since the aim of our study is to investigate the frequencies and modeshapes of the sloshing motion in rectangular and cylindrical tanks, among all of the analyses types which can be chosen eigenvalue analysis is employed. In addition, for creating the model of free surface, the linear static analysis is practiced.

Nastran uses a text-based user interface instead of a graphical user interface. For creating a model in Nastran, the user should open an input file which is a text file and fill this input file with Nastran's keywords by hand which basically give the form of the model and analysis. In Nastran parlance, these Nastran keywords are called "cards" [30]. If it is considered that a finite element model can have many nodes, elements, boundary conditions, loads and etc., it is noticed that writing all of these inputs by utilizing a text-based user interface will cause huge amount of time consumption to the user. In order to reduce the dedicated time for forming finite element models of rectangular and cylindrical tanks for our study, a computer script is written in a numerical computing software, Matlab, where the details of the script can be found in corresponding Appendix chapter "Computer Scripts for Creating Rectangular and Cylindrical Tank Models and Implementing SOL 1O3 Analyses in Nastran". When an input file is examined, generally it can be easily noticed that the majority of the keywords that are typed are nodes and elements as a result of the repetitive nature of them, and therefore, parallel to this situation, with this script, most of the time is saved by automatically creating tank nodes and elements. The input file of Nastran has the extension of "bdf" which is the abbreviation of Bulk Data File and it is divided into sections in order to form the file easily. These sections are shown below

Table 3.1. Sections of Nastran input text file

Nastran Statement	Optional Section
File Management Section	Optional Section
Executive Control Section	Required Section
CEND	Required Delimiter
Case Control Section	Required Section
BEGIN BULK	Required Delimiter
Bulk Data Section	Required Section
ENDDATA	Required Delimiter

Nastran Statement section is used to change the default values of operational parameters for controlling the inner solution steps of the program. For instance, by printing the card of PARALLEL=0 in this section, parallel processing of matrix operations are deactivated.

File Management Section lets the user attaching and initializing databases and files of Nastran. For example, by writing INCLUDE keyword, external files can be assigned to the input file.

Executive Control Section is the first required section that must be filled by the user. In this section the user chooses the analysis type. For our study, the keywords of “SOL 101” and “SOL 103” are written in this section where they denote linear static and eigenvalue analysis, respectively. This section ends by printing the required delimiter of CEND.

Case Control Section has the function of selecting constraints and loads that are defined in bulk data section, choosing output requests such as displacement and acceleration of grid points, and defining subcases that allows implementing multiple loadings in single analysis.

The last section of Nastran's input file is Bulk Data Section. It starts with the required delimiter of BEGIN BULK and it includes all the information for creating finite element model. These informations are nodes and elements, boundary conditions, loads, properties of materials and elements, coordinate systems and geometries. Finally the input file ends with ENDDATA keyword.

The finite element models of rectangular and cylindrical tanks that are formed in Nastran consist of tank bottom, tank wall, phantom surface and spring elements. In order to describe these finite element models and implement SOL 103, real eigenvalue analysis, in Nastran, the concept of phantom surface and spring elements from virtual mass method should be explained initially.

As it is explained in the previous chapter, the free surface of the fluid is not modelled with fluid elements in Nastran. Instead of fluid elements, free surface is modelled with a very thin shell triangular or quadrilateral elements. This surface is called "phantom surface" in Nastran parlance and it is attached to the ground from its nodes by linear elastic springs which have the direction of gravity. The purpose of modelling phantom surface is basically envision the sloshing motion of the free surface. For modelling the phantom surface well, some conditions have to be satisfied. Firstly, phantom surface must be very thin in order to have smallest possible stiffness added to system. The reason of this requirement is that since the phantom surface is only used to visualize the sloshing motion of free surface, its side effects are wanted to be minimized [31]. In addition, Nastran calculates the mass of the models by multiplying defined material density and its volume. In order to prevent adding the mass of the phantom surface to the system, density of phantom surface's material must not be defined [31]. Another point that needs to be paid attention is the aspect ratio of the phantom surface elements. The closest frequencies to the analytical results are reached

by using elements with aspect ratio that is under 2 [29]. This situation is valid for tank model, as well. In our study, several phantom surface mesh topologies are used for rectangular and cylindrical tanks. Structured mesh topology of rectangular tank can be seen from Figure 4.2 whereas unstructured, butterfly, and radial mesh topologies for phantom surface of cylindrical tank can be found in Figures of 4.30, 4.31, and 4.32.

To create the phantom surface geometry, GRID, CQUAD4, and CTRIA3 cards are used in Nastran. GRID card denotes the location of a node whereas CQUAD4 and CTRIA3 represent quadrilateral and triangular finite elements, respectively. These elements are formed by connecting GRID points with each other. After creating the geometry of the phantom surface, the material and element properties are assigned to the model by MAT1 and PSHELL cards, respectively. MAT1 card includes the information of Young Modulus, Poisson's ratio and density of the material. On the other hand, PSHELL card denotes thickness of the phantom surface in our study. A phantom surface model during sloshing motion for rectangular tank is shared below for visualizing it.

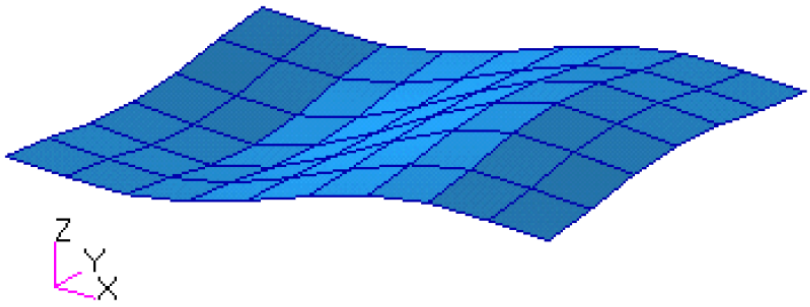

Figure 3.1. Representation of phantom surface of a rectangular tank during sloshing motion

Phantom surface should be able to represent the flexible nature of sloshing motion. That is why for the phantom surface a flexible enough material should be chosen. 3 different cases with 3 different Young Modulus values which are 1 GPa, 69 GPa, and 1000 GPa are tried for determining the most suitable phantom surface material to

be able to use in the analyses. Materials with 1 GPa and 1000 GPa Young Modulus values are examined to see the effects of having very flexible and rigid materials as phantom surface material to the natural frequency. On the other hand, material with 69 GPa Young Modulus is aluminum where it is used in Nastran document "Virtual Mass Problem" [31] and practicing this Nastran document's application is wanted to be examined, as well. It is seen that 1 GPa and 69 GPa materials gave almost the same reasonable results with each other for the static and eigenvalue analyses whereas material with 1000 GPa Young Modulus static analysis results are almost the same with other 2 cases and its natural frequency results are way too higher than 1 GPa and 69 GPa materials. Using an isotropic material for phantom surface is recommended in the document of Nastran "Virtual Mass Sample Problem" [31] by using MAT1 entry where MAT1 enrty is utilized in Nastran for defining isotropic materials. Since aluminum is an isotropic material as well, it is considered as a good choice for using in our analyses. For comparison, the images of phantom surface with aluminum and 1000 GPa material during sloshing are demonstrated below. When the Figures of 3.2 3.3 and 3.4 from laboratory experiment used in this study are compared it can be noticed that aluminum phantom surface is more similar to the image from experiment. Aluminum phantom surface is able to have curvatures around its lowest and highest pick points where phantom surface with 1000 GPa material has basically a more strict shape. From these figures, again, it can be concluded that the aluminum is a better material compare to material with 1000 GPa Young Modulus for using in the analyses.

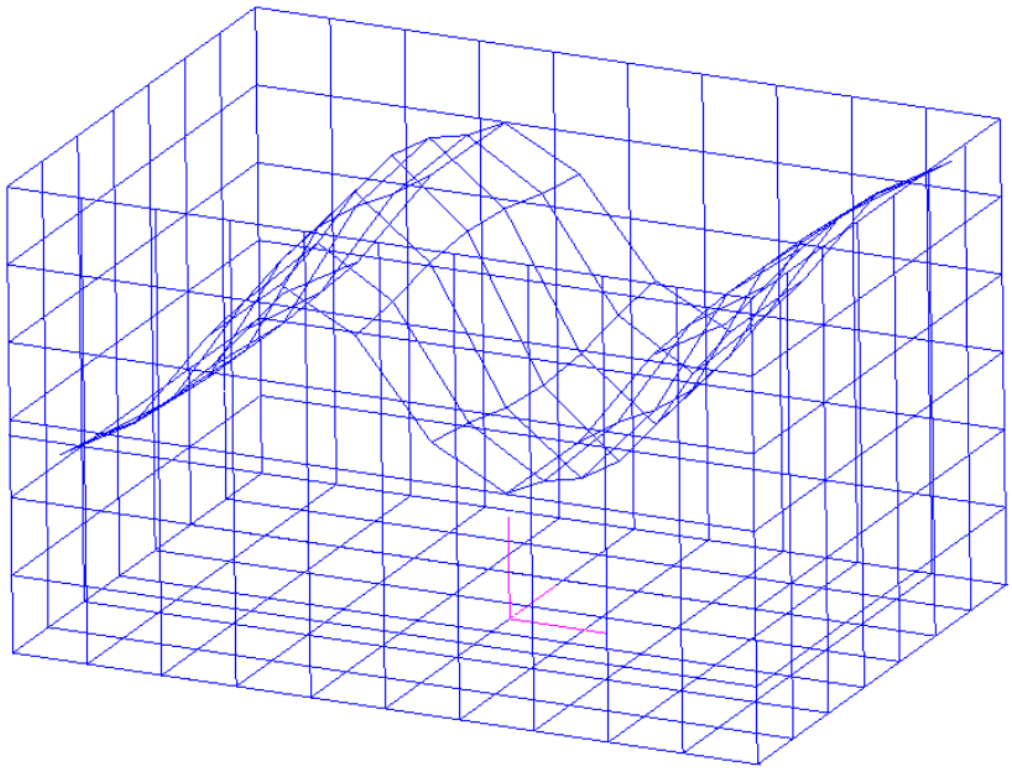

Figure 3.2. Sloshing motion of aluminum phantom surface

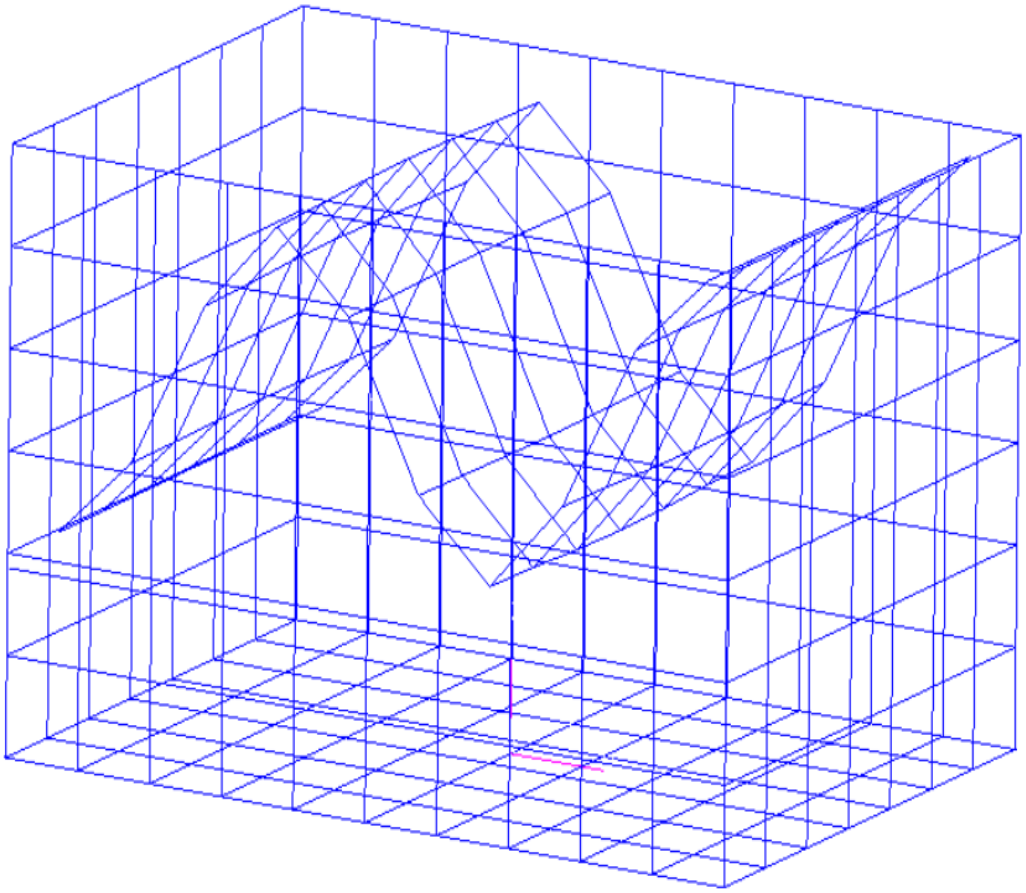

Figure 3.3. Sloshing motion of phantom surface that has material with 1000 GPa Young Modulus

The image from laboratory experiment are demonstrated below in order to compare with the images from numerical models above

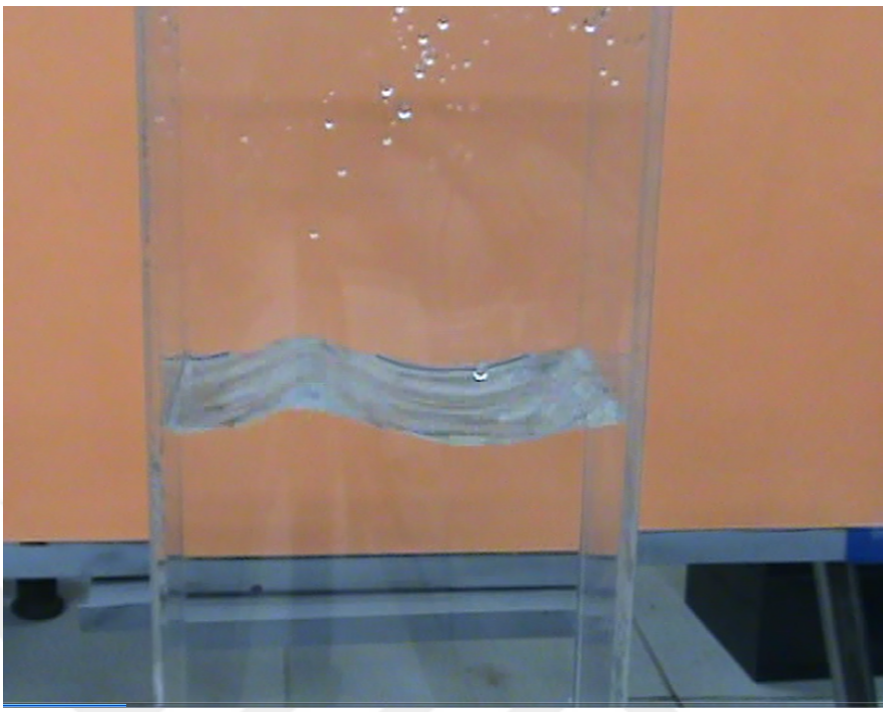

Figure 3.4. Representation of sloshing motion of free surface during laboratory experiment of plexiglass rectangular tank [3].

Translational boundary conditions on x and y axes, and rotational boundary conditions in all axes are implemented to all nodes of phantom surface model by using SPC1 card. SPC basically stands for "single point constraint" [30]. The reason of leaving translational boundary conditions on z axis unconstrained is to be able to show the sloshing motion of phantom surface.

The size of the phantom surface is another important aspect of creating the model. Phantom surface can not have the size of free surface, in other words, free surface can not be enclosed fully by phantom surface. This situation causes the singularity of the results, thus, in order to prevent this situation, a phantom surface that is smaller than free surface must be chosen. Since in the literature how close the phantom surface should be to the tank walls are not studied, in our study this topic is examined. The details of the study are found in chapter of "Numerical Analysis of Modes and Comparison of Analytical, Numerical and Experimental Results". The images of phantom

surface from the top of rectangular and cylindrical tanks which show gap distance can be found below

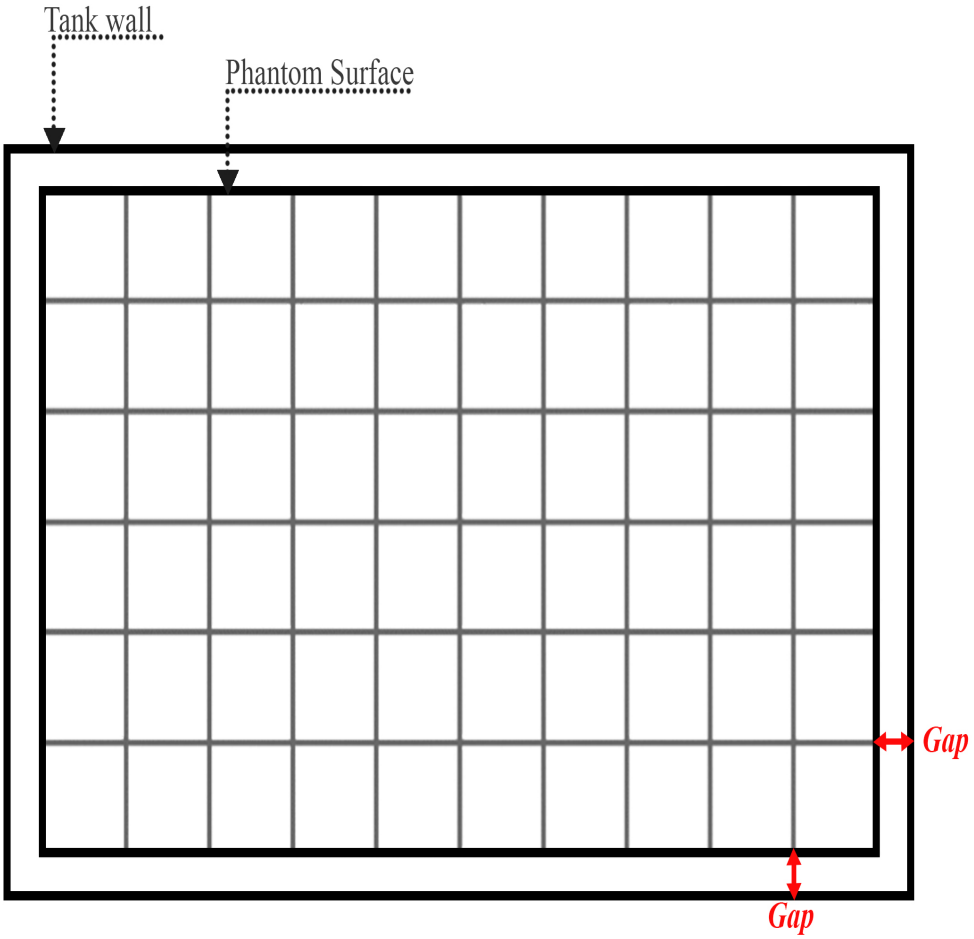

Figure 3.5. Representation of gap distance between phantom surface and tank wall from the top of the rectangular tank

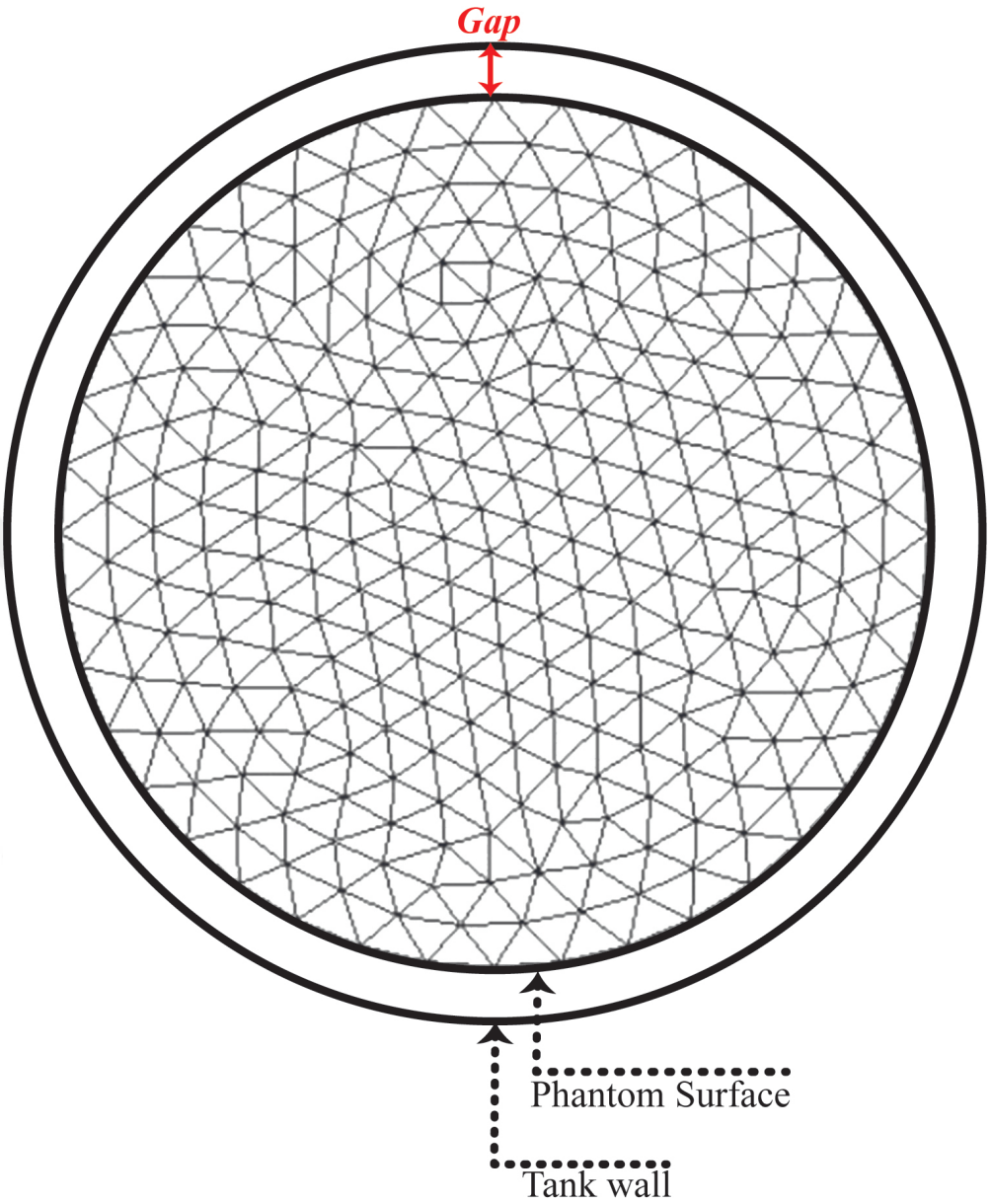

Figure 3.6. Representation of gap distance between phantom surface and tank wall from the top of the cylindrical tank

To create our model, lastly, phantom surface is attached to the ground from its nodes by linear springs which has the direction of gravity. These linear springs are assigned to the input file by CELAS2 card. CELAS2 card denotes the stiffness values of these linear springs. The reason of using these linear springs is to simulate the

sloshing behaviour of fluid under gravitational pull. For finding the stiffness value of them, the pressure which is the multiplication of the gravity and fluid density is implemented to the phantom surface's each element by using PLOAD2 card in a linear static analysis which is called SOL 101 in Nastran parlance. With PLOAD2 card a uniform static pressure load can be applied to shell elements such as CTRIA3 and CQUAD4 elements. For static analysis, all of the nodes of the phantom surface are constrained in all 6 directions and the reactions at these nodes are taken as the stiffness values of the spring elements [31].

The following equation demonstrates the formula to obtain the stiffness value of spring elements

$$K_i = A_i \times \rho \times g \tag{3.1}$$

where K_i is the stiffness value of one spring element, A_i is the area around i^{th} node of phantom surface, ρ is the fluid density, g is the acceleration of gravity and i is the node number of a phantom surface that a spring element is connected.

When the pressure is applied to the each phantom surface element, the net force is assigned to the nodes by multiplying the area, A_i, that affects that node and at these nodes the stiffness values of linear springs are calculated. These values changes with respect to its position on the phantom surface where it depends on 3 situations; the nodes on corner, edge and interior of the phantom surface. In the figure below, for the rectangular phantom surface case, this effected area is demonstrated

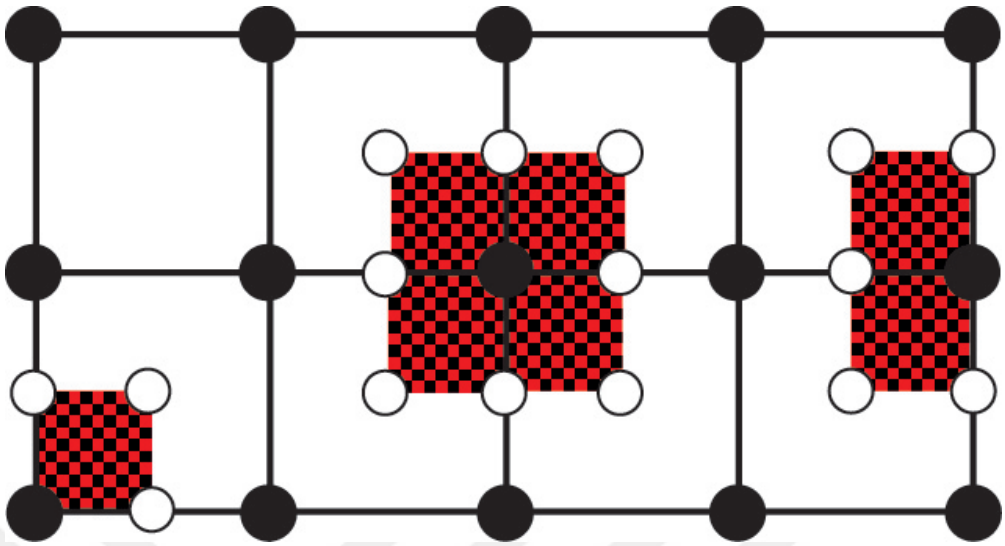

Figure 3.7. Area distribution over the nodes at corner, edge and interior of the phantom surface. Adapted from [4]

In the figure above, the areas that affects the nodes changes with respect to its positions at corner, edge or interior of the phantom surface are shown. The interior node gets the bigger area over itself since there are contribution of 4 elements whereas edge nodes gets only 2 parts of areas that comes from 2 adjacent elements, and lastly, the corner node has the smallest area on the calculations of reaction force since it has connection with only 1 element. Since the reaction force at these nodes corresponds to linear springs' stiffness values in our study, these distributed areas are basically A_i values from Equation 3.1. Therefore, by taking these areas and multiply them with density and gravitational acceleration, we will reach stiffness values of linear springs.

In order to give a better understanding to linear static analysis, the matrix operations behind it is studied. In Nastran, all of the local displacement at all of the grid and scalar points get together and named as global displacement. Global displacement can also be called as g-set where in matrix operations it is the top level set [7]. Notation of $\{u_g\}$ is used for denoting g-set displacement. Mathematically, finite element model's static equilibrium can be shown by using g-set as follows

$$[K_{gg}]\{u_g\} = \{P_g\} \tag{3.2}$$

where $\{P_g\}$ is the load vector that is implemented to grid and scalar points and $[K_{gg}]$ is the global stiffness matrix. This stiffness matrix $[K_{gg}]$ includes all of the elements' stiffness matrices. On the other hand, the load vector is created by assembling the loads within given loading condition. In Nastran, the loads which are used within the elements are assigned to the grid points. The sizes of $\{u_g\}$ and $\{P_g\}$ vectors are found by multiplying number of grid points with 6 that comes from degree of freedom and adding it with scalar points. On the other hand, the matrix of $[K_{gg}]$ is a symmetric and real matrix.

In Nastran calculations, g-set denotes the unconstrained set of structural equations and can be divided into two subsets where they are called m-sets and n-sets. m-set is used to denote dependent degree of freedom connections such as rigid body element, RBE2. n-set, on the other hand, denotes the independent degree of freedom when dependent ones are taken out from active set of equations [7]. By employing n-set, single point constraints can be implemented to the independent equations by continuing to the partition of equations. sb-set is called for the degrees of freedom that is defined by SPCi cards and sn-set is used for degrees of freedom that is denoted in GRID card's field 8. When we get sb-set and sn-set together s-set is obtained. After implementing s-set constraints to n-set, f-set is remained where it denotes the free degree of freedom. When implemented constraints are thoroughly chosen, f-set gives us the statically stable solution, in other words, a nonsingular stiffness matrix [7]. The partition of global displacement or g-set to f-set are demonstrated in the table below

Table 3.2. Partitioning steps of sets in static analysis. Adapted from [7]

g-set - m-set = n-set
n-set - s-set = f-set

As it was declared before The phantom surface is constrained with single point constraints by using SPC1 card for static analysis in all 6 degree of freedom in Nastran. These constraints are implemented to the s-set, $\{u_s\}$ as

$$\{u_s\} = \{y_s\} \tag{3.3}$$

where $\{y_s\}$ is the enforced deformation vector and its all or any elements can be zero. Afterwards, partitioning of n-set, $\{u_n\}$ into s-set, $\{u_s\}$ and f-set,$\{u_f\}$, is applied as

$$\{u_n\} = \begin{Bmatrix} u_s \\ u_f \end{Bmatrix} \tag{3.4}$$

The stiffness matrix, $[K_{nn}]$ is also partitioned as follows

$$K_{nn} = \begin{bmatrix} K_{ff} & K_{fs} \\ K_{fs}^T & K_{ss} \end{bmatrix} \tag{3.5}$$

Single point forces of constraint is written in matrix form too for having a complete structural equations matrix as it can be found below

$$\begin{bmatrix} K_{ff} & K_{fs} & 0 \\ K_{fs}^T & K_{ss} & -I \\ 0 & I & 0 \end{bmatrix} \begin{Bmatrix} u_f \\ u_s \\ q_s \end{Bmatrix} = \begin{Bmatrix} \bar{P}_f \\ P_s \\ Y_s \end{Bmatrix} \tag{3.6}$$

After the elimination

$$[K_{ff}]\{u_f\} = \{\bar{P}_f\} - [K_{fs}]\{Y_s\} = \{P_f\} \quad (3.7)$$

The forces of single point constraint are reached from Equation 3.7 as

$$\{q_s\} = -\{P_s\} + [K_{fs}^T]\{u_f\} + [K_{ss}]\{u_s\} \quad (3.8)$$

where $\{q_s\}$ is the vector of forces of single point constraint.

Since modelling phantom surface and spring elements are completed, now tank bottom and tank wall can be modelled, as well. Like in the case of phantom surface, the nodes of tank bottom and tank wall are formed by GRID card entries. For rectangular tank, nodes of tank bottom are joined by CQUAD4 quadrilateral element cards and created a structured mesh whereas in the case of cylindrical tank, CTRIA3 triangular element cards get the nodes of tank bottom together and created an unstructured mesh. In order to model the tank wall, for both rectangular and cylindrical tanks, again, the nodes are formed with GRID elements and they are joined with each other by CQUAD4 quadrilateral element cards.

X and y coordinates of the nodes at tank wall are taken same with tank bottom nodes' x and y coordinates and only the z coordinate of tank wall nodes are changed. By using this way, the quadrilateral elements of tank wall can have CQUAD4 structured elements. The material and element properties are again assigned by MAT1 and PSHELL cards. For tank bottom and tank wall, the same material and element properties are chosen.

Lastly, all of the tank bottom nodes are constrained in all directions by using SPC1 card in order to prevent its rigid body motion during analysis.

In Nastran, since there are no any fluid elements, the fluid volume must be defined by the user. In order to do this task, ELIST and MFLUID cards are used in Nastran. With ELIST card entry, the element identification numbers of structural elements in the tank, such as CQUAD4 or CTRIA3 elements, that are wetted are written. These wetted elements are used to generate virtual fluid mass matrix. When a structural element is printed in this entry, since it has 2 sides as a shell element, the wetted side of the element should be defined. In order to define this, the right hand rule is applied. In the right hand rule, the identification number of GRID points at the corner of the structural elements are used. When we move our right hand through the increasing sequence of GRID point numbers , our thumb shows the wetted side of the element by default. For choosing the other side of the same element as wetted, a minus sign can be inserted in front of element identification numbers in ELIST entry. Right hand rule is represented in the figure below

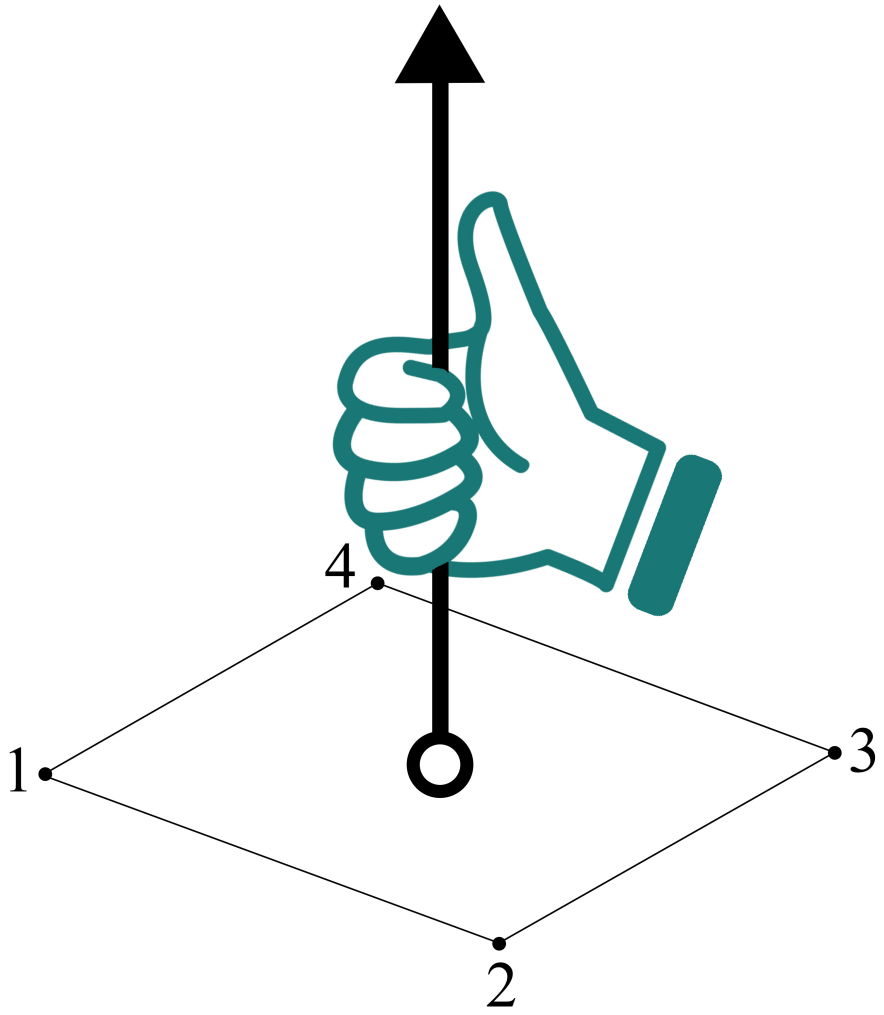

Figure 3.8. Right Hand Rule representation for deciding positive side of the CTRIA3 or CQUAD4 elements. Adapted from [4]

Another important card that is used to define fluid volume is MFLUID card. With MFLUID card, fluid volume properties are defined for forming virtual mass matrix. In this entry, as one of the fluid volume properties, the fluid density is determined. Also, MFLUID card is utilized to denote the height of the fluid. If only the ELIST entry would be used to decide the wetted elements, then the fluid height would always have been at the edges of the structural elements on the tank wall. However, by using MFLUID card's zero free surface (ZFS) field, the height of fluid can be freely adjusted

to any height. Defining ZFS height gives the freedom of having fluid at any height, but on the other hand, it causes to have partially wetted elements that are intersected by fluid height. In this situation virtual mass is found for partially wetted elements as well. As it can noticed, this case can cause error on calculations since the virtual mass above the fluid height is calculated, as well, even though the fluid is not at that level. However, by Nastran, for minimizing this effect, refined tank mesh density is suggested [4]. As the tank mesh gets refined, the area of the part above of ZFS will get smaller and its contribution to the virtual mass calculation will decrease. In addition, even though by ELIST card the wetted elements are indicated, only the ones under zero free surface height (ZFS) of the model are actually wetted. Thus, in order to make phantom surface elements wetted, ZFS entry must be higher than phantom surface height. The relation between ZFS and phantom surface (PS) can be found in the figure below

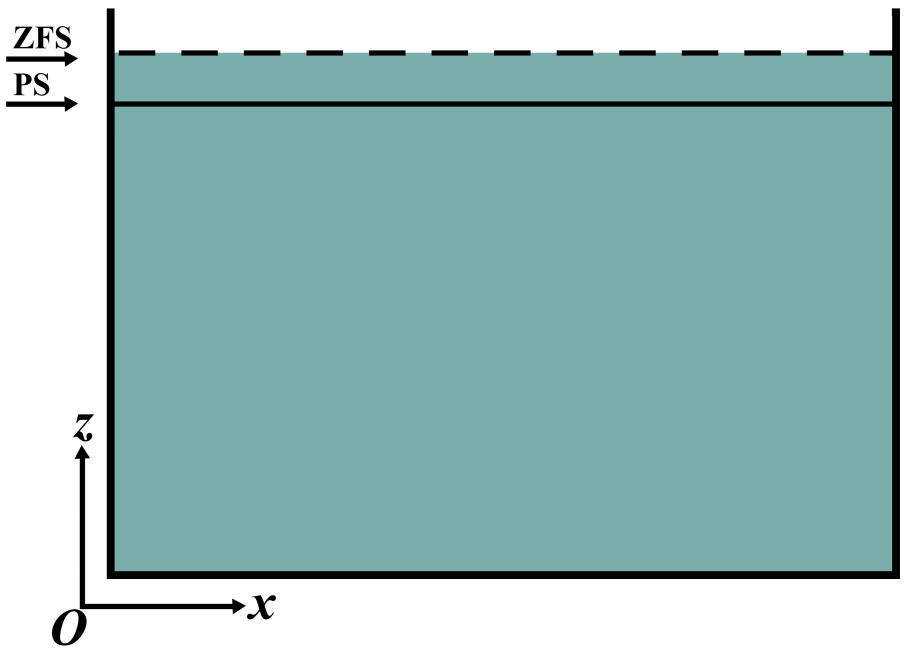

Figure 3.9. ZFS and free surface heights [5]

Lastly, EIGRL card is employed in order to define the real eigenvalue analysis by using Lanczos method which is an eigenvalue analysis procedure for large-scale problems [32]. Also, the number of desired natural frequencies extracted are defined by EIGRL card.

After implementing all the steps that are told in this chapter, finally, the model is formed and the eigenvalue analysis is ready to run. The following figures below shows samples of rectangular and cylindrical tanks that can be created when the steps above are followed

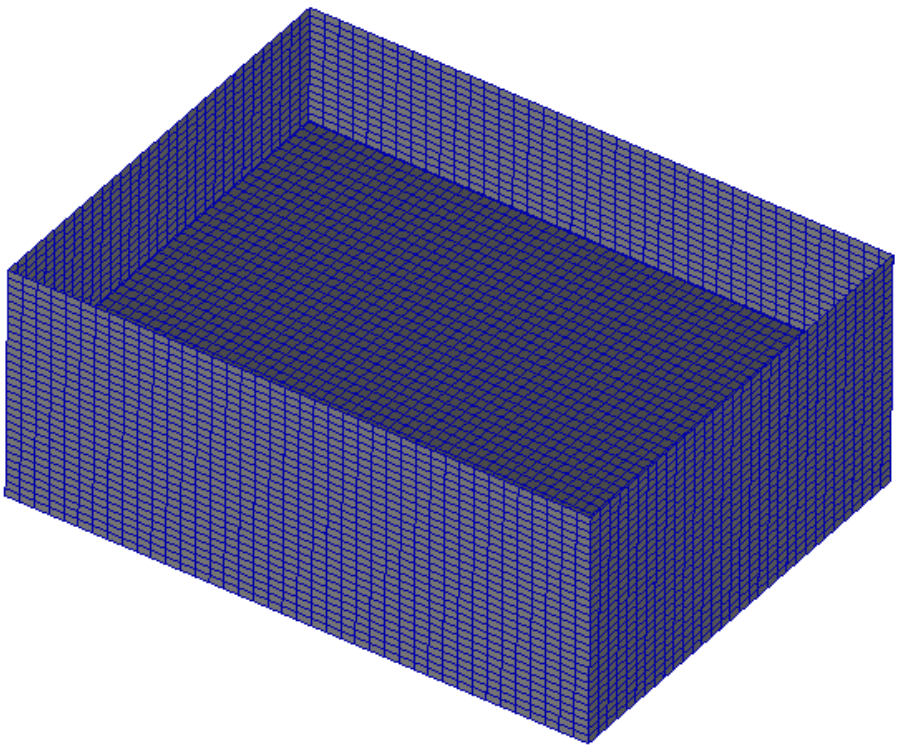

Figure 3.10. Representation of a rectangular tank model of Nastran

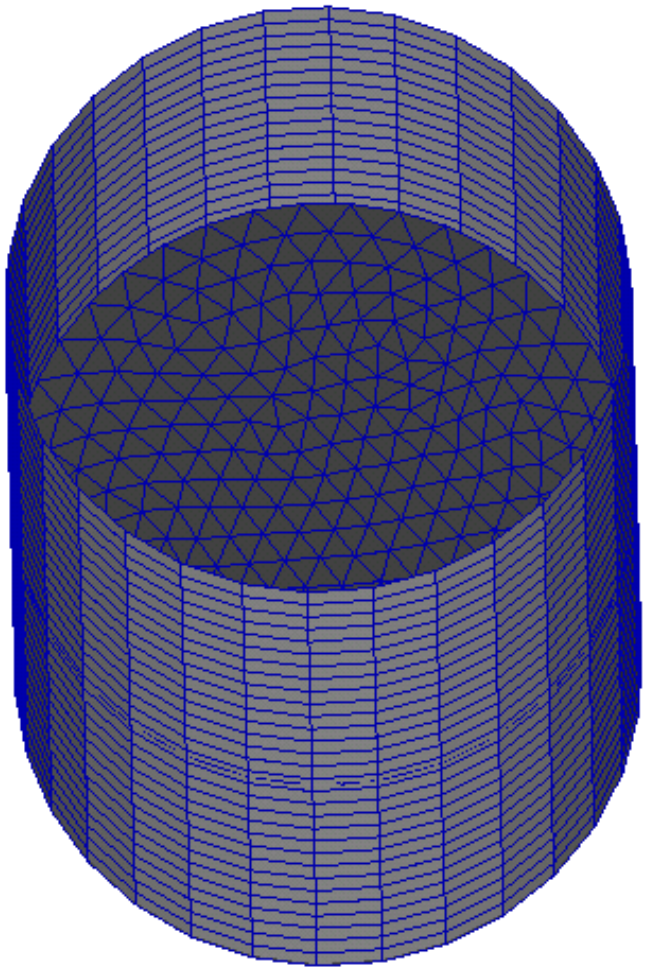

Figure 3.11. Representation of a cylindrical tank model of Nastran

As a result of creating the model and starting the eigenvalue analysis in Nastran, the virtual mass matrix is formed as it is explained in Appendix chapter of "Mathematical Derivation of Sloshing Motion for MSC Nastran". In terms of matrix operations of eigenvalue analysis, the following equation is formed

$$[M_s + M_v]\{\ddot{u}\} + [K_s]\{u\} = 0 \tag{3.9}$$

where M_s is the structural mass matrix, M_v is the virtual mass matrix, K_s is the structural stiffness matrix, u is the displacement and $\ddot{u}$ is the acceleration [33]. This equation is solved and natural frequencies are obtained from here. This equation in Nastran is solved by using Lanczos method [34].

The generalized eigenvalue problem of free vibration for the partially filled containers are demonstrated below

$$Kx = \omega^2 Mx \tag{3.10}$$

where K is a symmetric positive semi-definite stiffness matrix, x is the eigenvectors or modeshapes, ω is the eigenvalue and M is a symmetric positive definite matrix. Lanczos method solves standart eigenvalue problems, thus, in order to utilize Lanczos method, the generalized eigenvalue problem is transformed to the standart eigenvalue problem which has basically the form of $Av = \lambda v$. The solution of Equation 3.10 will give biggest eigenvalues, however, in our case the smallest eigenvalues are wanted to be obtained. Thus, a shift, σ, close to eigenvalue that we are looking for is implemented and afterwards the problem is inverted [32]. The shift and inversion is applied as follows

$$\omega^2 = 1/\lambda + \sigma \tag{3.11}$$

After applying Equation 3.11 into Equation 3.10, we will have

$$Kx = (1/\lambda + \sigma)Mx \tag{3.12}$$

After multiplying both sides of Equation 3.12 with λ

$$K\lambda x = Mx + \sigma\lambda Mx \tag{3.13}$$

After reorganizing Equation 3.13

$$\lambda[K - \sigma M]x = Mx \tag{3.14}$$

When both sides of Equation 3.14 is multiplied by $[K - \sigma]^{-1}$, it is reached to

$$\lambda x = [K - \sigma M]^{-1} Mx \tag{3.15}$$

If we call

$$A = [K - \sigma M]^{-1} M \tag{3.16}$$

and substituting Equation 3.16 into Equation 3.14, we have

$$Ax = \lambda x \tag{3.17}$$

where it is in the form of standart eigenvalue equation. Now Lanczos method can be applied to the problem.

Lanczos method needs the computation of the vector quantity Av for a given v. In order to prevent having computational cost in Equation 3.16 where it involves the calculation of inverse of a matrix, the following steps are implemented. Firstly, the matrix that is wanted to be inverted from Equation 3.16 is named as $\bar{K}$ and factorized as

$$\bar{K} = [K - \sigma M] = LDL^T \tag{3.18}$$

where L is a lower triangular matrix with unit diagonal, L^T is the upper triangular matrix with the help of symmetry, and D is a diagonal matrix. Afterwards, the equation above is reorganized and called as y

$$Av = (LDL^T)^{-1}Mv \tag{3.19}$$

$$L^TAv = LD^{-1}Mv = y \tag{3.20}$$

Solving for y

$$LDy = Mv \tag{3.21}$$

Then solving for Av gives

$$L^T(Av) = y \tag{3.22}$$

Lanczos method utilizes recursion formula in order to solve standart eigenvalue problem $Ax = \lambda x$. As a consequence of implementing Lanczos recursion, Lanczos vectors and elements of tridiagonal matrix, T, is created [32].

$$Tq = \lambda q \tag{3.23}$$

where T matrix has α on diagonal and β off diagonal as follows

$$\begin{bmatrix} \alpha_1 & \beta_2 & & & \\ \beta_2 & \alpha_2 & \beta_3 & & \\ & \beta_3 & \alpha_3 & \beta_4 & \\ & & \beta_4 & \alpha_4 & \beta_5 \\ & & ... & & \end{bmatrix}$$

The steps in order to reach the tridiagonal form can be seen below

1. Initialization

A starting vector v_1 is chosen and it is normalized, $|v_1| = 1$. Afterwards $\beta_1 = 0$ and $v_0 = 0$ are set.

2. Iteration

for i =1,2,3 .... m the steps are applied until convergence as follows

$$w = Av_i - \beta_i v_{i-1} \tag{3.24}$$

Afterwards

$$\alpha_i = v_i^T w \tag{3.25}$$

$$c = w - \alpha_i H v_i \tag{3.26}$$

$$\beta_{i+1} = [c^T H c]^{1/2} \tag{3.27}$$

$$v_{i+1} = c/\beta_{i+1} \tag{3.28}$$

where H denotes mass matrix M, w and c are temporary vectors, α vector is the diagonal terms of T matrix and β vector is the off-diagonal term. Lastly, Lanczos vectors are $v_1, v_2, ..v_m$. Order of m is usually equal to twice the desired number of eigenvalues and eigenvectors, usually less than 50.

Eigenvector q is found for each eigenvalue λ of T_m where

$$T_m q = \lambda q \tag{3.29}$$

Therefore, the natural frequencies are found by

$$\omega^2 = \sigma + 1/\lambda \tag{3.30}$$

4. NUMERICAL ANALYSIS OF MODES AND COMPARISON OF ANALYTICAL, NUMERICAL AND EXPERIMENTAL RESULTS

4.1. Rectangular Tanks

In this section, the frequencies that are obtained by analytical, numerical and experimental methods for a partially-filled rectangular tank are examined. 2 different analytical methods are employed in order to increase the reliability of our analytical results in comparison. For this aim, the frequency formulas from the chapter of "Mathematical Derivation of Natural Frequency from Housner's Analytical Method Study" and "Mathematical Derivation of Sloshing Motion for Rectangular and Cylindrical Tank" and are employed. The frequencies from numerical analyses are obtained by using MSC Nastran structural analysis program and for the laboratory experiments' results, the data of Erginbas [3] is used.

4.1.1. Small Scale Tank

The analyses are made for small scale models with the units of milimeters and for large scale models that are close their real applications in units of meters. For all the frequency analyses with small scales, the following tank properties are used

- Tank type: Rectangular
- Tank length: 150 mm
- Tank width: 100 mm
- Tank height: 500 mm
- Tank thickness: 3 mm
- Height of water: 300 mm
- Material types of tank: Steel (only for numerical analyses), Plexiglass (for numerical and experimental analyses), and a material with high rigidity (only for

numerical analyses)

- Young Modulus of steel: 207000 MPa
- Density of steel: $7800 \times 10^{-12} tonnes/mm^3$
- Poisson ratio of steel: 0.3
- Young Modulus of plexiglass: 3100 MPa
- Density of plexiglass: $1190 \times 10^{-12} tonnes/mm^3$
- Poisson ratio of plexiglass: 0.37
- Young Modulus of material with high rigidity: 1220000 MPa
- Density of material with high rigidity: $3520 \times 10^{-12} tonnes/mm^3$
- Poisson ratio of material with high rigidity: 0.2
- Density of water: $1000 \times 10^{-12} tonnes/mm^3$

4.1.2. Analytical Methods

As it is mentioned in the chapter of "Mathematical Derivation of Sloshing Motion for Rectangular and Cylindrical Tank" from Appendix, the frequency from Abramson's analytical method is

$$f_{m,n} = \sqrt{g.k. \tanh(kz)} \frac{1}{2\pi}$$

where m and n refers to half waves on x-axis and y-axis, respectively [35], and in addition $k = \pi \sqrt{\frac{m^2}{a^2} + \frac{n^2}{b^2}}$

where a and b refers to length and width of the tank, respectively.

The second analytical method from Housner is used in this study. The following formula is utilized in order to find first natural frequency of the sloshing motion

$$f = \frac{1}{2\pi}(\sqrt{\frac{5}{2}}\frac{g}{l}(tanh\sqrt{\frac{5}{2}}\frac{h}{l})) \tag{4.1}$$

4.1.3. Numerical Analyses

In order to carry out numerical analyses, the structural analyses programme MSC Nastran is used. Among the analyses options of Nastran, the eigenvalue analysis is employed and the frequencies of the partially-filled rectangular tank are reached. With numerical analyses, the effect of the following parameters to the tank's sloshing freqeuncy are examined

- Type of tank material
- Tank thickness
- Tank's mesh resolution
- Phantom surface's element length-gap distance ratio where gap distance is the distance between tank wall and phantom surface
- Phantom surface's mesh resolution

In order to use as a checkpoint for frequencies that are reached by numerical analyses, the results are compared with the analytical ones and an error rate is employed.

This error rate is calculated as

$$errorrate = \frac{(numericalfrequency - analyticalfrequency)}{analyticalfrequency} \cdot 100 \qquad (4.2)$$

For the analyses, the parameters mentioned above are given with following several different values

- Type of tank material: Plexiglass and aluminum
- Tank thickness: 0.1 mm, 0.25 mm, 0.5 mm, 1 mm, 2 mm, 3 mm
- Tank's mesh resolution (throughout tank's length x width x height): 6 x 4 x 12 elements, 12 x 8 x 24 elements, 24 x 16 x 48 elements
- Phantom surface's element length-gap distance ratio: 20%, 15%, 10%, 5%, 2.5%, 1%, 0.5%
- Phantom surface's mesh resolution: 15×10 elements, 30×20 elements, 60×40 elements

To give a better understanding, the parameter of "element length-gap distance ratio" will be explained here, and since other 4 parameters are basically self-descriptive, they are not explained. By the phrase of element length, phantom surface's one element's length is meant and by gap distance, the distance between phantom surface and the tank wall is implied. Thus, with this parameter, the effect of the ratio between element length and gap distance is investigated. In the figure below, the phantom surface is demonstrated from the top view of the tank. In this figure, the element length is demonstrated with "a" whereas the gap distance is shown with $\frac{na}{100}$. In this situation, "n" refers to desired gap ratio by the user.

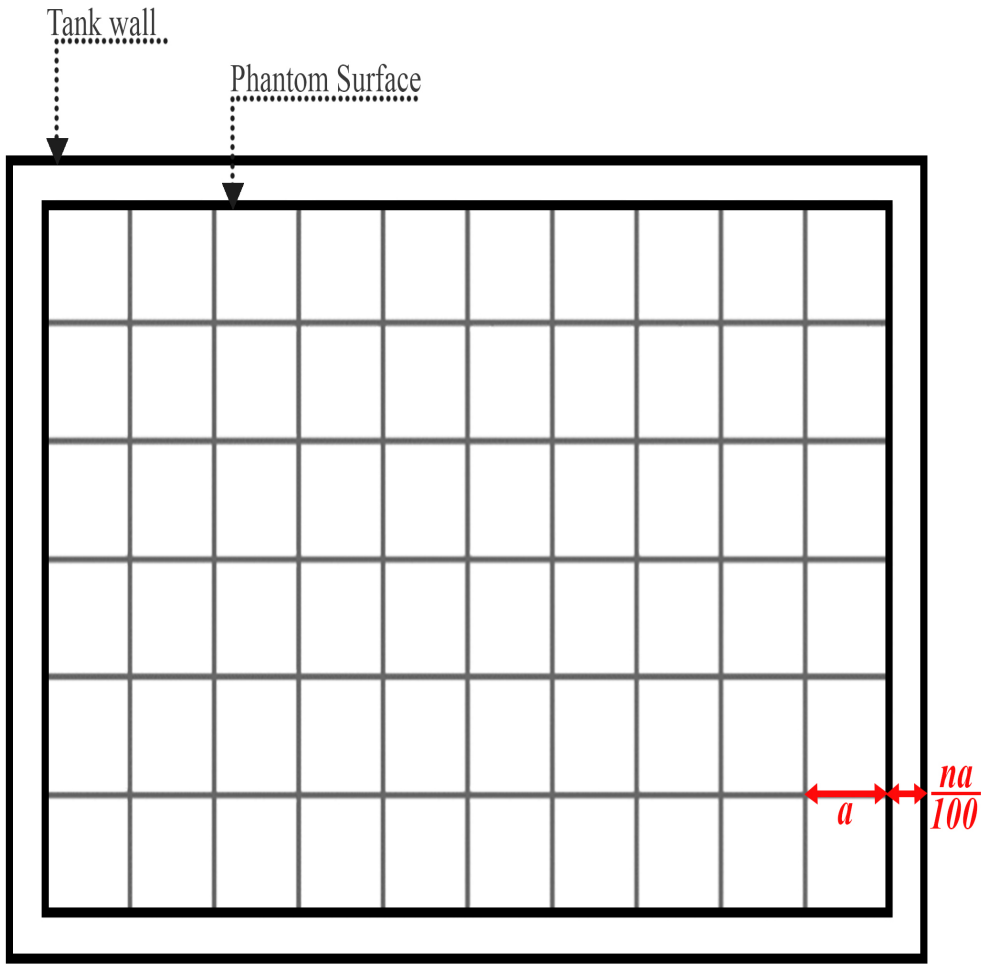

Figure 4.1. Representation of gap ratio, and gap distance between tank wall and phantom surface for rectangular tank

Some of the parameters are taken as constant during the change parameters of tank material, tank thickness, tank mesh resolution, element length - gap distance ratio and phantom mesh resolution are investigated. These parameters are demonstrated as follows

- Tank bottom's mesh type: Structured, quadrilateral elements
- Tank wall's mesh type: Structured, quadrilateral elements
- Material type of phantom surface: Aluminum

- Young Modulus of phantom surface's material: 69000 MPa
- Density of phantom surface's material: $2700 - 10^{-12} tonnes/mm^3$
- Poisson ratio of phantom surface's material: 0.33
- Phantom surface thickness: 0.001 mm

For visualizing the finite element models, MSC software's another program, Patran, is utilized. Patran is a software that is created for pre-processing and post-processing of finite element models and it is compatible with Nastran [30].

Some modeshapes of the sloshing motion are simulated with Patran can be found below. In figure captions below, the modeshapes are given in (m,n) format that comes from analytical formula.

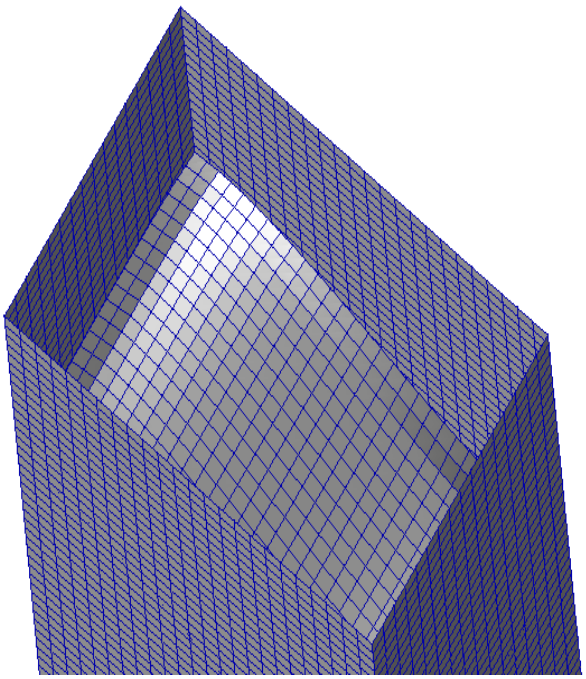

Figure 4.2. 1st modeshape of sloshing motion in Patran - Modeshape (1,0)

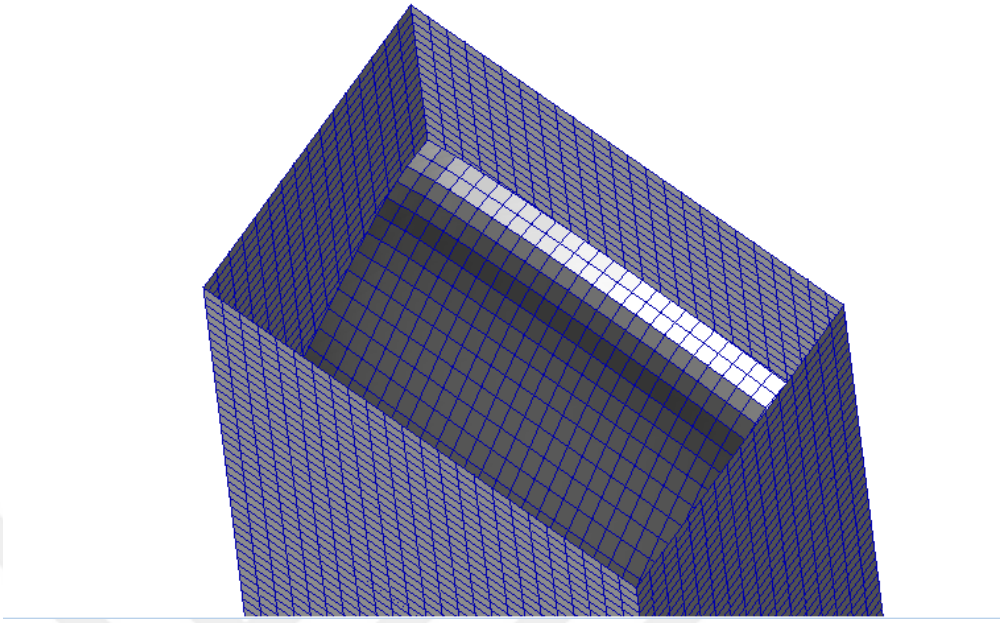

Figure 4.3. 2nd modeshape of sloshing motion in Patran - Modeshape (0,1)

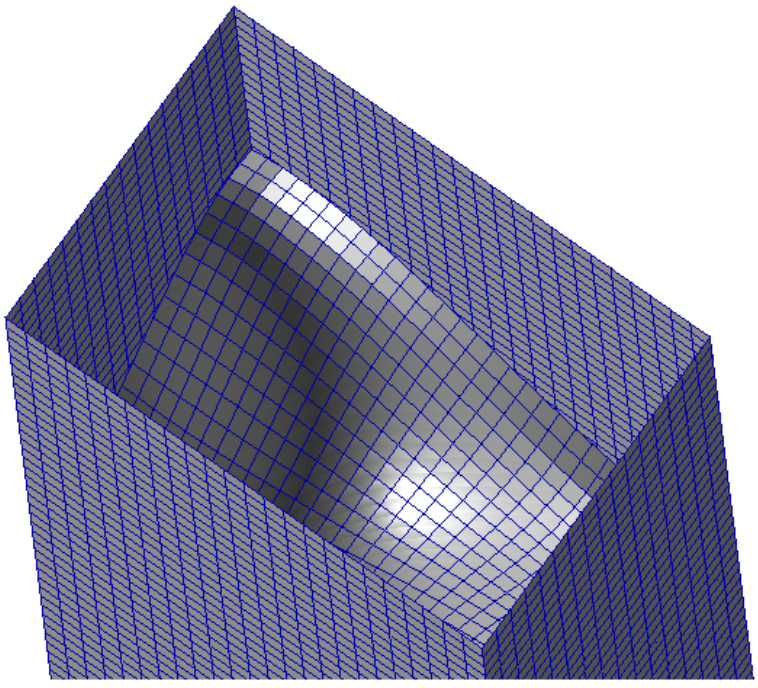

Figure 4.4. 3rd modeshape of sloshing motion in Patran - Modeshape (1,1)

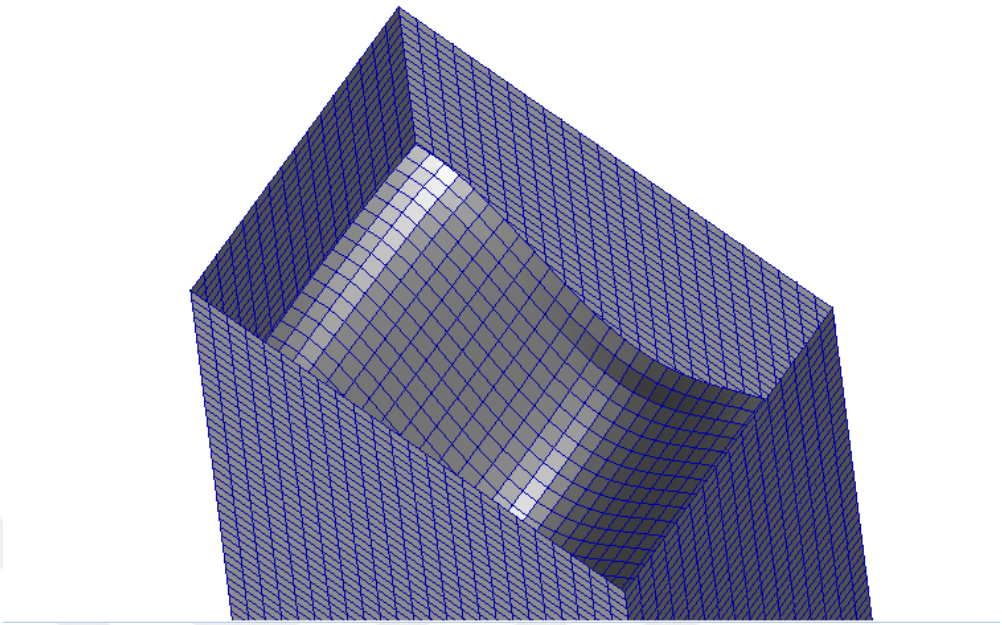

Figure 4.5. 4th modeshape of sloshing motion in Patran - Modeshape (2,0)

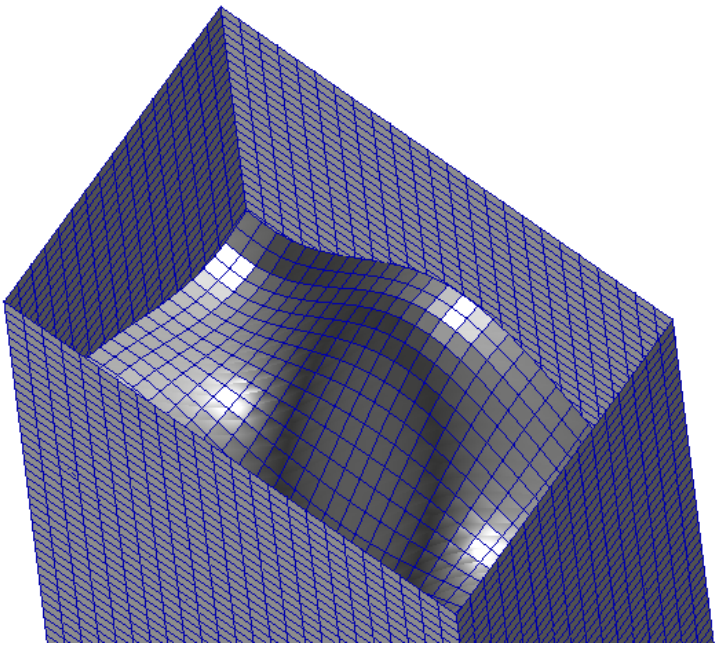

Figure 4.6. 5th modeshape of sloshing motion in Patran - Modeshape (2,1)

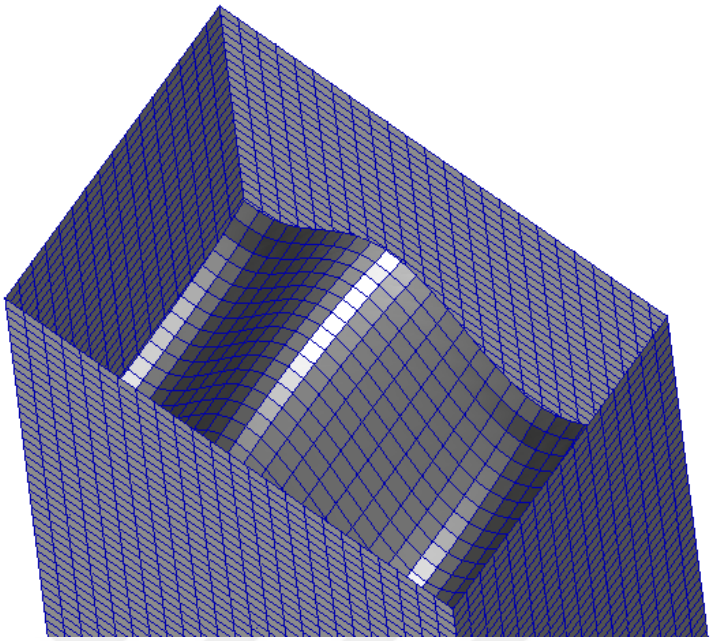

Figure 4.7. 6th modeshape of sloshing motion in Patran - Modeshape (3,0)

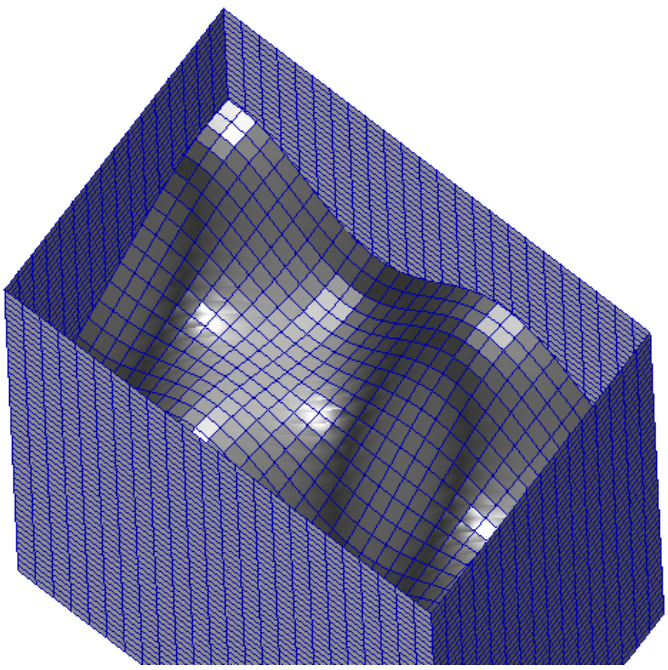

Figure 4.8. 9th modeshape of sloshing motion in Patran - Modeshape (3,1)

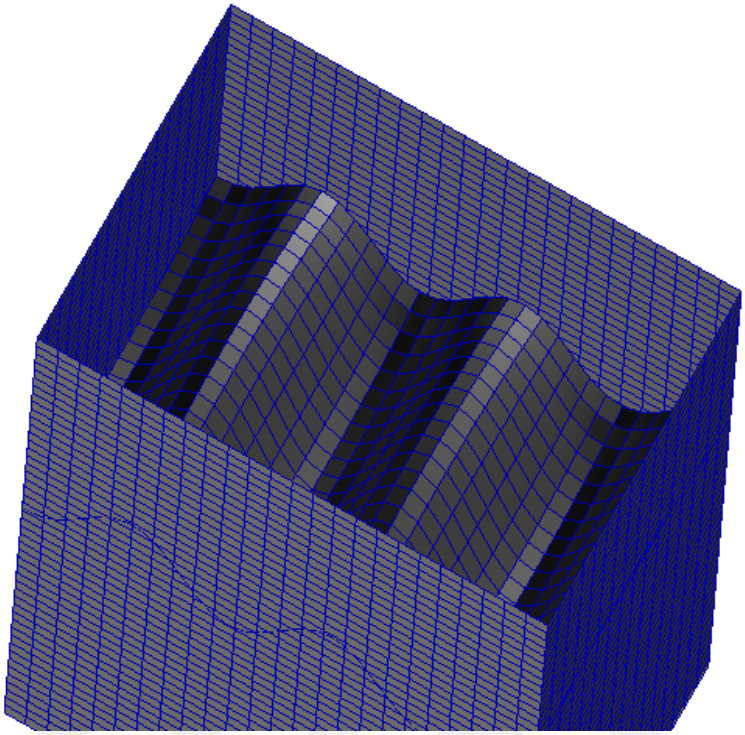

Figure 4.9. 16th modeshape of sloshing motion in Patran - Modeshape (5,0)

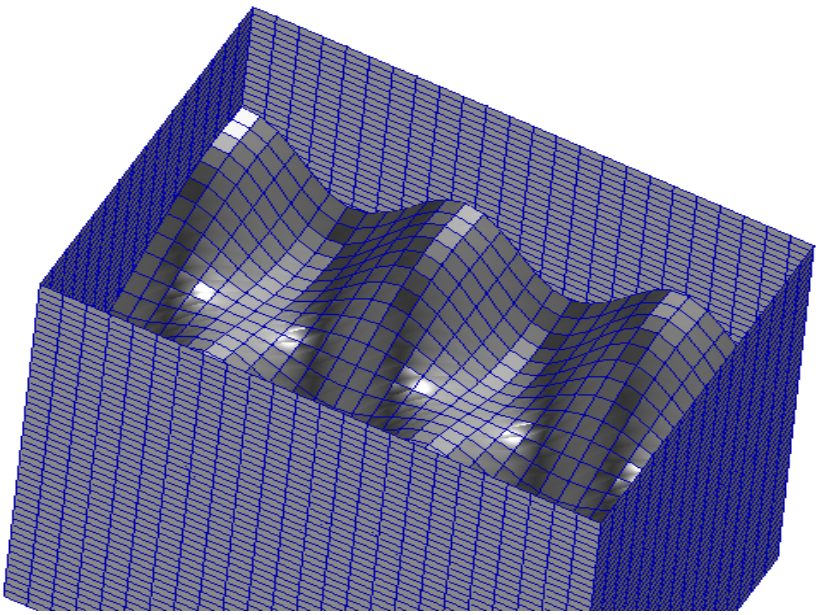

Figure 4.10. 19th modeshape of sloshing motion in Patran - Modeshape (5,1)

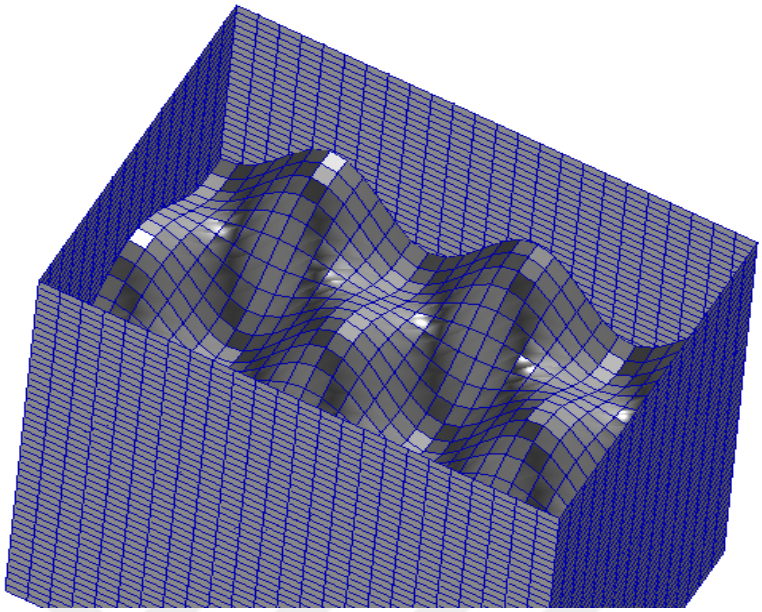

Figure 4.11. 21th modeshape of sloshing motion in Patran - Modeshape (5,2)

4.1.4. Laboratory Experiments

For our study, the datas of the shaking table experiments from Erginbas [3] are employed. The frequencies from the experiment are compared with analytical values by calculating the error rate which is obtained with a very similar way used in numerical analyses section.

$$errorrate = \frac{(experimentalfrequency - analyticalfrequency)}{analyticalfrequency} \cdot 100$$

For the experiment, the features of the tank and fluid, such as sizes and material properties for the tank, were as it was declared in the section of "tank properties". The choice of tank thickness was 3 mm and material of tank as plexiglass helped the researcher to have a rigid tank in practice. During the analysis, the shaking table excited the tank sinusoidally. Since it had the ability to excite with at least 2 Hz, the

experiment was started at 2 Hz. Even though there was this limitation, since the chosen sizes of the tank analytically gave the frequencies over 2 Hz, there was no problem in case of capturing the frequencies visually. The frequency of the shaking table was able to be increased by 0.01 Hz per step and it had the ability to have the acceleration of 0.1g utmost. The rectangular container was excited in the defined x-axis which can be seen in Figure 4.12.

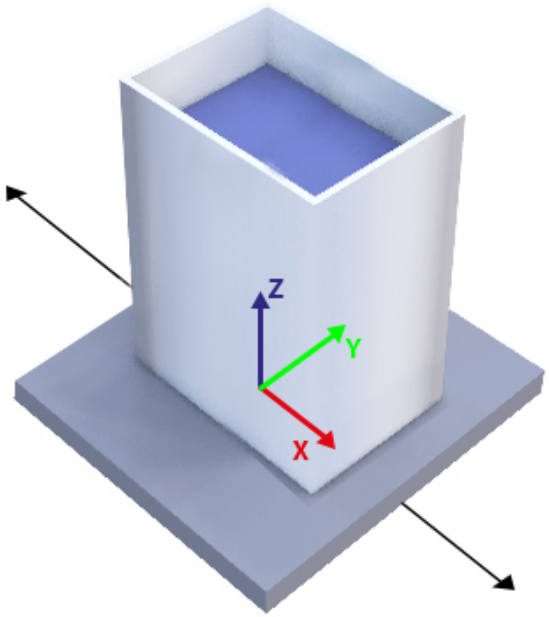

Figure 4.12. Demonstration of the excitation axis of the rectangular tank. Adapted from [5].

A camera was used for recording the movement of the container and sloshing of water. During the experiment, observation of sloshing of water with the frequency between 2 and 6 Hz was gave weight.After the experiment was done, the record of the tank excitation was examined and the frequencies were measured by visual inspection of modeshapes. The camera utilized had the frame rate of 25 frames per second, and

the computer program which was benefited to examine the record had the frame rate of 14 frames per second, however, since the frequency that was paid attention was 6 Hz utmost, 14 frame per second was sufficient to investigate the essential modeshapes. The camera was located to the front-top of the tank in order to have the best view of sloshing modes. The figures below show some images of modeshape which were taken during the experiment.



Figure 4.13. Representation of modeshape (1,0) during laboratory experiment of plexiglass rectangular tank [3].

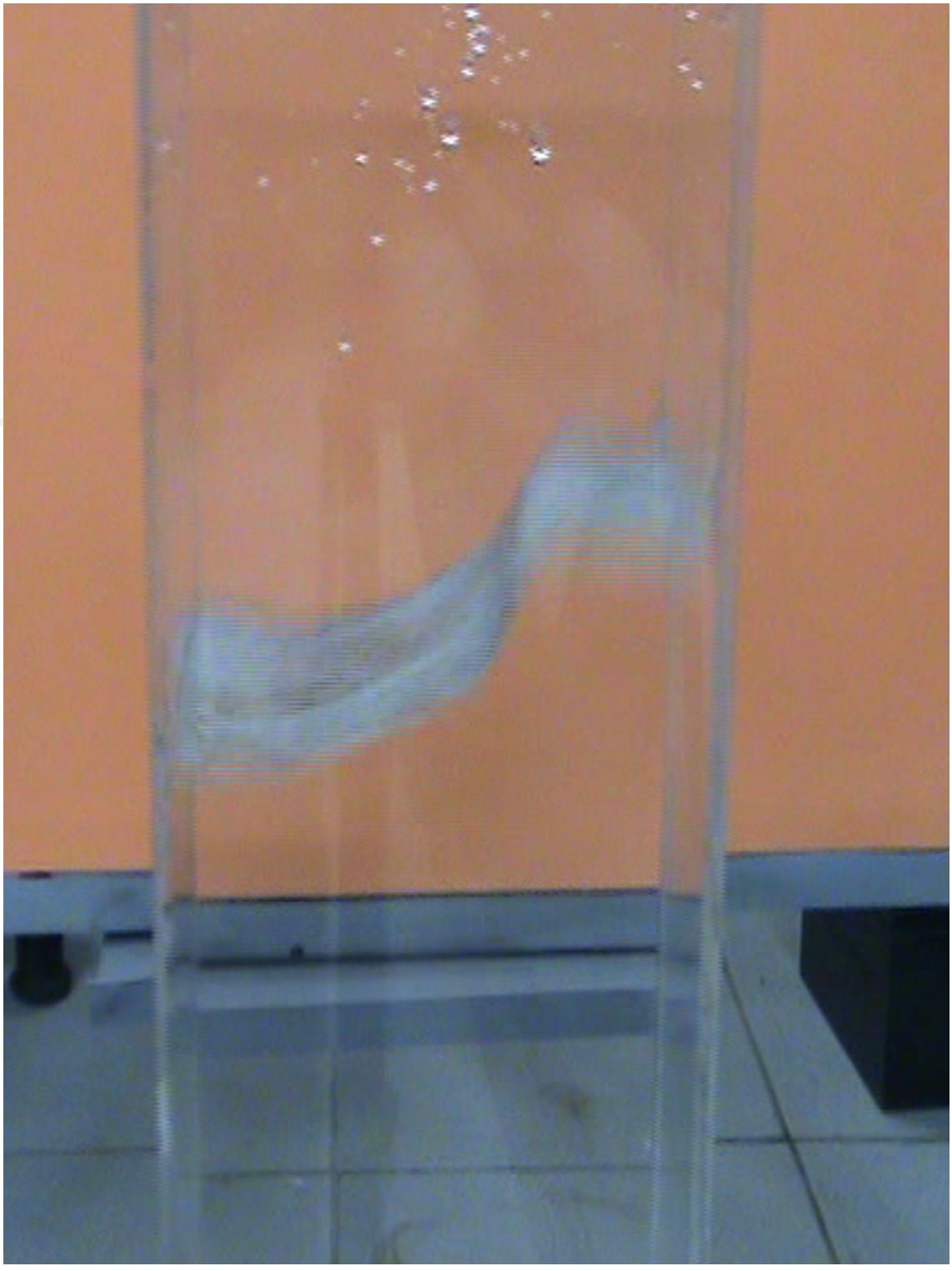

Figure 4.14. Representation of modeshape (2,0) during laboratory experiment of plexiglass rectangular tank [3].



Figure 4.15. Representation of modeshape (3,0) during laboratory experiment of plexiglass rectangular tank [3].

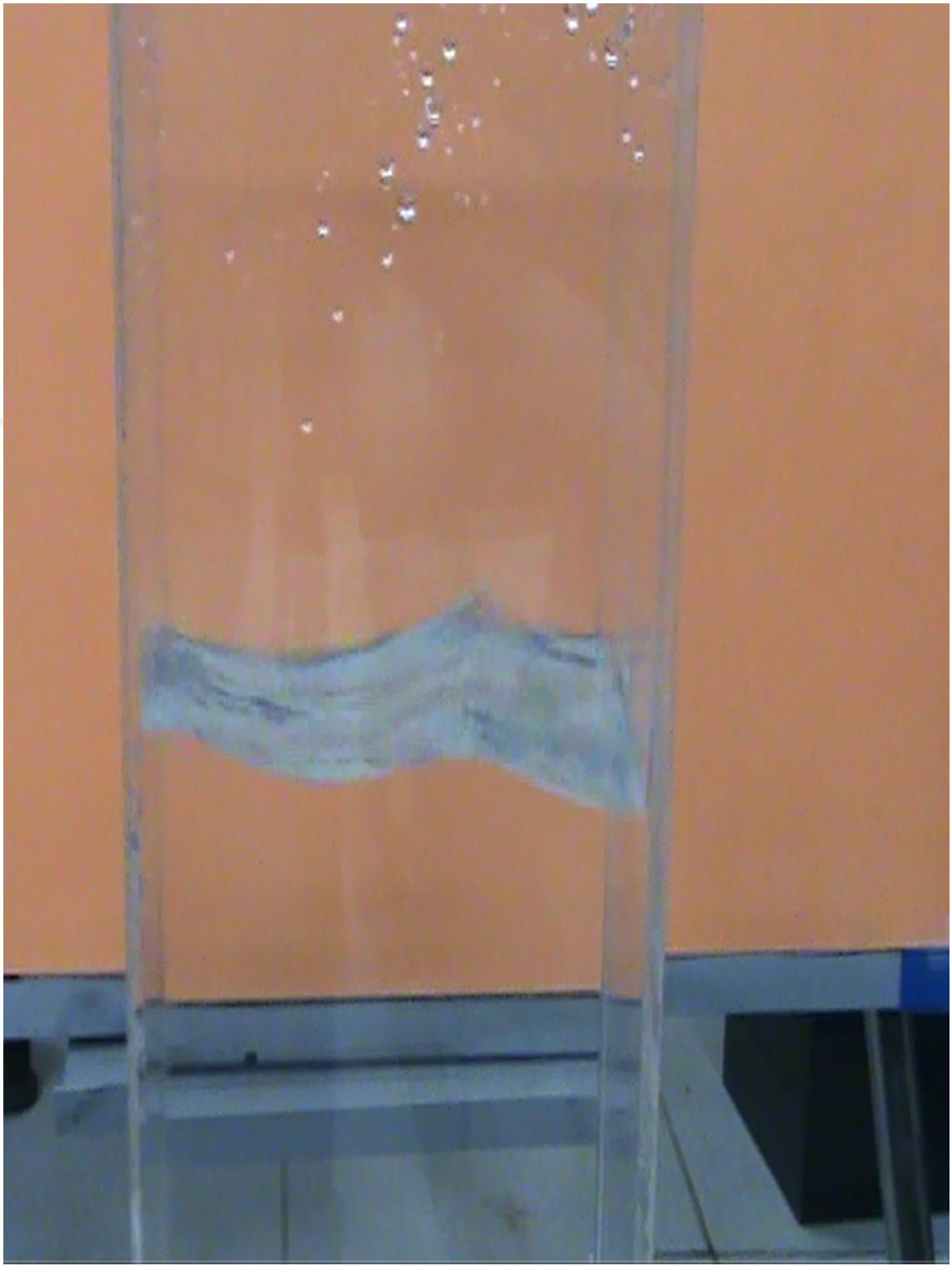

Figure 4.16. Representation of modeshape (3,1) during laboratory experiment of plexiglass rectangular tank [3].



Figure 4.17. Representation of modeshape (5,0) during laboratory experiment of plexiglass rectangular tank [3].



Figure 4.18. Representation of modeshape (5,1) during laboratory experiment of plexiglass rectangular tank [3].

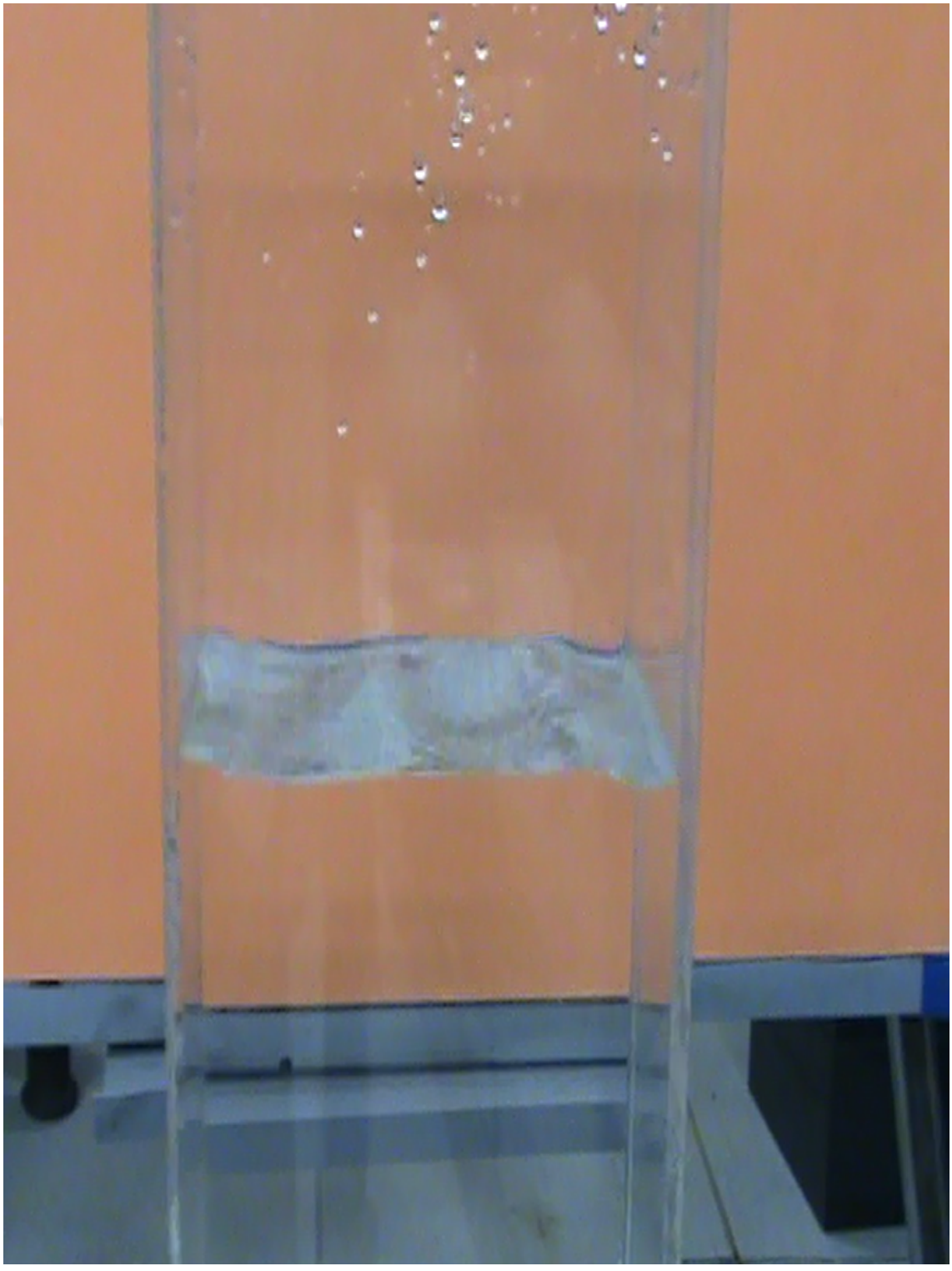

Figure 4.19. Representation of modeshape (5,2) during laboratory experiment of plexiglass rectangular tank [3].

4.1.5. Results

Table 4.1 below demonstrates the analytical frequencies that is employed from Abramson's work [1] for the rectangular tank with length of 150 mm, width of 100 mm and fluid height of 300 mm with respect to several m and n values.

Table 4.1. Analytical frequencies of small scale rectangular tank by using Abramson's method

m	**n=0**	**n=1**	**n=2**	**n=3**	**n=4**	**n=5**	**n=6**
0	0	2.79	3.95	4.84	5.59	6.25	6.84
1	2.28	3.06	4.06	4.9	5.62	6.27	6.86
2	3.23	3.61	4.33	5.06	5.74	6.35	6.92
3	3.95	4.18	4.7	5.3	5.91	6.48	7.02
4	4.56	4.71	5.1	5.6	6.12	6.65	7.16
5	5.1	5.21	5.51	5.92	6.37	6.85	7.32
6	5.59	5.67	5.91	6.25	6.64	7.07	7.5

The analytical result by using Housner's first natural frequency formula gives 2.28 Hz that is basically same first natural frequency with the frequency from Abramson's formula. Since they are equal to each other, in the tables below which show numerical results of eigenvalue analysis they are not written separately, but only written as "Analytical frequency".

The numerical analyses started with observing effect of tank thickness and tank material choice. For this purpose, firstly, a partially filled “steel” rectangular tank with its changing tank thickness values is analyzed.

The table of frequencies obtained from the eigenvalue analysis is shown below.

Table 4.2. First 5 frequencies of partially-filled steel rectangular tank with respect to changing tank thickness

Tank mesh (Lenght x Width x Height)	**Phantom mesh (Length x Width)**	**Gap**	**Tank thickness (mm)**	**1st freq (Hz)**	**2nd freq (Hz)**	**3rd freq (Hz)**	**4th freq (Hz)**	**5th freq (Hz)**
6x4x12	15x10	20%	0.1	1.72	2.3	3.22	3.54	3.64
6x4x12	15x10	20%	0.25	2.9	3.42	3.8	3.84	4.33
6x4x12	15x10	20%	0.5	2.94	3.49	3.83	3.88	4.42
6x4x12	15x10	20%	1	2.94	3.5	3.83	3.88	4.42
6x4x12	15x10	20%	2	2.94	3.5	3.83	3.88	4.42
6x4x12	15x10	20%	3	2.94	3.5	3.83	3.88	4.42
Analytical frequencies				2.28	2.79	3.06	3.23	3.61

In the next case, table of error rates of numerical values compare to analytical frequencies are demonstrated as

Table 4.3. Partially-filled steel rectangular tank's error rates for its first 5 modes with respect to changing tank thickness

Tank mesh (Lenght x Width x Height)	**Phantom mesh (Length x Width)**	**Gap**	**Tank thick-ness (mm)**	**Error rate of 1st mode (%)**	**Error rate of 2nd mode (%)**	**Error rate of 3rd mode (%)**	**Error rate of 4th mode (%)**	**Error rate of 5th mode (%)**
6x4x12	15x10	20%	0.1	-24.56	-17.56	5.23	9.60	0.83
6x4x12	15x10	20%	0.25	27.19	22.58	24.18	18.89	19.94
6x4x12	15x10	20%	0.5	28.95	25.09	25.16	20.12	22.44
6x4x12	15x10	20%	1	28.95	25.45	25.16	20.12	22.44
6x4x12	15x10	20%	2	28.95	25.45	25.16	20.12	22.44
6x4x12	15x10	20%	3	28.95	25.45	25.16	20.12	22.44

The graphical representation of Table 4.3 is now going to be shown in the figure below. By using graphical representation, the trend of the error rate can be easily understood. That is why, these figures are going to be utilized for all the parametric studies in this research.

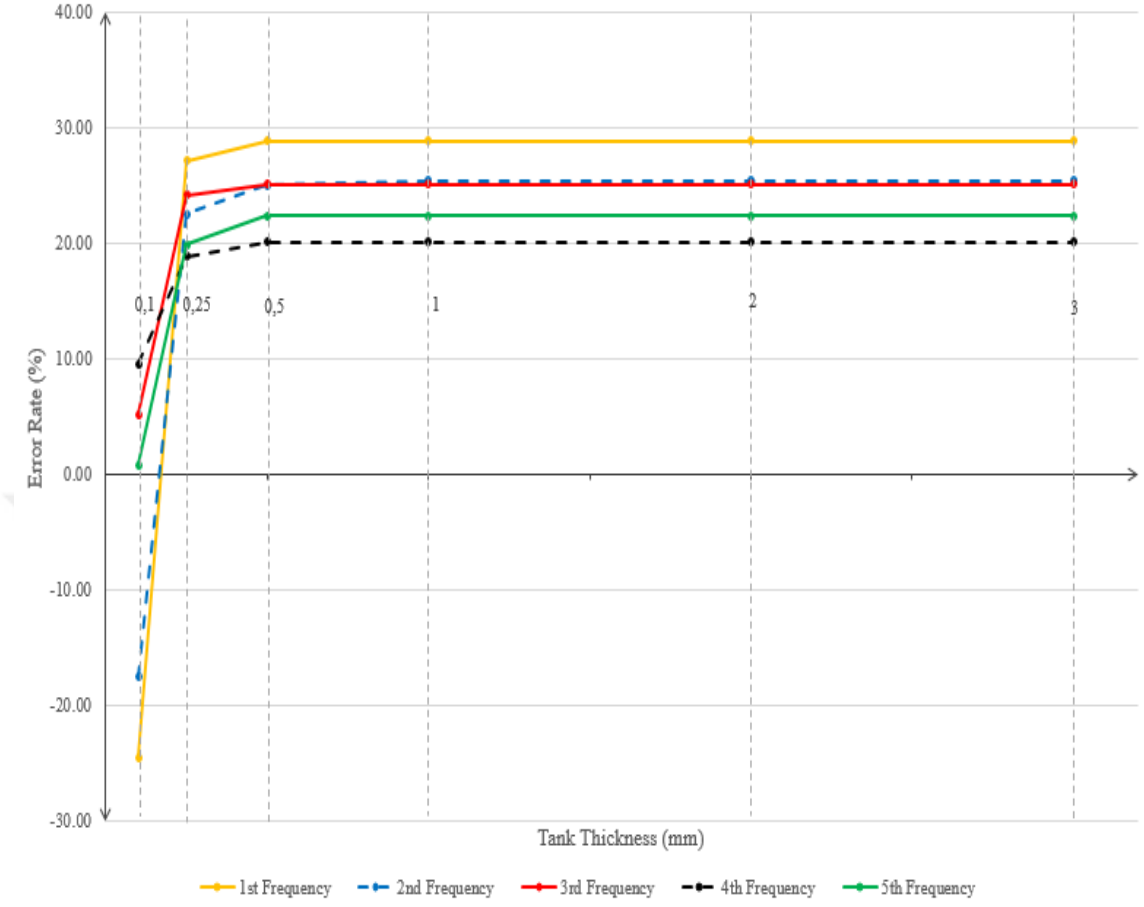

Figure 4.20. Representation of partially-filled steel rectangular tank's error rates for its first 5 modes with respect to changing tank thickness

A very similar numerical analyses to the one with steel rectangular tank is completed as the second analysis; an eigenvalue analysis for a partially filled "plexiglass" rectangular tank with its changing tank thickness values. The tables below demonstrate the frequencies and error rates from the study.

Table 4.4. First 5 frequencies of partially-filled plexiglass rectangular tank with respect to changing tank thickness

Tank mesh (Lenght x Width x Height)	**Phantom mesh (Length x Width)**	**Gap**	**Tank thickness (mm)**	**1st freq (Hz)**	**2nd freq (Hz)**	**3rd freq (Hz)**	**4th freq (Hz)**	**5th freq (Hz)**
6x4x12	15x10	20%	0.1	0.3	0.36	0.51	0.6	0.68
6x4x12	15x10	20%	0.25	1.12	1.43	1.97	2.13	2.47
6x4x12	15x10	20%	0.5	2.17	2.91	3.28	3.8	3.86
6x4x12	15x10	20%	1	2.94	3.48	3.79	3.87	4.02
6x4x12	15x10	20%	2	2.94	3.5	3.83	3.87	4.42
6x4x12	15x10	20%	3	2.94	3.5	3.83	3.88	4.42
Analytical frequencies				2.28	2.79	3.06	3.23	3.61

Table 4.5. Partially-filled plexiglass rectangular tank's error rates for its first 5 modes with respect to changing tank thickness

Tank mesh (Lenght x Width x Height)	**Phantom mesh (Length x Width)**	**Gap**	**Tank thick-ness (mm)**	**Error rate of 1st mode (%)**	**Error rate of 2nd mode (%)**	**Error rate of 3rd mode (%)**	**Error rate of 4th mode (%)**	**Error rate of 5th mode (%)**
6x4x12	15x10	20%	0.1	-86.84	-87.10	-83.33	-81.42	-81.16
6x4x12	15x10	20%	0.25	-50.88	-48.75	-35.62	-34.06	-31.58
6x4x12	15x10	20%	0.5	-4.82	4.30	7.19	17.65	6.93
6x4x12	15x10	20%	1	28.95	24.73	23.86	19.81	11.36
6x4x12	15x10	20%	2	28.95	25.45	25.16	19.81	22.44
6x4x12	15x10	20%	3	28.95	25.45	25.16	20.12	22.44

The results of Table 4.5 are demonstrated as a graph below

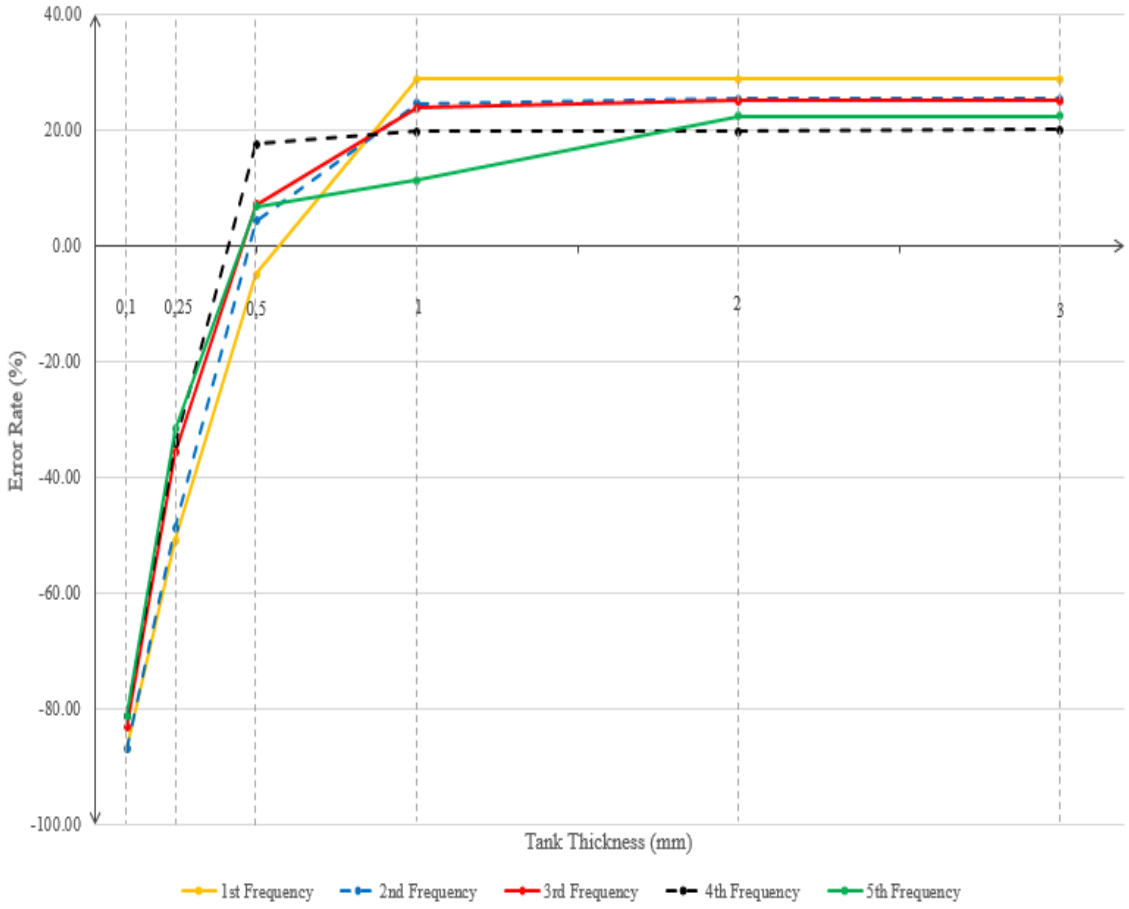

Figure 4.21. Representation of partially-filled plexiglass rectangular tank's error rates for its first 5 modes with respect to changing tank thickness

When the tables and the graphs for steel and plexiglass rectangular tanks are examined, it can be noticed that as the tank thickness is increasing, the frequencies are getting closer to the analytical results. The reason of this situation is that the analytical results are found by assuming the tank is rigid, in other words undeformed, and for both steel and plexiglass tanks, as the thickness increases, in practice, the tank walls act almost rigidly for numerical analyses.

The second consequence from these results is that since steel has greater Young's modulus than plexiglass, for thin tank thicknesses -0.1 mm, 0.25 mm, 0.5 mm- the steel tank' s frequencies are closer to the analytical values than plexiglass tank's frequencies. In addition, for thickness of 1 mm, 2 mm and 3 mm, since they are thick enough, the impact of different Young Modulus for steel and plexiglass can not be seen.

Since the tank used for laboratory experiment is made of 3 mm thick plexiglass, to be able to compare the numerical values with the laboratory experiments' frequencies later, this "3 mm thick plexiglass tank" is going to be used for the following rectangular tank analyses.

For the next numerical analysis, the effect of tank's mesh resolution is examined. The tables of frequencies, error rates from the analysis and the graphical representation of error rate table are demonstrated as follows

Table 4.6. First 5 frequencies of partially-filled plexiglass rectangular tank with respect to changing tank mesh resolution

Tank mesh (Lenght x Width x Height)	**Phantom mesh (Length x Width)**	**Gap**	**Tank thickness (mm)**	**1st freq (Hz)**	**2nd freq (Hz)**	**3rd freq (Hz)**	**4th freq (Hz)**	**5th freq (Hz)**
6x4x12	15x10	20%	3	2.94	3.5	3.83	3.88	4.42
12x8x24	15x10	20%	3	2.88	3.42	3.76	3.78	4.33
24x16x48	15x10	20%	3	2.87	3.38	3.72	3.74	4.28
Analytical frequencies				2.28	2.79	3.06	3.23	3.61

Table 4.7. Partially-filled plexiglass rectangular tank's error rates for its first 5 modes with respect to changing tank mesh resolution

Tank mesh (Lenght x Width x Height)	**Phantom mesh (Length x Width)**	**Gap**	**Tank thick-ness (mm)**	**Error rate of 1st mode (%)**	**Error rate of 2nd mode (%)**	**Error rate of 3rd mode (%)**	**Error rate of 4th mode (%)**	**Error rate of 5th mode (%)**
6x4x12	15x10	20%	3	28.95	25.45	25.16	20.12	22.44
12x8x24	15x10	20%	3	26.32	22.58	22.88	17.03	19.94
24x16x48	15x10	20%	3	25.88	21.15	21.57	15.79	18.56

The graphical representation of the error rate table for tank mesh resolution is

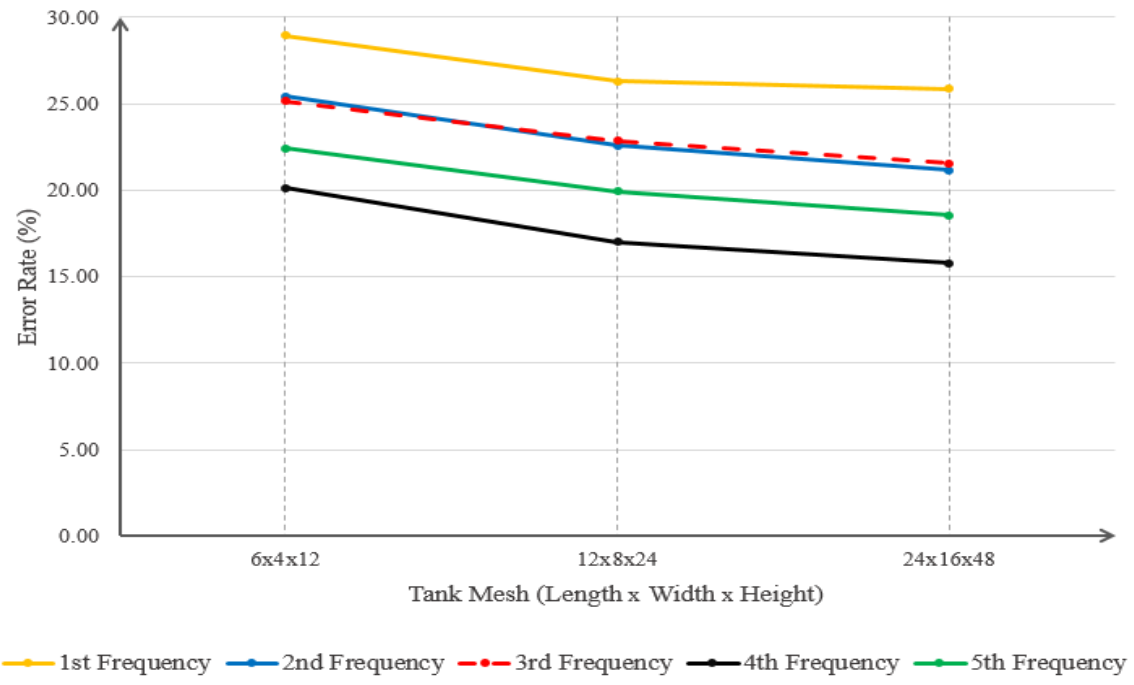

Figure 4.22. Representation of partially-filled plexiglass rectangular tank's error rates for its first 5 modes with respect to changing tank mesh resolution

As it can be noticed from Table 4.6, Table 4.7, and Figure 4.22, as the tank mesh resolution gets more refined, the frequencies are getting closer to the analytical values. The cause of this condition is based on the working principles of virtual mass method in Nastran. In Nastran, the fluid behaviour is defined by the sources located on the centers of finite elements at the model's boundary [4]. This fluid behaviour at an element's center due to these sources is measured by taking the superposition of all sources' effects at that point and if the distance between elements with source and element that the fluid behaviour is measured is too much, Nastran neglects this calculation [4]. In our case, by taking more refined mesh, we decrease the distance between these elements and as a result at each element fluid behaviour is calculated with representing more sources' effects.

Another variable which is investigated is the element length - gap distance ratio of phantom surface. As it is explained previously, length of phantom surface's one finite element which has the same dimension both on x and y axes are divided by the gap distance that is the distance between phantom surface and tank wall. In order to remember the gap ratio concept, Figure 4.1 can be examined again. The tables which show frequencies and error rates with respect to changing element length-gap distance ratio and the graph of the error rate's trend due to these changes are demonstrated below.

Table 4.8. First 5 frequencies of plexiglass rectangular tank with respect to changing element length-gap distance ratio (NR stands for "No results")

Tank mesh (Lenght x Width x Height)	**Phantom mesh (Length x Width)**	**Gap**	**Tank thickness (mm)**	**1st freq (Hz)**	**2nd freq (Hz)**	**3rd freq (Hz)**	**4th freq (Hz)**	**5th freq (Hz)**
24x16x48	15x10	20%	3	2.87	3.38	3.72	3.74	4.28
24x16x48	15x10	15%	3	2.76	3.27	3.62	3.64	4.17
24x16x48	15x10	10%	3	2.63	3.15	3.48	3.55	4.05
24x16x48	15x10	5%	3	2.48	3.01	3.33	3.44	3.92
24x16x48	15x10	2.5%	3	NR	NR	NR	NR	NR
24x16x48	15x10	1%	3	NR	NR	NR	NR	NR
Analytical frequencies				2.28	2.79	3.06	3.23	3.61

Table 4.9. Partially-filled plexiglass rectangular tank's error rates for its first 5 modes with respect to changing element length-gap distance ratio (NR stands for "No results")

Tank mesh (Lenght x Width x Height)	**Phantom mesh (Length x Width)**	**Gap**	**Tank thick-ness (mm)**	**Error rate of 1st mode (%)**	**Error rate of 2nd mode (%)**	**Error rate of 3rd mode (%)**	**Error rate of 4th mode (%)**	**Error rate of 5th mode (%)**
24x16x48	15x10	20%	3	25.88	21.15	21.57	15.79	18.56
24x16x48	15x10	15%	3	21.05	17.20	18.30	12.69	15.51
24x16x48	15x10	10%	3	15.35	12.90	13.73	9.91	12.19
24x16x48	15x10	5%	3	8.77	7.89	8.82	6.50	8.59
24x16x48	15x10	2.5%	3	NR	NR	NR	NR	NR
24x16x48	15x10	1%	3	NR	NR	NR	NR	NR

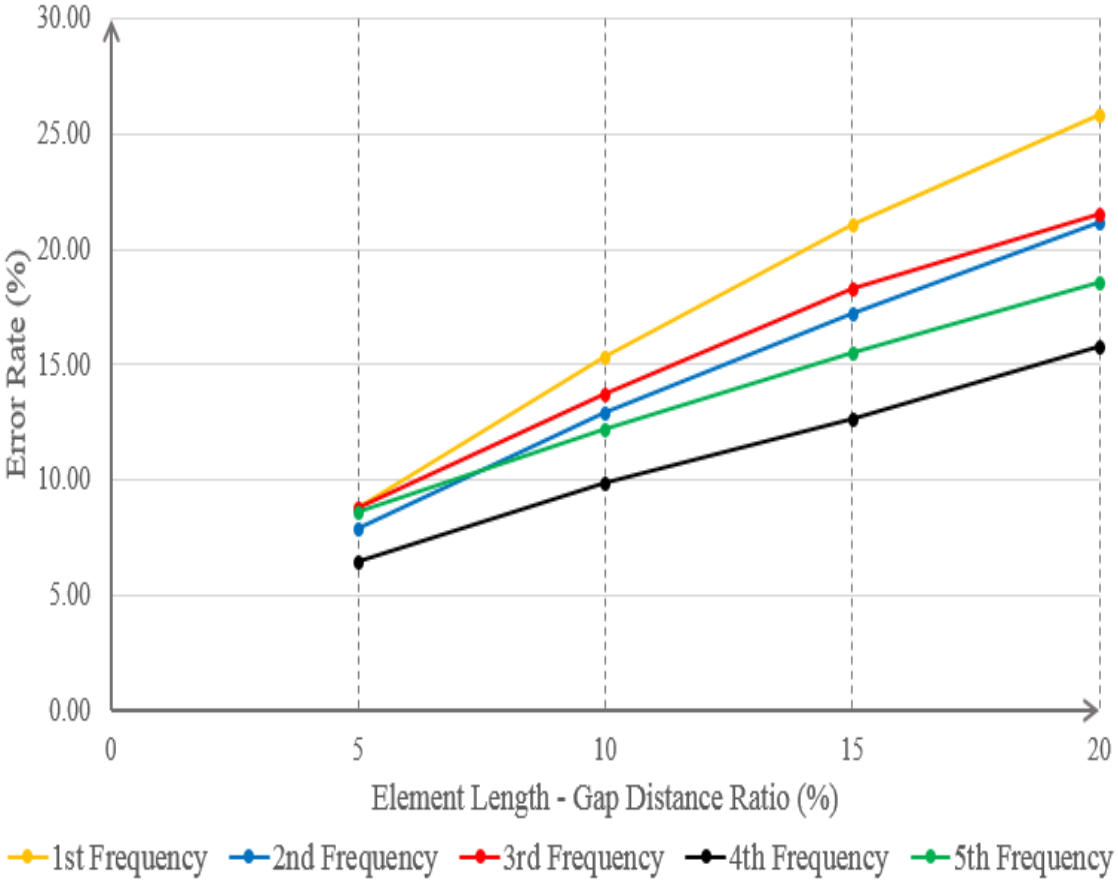

Figure 4.23. Representation of partially-filled plexiglass rectangular tank's error rates for its first 5 modes with respect to changing element length-gap distance ratio

When Table 4.8, Table 4.9, and Figure 4.23 are examined, it is clearly seen that as the gap ratio decreases, the frequencies get more accurate, in other words, they get closer to the analytical frequencies, however, if it gets too close to the tank wall, Nastran will not calculate the frequency. The reason of not having results is the working principle of eigenvalue analysis in Nastran. In Nastran, Laplace equation is solved by superposition of sources and doublets where they are located at the tank walls' centers, and as it is known, the sources have the singularity as the velocity value when it is calculated too close to the source's vicinity [4].

This situation can be understood as well from Equation C.50 in Appendix chapter of "Mathematical Derivation of Sloshing Motion for MSC Nastran" as follows

$$\phi(\bar{r}_i) = -\frac{S_j}{|r_i - r_j|} \tag{4.3}$$

where S_j denotes the source strength at location of $\bar{r}_j$(with the unit of $volume/steradian$), and ϕ is calculated at $\bar{r}_i$. Also, $|r_i - r_j|$ defines the absolute distance value between point j and i. It should be paid attention that the displacement potential of point source in the equation above represent the behaviour of fluid volume with excluding a small radius of a sphere that will cause singularity. Thus, r_i is basically radius of the sphere that is excluded from the calculation to prevent singularity and when r_i equals to r_j the calculation of $|r_i - r_j|$ in the denominator goes to zero and cause singularity. This situation represent a calculation of displacement potential at the point on the surface of that sphere. By keeping the gap distance between phantom surface and tank wall too short, in our case this is 2.5%, the frequencies can not be calculated since the velocity at the phantom surface's edge is in the singularity range of the source. In addition, the case with 1% ratio is investigated in order to see what happens when we get pass the point that causes singularity and it is seen that the same error is given by Nastran.

The cause of having better results with decreasing gap ratio can be described as simulating pull of gravity more accurately. As it can be remembered, the pull of gravity on the mass that is created by virtual mass at phantom surface is simulated by stiffness of spring elements [31] and this stiffness is made of area of ELAS elements, density of fluid and gravitational acceleration. When phantom surface gets bigger, the area in the stiffness formula 3.1 gets higher value. Even though due to the singularity limitation of phantom surface, it can not get too close to the wall, getting closest to the wall will give the best simulation of pull of gravity to represent fluid behaviour fully which is the natural case of a fluid in a container.

Lastly, the effect of phantom surface mesh resolution is investigated. The tables that include frequencies and error rates and the graphical representation of error rates table with respect to changing phantom surface mesh resolution can be found below.

Table 4.10. First 5 frequencies of plexiglass rectangular tank with respect to changing phantom mesh resolution

Tank mesh (Lenght x Width x Height)	**Phantom mesh (Length x Width)**	**Gap**	**Tank thickness (mm)**	**1st freq (Hz)**	**2nd freq (Hz)**	**3rd freq (Hz)**	**4th freq (Hz)**	**5th freq (Hz)**
24x16x48	15x10	5%	3	2.48	3.01	3.33	3.44	3.92
24x16x48	30x20	5%	3	2.47	2.99	3.31	3.4	3.86
24x16x48	60x40	5%	3	2.44	2.97	3.28	3.39	3.84
Analytical frequencies				2.28	2.79	3.06	3.23	3.61

Table 4.11. Partially-filled plexiglass rectangular tank's error rates for its first 5 modes with respect to changing phantom mesh resolution

Tank mesh (Lenght x Width x Height)	**Phantom mesh (Length x Width)**	**Gap**	**Tank thick-ness (mm)**	**Error rate of 1st mode (%)**	**Error rate of 2nd mode (%)**	**Error rate of 3rd mode (%)**	**Error rate of 4th mode (%)**	**Error rate of 5th mode (%)**
24x16x48	15x10	5%	3	8.77	7.89	8.82	6.50	8.59
24x16x48	30x20	5%	3	8.33	7.17	8.17	5.26	6.93
24x16x48	60x40	5%	3	7.02	6.45	7.19	4.95	6.37

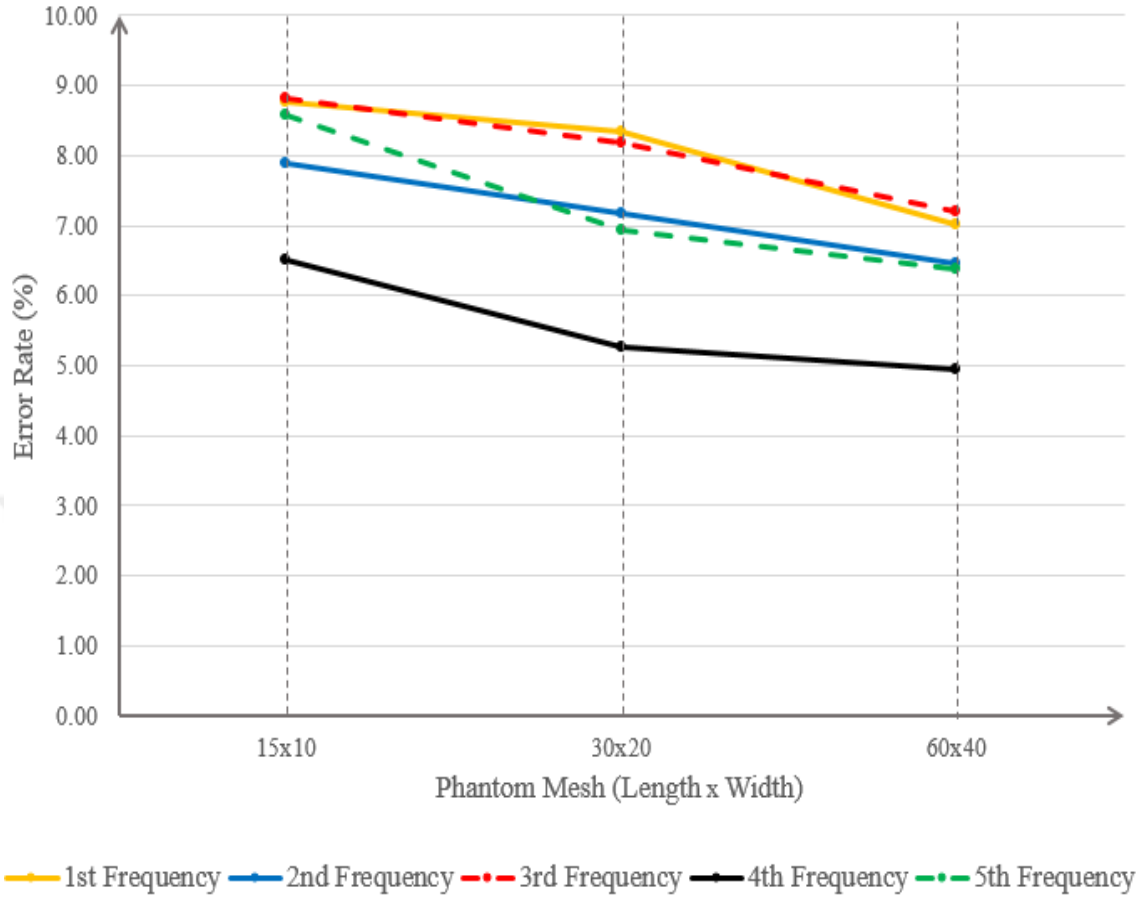

Figure 4.24. Representation of partially-filled plexiglass rectangular tank's error rates for its first 5 modes with respect to changing element length-gap distance ratio

From the tables and the figure above, it can be concluded that the denser phantom surface mesh reduces the error rate and gives more accurate results. The reason of this conclusion comes from the fact with more elements, the flexible nature of sloshing motion modeshapes at the phantom surface is represented more accurately compare to having lesser number of elements.

In order to have a broader look, the frequencies and the error rates from the eigenvalue analyses with partially-filled plexiglass rectangular tank are summarized as follows

Table 4.12. First 5 frequencies of plexiglass rectangular tank with respect to tank thickness, tank mesh resolution, element length-gap distance ratio and phantom mesh resolution

Tank mesh (Lenght x Width x Height)	**Phantom mesh (Length x Width)**	**Gap**	**Tank thickness (mm)**	**1st freq (Hz)**	**2nd freq (Hz)**	**3rd freq (Hz)**	**4th freq (Hz)**	**5th freq (Hz)**
6x4x12	15x10	20%	0.1	0.3	0.36	0.51	0.6	0.68
6x4x12	15x10	20%	0.25	1.12	1.43	1.97	2.13	2.47
6x4x12	15x10	20%	0.5	2.17	2.91	3.28	3.8	3.86
6x4x12	15x10	20%	1	2.94	3.48	3.79	3.87	4.02
6x4x12	15x10	20%	2	2.94	3.5	3.83	3.87	4.42
6x4x12	15x10	20%	3	2.94	3.5	3.83	3.88	4.42
12x8x24	15x10	20%	3	2.88	3.42	3.76	3.78	4.33
24x16x48	15x10	20%	3	2.87	3.38	3.72	3.74	4.28
24x16x48	15x10	15%	3	2.76	3.27	3.62	3.64	4.17
24x16x48	15x10	10%	3	2.63	3.15	3.48	3.55	4.05
24x16x48	15x10	5%	3	2.48	3.01	3.33	3.44	3.92
24x16x48	30x20	5%	3	2.47	2.99	3.31	3.4	3.86
24x16x48	60x40	5%	3	2.44	2.97	3.28	3.39	3.84
Analytical frequencies				2.28	2.79	3.06	3.23	3.61

Table 4.13. Partially-filled plexiglass rectangular tank's error rates for its first 5 modes with respect to tank thickness, tank mesh resolution, element length-gap distance ratio and phantom mesh resolution

Tank mesh (Lenght x Width x Height)	**Phantom mesh (Length x Width)**	**Gap**	**Tank thick-ness (mm)**	**Error rate of 1st mode (%)**	**Error rate of 2nd mode (%)**	**Error rate of 3rd mode (%)**	**Error rate of 4th mode (%)**	**Error rate of 5th mode (%)**
6x4x12	15x10	20%	0.1	-86.84	-87.10	-83.33	-81.42	-81.16
6x4x12	15x10	20%	0.25	-50.88	-48.75	-35.62	-34.06	-31.58
6x4x12	15x10	20%	0.5	-4.82	4.30	7.19	17.65	6.93
6x4x12	15x10	20%	1	28.95	24.73	23.86	19.81	11.36
6x4x12	15x10	20%	2	28.95	25.45	25.16	19.81	22.44
6x4x12	15x10	20%	3	28.95	25.45	25.16	20.12	22.44
12x8x24	15x10	20%	3	26.32	22.58	22.88	17.03	19.94
24x16x48	15x10	20%	3	25.88	21.15	21.57	15.79	18.56
24x16x48	15x10	15%	3	21.05	17.20	18.30	12.69	15.51
24x16x48	15x10	10%	3	15.35	12.90	13.73	9.91	12.19
24x16x48	15x10	5%	3	8.77	7.89	8.82	6.50	8.59
24x16x48	15x10	5%	3	8.77	7.89	8.82	6.50	8.59
24x16x48	30x20	5%	3	8.33	7.17	8.17	5.26	6.93
24x16x48	60x40	5%	3	7.02	6.45	7.19	4.95	6.37

By examining the two tables which summarize all the analyses, it can be accepted that by optimizing the values of tank thickness, tank mesh resolution, element length-gap distance ratio and phantom mesh resolution variables, a big progress has been achieved for having better frequencies and error rates.

After finishing the numerical analyses, in order to choose the most successful method which has the closest results to analytical frequencies, numerical analyses and laboratory experiments are compared with each other.

Among all the numerical frequencies, the plexiglass rectangular tank of last analysis which has $24 \times 16 \times 48$ tank mesh resolution, 60×40 phantom surface mesh resolution, 5% gap ratio, and 3 mm tank thickness is chosen.

For the laboratory experiment frequencies, as it is declared before, the data of Erginbas [3] is utilized.

In the first table below, the frequencies from analytical method, numerical analyses and laboratory experiment can be found. In the second table, the numerical and experimental error rates are included to compare them with each other.

In both of the tables, in addition to the modeshapes' representation as (m,n) dual from analytical formula, modeshapes' view order in Patran corresponding to those (m,n) duals are shown.

Table 4.14. Comparison of analytical, numerical and laboratory experiment frequencies for plexiglass rectangular tank

(m,n)	**View order of modeshapes in Patran**	**Analytical frequency (Hz)**	**Numerical frequency (Hz)**	**Laboratory experiment frequency (Hz)**
(1,0)	1st modeshape	2.28	2.44	2.03
(0,1)	2nd modeshape	2.79	2.97	2.51
(2,0)	4th modeshape	3.23	3.39	2.36
(2,1)	5th modeshape	3.61	3.84	3.44
(3,0)	6th modeshape	3.95	4.13	3.81
(1,2)	8th modeshape	4.06	4.3	3.15
(3,1)	9th modeshape	4.18	4.43	4.17
(3,2)	12th modeshape	4.7	5	4.38
(5,0)	16th modeshape	5.1	5.35	4.73
(2,3)	17th modeshape	5.06	5.39	4.86
(4,2)	18th modeshape	5.1	5.44	5.01
(5,1)	19th modeshape	5.21	5.54	4.76
(3,3)	20th modeshape	5.3	5.67	4.74
(5,2)	21st modeshape	5.51	5.9	5.42
(4,3)	24th modeshape	5.6	6	5.38

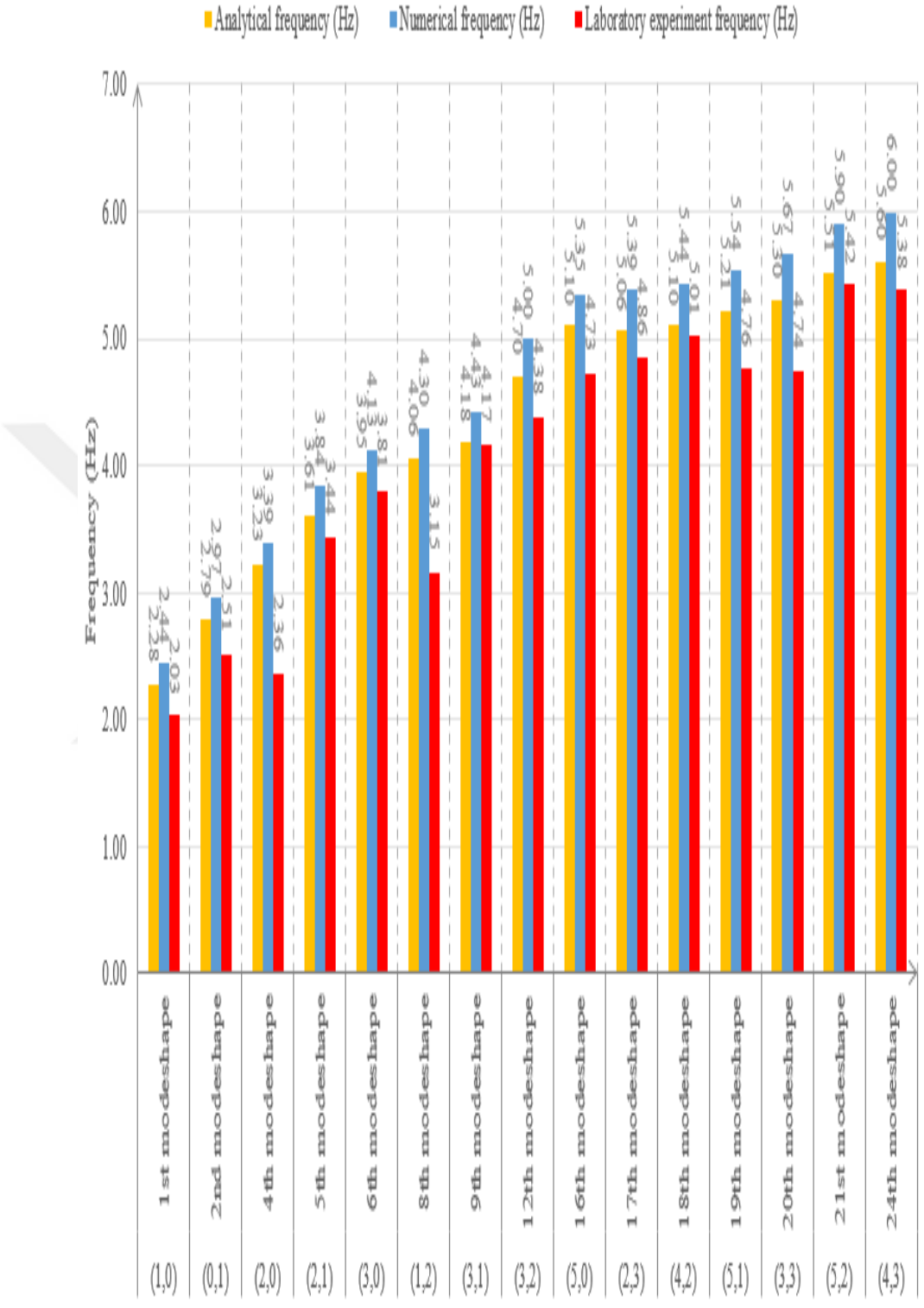

Figure 4.25. Representation of comparison of analytical, numerical and laboratory experiment frequencies for plexiglass rectangular tank

Table 4.15. Comparison of numerical and experimental error rates for plexiglass rectangular tank

(m,n)	**View order of modeshapes in Patran**	**Numerical error rate (%)**	**Laboratory experiment error rate (%)**
(1,0)	1st modeshape	7.02	-10.95
(0,1)	2nd modeshape	6.45	-10.07
(2,0)	4th modeshape	4.95	-26.93
(2,1)	5th modeshape	6.37	-4.58
(3,0)	6th modeshape	4.56	-3.66
(1,2)	8th modeshape	5.91	-22.36
(3,1)	9th modeshape	5.98	-0.30
(3,2)	12th modeshape	6.38	-6.72
(5,0)	16th modeshape	4.90	-7.24
(2,3)	17th modeshape	6.52	-4.03
(4,2)	18th modeshape	6.67	-1.67
(5,1)	19th modeshape	6.33	-8.59
(3,3)	20th modeshape	6.98	-10.55
(5,2)	21st modeshape	7.08	-1.57
(4,3)	24th modeshape	7.14	-3.94

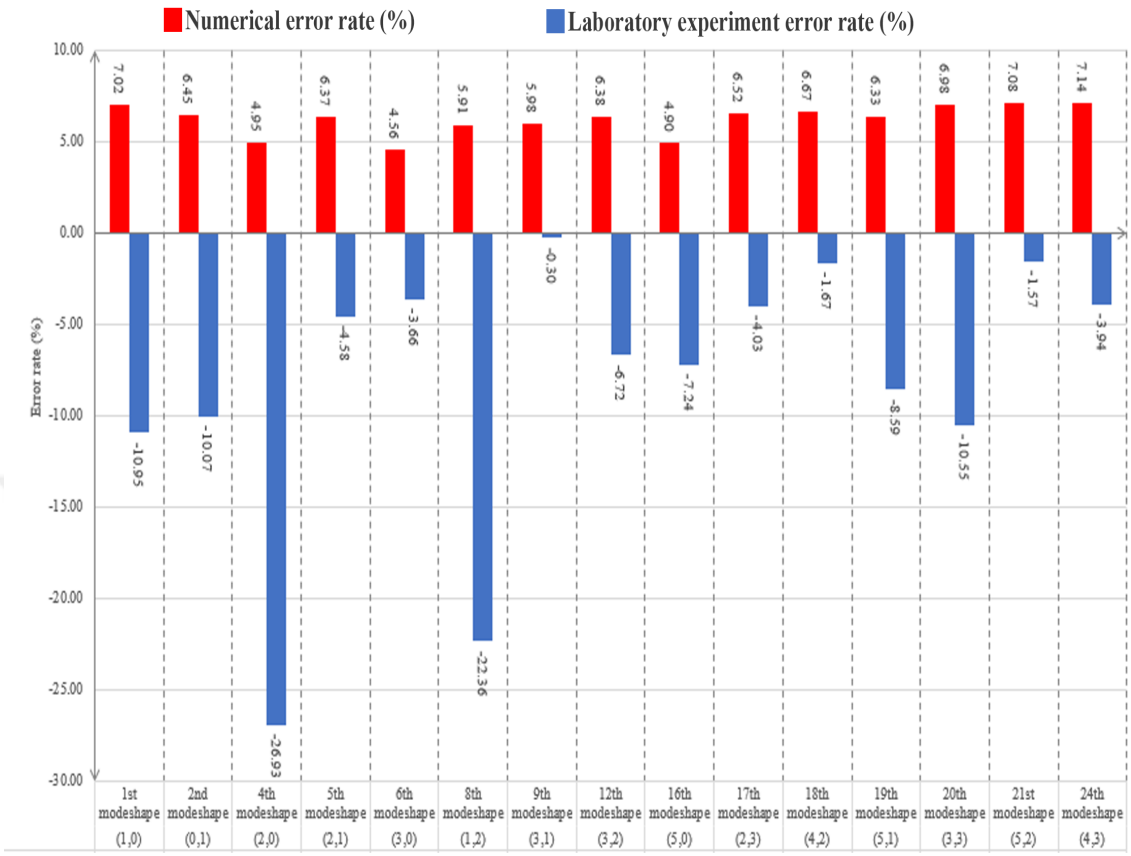

Figure 4.26. Representation of comparison of numerical and experimental error rates for plexiglass rectangular tank

From Table 4.14 and Table 4.15, it can be concluded that numerical analyses give more accurate results than laboratory experiment analysis for the fundamental modeshapes, such as 1st, 2nd and 4th ones. Also, for the 5th and 6th modeshapes which can be considered as fundamental modeshapes, as well, the difference between error rates are negligible. For the rest of the modeshapes, it is difficult to put forward a method since in some modes numerical analyses give better results whereas in some modes laboratory experiments give them better.

When the studies with plexiglass rectangular tanks are considered it is seen that with the optimum model numerical results could get 7.02% error rate compare to analytical frequencies in the best case scenario. One of the reasons that we were using plexiglass in our numerical analyses was being able to compare our numerical results with experimental results of Erginbas [3] and see the differences between these two approaches in terms of natural frequencies. However, this much numerical error rate with plexiglass can be considered as higher than it is expected. Thus, since analytical methods that we are using assume the tank wall as rigid, it is decided to use a very rigid tank material with the Young Modulus of 1220 GPa which is the Young Modulus of a diamond in order to enhance our model to its optimum case. Also the Poisson's ratio and the density of the material are chosen as the material properties of the diamond which is the most rigid material in the world.

All the analyses that are done above with plexiglass are completed without changing anything except using the rigid tank material. These analyses investigate the effect of tank thickness, tank mesh resolution, element length-gap distance ratio and phantom surface mesh resolution.

Additionally, for the study with a very rigid element, length-gap distance ratio for 0.5% are also examined. The frequencies of the mentioned numerical analyses with rigid tank material can be seen in the following table below

Table 4.16. First 5 frequencies of small scale rectangular tank with high rigidity with respect to tank thickness, tank mesh resolution, element length-gap distance ratio and phantom mesh resolution

Tank mesh (Length x Width x Height)	**Phantom mesh (Length x Width)**	**Gap**	**Tank thickness (mm)**	**1st freq (Hz)**	**2nd freq (Hz)**	**3rd freq (Hz)**	**4th freq (Hz)**	**5th freq (Hz)**
6x4x12	15x10	20%	0.5	2.92	3.5	3.82	3.87	4.4
6x4x12	15x10	20%	1	2.92	3.5	3.82	3.87	4.4
6x4x12	15x10	20%	2	2.92	3.5	3.82	3.87	4.4
6x4x12	15x10	20%	3	2.92	3.5	3.82	3.87	4.4
12x8x24	15x10	20%	3	2.87	3.42	3.75	3.77	4.34
24x16x48	15x10	20%	3	2.85	3.37	3.72	3.74	4.28
24x16x48	15x10	15%	3	2.73	3.25	3.63	3.64	4.16
24x16x48	15x10	10%	3	2.61	3.14	3.48	3.52	4.02
24x16x48	15x10	5%	3	2.46	3.01	3.32	3.44	3.9
24x16x48	15x10	2.5%	3	2.39	2.93	3.25	3.38	3.83
24x16x48	30x20	2.5%	3	2.33	2.86	3.19	3.36	3.78
24x16x48	60x40	2.5%	3	2.31	2.84	3.16	3.36	3.76
24x16x48	60x40	1.0%	3	NR	NR	NR	NR	NR
24x16x48	60x40	0.5%	3	NR	NR	NR	NR	NR
Analytical frequencies				2.28	2.79	3.06	3.23	3.61

Table 4.17. Error rates of partially-filled small scale rectangular tank with high rigidity for its first 5 modes with respect to tank thickness, tank mesh resolution, element length-gap distance ratio and phantom mesh resolution

Tank mesh (Lenght x Width x Height)	**Phantom mesh (Length x Width)**	**Gap**	**Tank thickness (mm)**	**Error rate of 1st mode (%)**	**Error rate of 2nd mode (%)**	**Error rate of 3rd mode (%)**	**Error rate of 4th mode (%)**	**Error rate of 5th mode (%)**
6x4x12	15x10	20%	0.5	28.07	25.45	24.84	19.81	21.88
6x4x12	15x10	20%	1	28.07	25.45	24.84	19.81	21.88
6x4x12	15x10	20%	2	28.07	25.45	24.84	19.81	21.88
6x4x12	15x10	20%	3	28.07	25.45	24.84	19.81	21.88
12x8x24	15x10	20%	3	25.88	22.58	22.55	16.72	20.22
24x16x48	15x10	20%	3	25.00	20.79	21.57	15.79	18.56
24x16x48	15x10	15%	3	19.74	16.49	18.63	12.69	15.24
24x16x48	15x10	10%	3	14.47	12.54	13.73	8.98	11.36
24x16x48	15x10	5%	3	7.89	7.89	8.50	6.50	8.03
24x16x48	15x10	2.5%	3	4.82	5.02	6.21	4.64	6.09
24x16x48	30x20	2.5%	3	2.19	2.51	4.25	4.02	4.71
24x16x48	60x40	2.5%	3	1.32	1.79	3.27	4.02	4.16

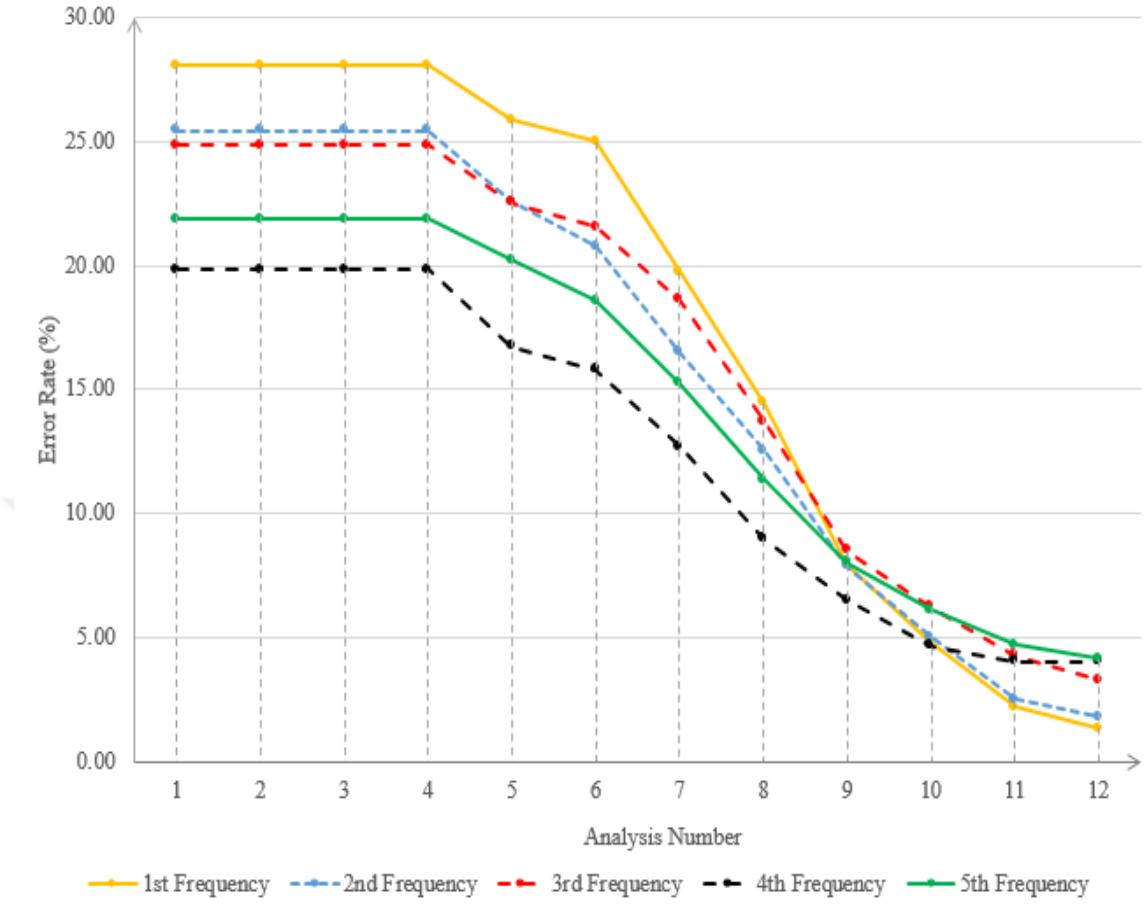

Figure 4.27. Error rates table representation of partially-filled small scale rectangular tank with high rigidity for its first 5 modes with respect to tank thickness, tank mesh resolution, element length-gap distance ratio and phantom mesh resolution

When the two tables and the graph above are examined, it is noticed that even very thin tank thicknesses, such as 0.1 mm and 0.25 mm, give the result of thickest tank case since the material acts very rigid. For tank mesh resolution analyses rigid tank basically show the same trend with plexiglass material; as the mesh resolution increases, the results are getting better.

The most important difference between studies with plexiglass and rigid tank material happens in the analyses of element length-gap distance ratio. In the analysis with plexiglass, gap ratio could be at most 5% whereas with rigid material case 2.5%

gap ratio could be checked. Gap ratio depends on the distance between phantom surface and tank wall. Phantom surface can not move horizontally since its horizontal movement is constrained where tank wall can move horizontally due to the effect of sloshing fluid. This difference between plexiglass and rigid materials about being able to do analysis with 2.5% gap ratio can be explained with these facts; when the plexiglass material with its Young Modulus of 3100 MPa is used it is expected that the tank wall will make bigger deformation compare to tank wall that has the properties of a very rigid material, diamond, with its Young Modulus of 1220 GPa. As a result of this situation, the tank with plexiglass material can get closer to the phantom surface during sloshing by doing larger deformation compare to tank with rigid material. When this deformation is in the range of singularity of the point sources, the potential will not be calculated at there. On the other hand, since it is expected to have a way smaller displacement with rigid material, tank wall may be able to get closer to the phantom surface without being in the singularity range of point source. After the analysis with 2.5% gap ratio, 1% and 0.5% gap ratios are implemented, however, the program can not calculate the frequencies by giving the same error with plexiglass tank that is due to singularity situation. Lastly, the phantom surface mesh resolution is increased and the results get closer to analytical frequencies. As a result of this study, it can be seen that by using a very rigid material numerical error rate for the first natural frequency is found as 1.32% which can be considered as a good value for our aim of having an optimum model.

4.1.6. Large Scale Tank

In addition to the analyses that are made for small scale models, the analyses for large scale models that have a size similar to real life applications are made as well in order to investigate the modelling parameters for different sizes of tanks.

4.1.7. Numerical Analyses

Compare to small scale models' analyses, in large scale models' analyses the geometry of the model, tank mesh resolution, element length-gap distance ratio, the tank thickness and tank material are changed.

All other parameters in this study are same with small scale models' analyses such as the properties of phantom surface. For all the frequency analyses with large scales, the following properties are used

- Tank type: Rectangular
- Tank length: 20 m
- Tank width: 15 m
- Tank height: 8 m
- Tank thickness: 20 mm
- Height of water: 4 m
- Material types of tank: Steel
- Young Modulus of steel: 207 GPa
- Density of steel: $7800 kg/m^3$
- Poisson ratio of steel: 0.3

4.1.8. Results

The analytical frequencies for large scale rectangular tank by using Abramson's formula can be found below

Table 4.18. Analytical frequencies of large scale partially filled rectangular tanks by using Abramson's method

m	**n=0**	**n=1**	**n=2**	**n=3**	**n=4**	**n=5**	**n=6**
0	0	0.19	0.31	0.39	0.46	0.51	0.56
1	0.15	0.23	0.32	0.4	0.46	0.51	0.56
2	0.26	0.29	0.36	0.42	0.47	0.52	0.57
3	0.33	0.35	0.39	0.44	0.49	0.53	0.58
4	0.39	0.4	0.43	0.47	0.51	0.55	0.59
5	0.44	0.45	0.47	0.5	0.53	0.57	0.61
6	0.48	0.49	0.51	0.53	0.56	0.59	0.62

In addition, the analytical result from Housner's method is also found and the first natural frequency from this method is found same with Abramson's as 0.15 Hz.

In order to envision the large scale rectangular tank, the image of the model can be found below. The sloshing behaviour in this tank in terms of shapes of the sloshing modes are going to be same with the small scale plexiglass rectangular tank that are examined previously in this study.

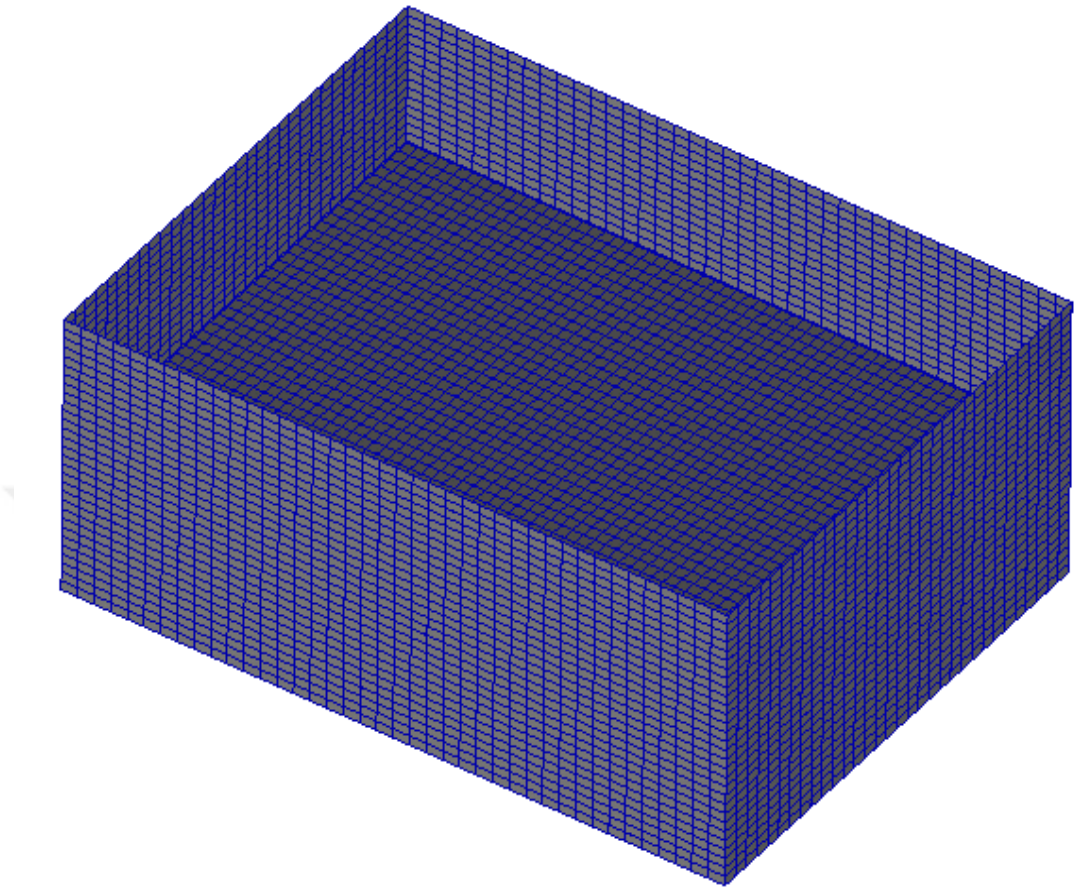

Figure 4.28. Large scale partially filled rectangular tank representation

The tables of natural frequency and error rates of the large scale rectangular tank can be found in the tables below. Also, from the graph of error rate table the trend of the frequency with respect to changes can be seen. In the following graph below x axis represents the order of analyses which are numbered according to following table of error rate. Number 1 on x axis of graph denotes the values from the top of error rate table whereas number 11 represents the values from the bottom of the error rate table.

Table 4.19. First 5 frequencies of large scale rectangular tank with high rigidity with respect to tank thickness, tank mesh resolution, element length-gap distance ratio and phantom mesh resolution

Tank mesh (Lenght x Width x Height)	**Phantom mesh (Length x Width)**	**Gap**	**Tank thickness (mm)**	**1st freq (Hz)**	**2nd freq (Hz)**	**3rd freq (Hz)**	**4th freq (Hz)**	**5th freq (Hz)**
10x8x8	15x10	20%	5	0.140	0.187	0.230	0.260	0.320
10x8x8	15x10	20%	10	0.196	0.250	0.276	0.330	0.354
10x8x8	15x10	20%	20	0.194	0.245	0.276	0.330	0.354
20x16x15	15x10	20%	20	0.190	0.238	0.270	0.329	0.351
40x32x30	15x10	20%	20	0.188	0.236	0.269	0.326	0.349
40x32x30	15x10	15%	20	0.185	0.230	0.265	0.322	0.345
40x32x30	15x10	10%	20	0.182	0.226	0.262	0.316	0.339
40x32x30	15x10	5%	20	0.173	0.223	0.257	0.306	0.331
40x32x30	15x10	2.5%	20	0.168	0.219	0.251	0.298	0.325
40x32x30	30x20	2.5%	20	0.165	0.214	0.245	0.294	0.322
40x32x30	60x40	2.5%	20	0.161	0.207	0.243	0.288	0.315
40x32x30	60x40	1.0%	20	NR	NR	NR	NR	NR
40x32x30	60x40	0.5%	20	NR	NR	NR	NR	NR
Analytical frequencies				0.15	0.19	0.22	0.26	0.29

Table 4.20. Partially-filled steel large scale rectangular tank's error rates for its first 5 modes with respect to tank thickness, tank mesh resolution, element length-gap distance ratio and phantom mesh resolution

Tank mesh (Lenght x Width x Height)	**Phantom mesh (Length x Width)**	**Gap**	**Tank thickness (mm)**	**Error rate of 1st mode (%)**	**Error rate of 2nd mode (%)**	**Error rate of 3rd mode (%)**	**Error rate of 4th mode (%)**	**Error rate of 5th mode (%)**
10x8x8	15x10	20%	5	-6.67	-1.58	4.55	0.00	10.34
10x8x8	15x10	20%	10	30.67	31.58	25.45	26.92	22.07
10x8x8	15x10	20%	20	29.33	28.95	25.45	26.92	22.07
20x16x15	15x10	20%	20	26.67	25.26	22.73	26.54	21.03
40x32x30	15x10	20%	20	25.33	24.21	22.27	25.38	20.34
40x32x30	15x10	15%	20	23.33	21.05	20.45	23.85	18.97
40x32x30	15x10	10%	20	21.33	18.95	19.09	21.54	16.90
40x32x30	15x10	5%	20	15.33	17.37	16.82	17.69	14.14
40x32x30	15x10	2.5%	20	12.00	15.26	14.09	14.62	12.07
40x32x30	30x20	2.5%	20	10.00	12.63	11.36	13.08	11.03
40x32x30	60x40	2.5%	20	7.33	8.95	10.45	10.77	8.62

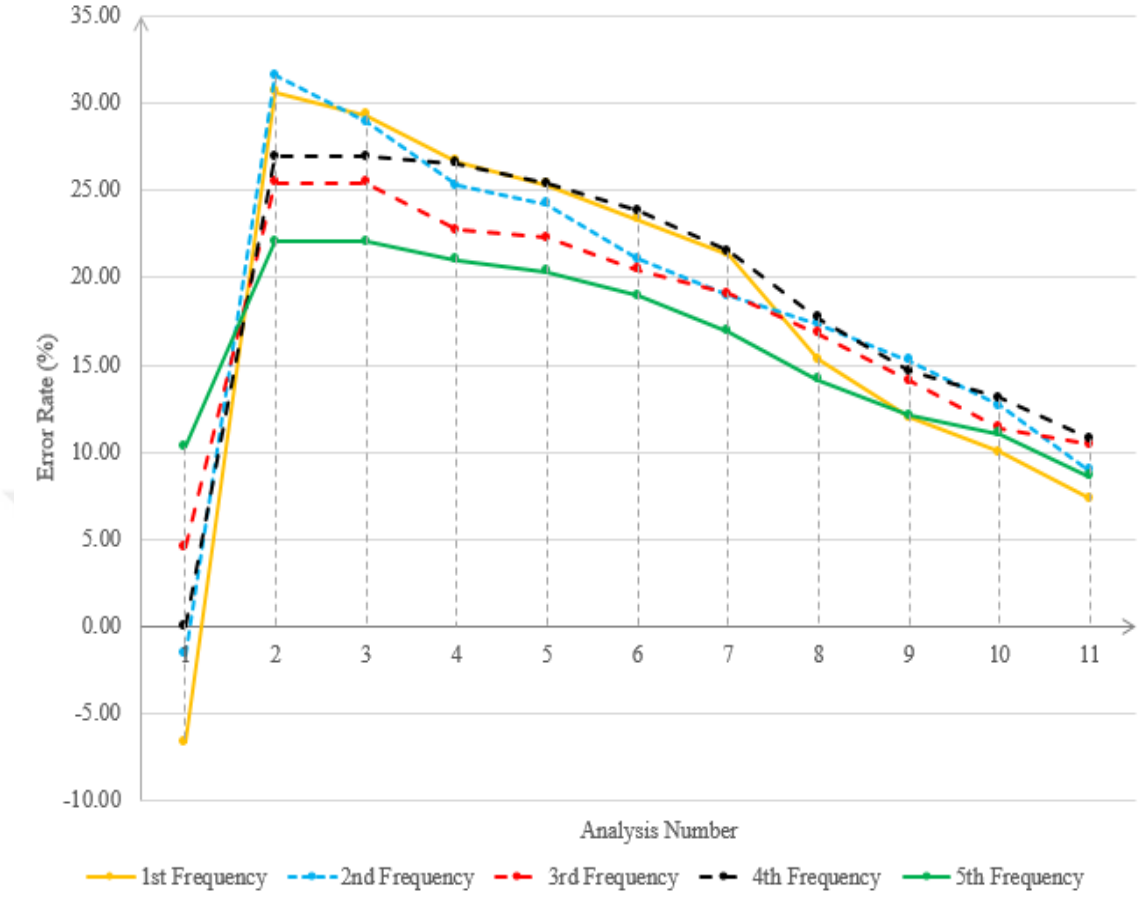

Figure 4.29. Representation of partially-filled steel large scale rectangular tank's error rates for its first 5 modes with respect to tank thickness, tank mesh resolution, element length-gap distance ratio and phantom mesh resolution

When the results are investigated it can be noticed that the large scale rectangular tank models' analyses have exactly the same trend with small scale plexiglass model. The frequencies tank change according to its tank thickness; after a point the results converges since it is thick enough. The tank mesh resolution makes the results better and when it is refined enough the frequencies again converge. The biggest effects on frequencies come from the study of element length-distance ratio. As the gap ratio decreases the results get better but when we get too close, which is 1.0% and 0.5% for this study, the program does not give us results due to the fact that the velocity potential can not be calculated when the point that we want to calculate is in the

range of singularity. Lastly, as phantom surface mesh resolution increases, the phantom surface is represented with more number of grid and elements and it helps to represent fluid behaviour better.

It can be noticed that the error rates of small scale and large scale models are pretty similar to each other. Even though for giving a rule of thumb recommendation these two models may not be enough and more number of geometries are needed to be investigated, it can be said that working on these parameters carefully may give us good results for both small and large scale models.

4.2. Cylindrical Tanks

In this section, very similar to the rectangular tank, the frequencies which are obtained by analytical, numerical and experimental methods for a cylindrical tank partially-filled with water will be discussed. For this aim, the chapter of "Mathematical Derivation of Natural Frequency from Housner's Analytical Method Study" and "Mathematical Derivation of Sloshing Motion for Rectangular and Cylindrical Tank" from appendix are utilized. For numerical analyses, the structural analysis programme Nastran is employed and for the laboratory experiments' results, the data of Erginbas [3] is used.

4.2.1. Small Scale Tank

Like in the case of rectangular tank, small scale and large scale models are created for the analyses.

For all the analyses mentioned above for small scale models, the same cylindrical tank is used with the following properties

- Tank type: Cylindrical
- Tank radius: 100 mm

- Tank height: 500 mm
- Tank thickness: 3 mm
- Height of water: 300 mm
- Material type of tank: Steel (only for numerical analyses), Plexiglass (for numerical and experimental analyses), and a material with high rigidity (only for numerical analyses)
- Young Modulus of steel: 207000 MPa
- Density of steel: $7800 \times 10^{-12} tonnes/mm^3$
- Poisson ratio of steel: 0.3
- Young Modulus of plexiglass: 3100 MPa
- Density of plexiglass: $1190 \times 10^{-12} tonnes/mm^3$
- Poisson ratio of plexiglass: 0.37
- Young Modulus of material with high rigidity: 1220000 MPa
- Density of material with high rigidity: $3520 \times 10^{-12} tonnes/mm^3$
- Poisson ratio of material with high rigidity: 0.2
- Density of water: $1000 \times 10^{-12} tonnes/mm^3$

4.2.2. Analytical Method

As it was expressed earlier in this document, the analytical frequency of a cylindrical tank was obtained with the following formula from the chapter of "Mathematical Derivation of Sloshing Motion for Rectangular and Cylindrical Tank" where it is the frequency formula from Abramson's analytical method. This natural frequency formula can be seen as follows

$$f_{m,n} = \frac{1}{2\pi} \sqrt{g. \tanh\left(\frac{\alpha_m(n).h}{a}\right) \frac{\alpha_m(n)}{a}}$$

where m and n refers to nodal diameters and nodal circles, respectively [35].

As a second analytical method, the analytical method of Housner is utilized in order to find first natural frequency of the sloshing motion

$$f = \frac{1}{2\pi}(\frac{g}{R}\sqrt{\frac{27}{8}}(tanh\sqrt{\frac{27}{8}}\frac{h}{R})) \tag{4.4}$$

4.2.3. Numerical Analyses

Like in the case of rectangular tanks, eigenvalue analyses in Nastran are done, for partially-filled cylindrical tanks, as well. The parameters with their values shown below are investigated for their impacts over the sloshing frequency.

- Type of tank material: Plexiglass and aluminum
- Tank thickness: 0.1 mm, 0.25 mm, 0.5 mm, 1 mm, 2 mm, 3 mm
- Tank's mesh resolution (throughout angular and vertical axis, respectively): 20×12, 30×18, 40×24
- Gap ratio between phantom surface element size and gap distance: 26%, 20%, 13%, 6%, 3%, 1.5%, 0.75%, 0.375%
- Phantom surface's mesh topology: Unstructured, butterfly, radial

In order to make mentioned phantom surface mesh topologies understood, they are demonstrated in the figures below

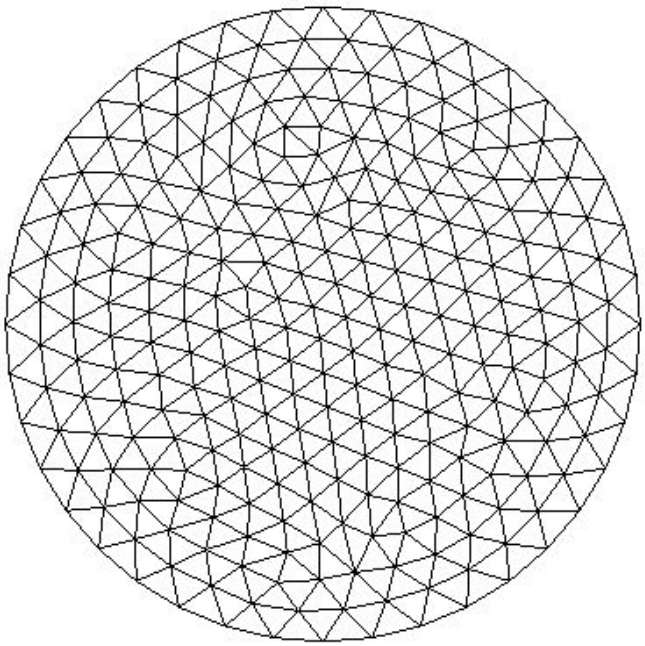

Figure 4.30. Unstructured mesh used for phantom surface.

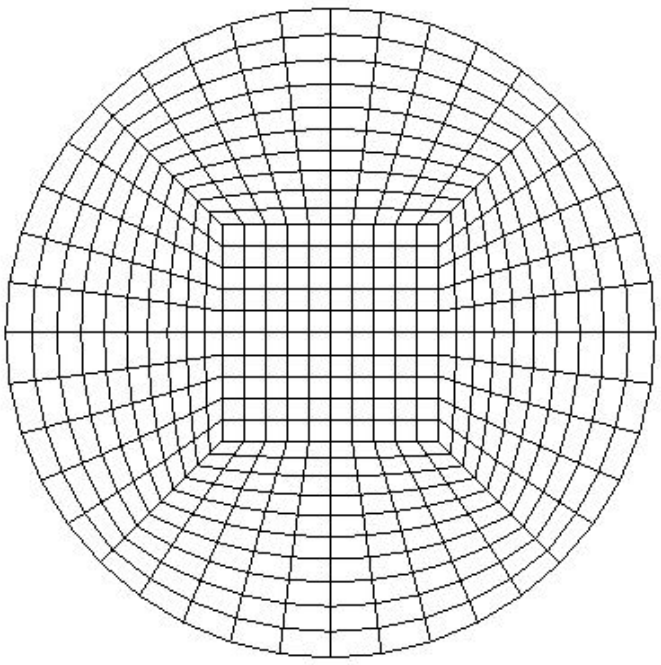

Figure 4.31. Butterfly mesh used for phantom surface.

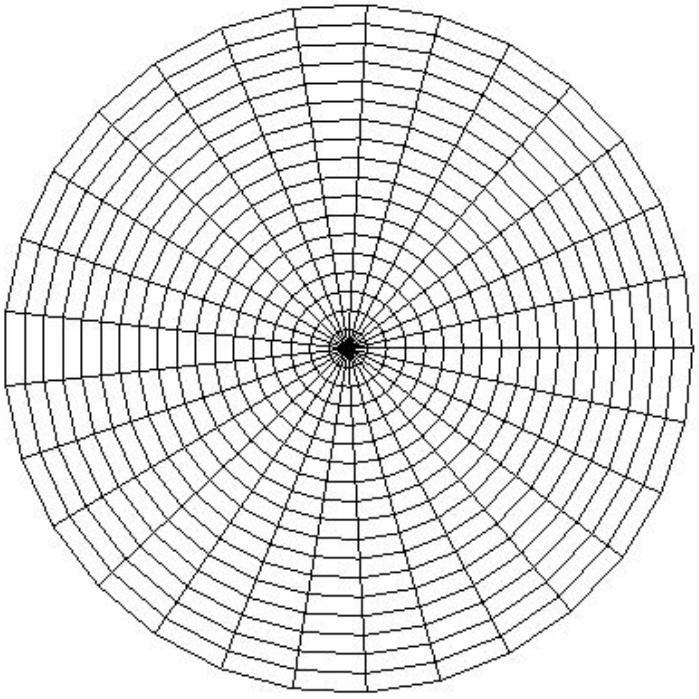

Figure 4.32. Radial mesh used for phantom surface.

In order to give a better understanding to the case, similar to the rectangular tank case, gap ratio between phantom surface element size and gap distance for cylindrical tanks' different topologies are demonstrated below. In the figures "n" denotes the gap ratio

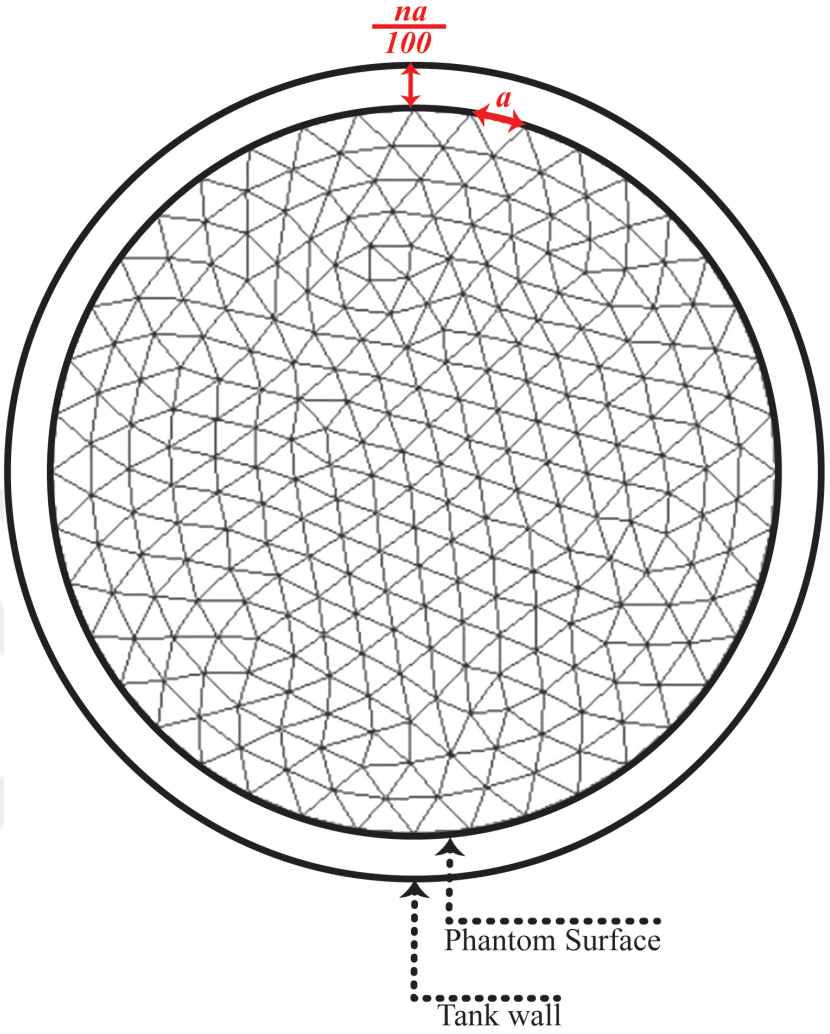

Figure 4.33. Demonstration of gap ratio between phantom surface element size and gap distance for phantom surface with unstructured mesh

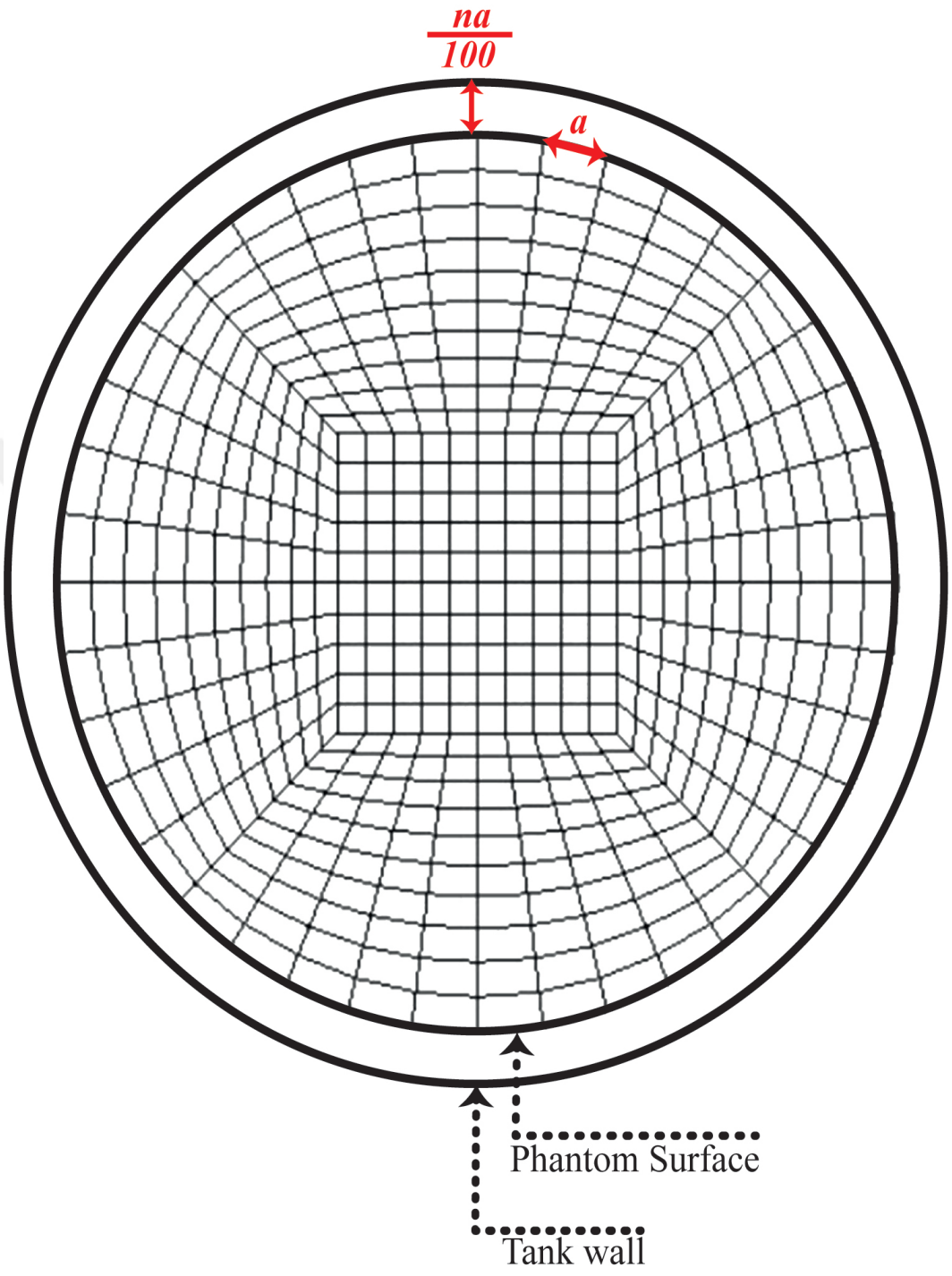

Figure 4.34. Demonstration of gap ratio between phantom surface element size and gap distance for phantom surface with butterfly mesh

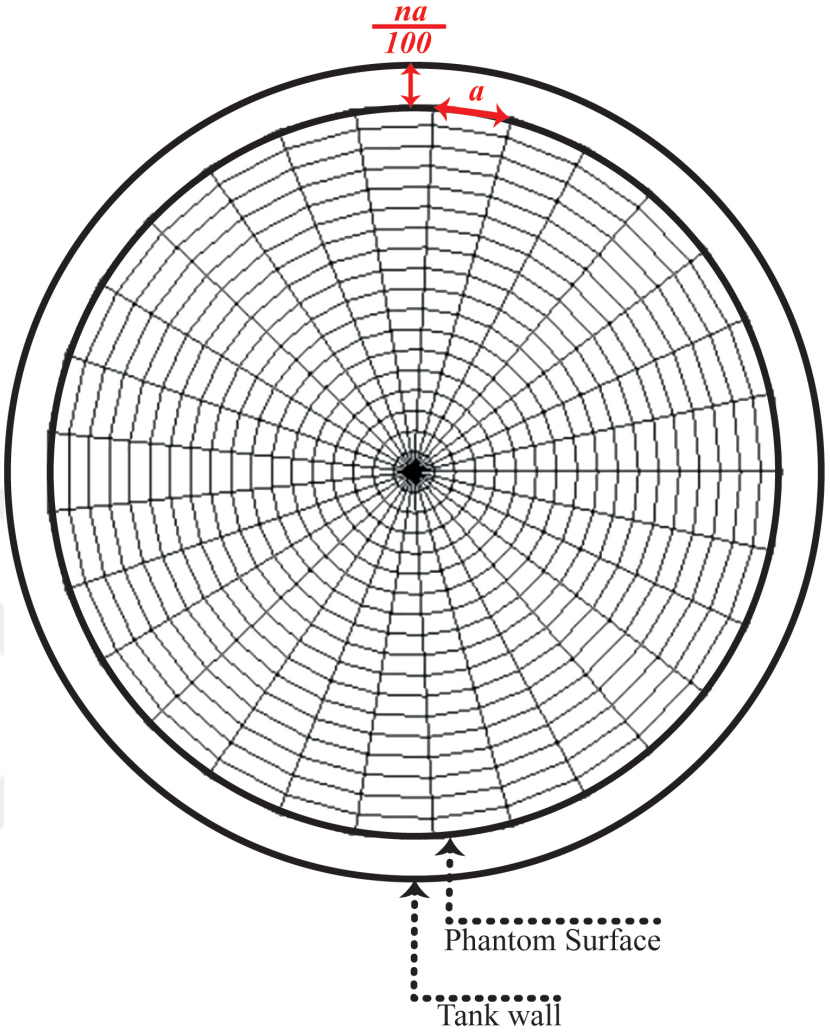

Figure 4.35. Demonstration of gap ratio between phantom surface element size and gap distance for phantom surface with radial mesh

Meanwhile, in all numerical analyses, the type of tank material, tank thickness, tank mesh resolution, phantom surface's radius and its mesh topology are examined, some other variables are taken as fixed.

These variables are shown below

- Tank bottom's mesh type: Unstructured, triangle elements
- Tank wall's mesh type: Structured, quadrilateral elements
- Material type of phantom surface: Aluminum
- Young Modulus of phantom surface's material: 69000 MPa
- Density of phantom surface's material: $2700 - 10^{-12} tonnes/mm^3$
- Poisson ratio of phantom surface's material: 0.33
- Phantom surface thickness: 0.001 mm

To check how close are the numerical results to analytical ones, they are compared with each other and error rate between them is declared as a percentage. As it was declared before, the numerical error rate is calculated from Equation 4.2

To demonstrate the sloshing motion in cylindrical tank as a result of numerical analyses mentioned above, some modeshapes of sloshing motion in cylindrical tank with unstructured phantom mesh from Patran are shown below. These modeshapes are in (m,n) format which comes from the derivation of frequency for cylindrical tanks.

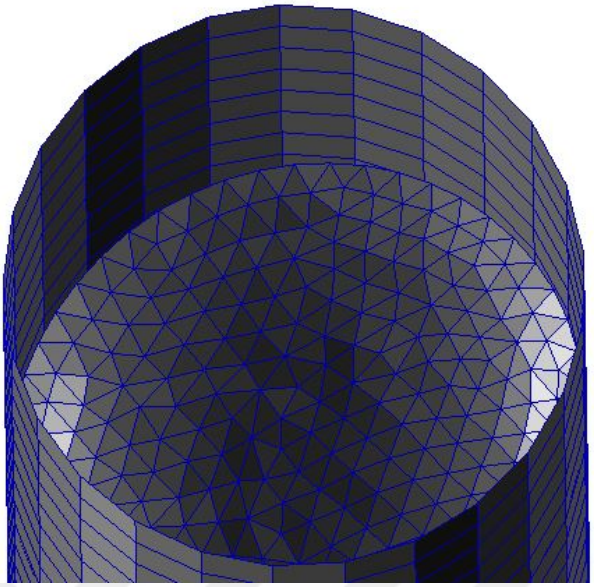

Figure 4.36. Modeshape (1,1) for cylindrical tank with unstructured mesh.

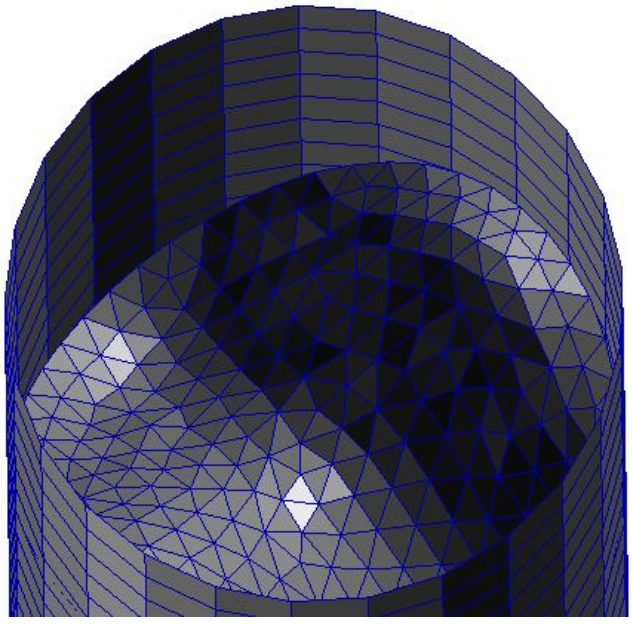

Figure 4.37. Modeshape (2,1) for cylindrical tank with unstructured mesh.

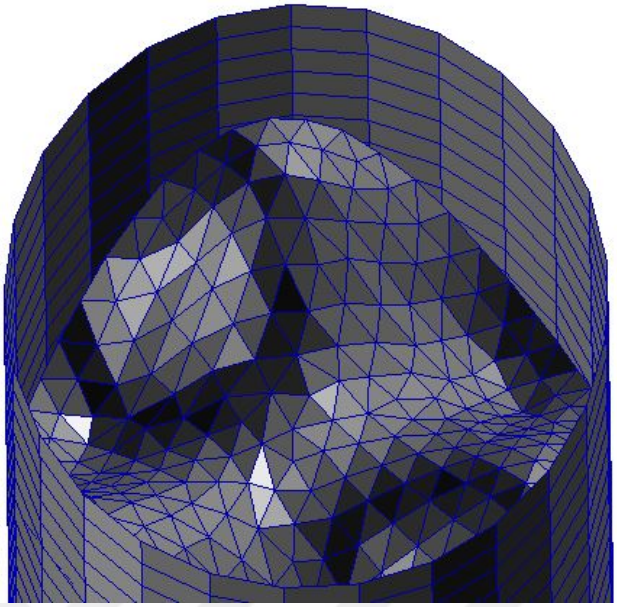

Figure 4.38. Modeshape (3,1) for cylindrical tank with unstructured mesh.

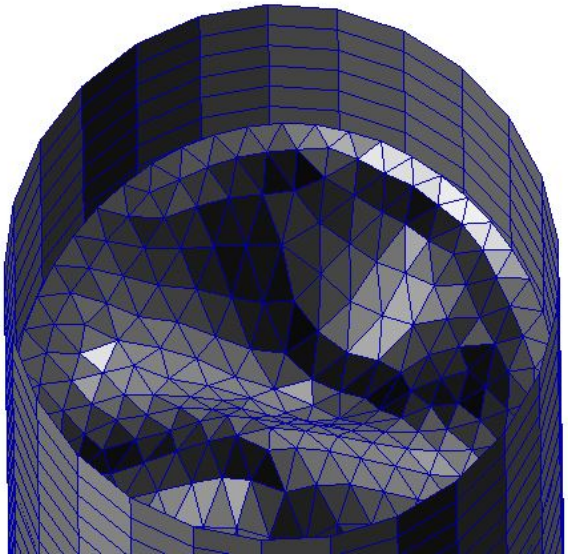

Figure 4.39. Modeshape (1,2) for cylindrical tank with unstructured mesh.

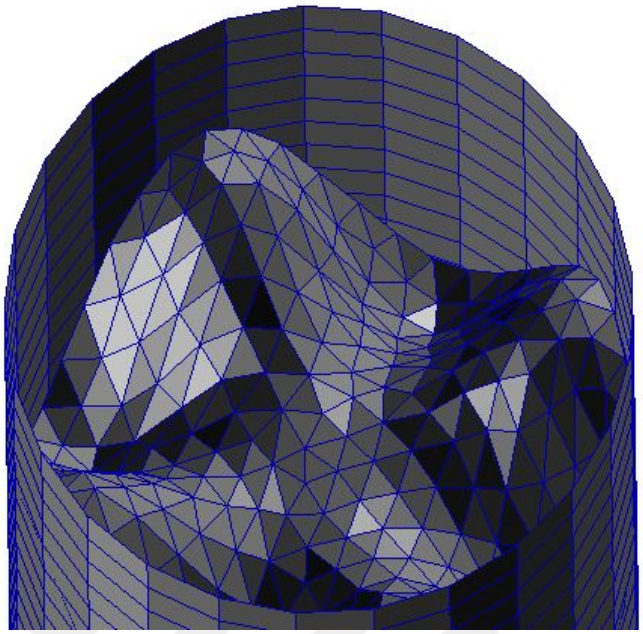

Figure 4.40. Modeshape (4,1) for cylindrical tank with unstructured mesh.

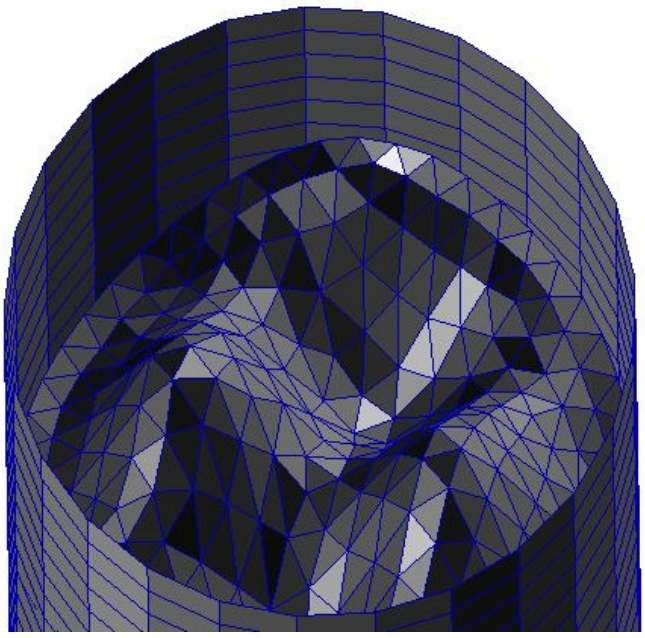

Figure 4.41. Modeshape (2,2) for cylindrical tank with unstructured mesh.

4.2.4. Laboratory Experiments

For laboratory experiments, like in the case of rectangular tanks, the results of the shaking table experiments by Erginbas [3] are used. For cylindrical tank, exactly the same steps of the rectangular tank experiment were taken, except the step that the container was only excited in one axis which can be seen in Figure 4.42 since the container was axisymmetrical and the axis of excitation was insignificant, compare to the rectangular tank which was excited in x and y axes, separately.

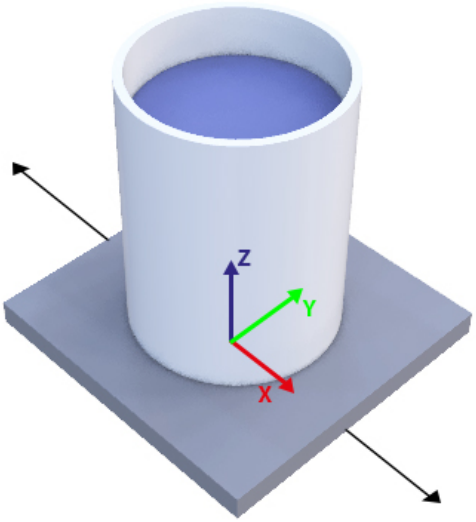

Figure 4.42. Demonstration of the excitation axis of the cylindrical tank. Adapted from [5].

In order to envision the laboratory experiment for cylindrical tanks in mind, the figures below can be examined



Figure 4.43. Representation of modeshape (1,1) during laboratory experiment of plexiglass cylindrical tank [3].



Figure 4.44. Representation of modeshape (2,1) during laboratory experiment of plexiglass cylindrical tank [3].



Figure 4.45. Representation of modeshape (1,2) during laboratory experiment of plexiglass cylindrical tank [3].



Figure 4.46. Representation of modeshape (4,1) during laboratory experiment of plexiglass cylindrical tank [3].



Figure 4.47. Representation of modeshape (1,3) during laboratory experiment of plexiglass cylindrical tank [3].

4.2.5. Results

Table 4.62 shows the analytical frequencies for sloshing motion of the fluid in the cylindrical tank with the features of "tank properties" section.

Table 4.21. Analytical frequencies of small scale partially filled cylindrical tanks by using Abramson's method (m and n refers to nodal diameters and nodal circles, respectively [35]).

m	**n=1**	**n=2**	**n=3**	**n=4**	**n=5**	**n=6**
0	0	3.08	4.17	5.03	5.75	6.4
1	2.13	3.64	4.60	5.39	6.08	6.69
2	2.75	4.08	4.98	5.72	6.37	6.96
3	3.23	4.46	5.31	6.02	6.65	7.22
4	3.63	4.80	5.61	6.3	6.91	7.46
5	3.99	5.11	5.89	6.56	7.15	7.69
6	4.31	5.40	6.16	6.8	7.38	7.91

As in the case of rectangular tank, analytical method of Housner gave the same first natural frequency with Abramson's first natural frequency as 2.13 Hz. Due to this reason, in the tables below, the analytical results are demonstrated together under the name of "Analytical frequencies". Again, like in the case of rectangular tank analyses, the first parameters that are investigated for cylindrical tank are tank material and its changing thickness. In the tables below, the frequencies of an steel tank with phantom surfaces of unstructured, butterfly and radial meshes with respect to its changing tank thickness values, the error rates that are obtained to compare the numerical frequencies with analytical ones and the graph of the error rate tables are shown

Table 4.22. First 5 frequencies of partially-filled steel cylindrical tank with phantom surface of unstructured mesh with respect to changing tank thickness

Tank mesh	**Phantom mesh type**	**Gap**	**Tank thickness (mm)**	**1st freq (Hz)**	**2nd freq (Hz)**	**3rd freq (Hz)**	**4th freq (Hz)**	**5th freq (Hz)**
20x12	Unstructured	26%	0.1	1.8	2.7	3.3	3.36	3.51
20x12	Unstructured	26%	0.25	2.7	2.71	3.36	3.37	3.52
20x12	Unstructured	26%	0.5	2.7	2.71	3.36	3.37	3.52
20x12	Unstructured	26%	1	2.7	2.71	3.36	3.37	3.52
20x12	Unstructured	26%	2	2.7	2.71	3.36	3.37	3.52
20x12	Unstructured	26%	3	2.7	2.71	3.36	3.37	3.52
Analytical frequencies				2.14	2.14	2.75	2.75	3.23

Table 4.23. Error rates of partially-filled steel cylindrical tank with phantom surface of unstructured mesh for its first 5 modes with respect to changing tank thickness

Tank mesh	**Phantom mesh type**	**Gap**	**Tank thick-ness (mm)**	**Error rate of 1st mode (%)**	**Error rate of 2nd mode (%)**	**Error rate of 3rd mode (%)**	**Error rate of 4th mode (%)**	**Error rate of 5th mode (%)**
20x12	Unstructured	26%	0.1	-15.89	26.17	20.00	22.18	8.67
20x12	Unstructured	26%	0.25	26.17	26.64	22.18	22.55	8.98
20x12	Unstructured	26%	0.5	26.17	26.64	22.18	22.55	8.98
20x12	Unstructured	26%	1	26.17	26.64	22.18	22.55	8.98
20x12	Unstructured	26%	2	26.17	26.64	22.18	22.55	8.98
20x12	Unstructured	26%	3	26.17	26.64	22.18	22.55	8.98

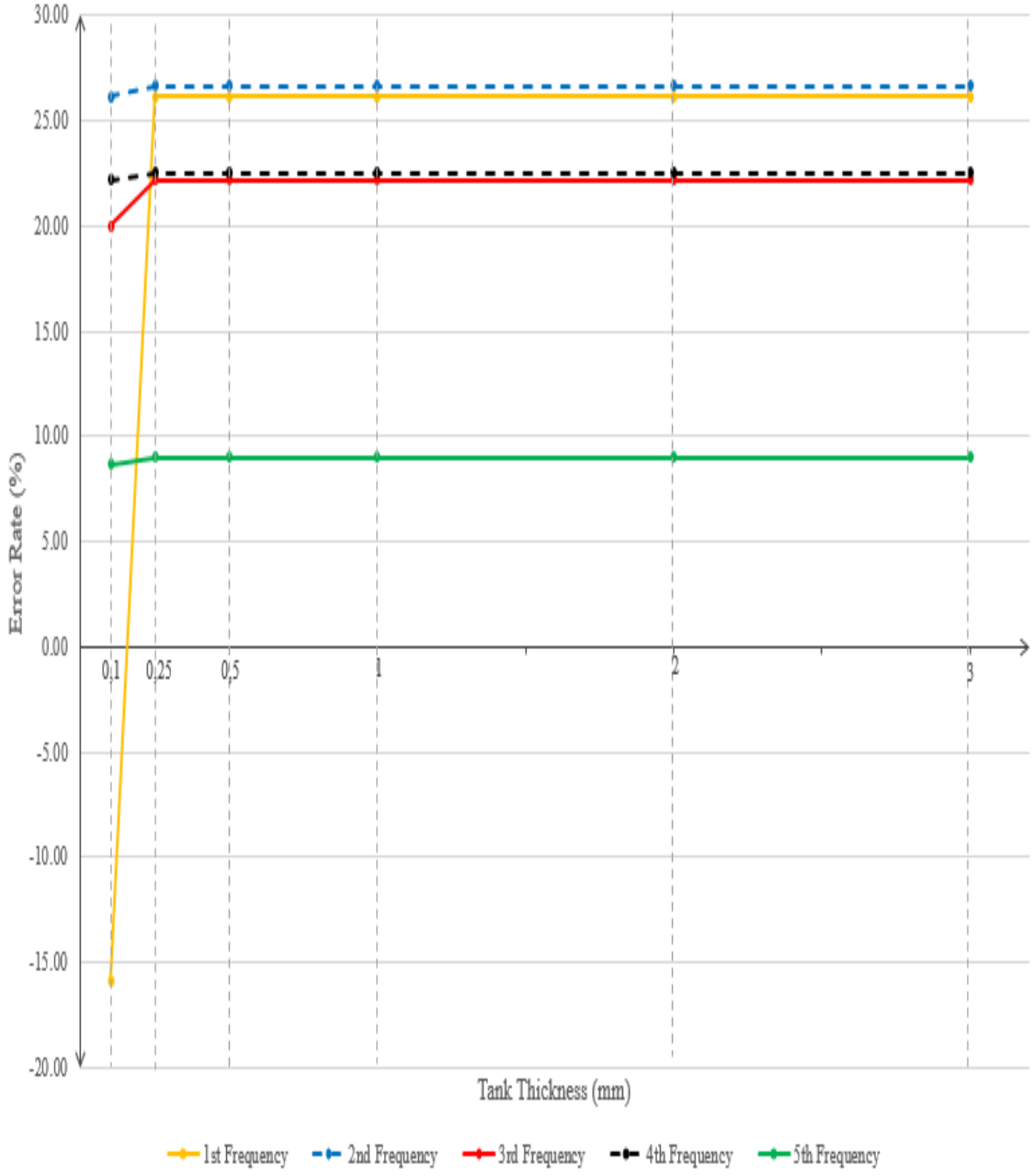

Figure 4.48. Error rates representation of partially-filled steel cylindrical tank with phantom surface of unstructured mesh for its first 5 modes with respect to changing tank thickness

Table 4.24. First 5 frequencies of partially-filled steel cylindrical tank with phantom surface of butterfly mesh with respect to changing tank thickness

Tank mesh	**Phantom mesh type**	**Gap**	**Tank thickness (mm)**	**1st freq (Hz)**	**2nd freq (Hz)**	**3rd freq (Hz)**	**4th freq (Hz)**	**5th freq (Hz)**
20x12	Butterfly	26%	0.1	1.8	2.7	3.3	3.36	3.47
20x12	Butterfly	26%	0.25	2.71	2.71	3.36	3.39	3.48
20x12	Butterfly	26%	0.5	2.71	2.71	3.36	3.39	3.48
20x12	Butterfly	26%	1	2.71	2.71	3.36	3.39	3.48
20x12	Butterfly	26%	2	2.71	2.71	3.36	3.39	3.48
20x12	Butterfly	26%	3	2.71	2.71	3.36	3.39	3.48
Analytical frequencies				2.14	2.14	2.75	2.75	3.23

Table 4.25. Error rates of partially-filled steel cylindrical tank with phantom surface of butterfly mesh for its first 5 modes with respect to changing tank thickness

Tank mesh	**Phantom mesh type**	**Gap**	**Tank thick-ness (mm)**	**Error rate of 1st mode (%)**	**Error rate of 2nd mode (%)**	**Error rate of 3rd mode (%)**	**Error rate of 4th mode (%)**	**Error rate of 5th mode (%)**
20x12	Butterfly	26%	0.1	-15.89	26.17	20.00	22.18	7.43
20x12	Butterfly	26%	0.25	26.64	26.64	22.18	23.27	7.74
20x12	Butterfly	26%	0.5	26.64	26.64	22.18	23.27	7.74
20x12	Butterfly	26%	1	26.64	26.64	22.18	23.27	7.74
20x12	Butterfly	26%	2	26.64	26.64	22.18	23.27	7.74
20x12	Butterfly	26%	3	26.64	26.64	22.18	23.27	7.74

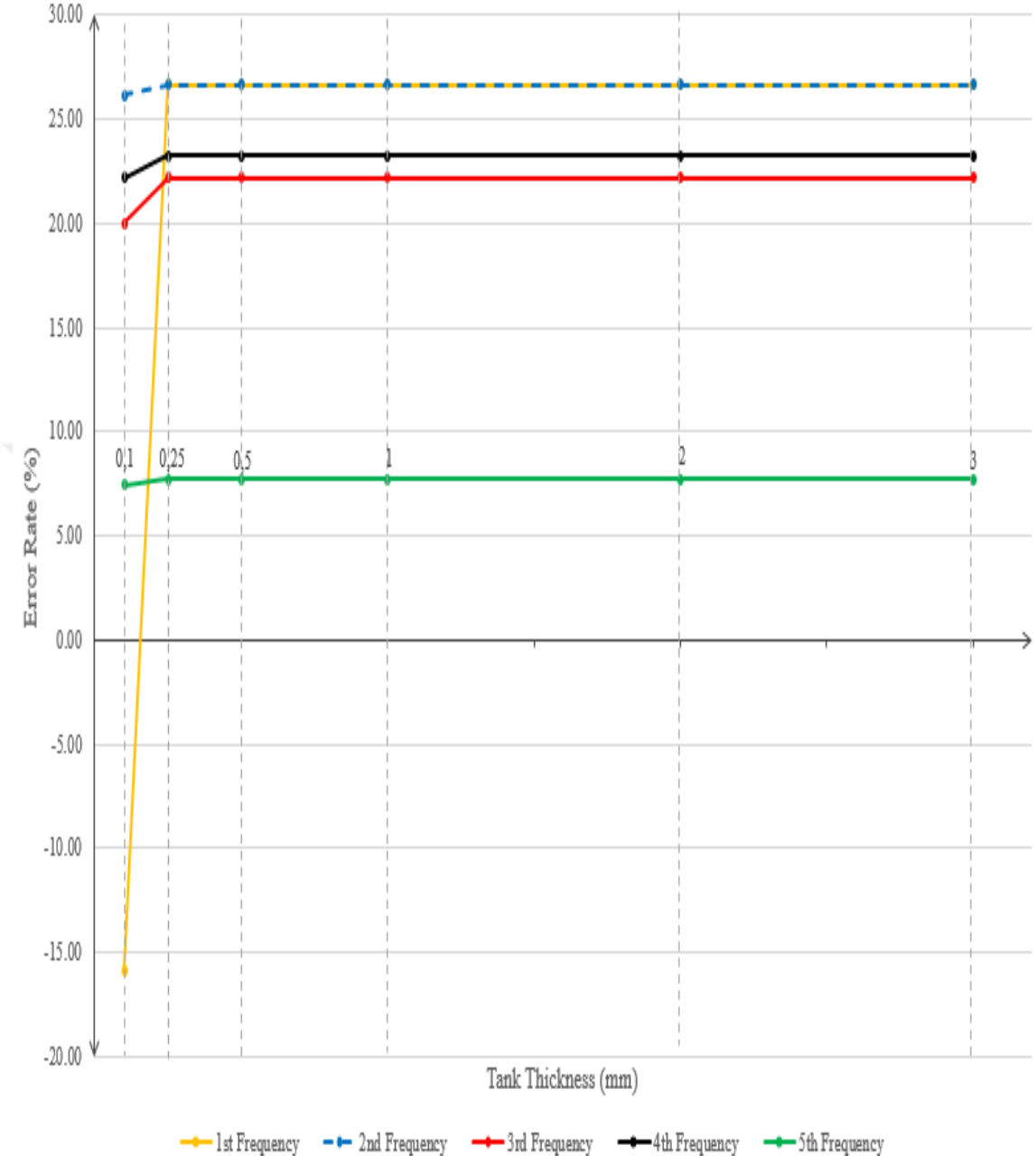

Figure 4.49. Error rates representation of partially-filled steel cylindrical tank with butterfly phantom surface for its first 5 modes with respect to changing tank thickness

Table 4.26. First 5 frequencies of partially-filled steel cylindrical tank with phantom surface of radial mesh with respect to changing tank thickness

Tank mesh	**Phantom mesh type**	**Gap**	**Tank thickness (mm)**	**1st freq (Hz)**	**2nd freq (Hz)**	**3rd freq (Hz)**	**4th freq (Hz)**	**5th freq (Hz)**
20x12	Radial	26%	0.1	1.8	2.7	3.3	3.36	3.47
20x12	Radial	26%	0.25	2.73	2.73	3.43	3.43	3.48
20x12	Radial	26%	0.5	2.73	2.73	3.43	3.43	3.48
20x12	Radial	26%	1	2.73	2.73	3.43	3.43	3.48
20x12	Radial	26%	2	2.73	2.73	3.43	3.43	3.48
20x12	Radial	26%	3	2.73	2.73	3.43	3.43	3.48
Analytical frequencies				2.14	2.14	2.75	2.75	3.23

Table 4.27. Error rates of partially-filled steel cylindrical tank with phantom surface of radial mesh for its first 5 modes with respect to changing tank thickness

Tank mesh	**Phantom mesh type**	**Gap**	**Tank thick-ness (mm)**	**Error rate of 1st mode (%)**	**Error rate of 2nd mode (%)**	**Error rate of 3rd mode (%)**	**Error rate of 4th mode (%)**	**Error rate of 5th mode (%)**
20x12	Radial	26%	0.1	27.57	26.17	20.00	22.18	7.43
20x12	Radial	26%	0.25	27.57	27.57	24.73	24.73	7.74
20x12	Radial	26%	0.5	27.57	27.57	24.73	24.73	7.74
20x12	Radial	26%	1	27.57	27.57	24.73	24.73	7.74
20x12	Radial	26%	2	27.57	27.57	24.73	24.73	7.74
20x12	Radial	26%	3	27.57	27.57	24.73	24.73	7.74

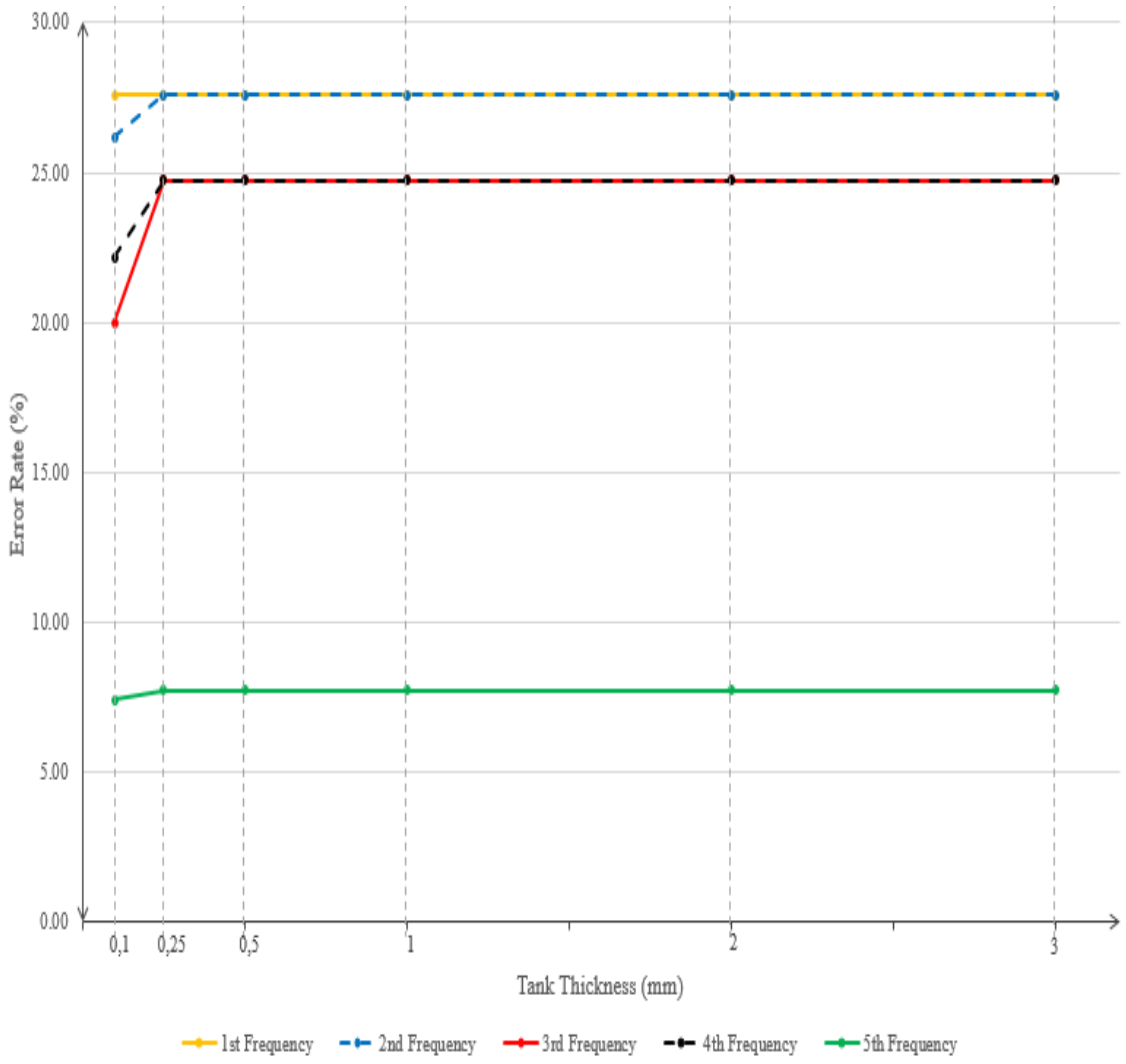

Figure 4.50. Error rates representation of partially-filled steel cylindrical tank with phantom surface of radial mesh for its first 5 modes with respect to changing tank thickness

Instead of using steel tank, the same analyses are done for the plexiglass cylindrical tank. The results are shown as follows

Table 4.28. First 5 frequencies of partially-filled plexiglass cylindrical tank with phantom surface of unstructured mesh respect to changing tank thickness

Tank mesh	**Phantom mesh type**	**Gap**	**Tank thickness (mm)**	**1st freq (Hz)**	**2nd freq (Hz)**	**3rd freq (Hz)**	**4th freq (Hz)**	**5th freq (Hz)**
20x12	Unstructured	26%	0.1	1.05	1.07	1.57	2.32	2.33
20x12	Unstructured	26%	0.25	1.66	2.7	2.71	3.36	3.36
20x12	Unstructured	26%	0.5	2.63	2.7	2.71	3.36	3.37
20x12	Unstructured	26%	1	2.7	2.71	3.37	3.37	3.52
20x12	Unstructured	26%	2	2.7	2.7	3.36	3.37	3.52
20x12	Unstructured	26%	3	2.7	2.7	3.36	3.37	3.52
Analytical frequencies				2.14	2.14	2.75	2.75	3.23

Table 4.29. Error rates of partially-filled plexiglass cylindrical tank with phantom surface of unstructured mesh for its first 5 modes with respect to changing tank thickness

Tank mesh	**Phantom mesh type**	**Gap**	**Tank thick-ness (mm)**	**Error rate of 1st mode (%)**	**Error rate of 2nd mode (%)**	**Error rate of 3rd mode (%)**	**Error rate of 4th mode (%)**	**Error rate of 5th mode (%)**
20x12	Unstructured	26%	0.1	-50.93	-50.00	-42.91	-15.64	-27.86
20x12	Unstructured	26%	0.25	-22.43	26.17	-1.45	22.18	4.02
20x12	Unstructured	26%	0.5	22.90	26.17	-1.45	22.18	4.33
20x12	Unstructured	26%	1	26.17	26.64	22.55	22.55	8.98
20x12	Unstructured	26%	2	26.17	26.17	22.18	22.55	8.98
20x12	Unstructured	26%	3	26.17	26.17	22.18	22.55	8.98

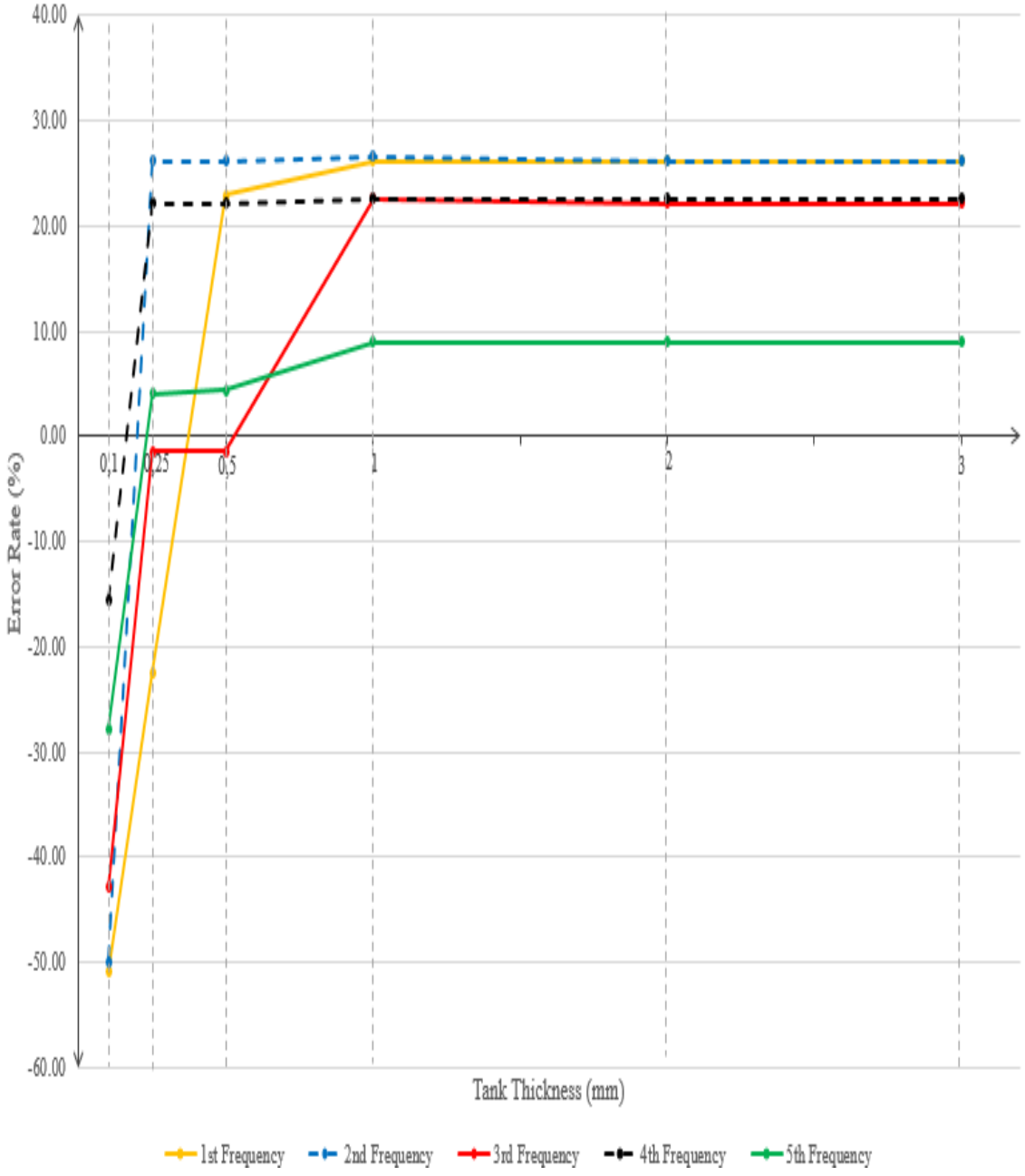

Figure 4.51. Error rates representation of partially-filled plexiglass cylindrical tank with phantom surface of unstructured mesh for its first 5 modes with respect to changing tank thickness

Table 4.30. First 5 frequencies of partially-filled plexiglass cylindrical tank with phantom surface of butterfly mesh with respect to changing tank thickness

Tank mesh	**Phantom mesh type**	**Gap**	**Tank thickness (mm)**	**1st freq (Hz)**	**2nd freq (Hz)**	**3rd freq (Hz)**	**4th freq (Hz)**	**5th freq (Hz)**
20x12	Butterfly	26%	0.1	1.05	1.07	1.57	2.32	2.33
20x12	Butterfly	26%	0.25	1.66	2.71	2.71	3.36	3.38
20x12	Butterfly	26%	0.5	2.63	2.71	2.71	3.36	3.39
20x12	Butterfly	26%	1	2.71	2.71	3.36	3.39	3.47
20x12	Butterfly	26%	2	2.71	2.71	3.36	3.39	3.48
20x12	Butterfly	26%	3	2.71	2.71	3.36	3.39	3.48
Analytical frequencies				2.14	2.14	2.75	2.75	3.23

Table 4.31. Error rates of partially-filled plexiglass cylindrical tank with butterfly phantom surface for its first 5 modes with respect to changing tank thickness

Tank mesh	**Phantom mesh type**	**Gap**	**Tank thick-ness (mm)**	**Error rate of 1st mode (%)**	**Error rate of 2nd mode (%)**	**Error rate of 3rd mode (%)**	**Error rate of 4th mode (%)**	**Error rate of 5th mode (%)**
20x12	Butterfly	26%	0.1	-50.93	-50.00	-42.91	-15.64	-27.86
20x12	Butterfly	26%	0.25	-22.43	26.64	-1.45	22.18	4.64
20x12	Butterfly	26%	0.5	22.90	26.64	-1.45	22.18	4.95
20x12	Butterfly	26%	1	26.64	26.64	22.18	23.27	7.43
20x12	Butterfly	26%	2	26.64	26.64	22.18	23.27	7.74
20x12	Butterfly	26%	3	26.64	26.64	22.18	23.27	7.74

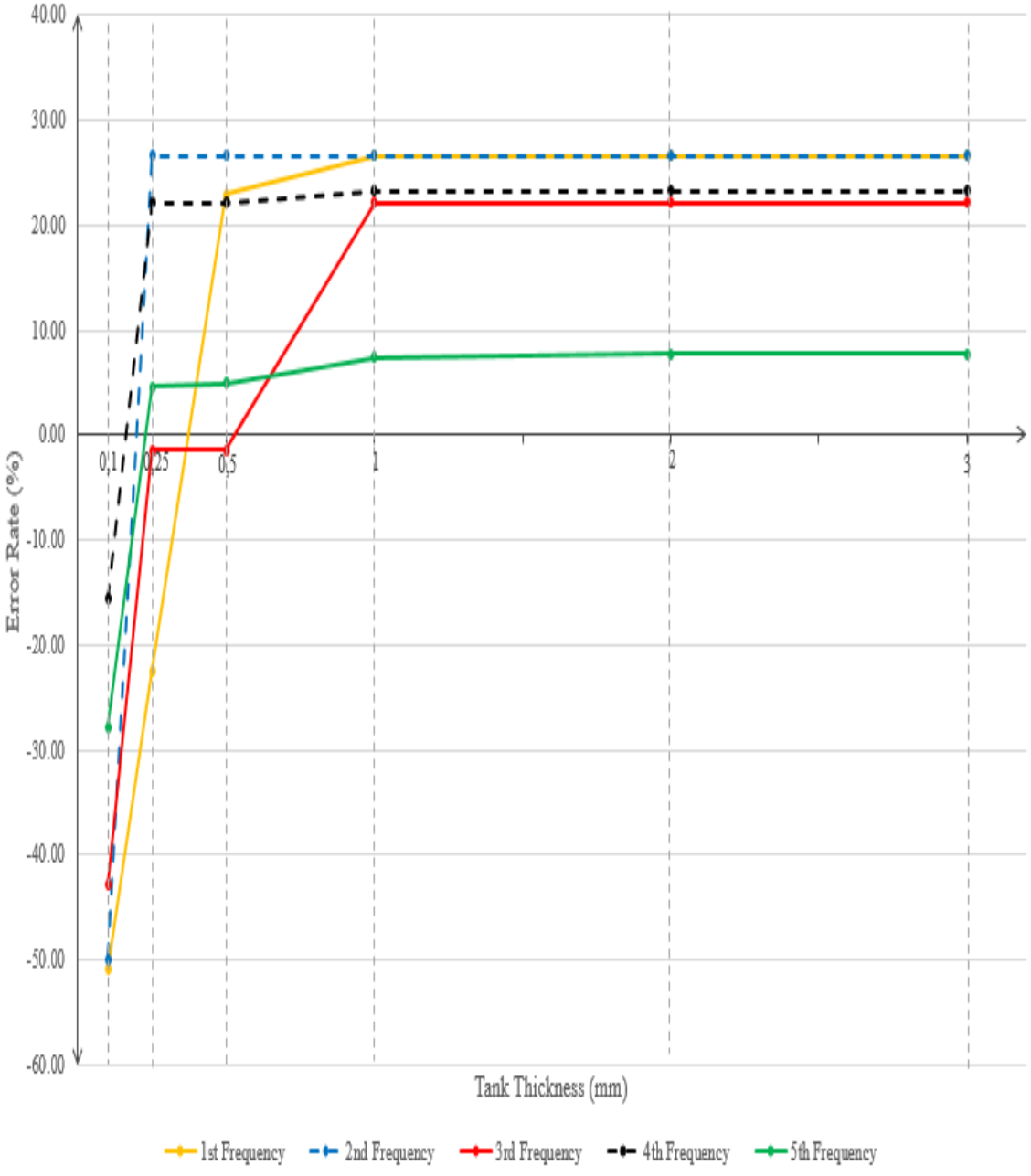

Figure 4.52. Error rates representation of partially-filled plexiglass cylindrical tank with phantom surface of butterfly mesh for its first 5 modes with respect to changing tank thickness

Table 4.32. First 5 frequencies of partially-filled plexiglass cylindrical tank with phantom surface of radial mesh with respect to changing tank thickness

Tank mesh	**Phantom mesh type**	**Gap**	**Tank thickness (mm)**	**1st freq (Hz)**	**2nd freq (Hz)**	**3rd freq (Hz)**	**4th freq (Hz)**	**5th freq (Hz)**
20x12	Radial	26%	0.1	1.05	1.07	1.57	2.32	2.33
20x12	Radial	26%	0.25	1.66	2.73	2.73	3.42	3.43
20x12	Radial	26%	0.5	2.62	2.73	2.73	3.42	3.43
20x12	Radial	26%	1	2.73	2.73	3.42	3.43	3.48
20x12	Radial	26%	2	2.73	2.73	3.42	3.43	3.48
20x12	Radial	26%	3	2.73	2.73	3.42	3.43	3.48
Analytical frequencies				2.14	2.14	2.75	2.75	3.23

Table 4.33. Error rates of partially-filled plexiglass cylindrical tank with phantom surface of radial mesh for its first 5 modes with respect to changing tank thickness

Tank mesh	**Phantom mesh type**	**Gap**	**Tank thick-ness (mm)**	**Error rate of 1st mode (%)**	**Error rate of 2nd mode (%)**	**Error rate of 3rd mode (%)**	**Error rate of 4th mode (%)**	**Error rate of 5th mode (%)**
20x12	Radial	26%	0.1	-50.93	-50.00	-42.91	-15.64	-27.86
20x12	Radial	26%	0.25	-22.43	27.57	-0.73	24.36	6.19
20x12	Radial	26%	0.5	22.43	27.57	-0.73	24.36	6.19
20x12	Radial	26%	1	27.57	27.57	24.36	24.73	7.74
20x12	Radial	26%	2	27.57	27.57	24.36	24.73	7.74
20x12	Radial	26%	3	27.57	27.57	24.36	24.73	7.74

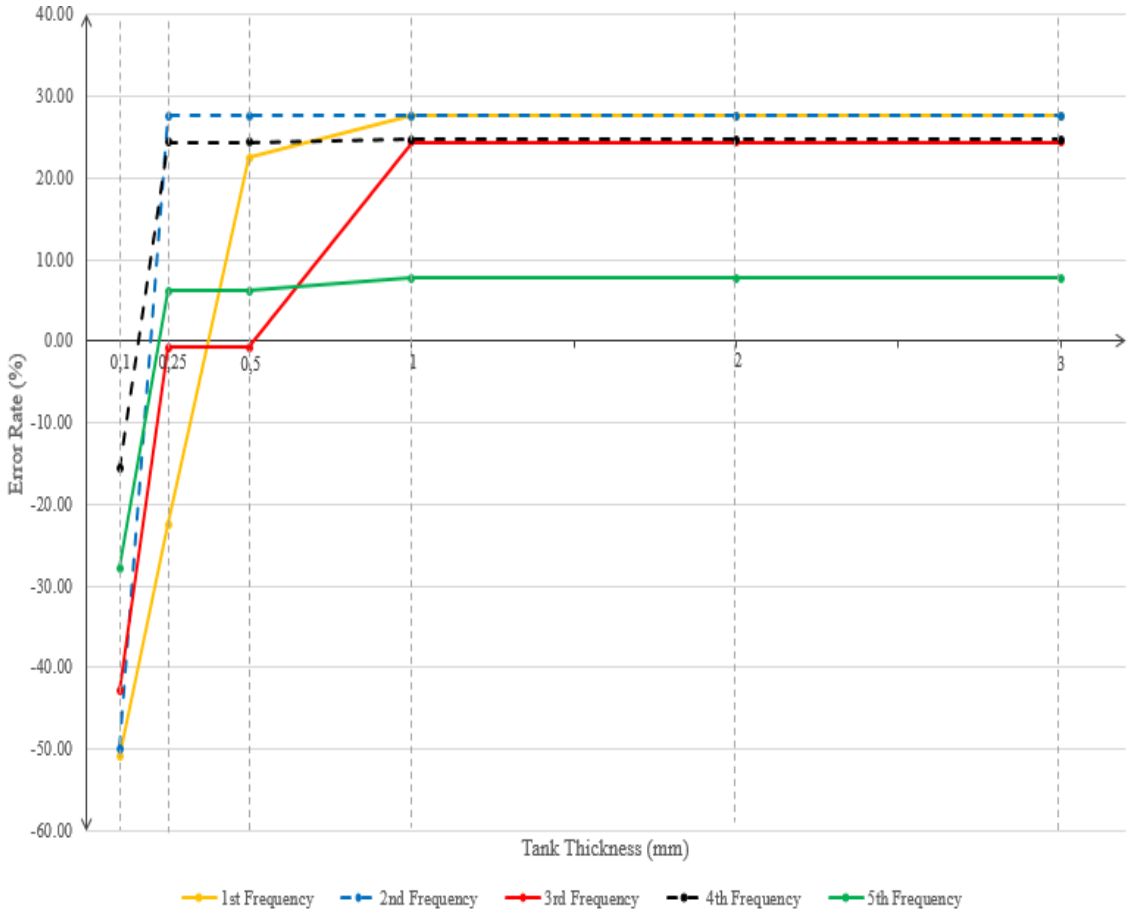

Figure 4.53. Error rates representation of partially-filled plexiglass cylindrical tank with phantom surface of radial mesh for its first 5 modes with respect to changing tank thickness

After the tables and the graphs above are investigated, it is seen that the results for all mesh topologies are in exactly the same trend with rectangular tank's material and thickness analyses. The frequencies above are getting closer to the analytical values as the thickness of tank gets bigger. This situation comes true due to the fact that in the analytical method, the tank is considered as rigid and as in the numerical analyses the tank thickness increases, the tank becomes more rigid and as a result its frequencies gets closer to the analytical values.

In addition to the outcome from tank thickness change, tank material choice affected the results. As in the case of rectangular tank analysis, since steel has greater Young's modulus compare to plexiglass, in the analyses with 0.1 mm and 0.25 mm, the effect of this greatness is appeared in the results as frequencies closer to analytical values.

In order to compare the numerical results with laboratory experiment results, the thickness is chosen as 3 mm due to the fact that in laboratory experiments tank thickness was this value.

After examining the effect of tank material and thickness, the change in the tank mesh resolution of the cylindrical tanks with unstructured, butterfly and radial phantom surfaces are investigated. The tables of frequencies and error rates, and the graph of the error rate table for this study are shown below

Table 4.34. First 5 frequencies of partially-filled plexiglass cylindrical tank with phantom surface of unstructured mesh with respect to changing tank mesh resolution

Tank mesh	**Phantom mesh type**	**Gap**	**Tank thickness (mm)**	**1st freq (Hz)**	**2nd freq (Hz)**	**3rd freq (Hz)**	**4th freq (Hz)**	**5th freq (Hz)**
20x12	Unstructured	26%	3	2.7	2.7	3.36	3.37	3.52
30x18	Unstructured	26%	3	2.68	2.68	3.31	3.32	3.48
40x24	Unstructured	26%	3	2.68	2.68	3.32	3.33	3.49
Analytical frequencies				2.14	2.14	2.75	2.75	3.23

Table 4.35. Error rates of partially-filled plexiglass cylindrical tank with phantom surface of unstructured mesh for its first 5 modes with respect to changing tank mesh resolution

Tank mesh	**Phantom mesh type**	**Gap**	**Tank thick-ness (mm)**	**Error rate of 1st mode (%)**	**Error rate of 2nd mode (%)**	**Error rate of 3rd mode (%)**	**Error rate of 4th mode (%)**	**Error rate of 5th mode (%)**
20x12	Unstructured	26%	3	26.17	26.17	22.18	22.55	8.98
30x18	Unstructured	26%	3	25.23	25.23	20.36	20.73	7.74
40x24	Unstructured	26%	3	25.23	25.23	20.73	21.09	8.05

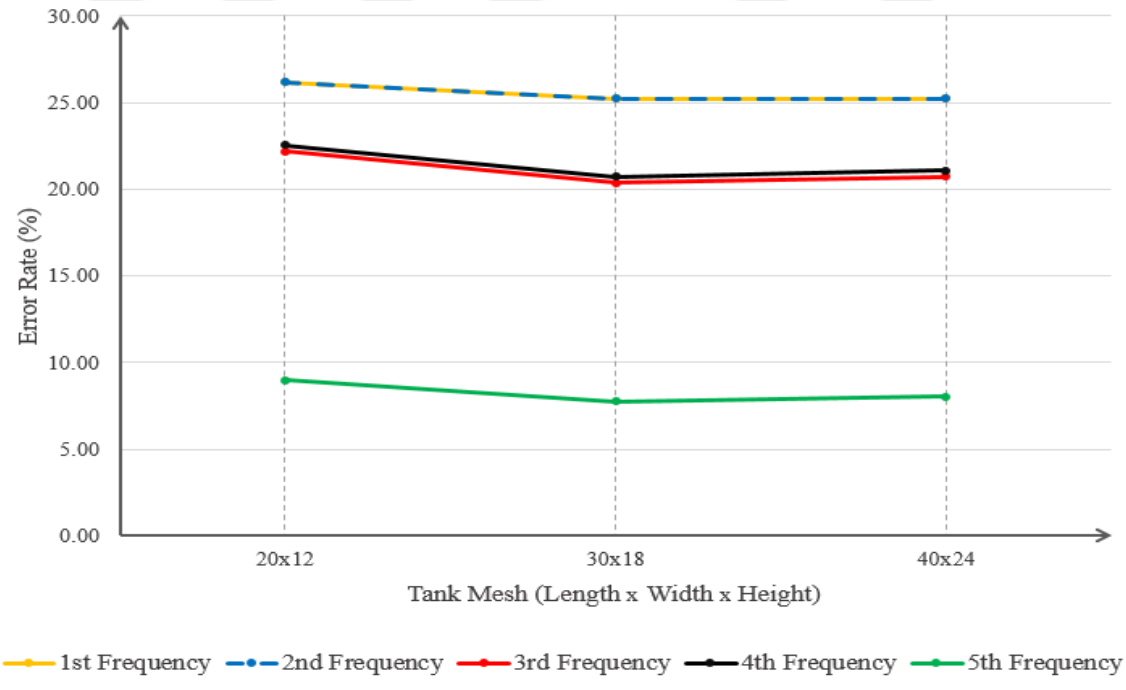

Figure 4.54. Error rates representation of partially-filled plexiglass cylindrical tank with phantom surface of unstructured mesh for its first 5 modes with respect to changing tank mesh resolution

Table 4.36. First 5 frequencies of partially-filled plexiglass cylindrical tank with phantom surface of butterfly mesh with respect to changing tank mesh resolution

Tank mesh	**Phantom mesh type**	**Gap**	**Tank thickness (mm)**	**1st freq (Hz)**	**2nd freq (Hz)**	**3rd freq (Hz)**	**4th freq (Hz)**	**5th freq (Hz)**
20x12	Butterfly	26%	3	2.71	2.71	3.36	3.39	3.48
30x18	Butterfly	26%	3	2.68	2.69	3.31	3.34	3.43
40x24	Butterfly	26%	3	2.68	2.69	3.3	3.33	3.42
Analytical frequencies				2.14	2.14	2.75	2.75	3.23

Table 4.37. Error rates of partially-filled plexiglass cylindrical tank with phantom surface of butterfly mesh for its first 5 modes with respect to changing tank mesh resolution

Tank mesh	**Phantom mesh type**	**Gap**	**Tank thick-ness (mm)**	**Error rate of 1st mode (%)**	**Error rate of 2nd mode (%)**	**Error rate of 3rd mode (%)**	**Error rate of 4th mode (%)**	**Error rate of 5th mode (%)**
20x12	Butterfly	26%	3	26.64	26.64	22.18	23.27	7.74
30x18	Butterfly	26%	3	25.23	25.70	20.36	21.45	6.19
40x24	Butterfly	26%	3	25.23	25.70	20.00	21.09	5.88

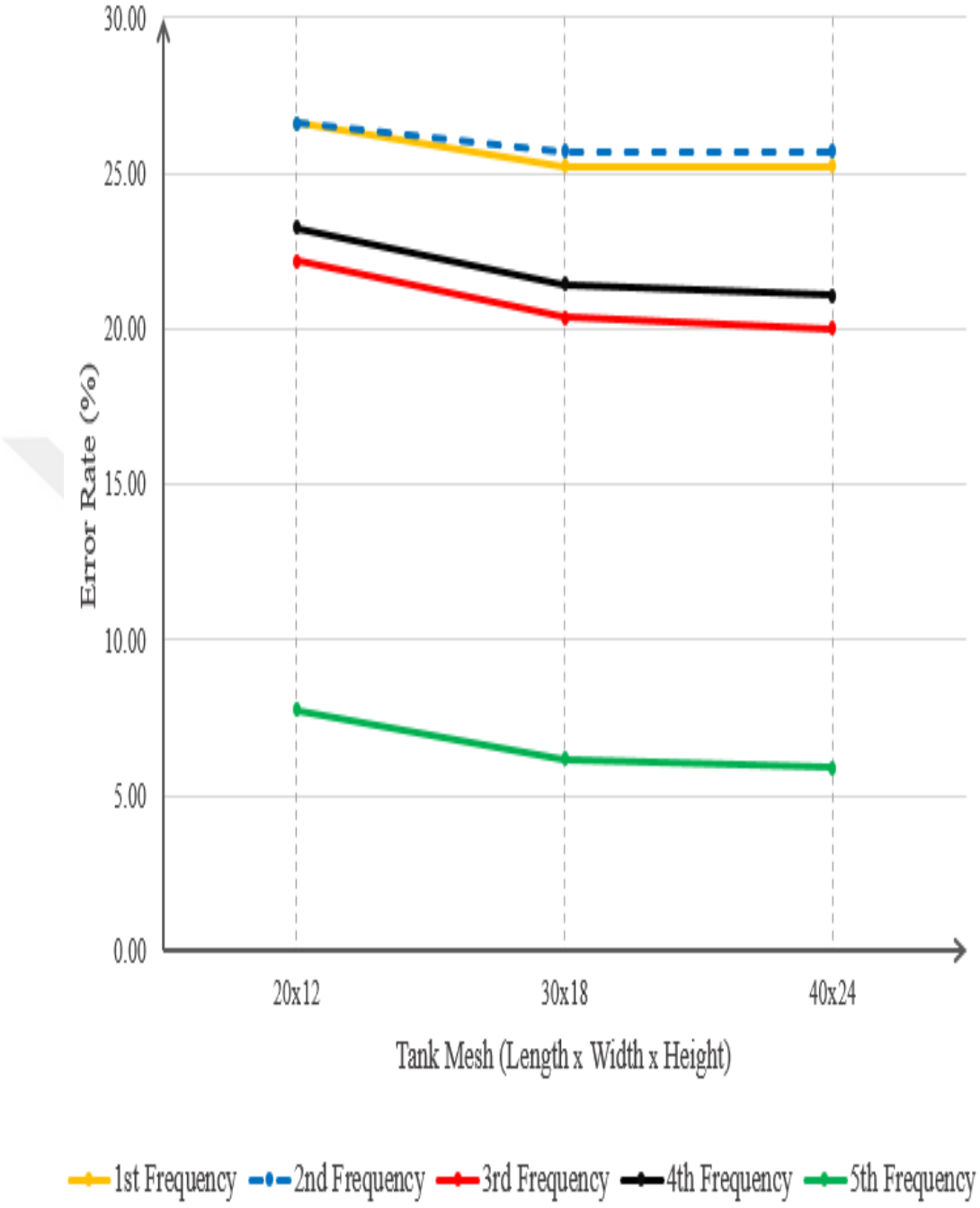

Figure 4.55. Error rates representation of partially-filled plexiglass cylindrical tank with phantom surface of butterfly mesh for its first 5 modes with respect to changing tank mesh resolution

Table 4.38. First 5 frequencies of partially-filled plexiglass cylindrical tank with phantom surface of radial mesh with respect to changing tank mesh resolution

Tank mesh	**Phantom mesh type**	**Gap**	**Tank thickness (mm)**	**1st freq (Hz)**	**2nd freq (Hz)**	**3rd freq (Hz)**	**4th freq (Hz)**	**5th freq (Hz)**
20x12	Radial	26%	3	2.73	2.73	3.42	3.43	3.48
30x18	Radial	26%	3	2.71	2.71	3.38	3.39	3.44
40x24	Radial	26%	3	2.7	2.71	3.38	3.38	3.44
Analytical frequencies				2.14	2.14	2.75	2.75	3.23

Table 4.39. Error rates of partially-filled plexiglass cylindrical tank with phantom surface of radial mesh for its first 5 modes with respect to changing tank mesh resolution

Tank mesh	**Phantom mesh type**	**Gap**	**Tank thick-ness (mm)**	**Error rate of 1st mode (%)**	**Error rate of 2nd mode (%)**	**Error rate of 3rd mode (%)**	**Error rate of 4th mode (%)**	**Error rate of 5th mode (%)**
20x12	Radial	26%	3	27.57	27.57	24.36	24.73	7.74
30x18	Radial	26%	3	26.64	26.64	22.91	23.27	6.50
40x24	Radial	26%	3	26.17	26.64	22.91	22.91	6.50

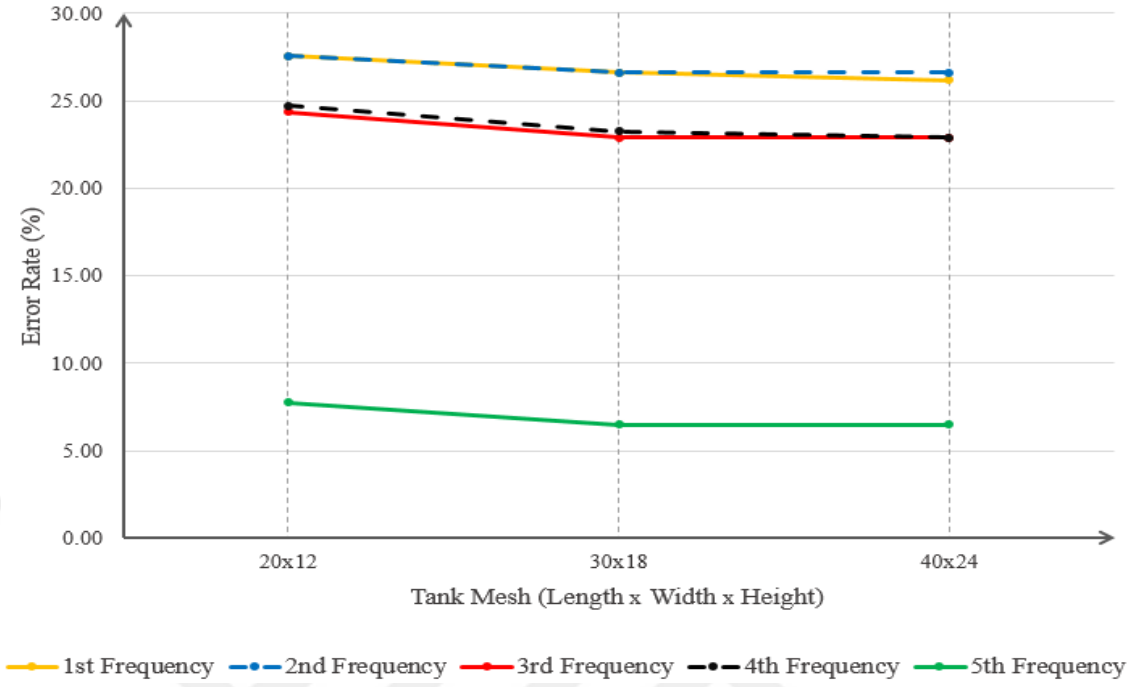

Figure 4.56. Error rates representation of partially-filled plexiglass cylindrical tank with phantom surface of radial mesh for its first 5 modes with respect to changing tank mesh resolution

From the tables and the graph above for the cylindrical tanks with phantom surface of unstructured, butterfly and radial meshes, it can be concluded that as the tank mesh resolution increases, the frequencies gets closer to analytical results and they converge after a point. The reason of this situation is the working principle described at tank mesh resolution study for rectangular tank.

As it can be remembered, with coarse source distribution, as the distance between element with source and the element that fluid behaviour is measured gets greater, the fluid behaviour is represented poorly.

Since 30×18 elements and 40×24 elements on tank mesh give same frequencies, for preventing computational cost 30×18 elements are used for meshing the tank for the next analyses.

In the next case, the effect of gap ratio between phantom surface's element size and phantom surface-tank wall gap distance with unstructured, butterfly and radial mesh topology to frequencies are studied. The frequency and error rate tables, and the graph of error rate table can be seen below

Table 4.40. First 5 frequencies of partially-filled plexiglass cylindrical tank with phantom surface of unstrucrured mesh with respect to changing gap (NR stands for "No results").

Tank mesh	**Phantom mesh type**	**Gap**	**Tank thickness (mm)**	**1st freq (Hz)**	**2nd freq (Hz)**	**3rd freq (Hz)**	**4th freq (Hz)**	**5th freq (Hz)**
30x18	Unstructured	26%	3	2.68	2.68	3.31	3.32	3.48
30x18	Unstructured	20%	3	2.6	2.6	3.25	3.25	3.43
30x18	Unstructured	13%	3	2.5	2.51	3.16	3.17	3.37
30x18	Unstructured	6%	3	2.38	2.38	3.05	3.06	3.32
30x18	Unstructured	3%	3	NR	NR	NR	NR	NR
30x18	Unstructured	1.5%	3	NR	NR	NR	NR	NR
Analytical frequencies				2.14	2.14	2.75	2.75	3.23

Table 4.41. Error rates of partially-filled plexiglass cylindrical tank with phantom surface of unstructured mesh for its first 5 modes with respect to changing gap

Tank mesh	**Phantom mesh type**	**Gap**	**Tank thick-ness (mm)**	**Error rate of 1st mode (%)**	**Error rate of 2nd mode (%)**	**Error rate of 3rd mode (%)**	**Error rate of 4th mode (%)**	**Error rate of 5th mode (%)**
30x18	Unstructured	26%	3	25.23	25.23	20.36	20.73	7.74
30x18	Unstructured	20%	3	21.50	21.50	18.18	18.18	6.19
30x18	Unstructured	13%	3	16.82	17.29	14.91	15.27	4.33
30x18	Unstructured	6%	3	11.21	11.21	10.91	11.27	2.79
30x18	Unstructured	3%	3	NR	NR	NR	NR	NR
30x18	Unstructured	1.5%	3	NR	NR	NR	NR	NR

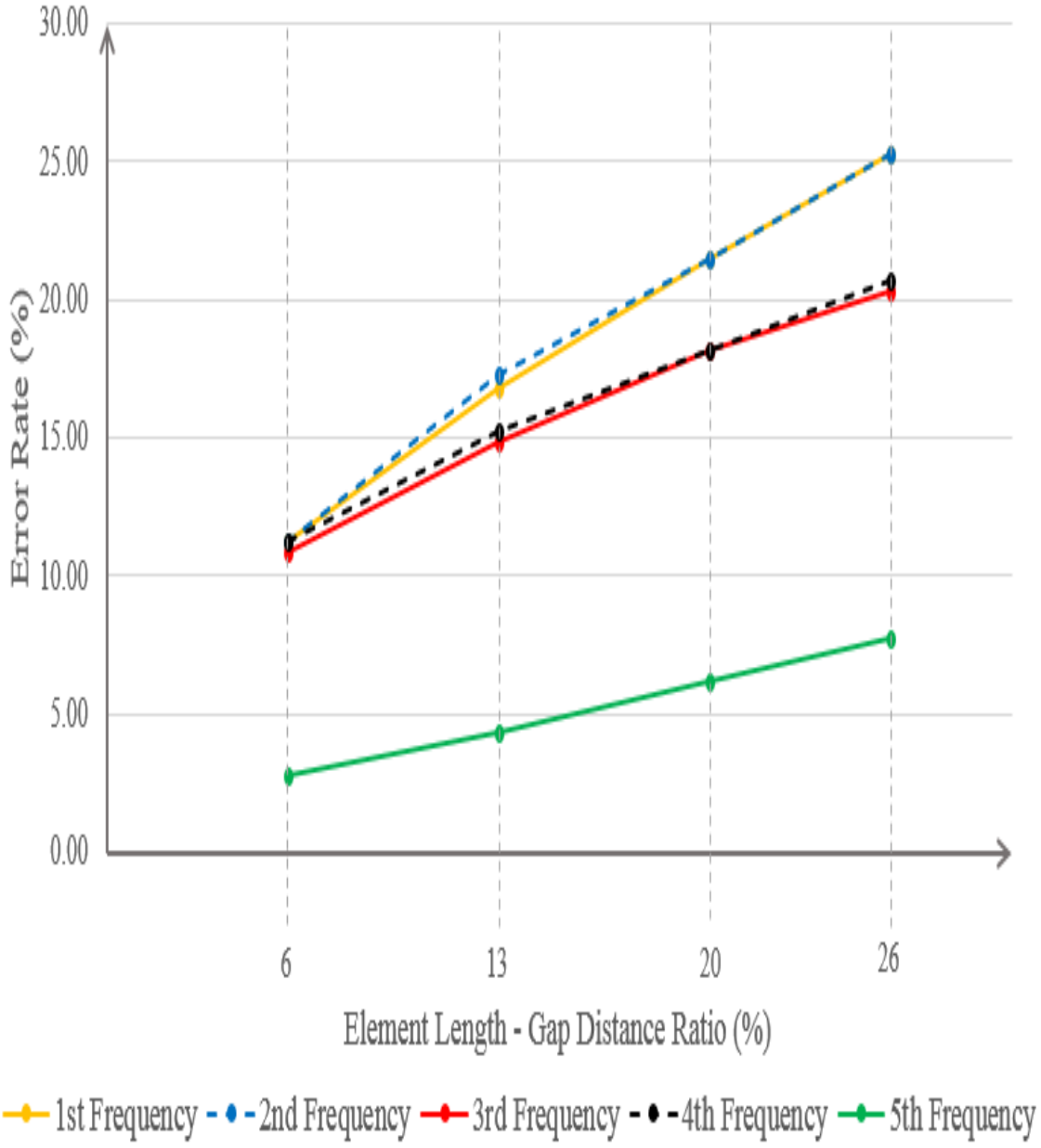

Figure 4.57. Error rates representation of partially-filled plexiglass cylindrical tank with phantom surface of unstructured mesh for its first 5 modes with respect to changing gap

Table 4.42. First 5 frequencies of partially-filled plexiglass cylindrical tank with phantom surface of butterfly mesh with respect to changing gap (NR stands for "No results").

Tank mesh	**Phantom mesh type**	**Gap**	**Tank thickness (mm)**	**1st freq (Hz)**	**2nd freq (Hz)**	**3rd freq (Hz)**	**4th freq (Hz)**	**5th freq (Hz)**
30x18	Butterfly	26%	3	2.68	2.69	3.31	3.34	3.43
30x18	Butterfly	20%	3	2.6	2.6	3.25	3.28	3.37
30x18	Butterfly	13%	3	2.5	2.51	3.17	3.19	3.31
30x18	Butterfly	6%	3	2.4	2.4	3.06	3.09	3.29
30x18	Butterfly	3%	3	NR	NR	NR	NR	NR
30x18	Butterfly	1.5%	3	NR	NR	NR	NR	NR
Analytical frequencies				2.14	2.14	2.75	2.75	3.23

Table 4.43. Error rates of partially-filled plexiglass cylindrical tank with phantom surface of butterfly mesh for its first 5 modes with respect to changing gap

Tank mesh	**Phantom mesh type**	**Gap**	**Tank thick-ness (mm)**	**Error rate of 1st mode (%)**	**Error rate of 2nd mode (%)**	**Error rate of 3rd mode (%)**	**Error rate of 4th mode (%)**	**Error rate of 5th mode (%)**
30x18	Butterfly	26%	3	25.23	25.70	20.36	21.45	6.19
30x18	Butterfly	20%	3	21.50	21.50	18.18	19.27	4.33
30x18	Butterfly	13%	3	16.82	17.29	15.27	16.00	2.48
30x18	Butterfly	6%	3	12.15	12.15	11.27	12.36	1.86
30x18	Butterfly	3%	3	NR	NR	NR	NR	NR
30x18	Butterfly	1.5%	3	NR	NR	NR	NR	NR

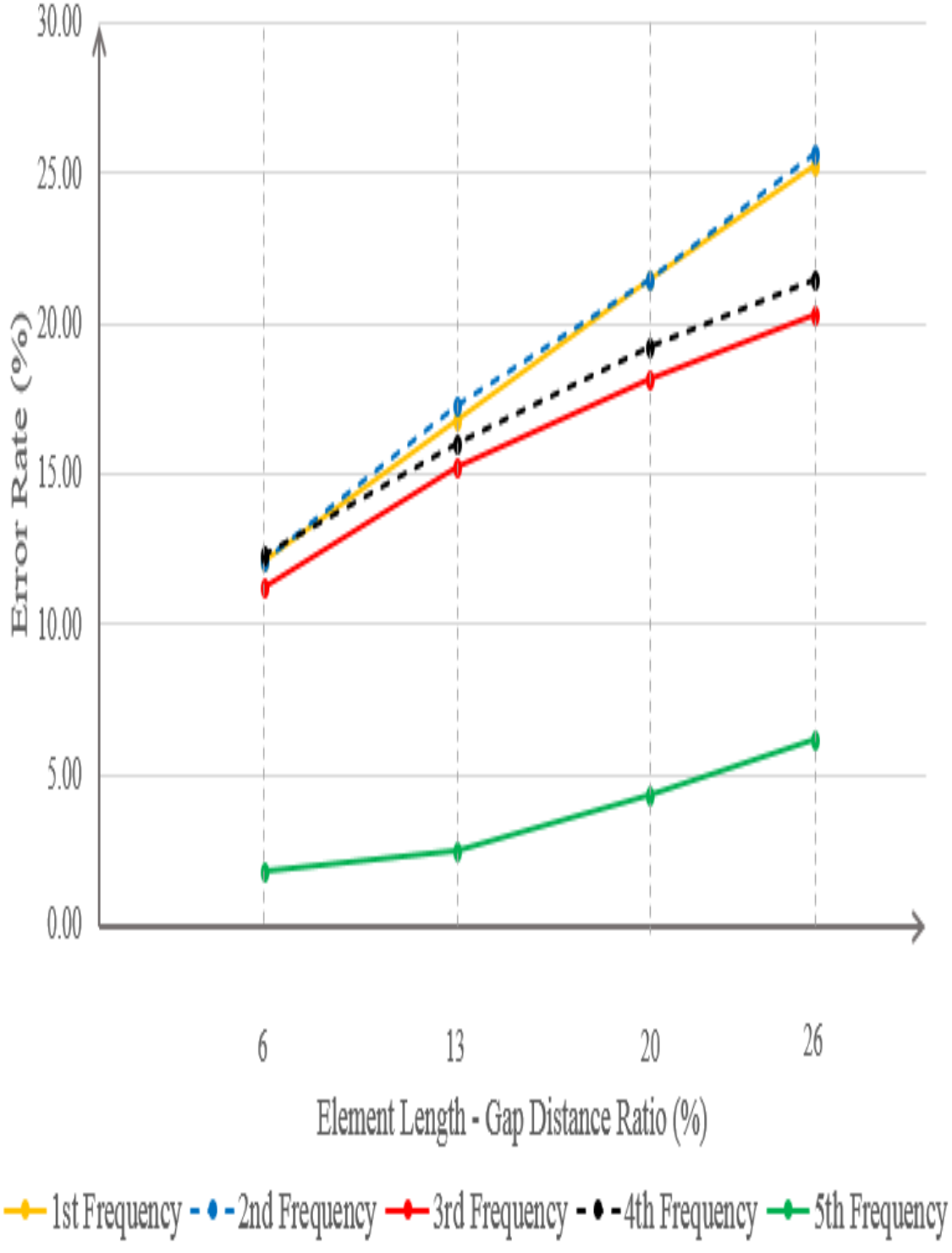

Figure 4.58. Error rates representation of partially-filled plexiglass cylindrical tank with phantom surface of butterfly mesh for its first 5 modes with respect to gap

Table 4.44. First 5 frequencies of partially-filled plexiglass cylindrical tank with phantom surface of radial mesh with respect to changing gap (NR stands for "No results").

Tank mesh	**Phantom mesh type**	**Gap**	**Tank thickness (mm)**	**1st freq (Hz)**	**2nd freq (Hz)**	**3rd freq (Hz)**	**4th freq (Hz)**	**5th freq (Hz)**
30x18	Radial	26%	3	2.71	2.71	3.38	3.39	3.44
30x18	Radial	20%	3	2.64	2.64	3.32	3.32	3.39
30x18	Radial	13%	3	2.56	2.56	3.25	3.25	3.34
30x18	Radial	6%	3	2.45	2.46	3.15	3.15	3.3
30x18	Radial	3%	3	NR	NR	NR	NR	NR
30x18	Radial	1.5%	3	NR	NR	NR	NR	NR
Analytical frequencies				2.14	2.14	2.75	2.75	3.23

Table 4.45. Error rates of partially-filled plexiglass cylindrical tank with phantom surface of radial mesh for its first 5 modes with respect to changing gap

Tank mesh	**Phantom mesh type**	**Gap**	**Tank thick-ness (mm)**	**Error rate of 1st mode (%)**	**Error rate of 2nd mode (%)**	**Error rate of 3rd mode (%)**	**Error rate of 4th mode (%)**	**Error rate of 5th mode (%)**
30x18	Radial	26%	3	26.64	26.64	22.91	23.27	6.50
30x18	Radial	20%	3	23.36	23.36	20.73	20.73	4.95
30x18	Radial	13%	3	19.63	19.63	18.18	18.18	3.41
30x18	Radial	6%	3	14.49	14.95	14.55	14.55	2.17
30x18	Radial	3%	3	NR	NR	NR	NR	NR
30x18	Radial	1.5%	3	NR	NR	NR	NR	NR

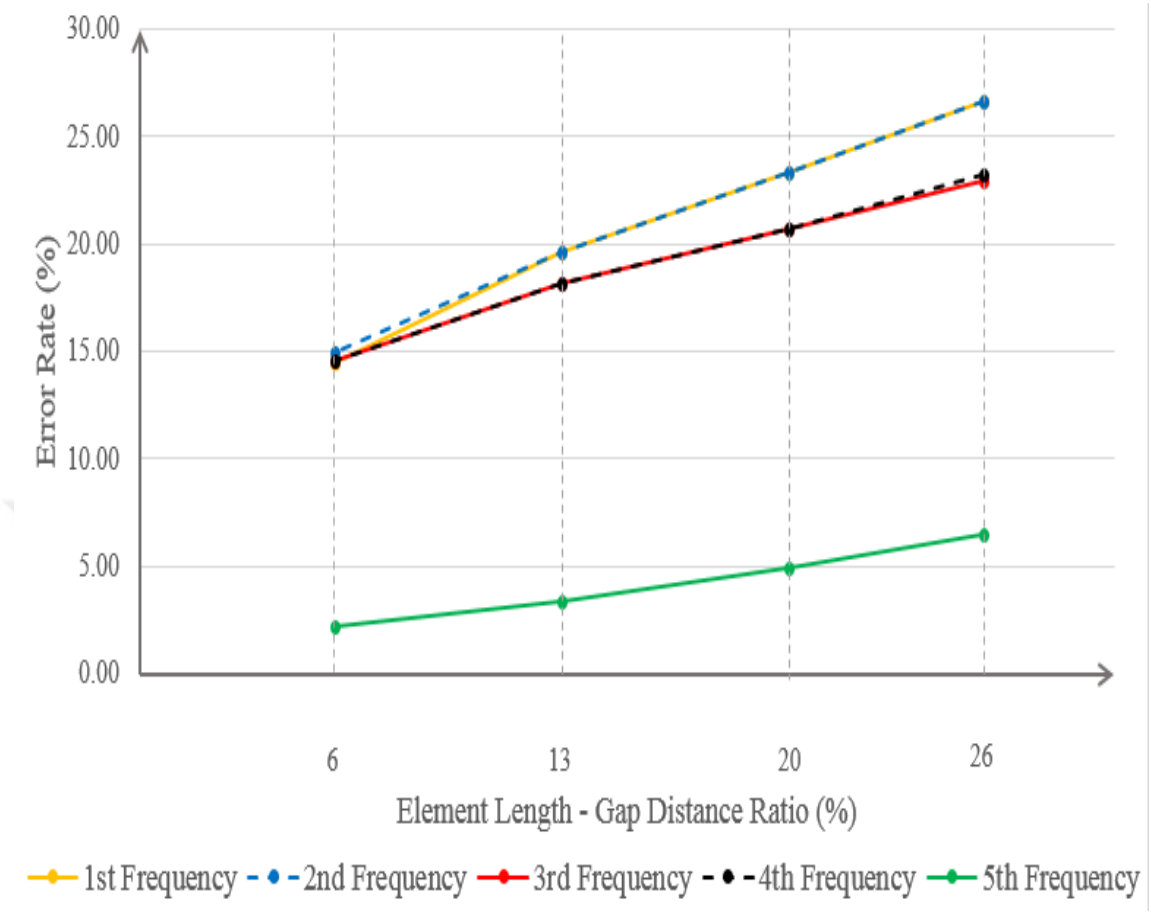

Figure 4.59. Error rates representation of partially-filled plexiglass cylindrical tank with phantom surface of radial mesh for its first 5 modes with respect to gap

As it can be noticed from tables and the graphs above the frequencies are getting more accurate as the phantom surface gap ratios gets smaller, however, when the phantom surface gets too close to the wall, Nastran gives no results of frequency. The reason of this situation is exactly the same with rectangular tank's element length - gap distance ratio study. As a summary, Nastran calculates the fluid behaviour as a superposition of sources located on the tank's boundary, and sources are not able to calculate the velocity for the locations that is too close to the source. When phantom surface gets too close to the wall that has sources on it, Nastran can not calculate the phantom surface's behaviour if the phantom surface is in the range of singularity.

As the phantom surface gap ratio decreases, the frequencies gets closer to the analytical values. The reason of this situation is exactly same with the rectangular tank's element length - gap distance ratio study which is representing the pull of gravity more accurately by using greater element area on the phantom surface.

The last study for the cylindrical tank is done for seeing the effect of changing phantom surface mesh topology. Unstructured mesh is modelled with 511 elements whereas butterfly and radial meshes are created with 500 and 522 elements respectively. The aim to keep the element numbers of phantom surfaces around 500 is to provide equal conditions for comparison of them. The tables of frequencies and error rates and the graphical representation of error rate for the phantom surfaces with unstructured, butterfly and radial meshes are demonstrated below

Table 4.46. First 5 frequencies of partially-filled plexiglass cylindrical tank with respect to changing phantom surface mesh topology

Tank mesh	**Phantom mesh type**	**Gap**	**Tank thickness (mm)**	**1st freq (Hz)**	**2nd freq (Hz)**	**3rd freq (Hz)**	**4th freq (Hz)**	**5th freq (Hz)**
30x18	Unstructured	6%	3	2.38	2.38	3.05	3.06	3.32
30x18	Butterfly	6%	3	2.4	2.4	3.06	3.09	3.29
30x18	Radial	6%	3	2.45	2.46	3.15	3.15	3.3
Analytical frequencies				2.14	2.14	2.75	2.75	3.23

Table 4.47. Partially-filled plexiglass cylindrical tank's error rates for its first 5 modes with respect to changing phantom surface mesh topology

Tank mesh	**Phantom mesh type**	**Gap**	**Tank thick-ness (mm)**	**Error rate of 1st mode (%)**	**Error rate of 2nd mode (%)**	**Error rate of 3rd mode %)**	**Error rate of 4th mode (%)**	**Error rate of 5th mode (%)**
30x18	Unstructured	6%	3	11.21	11.21	10.91	11.27	2.79
30x18	Butterfly	6%	3	12.15	12.15	11.27	12.36	1.86
30x18	Radial	6%	3	14.49	14.95	14.55	14.55	2.17

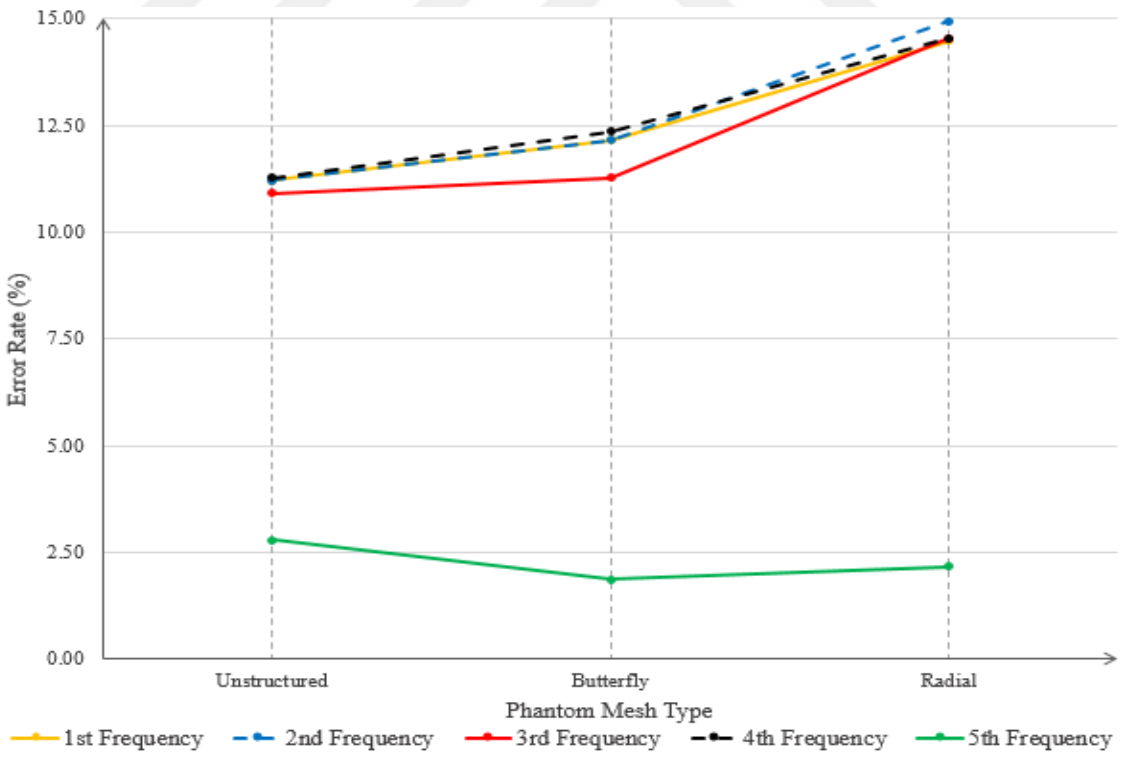

Figure 4.60. Representation of partially-filled plexiglass cylindrical tank's error rates for its first 5 modes with respect to changing phantom surface mesh topology

When the tables of frequency and error rate, and the graph of error rate above are investigated, even though there is really small difference between values, it is seen that the best result has been reached by using unstructured phantom surface.

As it is declared in the book of "Computational Fluid Dynamics: A Practical Approach" [36], to model the domains with highly curved boundaries unstructured meshes are very suitable. Due to this fact, in our study, the best frequencies are reached with unstructured meshed phantom surface.

The reason of having butterfly mesh results a little bit worse than unstructured one can be the high aspect ratio of its non-rectangular elements. As it is declared as well in [30], aspect ratio for Nastran models should be kept below 2. Apparently, the high aspect ratio of these elements affected the result, however since the amount of these elements are not too much, it could not effected a lot.

Lastly, for the results of radial mesh, even though there is a neglectible difference with other 2 mesh topologies, the reason of radial mesh showing worst error rate can be seen as the effect of high aspect ratio of radial mesh topology.

For checking all the analyses done for cylindrical tank with phantom surface of unstructured, butterfly and radial meshes, the tables with all frequencies and error rates are shared below

Table 4.48. First 5 frequencies of partially-filled plexiglass cylindrical tank with phantom surface of unstructured mesh with respect to changing tank thickness, tank mesh resolution, phantom surface gap ratio and phantom surface mesh topology

Tank mesh	**Phantom mesh type**	**Gap**	**Tank thickness (mm)**	**1st freq (Hz)**	**2nd freq (Hz)**	**3rd freq (Hz)**	**4th freq (Hz)**	**5th freq (Hz)**
20x12	Unstructured	26%	0.1	1.05	1.07	1.57	2.32	2.33
20x12	Unstructured	26%	0.25	1.66	2.7	2.71	3.36	3.36
20x12	Unstructured	26%	0.5	2.63	2.7	2.71	3.36	3.37
20x12	Unstructured	26%	1	2.7	2.71	3.37	3.37	3.52
20x12	Unstructured	26%	2	2.7	2.7	3.36	3.37	3.52
20x12	Unstructured	26%	3	2.7	2.7	3.36	3.37	3.52
30x18	Unstructured	26%	3	2.68	2.68	3.31	3.32	3.48
40x24	Unstructured	26%	3	2.68	2.68	3.32	3.33	3.49
30x18	Unstructured	20%	3	2.6	2.6	3.25	3.25	3.43
30x18	Unstructured	13%	3	2.5	2.51	3.16	3.17	3.37
30x18	Unstructured	6%	3	2.38	2.38	3.05	3.06	3.32
Analytical frequencies				2.14	2.14	2.75	2.75	3.23

After giving the frequencies of cylindrical plexiglass tank with unstructured phantom surface, the error rate of these frequencies are going to be shown

Table 4.49. Error rates of partially-filled plexiglass cylindrical tank with unstructured mesh for its first 5 modes with respect to changing tank thickness, tank mesh resolution, phantom surface gap ratio and phantom surface mesh topology

Tank mesh	**Phantom mesh type**	**Gap**	**Tank thick-ness (mm)**	**Error rate of 1st mode (%)**	**Error rate of 2nd mode (%)**	**Error rate of 3rd mode (%)**	**Error rate of 4th mode (%)**	**Error rate of 5th mode (%)**
20x12	Unstructured	26%	0.1	-50.93	-50.00	-42.91	-15.64	-27.86
20x12	Unstructured	26%	0.25	-22.43	26.17	-1.45	22.18	4.02
20x12	Unstructured	26%	0.5	22.90	26.17	-1.45	22.18	4.33
20x12	Unstructured	26%	1	26.17	26.64	22.55	22.55	8.98
20x12	Unstructured	26%	2	26.17	26.17	22.18	22.55	8.98
20x12	Unstructured	26%	3	26.17	26.17	22.18	22.55	8.98
30x18	Unstructured	26%	3	25.23	25.23	20.36	20.73	7.74
40x24	Unstructured	26%	3	25.23	25.23	20.73	21.09	8.05
30x18	Unstructured	20%	3	21.50	21.50	18.18	18.18	6.19
30x18	Unstructured	13%	3	16.82	17.29	14.91	15.27	4.33
30x18	Unstructured	6%	3	11.21	11.21	10.91	11.27	2.79

As the next step, the frequencies of the plexiglass cylindrical tank with butterfly mesh is going to be shown ,n the following tank

Table 4.50. First 5 frequencies of partially-filled plexiglass cylindrical tank with butterfly mesh with respect to changing tank thickness, tank mesh resolution, phantom surface gap ratio and phantom surface mesh topology

Tank mesh	**Phantom mesh type**	**Gap**	**Tank thickness (mm)**	**1st freq (Hz)**	**2nd freq (Hz)**	**3rd freq (Hz)**	**4th freq (Hz)**	**5th freq (Hz)**
20x12	Butterfly	26%	0.1	1.05	1.07	1.57	2.32	2.33
20x12	Butterfly	26%	0.25	1.66	2.71	2.71	3.36	3.38
20x12	Butterfly	26%	0.5	2.63	2.71	2.71	3.36	3.39
20x12	Butterfly	26%	1	2.71	2.71	3.36	3.39	3.47
20x12	Butterfly	26%	2	2.71	2.71	3.36	3.39	3.48
20x12	Butterfly	26%	3	2.71	2.71	3.36	3.39	3.48
30x18	Butterfly	26%	3	2.68	2.69	3.31	3.34	3.43
40x24	Butterfly	26%	3	2.68	2.69	3.3	3.33	3.42
30x18	Butterfly	20%	3	2.6	2.6	3.25	3.28	3.37
30x18	Butterfly	13%	3	2.5	2.51	3.17	3.19	3.31
30x18	Butterfly	6%	3	2.4	2.4	3.06	3.09	3.29
Analytical frequencies				2.14	2.14	2.75	2.75	3.23

Like in the case of tank with unstructured phantom surface, for cylindrical tank with butterfly surface too, the error rate of numerical frequencies compare to analytical results are in the table below as follows

Table 4.51. Error rates of partially-filled plexiglass cylindrical tank with phantom surface of butterfly mesh for its first 5 modes with respect to changing tank thickness, tank mesh resolution, phantom surface gap ratio and phantom surface mesh topology

Tank mesh	**Phantom mesh type**	**Gap**	**Tank thick-ness (mm)**	**Error rate of 1st mode (%)**	**Error rate of 2nd mode (%)**	**Error rate of 3rd mode (%)**	**Error rate of 4th mode (%)**	**Error rate of 5th mode (%)**
20x12	Butterfly	26%	0.1	-50.93	-50.00	-42.91	-15.64	-27.86
20x12	Butterfly	26%	0.25	-22.43	26.64	-1.45	22.18	4.64
20x12	Butterfly	26%	0.5	22.90	26.64	-1.45	22.18	4.95
20x12	Butterfly	26%	1	26.64	26.64	22.18	23.27	7.43
20x12	Butterfly	26%	2	26.64	26.64	22.18	23.27	7.74
20x12	Butterfly	26%	3	26.64	26.64	22.18	23.27	7.74
30x18	Butterfly	26%	3	25.23	25.70	20.36	21.45	6.19
40x24	Butterfly	26%	3	25.23	25.70	20.00	21.09	5.88
30x18	Butterfly	20%	3	21.50	21.50	18.18	19.27	4.33
30x18	Butterfly	13%	3	16.82	17.29	15.27	16.00	2.48
30x18	Butterfly	6%	3	12.15	12.15	11.27	12.36	1.86

Lastly, the frequencies of plexiglass cylindrical tank with radial phantom surface mesh topology are going to be shown in the following table below

Table 4.52. First 5 frequencies of partially-filled plexiglass cylindrical tank with radial mesh with respect to changing tank thickness, tank mesh resolution, phantom surface gap ratio and phantom surface mesh topology

Tank mesh	**Phantom mesh type**	**Gap**	**Tank thickness (mm)**	**1st freq (Hz)**	**2nd freq (Hz)**	**3rd freq (Hz)**	**4th freq (Hz)**	**5th freq (Hz)**
20x12	Radial	26%	0.1	1.05	1.07	1.57	2.32	2.33
20x12	Radial	26%	0.25	1.66	2.73	2.73	3.42	3.43
20x12	Radial	26%	0.5	2.62	2.73	2.73	3.42	3.43
20x12	Radial	26%	1	2.73	2.73	3.42	3.43	3.48
20x12	Radial	26%	2	2.73	2.73	3.42	3.43	3.48
20x12	Radial	26%	3	2.73	2.73	3.42	3.43	3.48
30x18	Radial	26%	3	2.71	2.71	3.38	3.39	3.44
40x24	Radial	26%	3	2.7	2.71	3.38	3.38	3.44
30x18	Radial	20%	3	2.64	2.64	3.32	3.32	3.39
30x18	Radial	13%	3	2.56	2.56	3.25	3.25	3.34
30x18	Radial	6%	3	2.45	2.46	3.15	3.15	3.3
Analytical frequencies				2.14	2.14	2.75	2.75	3.23

The error rate table below again is obtained by comparing numerical frequencies and analytical ones with each other and it is normalized with analytical frequency values.

Table 4.53. Error rates of partially-filled plexiglass cylindrical tank with phantom surface of radial mesh for its first 5 modes with respect to changing tank thickness, tank mesh resolution, phantom surface gap ratio and phantom surface mesh topology

Tank mesh	**Phantom mesh type**	**Gap**	**Tank thick-ness (mm)**	**Error rate of 1st mode (%)**	**Error rate of 2nd mode (%)**	**Error rate of 3rd mode (%)**	**Error rate of 4th mode (%)**	**Error rate of 5th mode (%)**
20x12	Radial	26%	0.1	-50.93	-50.00	-42.91	-15.64	-27.86
20x12	Radial	26%	0.25	-22.43	27.57	-0.73	24.36	6.19
20x12	Radial	26%	0.5	22.43	27.57	-0.73	24.36	6.19
20x12	Radial	26%	1	27.57	27.57	24.36	24.73	7.74
20x12	Radial	26%	2	27.57	27.57	24.36	24.73	7.74
20x12	Radial	26%	3	27.57	27.57	24.36	24.73	7.74
30x18	Radial	26%	3	26.64	26.64	22.91	23.27	6.50
40x24	Radial	26%	3	26.17	26.64	22.91	22.91	6.50
30x18	Radial	20%	3	23.36	23.36	20.73	20.73	4.95
30x18	Radial	13%	3	19.63	19.63	18.18	18.18	3.41
30x18	Radial	6%	3	14.49	14.95	14.55	14.55	2.17

The tables above show that by choosing the best values for the parameters of tank material, tank thickness, tank mesh resolution, phantom surface gap ratio and phantom surface mesh topology, the numerical results can be developed to a really good level.

Like it has done for rectangular tank analysis, for choosing the best method that gives the closest results to analytical ones, numerical and experimental results are compared in the tables below by using their frequencies and error rates. By doing this, the best method in order to obtain the natural frequencies and modeshapes is wanted to find.

In the case comparison between analytical, numerical and experimental results, the analytical results are used as benchmark.

By numerical frequencies, the models with unstructured, butterfly and radial phantom surface meshes are meant. In order to use in comparison, the numerical results with 6% phantom surface gap ratio are utilized.

In addition to the numerical results, the images of modeshapes (2,1) and (4,1) for numerical and experimental analysis are demonstrated below for helping the user about comparing them with each other visually as well.

On the other hand, the frequencies that are reached as a result of visual inspection of mode shapes from laboratory experiment are also demonstrated for the comparison below.

Table 4.54. Comparison of analytical, numerical and laboratory experiment frequencies with each other for several modeshapes in cylindrical tank.

(m,n)	**View order of mode-shapes**	**Analytical freq (Hz)**	**Unstruc-tured freq (Hz)**	**Butterfly freq (Hz)**	**Radial freq (Hz)**	**Lab experiment (Hz)**
(1,1)	1st and 2nd modes	2.14	2.38	2.4	2.46	2.28
(2,1)	3rd or 4th modes	2.75	3.05	3.06	3.15	2.76
(3,1)	6th or 7th modes	3.23	3.6	3.86	3.76	3.80
(2,2)	13th or 14th modes	4.08	4.48	4.41	4.45	4.30
(1,3)	16th mode	4.6	5.2	4.68	4.95	5.64

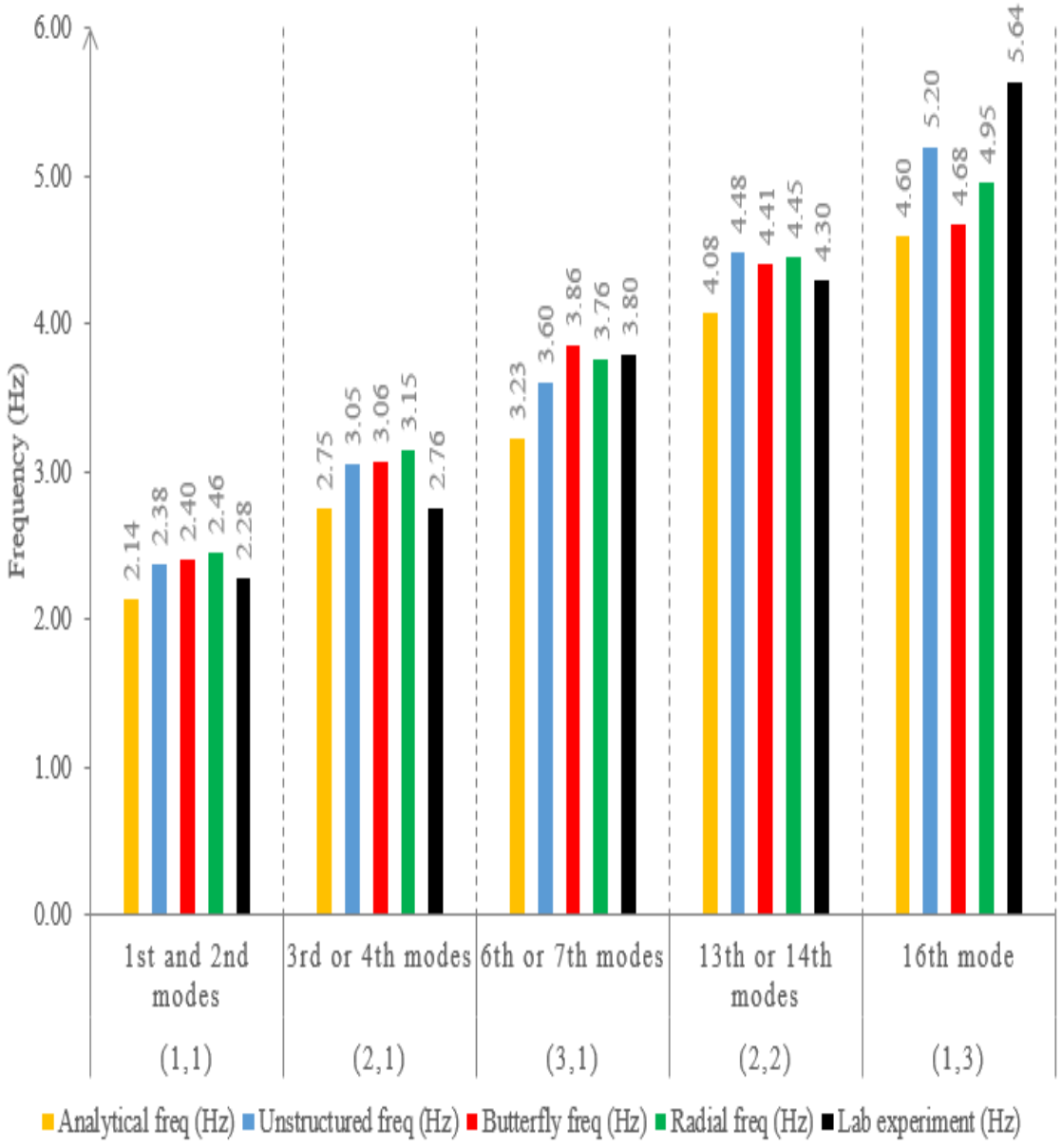

Figure 4.61. Representation of comparison of analytical, numerical and laboratory experiment frequencies with each other for several modeshapes in cylindrical tank

Table 4.55. Comparison of numerical and laboratory experiment error rates with each other for several modeshapes in cylindrical tank.

(m,n)	**View order of modes**	**Error rate of model with unstructured phantom mesh (%)**	**Error rate of model with butterfly phantom mesh (%)**	**Error rate of model with radial phantom mesh (%)**	**Error rate of model of lab. exp. study (%)**
(1,1)	1st and 2nd modes	11.21	12.15	14.95	6.5
(2,1)	3rd or 4th modes	10.91	11.27	14.55	0.2
(3,1)	6th or 7th modes	11.46	19.50	16.41	17.6
(2,2)	13th or 14th modes	9.80	8.09	9.07	0.7
(1,3)	16th mode	13.04	1.74	7.61	5.4

The error rate of natural frequencies of plexiglass cylindrical tanks with unstructured, butterfly and radial meshes, and laboratory experiment results are demonstrated in the table above. Now that table is going to be demonstrated in a bar chart below

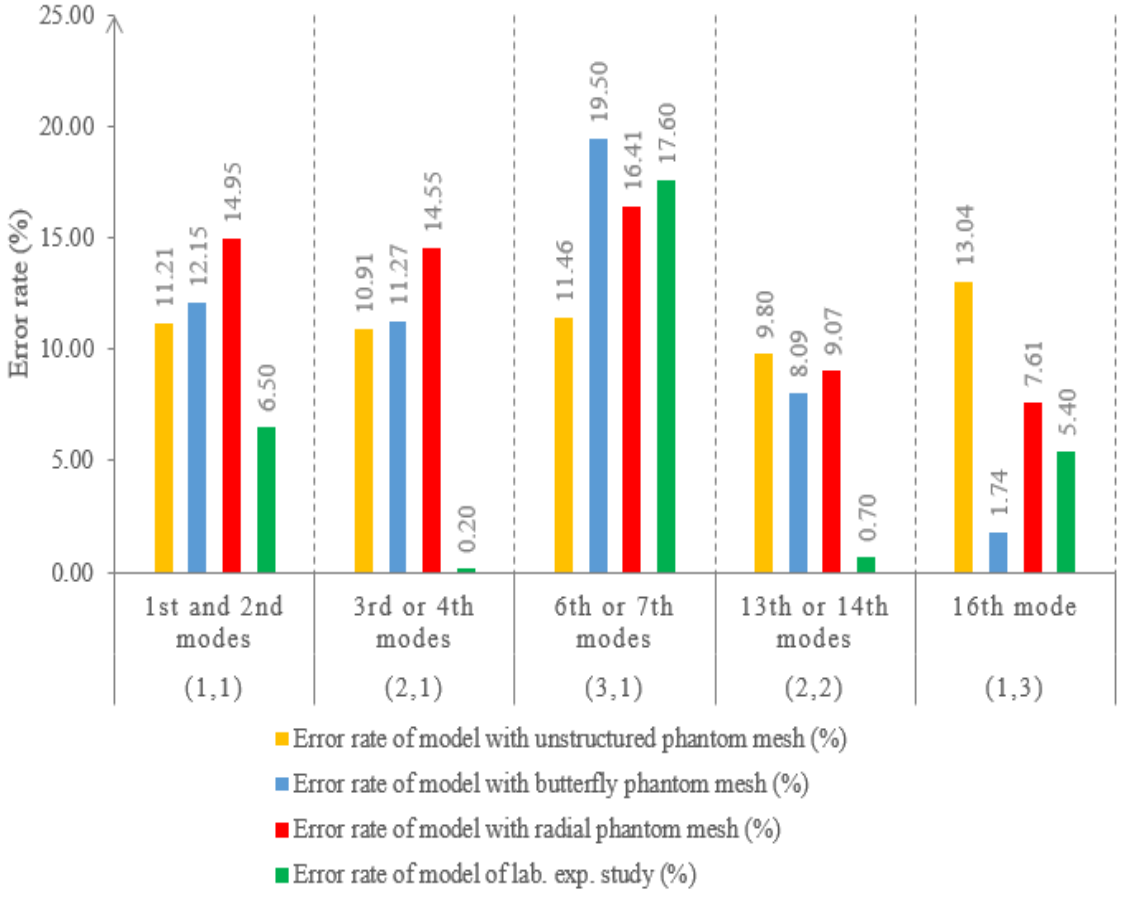

Figure 4.62. Representation of comparison of numerical and laboratory experiment error rates with each other for several modeshapes in cylindrical tank.

From Table 4.54 and Table 4.55, it can be noticed that for the fundamental modeshapes of the tank, 1st, 2nd, 3rd and 4th ones, experimental method gives better results compare to numerical ones and for overall modeshapes are considered, the majority of the frequencies are reached more accurately, again, by experimental method.

Modeshapes of phantom surfaces with unstructured, butterfly, radial meshes, and laboratory experiment images are shown below to compare for mode (2,1)

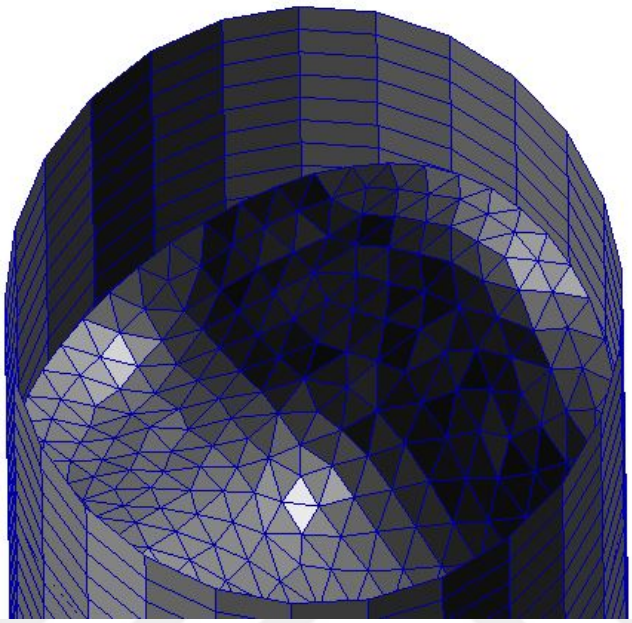

Figure 4.63. Modeshape (2,1) in cylindrical tank with unstructured mesh

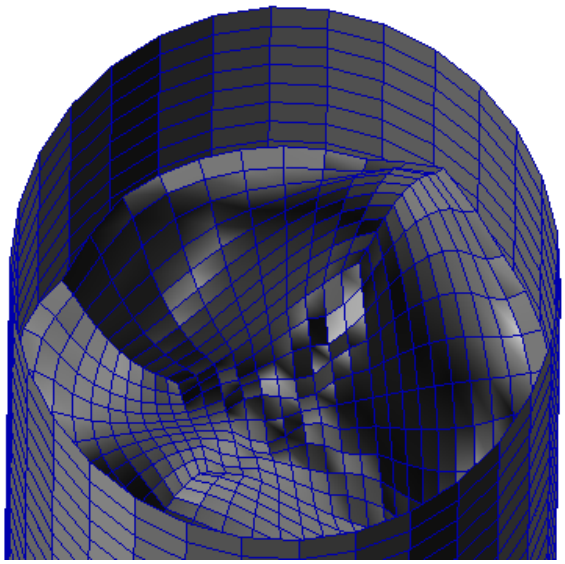

Figure 4.64. Modeshape (2,1) in cylindrical tank with butterfly mesh

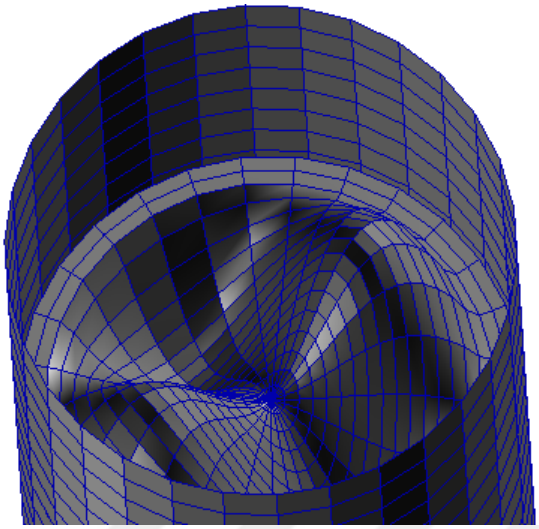

Figure 4.65. Modeshape (2,1) in cylindrical tank with radial mesh



Figure 4.66. Modeshape (2,1) in cylindrical tank from laboratory experiment

Modeshapes of phantom surfaces with unstructured, butterfly, radial meshes, and laboratory experiment images are shown below to compare for mode (4,1)

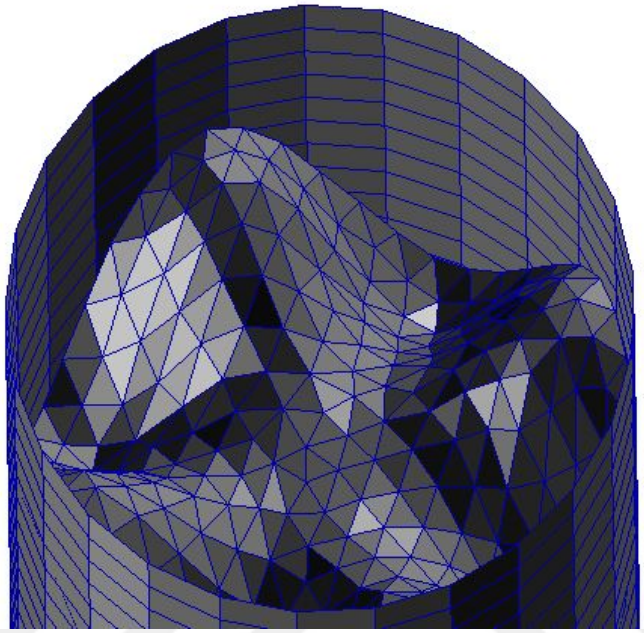

Figure 4.67. Modeshape (4,1) in cylindrical tank with unstructured mesh

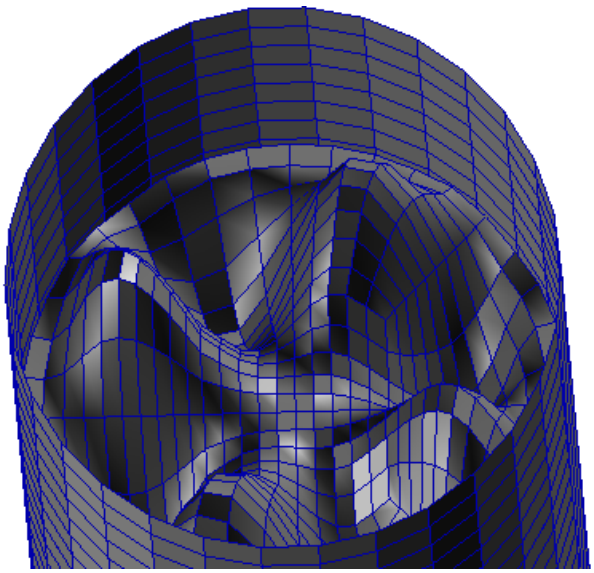

Figure 4.68. Modeshape (4,1) in cylindrical tank with butterfly mesh

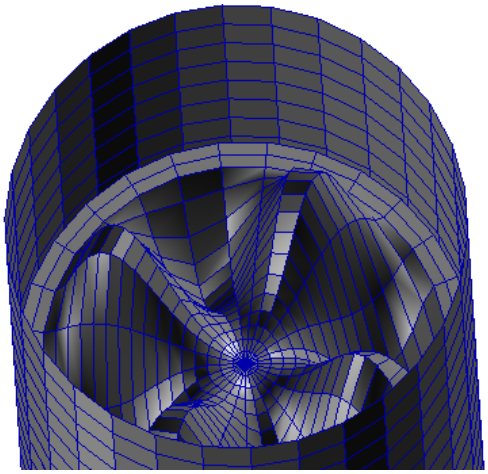

Figure 4.69. Modeshape (4,1) in cylindrical tank with radial mesh



Figure 4.70. Modeshape (4,1) in cylindrical tank from laboratory experiment

The analyses with plexiglass cylindrical tanks that have unstructured, butterfly and radial meshes give around 11%, 12%, 14% error rates respectively with respect to analytical frequencies as it can be noticed from the tables above. These values are higher than we are expecting for an optimum model.

As it was mentioned for the rectangular tank study, using plexiglass tanks in our Nastran analysis gives us the benefit of being able to compare our results with experimental results of Erginbas [3] where sloshing in plexiglass rectangular and cylindrical tanks was examined.

Like exactly done in the numerical analysis of rectangular tank study, instead of plexiglass, a very rigid material that is the one employed in rectangular tank study is used as tank material for the cylindrical tank study. Since the analytical methods that we are using have the assumption of rigid tank, using a very rigid material can give us closer results to analytical frequencies.

The analyses that are implemented for the cylindrical models with plexiglass tank are applied again for model with rigid tank material. In addition to plexiglass tank case, in this study the gap ratio of 0.75% and 0.375% are also examined. The results of the study can be found below

Table 4.56. First 5 frequencies of partially-filled highly rigid cylindrical tank with phantom surface of unstructured mesh with respect to changing tank thickness, tank mesh resolution, phantom surface gap ratio and phantom surface mesh topology

Tank mesh	**Phantom mesh type**	**Gap**	**Tank thickness (mm)**	**1st freq (Hz)**	**2nd freq (Hz)**	**3rd freq (Hz)**	**4th freq (Hz)**	**5th freq (Hz)**
20x12	Unstructured	26%	0.5	2.63	2.7	2.71	3.36	3.37
20x12	Unstructured	26%	1	2.7	2.71	3.37	3.37	3.52
20x12	Unstructured	26%	2	2.7	2.7	3.36	3.37	3.52
20x12	Unstructured	26%	3	2.7	2.7	3.36	3.37	3.52
30x18	Unstructured	26%	3	2.68	2.68	3.31	3.32	3.48
40x24	Unstructured	26%	3	2.68	2.68	3.32	3.33	3.49
30x18	Unstructured	20%	3	2.6	2.6	3.25	3.25	3.43
30x18	Unstructured	13%	3	2.5	2.51	3.16	3.17	3.37
30x18	Unstructured	6%	3	2.38	2.39	3.05	3.06	3.32
30x18	Unstructured	3%	3	2.25	2.25	2.89	2.96	3.28
30x18	Unstructured	1.5%	3	2.18	2.18	2.79	2.81	3.25
30x18	Unstructured	0.75%	3	NR	NR	NR	NR	NR
30x18	Unstructured	0.375%	3	NR	NR	NR	NR	NR
Analytical frequencies				2.14	2.14	2.75	2.75	3.23

The natural frequencies of rigid cylindrical tanks are obtained in the table above. As next step, the error rates of these natural frequencies are found as follows

Table 4.57. Error rates of partially-filled highly rigid cylindrical tank with phantom surface of unstructured mesh for its first 5 modes with respect to changing tank thickness,tank mesh resolution, phantom surface gap ratio and phantom surface mesh topology

Tank mesh	**Phantom mesh type**	**Gap**	**Tank thickness (mm)**	**Error rate of 1st mode (%)**	**Error rate of 2nd mode (%)**	**Error rate of 3rd mode (%)**	**Error rate of 4th mode (%)**	**Error rate of 5th mode (%)**
20x12	Unstructured	26%	0.5	22.90	26.17	-1.45	22.18	4.33
20x12	Unstructured	26%	1	26.17	26.64	22.55	22.55	8.98
20x12	Unstructured	26%	2	26.17	26.17	22.18	22.55	8.98
20x12	Unstructured	26%	3	26.17	26.17	22.18	22.55	8.98
30x18	Unstructured	26%	3	25.23	25.23	20.36	20.73	7.74
40x24	Unstructured	26%	3	25.23	25.23	20.73	21.09	8.05
30x18	Unstructured	20%	3	21.50	21.50	18.18	18.18	6.19
30x18	Unstructured	13%	3	16.82	17.29	14.91	15.27	4.33
30x18	Unstructured	6%	3	11.21	11.68	10.91	11.27	2.79
30x18	Unstructured	3%	3	5.14	5.14	5.09	7.64	1.55
30x18	Unstructured	1.5%	3	1.87	1.87	1.45	2.18	0.62

The graphical representation of error rate tabşe for rigid cylindrical tank with unstructured phantom surface can be seen below

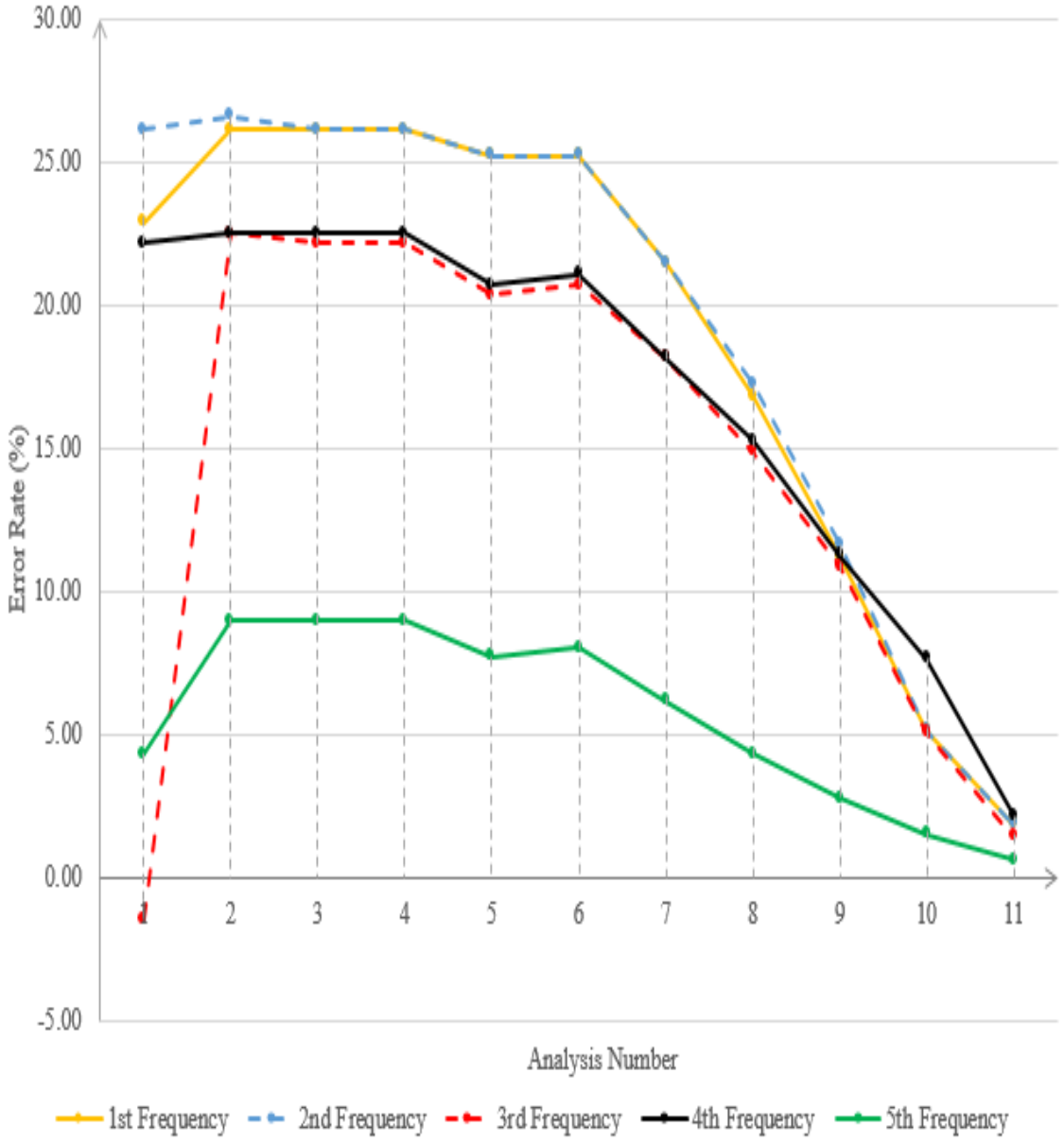

Figure 4.71. Representation of error rates of partially-filled highly rigid cylindrical tank with phantom surface of unstructured mesh for its first 5 modes with respect to changing tank thickness, tank mesh resolution, phantom surface gap ratio and phantom surface mesh topology

Table 4.58. First 5 frequencies of partially-filled highly rigid cylindrical tank with phantom surface of butterfly mesh with respect to changing tank thickness, tank mesh resolution, phantom surface gap ratio and phantom surface mesh topology

Tank mesh	**Phantom mesh type**	**Gap**	**Tank thickness (mm)**	**1st freq (Hz)**	**2nd freq (Hz)**	**3rd freq (Hz)**	**4th freq (Hz)**	**5th freq (Hz)**
20x12	Butterfly	26%	0.5	2.63	2.71	2.71	3.36	3.39
20x12	Butterfly	26%	1	2.71	2.71	3.36	3.39	3.47
20x12	Butterfly	26%	2	2.71	2.71	3.36	3.39	3.48
20x12	Butterfly	26%	3	2.71	2.71	3.36	3.39	3.48
30x18	Butterfly	26%	3	2.68	2.69	3.31	3.34	3.43
40x24	Butterfly	26%	3	2.68	2.69	3.3	3.33	3.42
30x18	Butterfly	20%	3	2.6	2.6	3.25	3.28	3.37
30x18	Butterfly	13%	3	2.5	2.51	3.17	3.19	3.31
30x18	Butterfly	6%	3	2.4	2.4	3.06	3.09	3.29
30x18	Butterfly	3%	3	2.28	2.28	2.9	3.01	3.27
30x18	Butterfly	1.5%	3	2.2	2.2	2.8	2.86	3.26
30x18	Butterfly	0.75%	3	NR	NR	NR	NR	NR
30x18	Butterfly	0.375%	3	NR	NR	NR	NR	NR
Analytical frequencies				2.14	2.14	2.75	2.75	3.23

The same analyses that are done with tank that has unstructured phantom surface are done with butterfly mesh this time as follows

Table 4.59. Error rates of partially-filled highly rigid cylindrical tank with phantom surface of butterfly mesh for its first 5 modes with respect to changing tank thickness,tank mesh resolution, phantom surface gap ratio and phantom surface mesh topology

Tank mesh	**Phantom mesh type**	**Gap**	**Tank thickness (mm)**	**Error rate of 1st mode (%)**	**Error rate of 2nd mode (%)**	**Error rate of 3rd mode (%)**	**Error rate of 4th mode (%)**	**Error rate of 5th mode (%)**
20x12	Butterfly	26%	0.5	22.90	26.64	-1.45	22.18	4.95
20x12	Butterfly	26%	1	26.64	26.64	22.18	23.27	7.43
20x12	Butterfly	26%	2	26.64	26.64	22.18	23.27	7.74
20x12	Butterfly	26%	3	26.64	26.64	22.18	23.27	7.74
30x18	Butterfly	26%	3	25.23	25.70	20.36	21.45	6.19
40x24	Butterfly	26%	3	25.23	25.70	20.00	21.09	5.88
30x18	Butterfly	20%	3	21.50	21.50	18.18	19.27	4.33
30x18	Butterfly	13%	3	16.82	17.29	15.27	16.00	2.48
30x18	Butterfly	6%	3	12.15	12.15	11.27	12.36	1.86
30x18	Butterfly	3%	3	6.54	6.54	5.45	9.45	1.24
30x18	Butterfly	1.5%	3	2.80	2.80	1.82	4.00	0.93

The error rates of rigid cylindrical tank with butterfly meshed phantom surface that are found is demonstrated in the graph below as follows

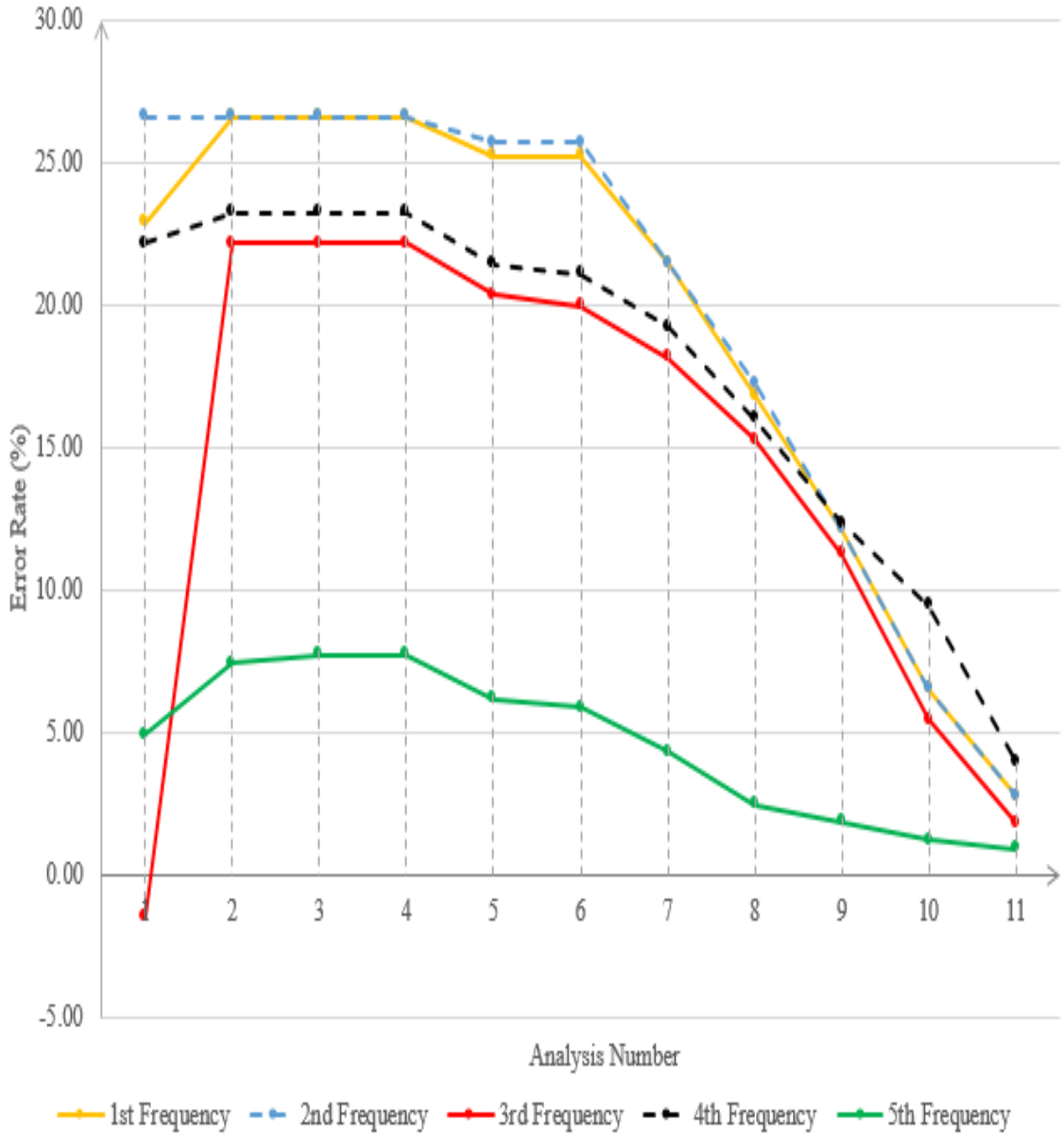

Figure 4.72. Representation of error rates of partially-filled highly rigid cylindrical tank with phantom surface of butterfly mesh for its first 5 modes with respect to changing tank thickness,tank mesh resolution, phantom surface gap ratio and phantom surface mesh topology

Table 4.60. First 5 frequencies of partially-filled highly rigid cylindrical tank with phantom surface of radial mesh with respect to changing tank thickness, tank mesh resolution, phantom surface gap ratio and phantom surface mesh topology

Tank mesh	**Phantom mesh type**	**Gap**	**Tank thickness (mm)**	**1st freq (Hz)**	**2nd freq (Hz)**	**3rd freq (Hz)**	**4th freq (Hz)**	**5th freq (Hz)**
20x12	Radial	26%	0.5	2.62	2.73	2.73	3.42	3.43
20x12	Radial	26%	1	2.73	2.73	3.42	3.43	3.48
20x12	Radial	26%	2	2.73	2.73	3.42	3.43	3.48
20x12	Radial	26%	3	2.73	2.73	3.42	3.43	3.48
30x18	Radial	26%	3	2.71	2.71	3.38	3.39	3.44
40x24	Radial	26%	3	2.7	2.71	3.38	3.38	3.44
30x18	Radial	20%	3	2.64	2.64	3.32	3.32	3.39
30x18	Radial	13%	3	2.56	2.56	3.25	3.27	3.34
30x18	Radial	6%	3	2.45	2.46	3.15	3.16	3.3
30x18	Radial	3%	3	2.32	2.32	2.98	2.99	3.29
30x18	Radial	1.5%	3	2.24	2.24	2.87	2.9	3.28
30x18	Radial	0.75%	3	NR	NR	NR	NR	NR
30x18	Radial	0.375%	3	NR	NR	NR	NR	NR
Analytical frequencies				2.14	2.14	2.75	2.75	3.23

The natural frequencies of rigid cylindrical tank with radial mesh are shown in previous table. Like it has been done for the other cases, the error rates that are calculated from those natural frequencies and analytical frequencies are demonstrated below

Table 4.61. Error rates of partially-filled highly rigid cylindrical tank with phantom surface of radial mesh for its first 5 modes with respect to changing tank thickness,tank mesh resolution, phantom surface gap ratio and phantom surface mesh topology

Tank mesh	**Phantom mesh type**	**Gap**	**Tank thickness (mm)**	**Error rate of 1st mode (%)**	**Error rate of 2nd mode (%)**	**Error rate of 3rd mode (%)**	**Error rate of 4th mode (%)**	**Error rate of 5th mode (%)**
20x12	Radial	26%	0.5	22.43	27.57	-0.73	24.36	6.19
20x12	Radial	26%	1	27.57	27.57	24.36	24.73	7.74
20x12	Radial	26%	2	27.57	27.57	24.36	24.73	7.74
20x12	Radial	26%	3	27.57	27.57	24.36	24.73	7.74
30x18	Radial	26%	3	26.64	26.64	22.91	23.27	6.50
40x24	Radial	26%	3	26.17	26.64	22.91	22.91	6.50
30x18	Radial	20%	3	23.36	23.36	20.73	20.73	4.95
30x18	Radial	13%	3	19.63	19.63	18.18	18.91	3.41
30x18	Radial	6%	3	14.49	14.95	14.55	14.91	2.17
30x18	Radial	3%	3	8.41	8.41	8.36	8.73	1.86
30x18	Radial	1.5%	3	4.67	4.67	4.36	5.45	1.55

Th error rate table above are visualized in the figure below in order to be able to see the trend of error rates that change with respect to changing parameters

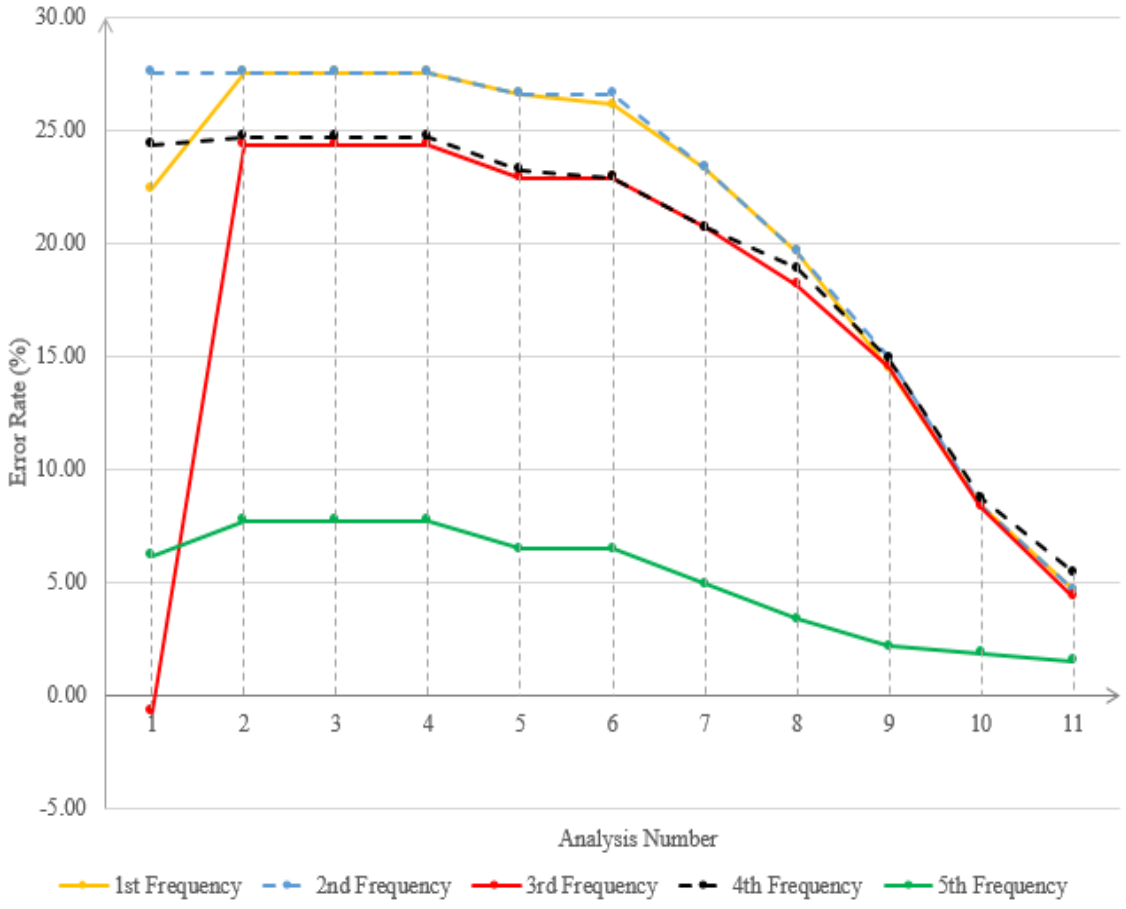

Figure 4.73. Representation of error rates of partially-filled highly rigid cylindrical tank with phantom surface of unstructured mesh for its first 5 modes with respect to changing tank thickness, tank mesh resolution, phantom surface gap ratio and phantom surface mesh topology

When the results of rigid cylindrical tank are investigated it can be seen that for all mesh topologies the change of the natural frequencies shows the same trend with plexiglass tank case. The difference between plexiglass tank and rigid material tank can be seen in the capability of having lower gap ratio. The analyses with plexiglass tank does not give any results in Nastran for 3% and 1.5% whereas for tank with rigid material gives very good results for reaching an optimum model. As it is explained in the rectangular tank case, the reason of being able to reach results with 3% and 1.5% gap ratio is the displacement of the tank wall. By using rigid material, the tank wall

does not get too close the phantom surface and phantom surface can be away from the singularity range of point sources at tank wall. As a result of of this study, we reached the numerical error rate of 1.87% for unstructured mesh case which is good value for an optimum model.

4.2.6. Large Scale Tank

To examine our optimum model study for real life cases, a partially filled large scale cylindrical tank is created and its sloshing motion is investigated.

4.2.7. Numerical Analyses

The properties of phantom surface from small scale tank study are used in this study, as well. During the analyses the properties below are employed

- Tank type: Cylindrical
- Tank radius: 10 m
- Tank height: 25 m
- Tank thickness: 20 mm
- Height of fluid: 12 m
- Type of fluid: Water
- Material types of tank: Steel
- Young Modulus of steel: 207 GPa
- Density of steel: $7800 kg/m^3$
- Poisson ratio of steel: 0.3
- Density of water: $1000 kg/m^3$

4.2.8. Results

The analytical frequencies of cylindrical tank from Abramson's formula can be seen as follows

Table 4.62. Analytical frequencies of large scale partially filled cylindrical tanks by using Abramson's method (m and n refers to nodal diameters and nodal circles, respectively [35]).

m	**n=1**	**n=2**	**n=3**	**n=4**	**n=5**
0	0.31	0.42	0.5	0.58	0.64
1	0.2	0.36	0.46	0.54	0.61
2	0.27	0.41	0.5	0.57	0.64
3	0.32	0.45	0.53	0.6	0.67
4	0.36	0.48	0.56	0.63	0.69
5	0.4	0.51	0.59	0.66	0.72

The natural frequency from Housner's method also gives 0.2 Hz as first natural frequency as Abramson's formula did.

In order to visualize the the large scale cylindrical tank model in Nastran, the image of the model is demonstrated below

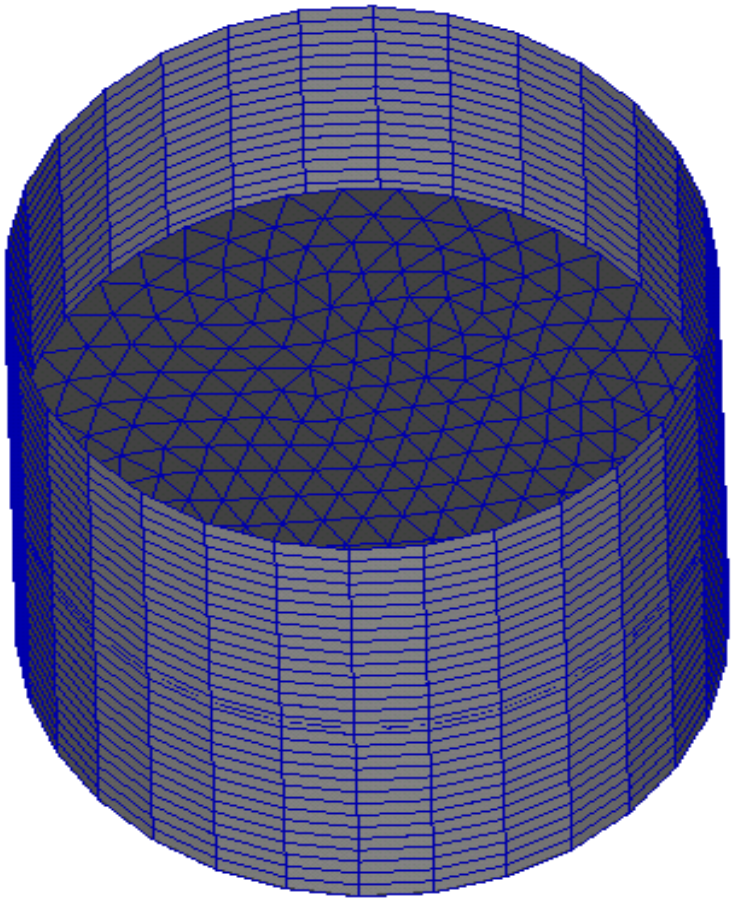

Figure 4.74. Representation of large scale cylindrical tank with phantom surface of unstructured mesh

The results of this study are demonstrated in the tables and graph below. The x axis of the graph includes the analysis number that corresponds to analyses in error rate table. For instance, number one in graph corresponds to analysis at the top of error rate table whereas number 12 shows the values at the bottom of the error rate table.

Table 4.63. First 5 frequencies of partially-filled steel large scale cylindrical tank with phantom surface of unstructured mesh with respect to changing tank thickness, tank mesh resolution, phantom surface gap ratio and phantom surface mesh topology

Tank mesh	**Phantom mesh type**	**Gap**	**Tank thickness (mm)**	**1st freq (Hz)**	**2nd freq (Hz)**	**3rd freq (Hz)**	**4th freq (Hz)**	**5th freq (Hz)**
10x10	Unstructured	26%	2.5	0.063	0.064	0.134	0.136	0.137
10x10	Unstructured	26%	5	0.16	0.18	0.18	0.27	0.27
10x10	Unstructured	26%	10	0.249	0.253	0.34	0.344	0.391
10x10	Unstructured	26%	20	0.249	0.253	0.34	0.344	0.387
30x30	Unstructured	26%	20	0.247	0.249	0.335	0.337	0.374
40x40	Unstructured	26%	20	0.245	0.246	0.331	0.333	0.373
40x40	Unstructured	20%	20	0.242	0.243	0.329	0.328	0.365
40x40	Unstructured	13%	20	0.238	0.237	0.322	0.322	0.358
40x40	Unstructured	6%	20	0.232	0.23	0.318	0.316	0.35
40x40	Unstructured	3%	20	0.227	0.228	0.31	0.309	0.343
40x40	Unstructured	1.5%	20	0.225	0.225	0.307	0.308	0.338
40x40	Unstructured	0.75%	20	0.224	0.224	0.303	0.304	0.332
40x40	Unstructured	0.375%	20	NR	NR	NR	NR	NR
40x40	Unstructured	0.19%	20	NR	NR	NR	NR	NR
Analytical frequencies				0.2	0.2	0.27	0.27	0.32

Table 4.64. Error rates of partially-filled steel large scale cylindrical tank with phantom surface of unstructured mesh for its first 5 modes with respect to changing tank thickness,tank mesh resolution, phantom surface gap ratio and phantom surface mesh topology

Tank mesh	**Phantom mesh type**	**Gap**	**Tank thickness (mm)**	**Error rate of 1st mode (%)**	**Error rate of 2nd mode (%)**	**Error rate of 3rd mode (%)**	**Error rate of 4th mode (%)**	**Error rate of 5th mode (%)**
10x10	Unstructured	26%	2.5	-68.97	-68.47	-50.92	-50.18	-57.19
10x10	Unstructured	26%	5	-21.18	-11.33	-34.07	-1.10	-15.63
10x10	Unstructured	26%	10	22.66	24.63	24.54	26.01	22.19
10x10	Unstructured	26%	20	22.66	24.63	24.54	26.01	20.94
30x30	Unstructured	26%	20	21.67	22.66	22.71	23.44	16.88
40x40	Unstructured	26%	20	20.69	21.18	21.25	21.98	16.56
40x40	Unstructured	20%	20	19.21	19.70	20.51	20.15	14.06
40x40	Unstructured	13%	20	17.24	16.75	17.95	17.95	11.88
40x40	Unstructured	6%	20	14.29	13.30	16.48	15.75	9.37
40x40	Unstructured	3%	20	11.82	12.32	13.55	13.19	7.19
40x40	Unstructured	1.5%	20	10.84	10.84	12.45	12.82	5.63
40x40	Unstructured	0.75%	20	10.34	10.34	10.99	11.36	3.75

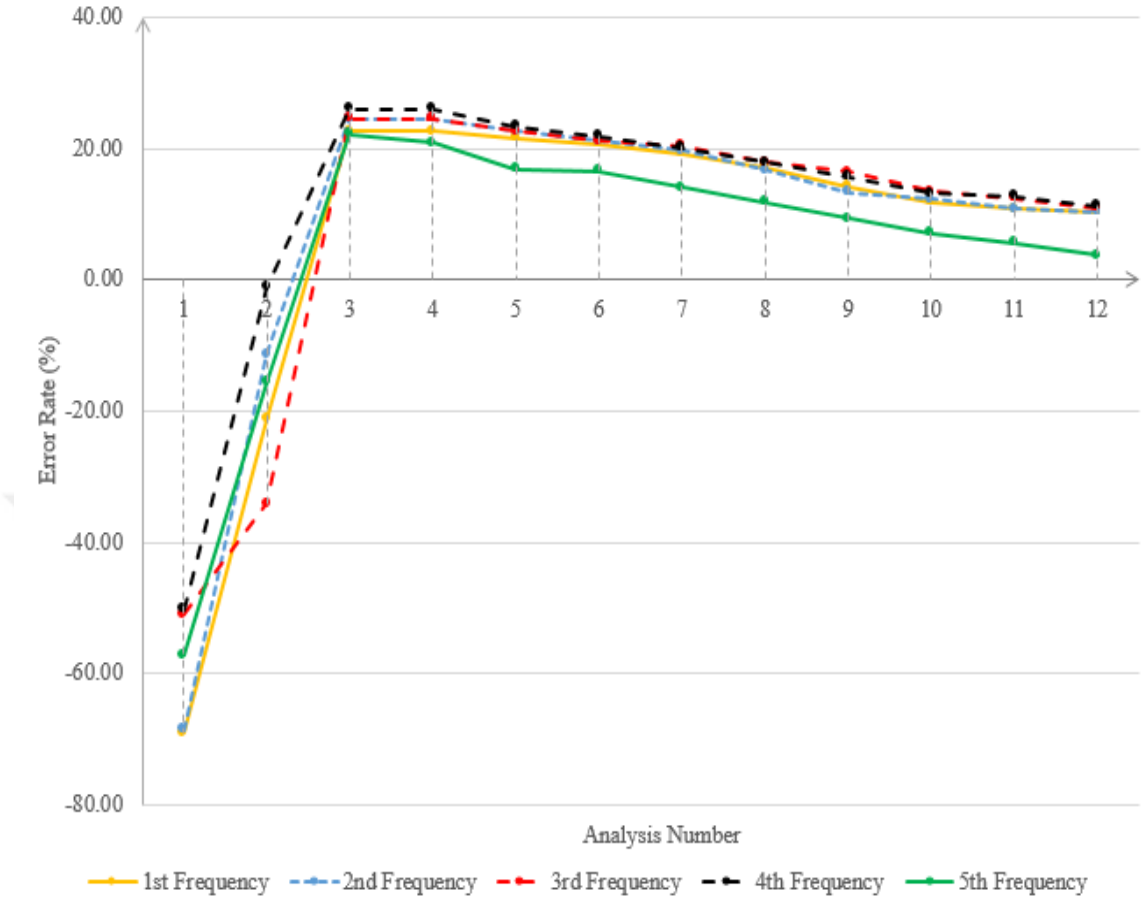

Figure 4.75. Representation of error rates of partially-filled steel large scale cylindrical tank with phantom surface of unstructured mesh for its first 5 modes with respect to changing tank thickness,tank mesh resolution, phantom surface gap ratio and phantom surface mesh topology

Table 4.65. First 5 frequencies of partially-filled steel large scale cylindrical tank with phantom surface of butterfly mesh with respect to changing tank thickness, tank mesh resolution, phantom surface gap ratio and phantom surface mesh topology

Tank mesh	**Phantom mesh type**	**Gap**	**Tank thickness (mm)**	**1st freq (Hz)**	**2nd freq (Hz)**	**3rd freq (Hz)**	**4th freq (Hz)**	**5th freq (Hz)**
10x10	Butterfly	26%	2.5	0.063	0.064	0.135	0.136	0.151
10x10	Butterfly	26%	5	0.178	0.18	0.18	0.28	0.28
10x10	Butterfly	26%	10	0.251	0.258	0.345	0.348	0.38
10x10	Butterfly	26%	20	0.251	0.258	0.345	0.348	0.381
30x30	Butterfly	26%	20	0.248	0.254	0.34	0.341	0.372
40x40	Butterfly	26%	20	0.247	0.252	0.337	0.34	0.366
40x40	Butterfly	20%	20	0.244	0.248	0.332	0.335	0.362
40x40	Butterfly	13%	20	0.24	0.241	0.326	0.328	0.355
40x40	Butterfly	6%	20	0.235	0.237	0.32	0.321	0.344
40x40	Butterfly	3%	20	0.231	0.234	0.312	0.316	0.338
40x40	Butterfly	1.5%	20	0.229	0.23	0.307	0.307	0.331
40x40	Butterfly	0.75%	20	0.228	0.229	0.306	0.306	0.328
40x40	Butterfly	0.375%	20	NR	NR	NR	NR	NR
40x40	Butterfly	0.19%	20	NR	NR	NR	NR	NR
Analytical frequencies				0.203	0.203	0.273	0.273	0.32

Table 4.66. Error rates of partially-filled large scale cylindrical tank with phantom surface of butterfly mesh for its first 5 modes with respect to changing tank thickness, tank mesh resolution, phantom surface gap ratio and phantom surface mesh topology

Tank mesh	**Phantom mesh type**	**Gap**	**Tank thickness (mm)**	**Error rate of 1st mode (%)**	**Error rate of 2nd mode (%)**	**Error rate of 3rd mode (%)**	**Error rate of 4th mode (%)**	**Error rate of 5th mode (%)**
10x10	Butterfly	26%	2.5	-68.97	-68.47	-50.55	-50.18	-52.81
10x10	Butterfly	26%	5	-12.32	-11.33	-34.07	2.56	-12.50
10x10	Butterfly	26%	10	23.65	27.09	26.37	27.47	18.75
10x10	Butterfly	26%	20	23.65	27.09	26.37	27.47	19.06
30x30	Butterfly	26%	20	22.17	25.12	24.54	24.91	16.25
40x40	Butterfly	26%	20	21.67	24.14	23.44	24.54	14.38
40x40	Butterfly	20%	20	20.20	22.17	21.61	22.71	13.13
40x40	Butterfly	13%	20	18.23	18.72	19.41	20.15	10.94
40x40	Butterfly	6%	20	15.76	16.75	17.22	17.58	7.50
40x40	Butterfly	3%	20	13.79	15.27	14.29	15.75	5.63
40x40	Butterfly	1.5%	20	12.81	13.30	12.45	12.45	3.44
40x40	Butterfly	0.75%	20	12.32	12.81	12.09	12.09	2.50

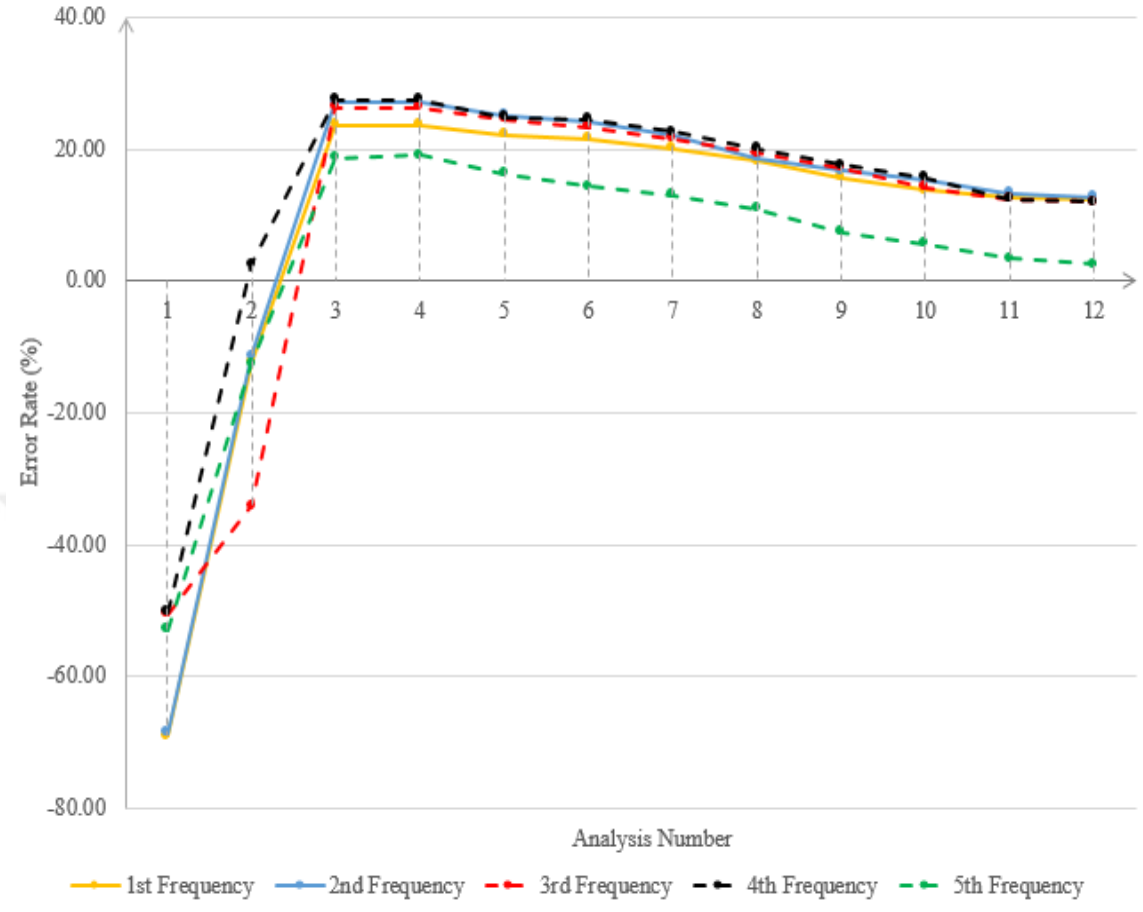

Figure 4.76. Representation of error rates of partially-filled large scale cylindrical tank with phantom surface of butterfly mesh for its first 5 modes with respect to changing tank thickness, tank mesh resolution, phantom surface gap ratio and phantom surface mesh topology

Table 4.67. First 5 frequencies of partially-filled steel large scale cylindrical tank with phantom surface of radial mesh with respect to changing tank thickness, tank mesh resolution, phantom surface gap ratio and phantom surface mesh topology

Tank mesh	**Phantom mesh type**	**Gap**	**Tank thickness (mm)**	**1st freq (Hz)**	**2nd freq (Hz)**	**3rd freq (Hz)**	**4th freq (Hz)**	**5th freq (Hz)**
10x10	Radial	26%	2.5	0.063	0.065	0.136	0.136	0.155
10x10	Radial	26%	5	0.182	0.182	0.185	0.29	0.29
10x10	Radial	26%	10	0.258	0.26	0.355	0.358	0.38
10x10	Radial	26%	20	0.258	0.26	0.355	0.358	0.385
30x30	Radial	26%	20	0.254	0.256	0.349	0.353	0.376
40x40	Radial	26%	20	0.254	0.254	0.345	0.351	0.371
40x40	Radial	20%	20	0.251	0.251	0.34	0.344	0.367
40x40	Radial	13%	20	0.248	0.248	0.332	0.339	0.359
40x40	Radial	6%	20	0.242	0.243	0.325	0.328	0.352
40x40	Radial	3%	20	0.239	0.24	0.32	0.323	0.344
40x40	Radial	1.5%	20	0.236	0.237	0.316	0.319	0.337
40x40	Radial	0.75%	20	0.234	0.236	0.314	0.316	0.332
40x40	Radial	0.375%	20	NR	NR	NR	NR	NR
40x40	Radial	0.19%	20	NR	NR	NR	NR	NR
Analytical frequencies				0.203	0.203	0.273	0.273	0.32

Table 4.68. Error rates of partially-filled large scale cylindrical tank with phantom surface of radial mesh for its first 5 modes with respect to changing tank thickness, tank mesh resolution, phantom surface gap ratio and phantom surface mesh topology

Tank mesh	**Phantom mesh type**	**Gap**	**Tank thickness (mm)**	**Error rate of 1st mode (%)**	**Error rate of 2nd mode (%)**	**Error rate of 3rd mode (%)**	**Error rate of 4th mode (%)**	**Error rate of 5th mode (%)**
10x10	Radial	26%	2.5	-68.97	-67.98	-50.18	-50.18	-51.56
10x10	Radial	26%	5	-10.34	-10.34	-32.23	6.23	-9.38
10x10	Radial	26%	10	27.09	28.08	30.04	31.14	18.75
10x10	Radial	26%	20	27.09	28.08	30.04	31.14	20.31
30x30	Radial	26%	20	25.12	26.11	27.84	29.30	17.50
40x40	Radial	26%	20	25.12	25.12	26.37	28.57	15.94
40x40	Radial	20%	20	23.65	23.65	24.54	26.01	14.69
40x40	Radial	13%	20	22.17	22.17	21.61	24.18	12.19
40x40	Radial	6%	20	19.21	19.70	19.05	20.15	10.00
40x40	Radial	3%	20	17.73	18.23	17.22	18.32	7.50
40x40	Radial	1.5%	20	16.26	16.75	15.75	16.85	5.31
40x40	Radial	0.75%	20	15.27	16.26	15.02	15.75	3.75

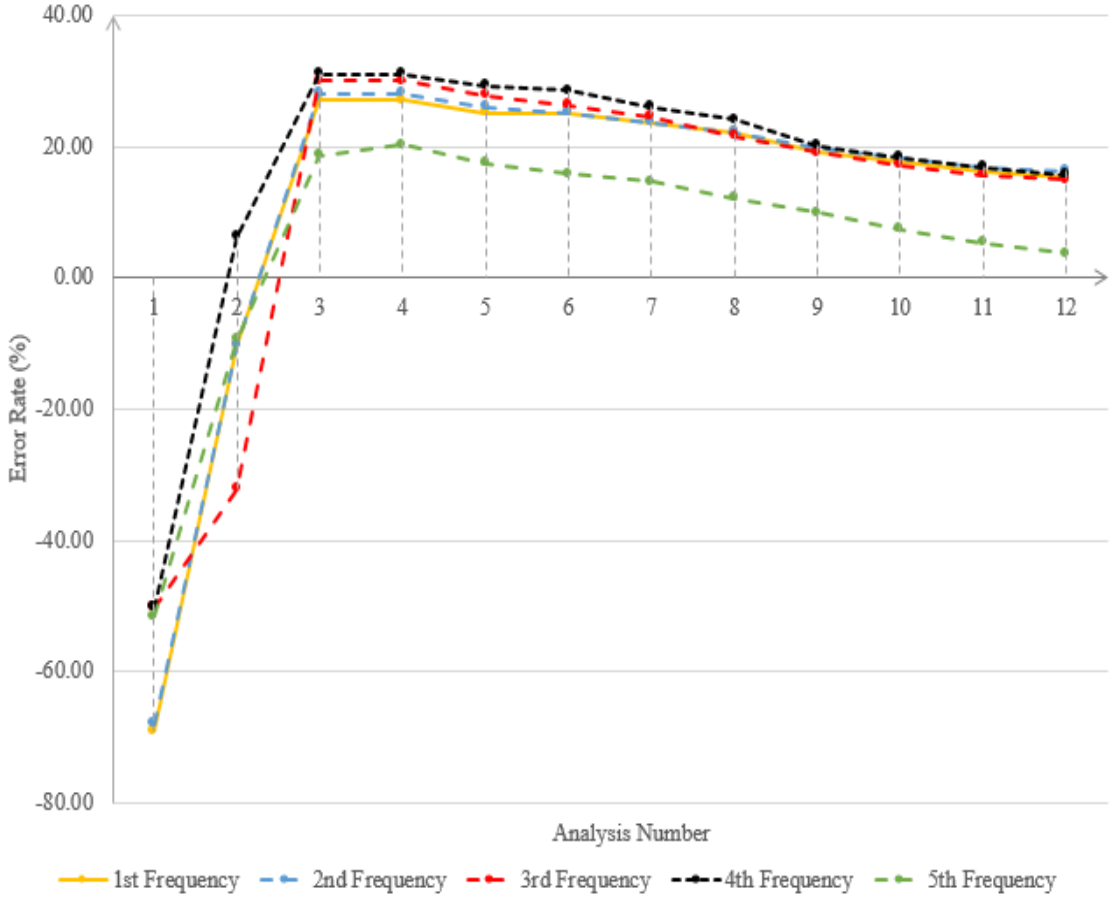

Figure 4.77. Representation of error rates of partially-filled steel large scalecylindrical tank with phantom surface of radial mesh for its first 5 modes withrespect to changing tank thickness,tank mesh resolution, phantom surface gap ratioand phantom surface mesh topology

The results show us that large scale cylindrical tank analyses demonstrates the same trend with small scale plexiglass model. The tank thickness gets better as it gets bigger whereas as tank mesh resolution gets more refined the results are getting closer to analytical ones. The gap ratio decrease the error rate, and too close phantom surface to tank wall causes singularity again. Compare to plexiglass model, the natural frequencies with the gap ratios of 3%, 1.5% and 0.75% can be found. This means that the same gap ratio percentages may not give the same error rates for different tank geometries, however, it can be said that like in the case rectangular tank, working on

these modelling parameters helps us to optimize our results.

5. CONCLUSION

This study begin with understanding theoretical background knowledge of the sloshing phenomena by derivation of sloshing motion in rectangular and cylindrical tanks and these results are used as a benchmark for our comparisons. In order to reach optimum design of virtual mass models in Nastran as one of the goals of this study, firstly, the working principle of virtual mass method is examined deeply by taking its derivation. Afterwards many parametric studies are completed for different tank materials, tank thicknesses, tank mesh resolutions, phantom surface gap ratios, phantom surface mesh resolutions and mesh topologies with rectangular and cylindrical tanks that have different sizes.

The results show that for plexiglass rectangular tanks the error rates of numerical results compare to analytical results can drop from 29% to 7%, and for plexiglass cylindrical tanks from 25% to 11% by making better choices in terms of these parameters. Numerical results for plexiglass rectangular tank study give better results in fundamental natural frequencies such as 1st, 2nd and 4th compare to experimental study whereas for plexiglass cylindrical tank experimental results are better. Among 3 types of phantom surface mesh topologies which are unstructured, butterfly and radial meshes for cylindrical tank, unstructured mesh is the best one since it is more suitable for sloshing motion's highly curved boundaries.

Since for the analytical methods that we use assume that the tank is rigid, for reaching the aim of optimum model, the cylindrical and rectangular tanks are also modelled with a very rigid material. For rigid material, the material properties of the diamond is taken. As a result of the studies with these tanks, for rectangular tank the error rate of natural frequency dropped from 28% to 1.3% whereas for cylindrical tank it is dropped from 26% to 1.87%. This situation is obtained by being able to have lower phantom surface gap ratio which is 2.5% as a result of having a very rigid material. In plexiglass rectangular tank with 5% gap ratio, the numerical error rate is 7% whereas with rigid rectangular tank with 2.5% gap ratio, it is 1.32%. When we compare these

two situations, we can notice again the importance of phantom surface gap ratio over the frequencies. On the other hand, in plexiglass cylindrical tank with 6% gap ratio, the numerical error rate is 11% whereas with rigid cylindrical tank with 2% gap ratio, it is 1.87%. This result for rigid cylindrical tank shows us again the importance of phantom surface gap ratio parameter. In addition, like in the case plexiglass cylindrical tank, unstructured phantom surface gave the best results.

In another study, large scale rectangular and cylindrical tanks that have sizes of real life applications are investigated to increase the diversity of our work. As a result of this study, the error rate of natural frequency of steel rectangular tank is dropped from 30.7% to 7.3% whereas for steel cylindrical tank the values changed from 22% to 10.3%. Unstructured phantom mesh again gave the better results than butterfly and radial phantom surfaces.

When the parameters from all the analyses above are investigated, it is seen that the most crucial parameters are tank thickness and phantom surface gap ratio for both rectangular and cylindrical tanks since they have the greatest effect over the frequencies by their changing. Also it can be concluded that in Nastran the optimum model is not given to the user easily; it needs great effort to reach the proposed optimum model by sensitively implementing different values to these parameters. The most crucial modelling parameter can be seen as the phantom surface gap ratio. From the results, it can be said that this gap ratio should be smaller than 2% in order to obtain the optimum model, however, it should not be too low since in this case Nastran does not do the analyses due to singularity problem. For the future studies, the singularity problem of Nastran due to having low phantom surface gap ratio can be investigated. Another thing that can be concluded from this study is the importance of tank mesh and phantom surface mesh resolution. For small scale rectangular tank with the size of 150 mm length, 100 mm width and 500 mm height, tank mesh resolution of 24 x 16 x 48 and phantom surface mesh resolution on 60 x 40 give the best results. In the case of large scale rectangular tank with the size of 20 m length, 15 m width and 8 m height, tank mesh resolution of 40 x 32 x 30 and phantom surface mesh resolution on 60 x 40 give the closest frequencies to analytical values. On the other hand, for

small scale cylindrical tank with the size of 100 mm radius, and 500 mm height, tank mesh resolution of 40 x 24 and unstructured phantom surface mesh topology give the best results. Finally, for small large cylindrical tank with the size of 10 m radius, and 25 m height, tank mesh resolution of 40 x 40 and unstructured phantom surface mesh topology give us the most accurate results. Even though these results are obtained for these sizes of the geometries and can not be generalized for every model, it can be concluded that refined tank mesh and phantom surface mesh topology give us better results compare to coarse ones and after a point the values converges. Thus, the proposed optimum model is obtained by sensitively implementing more refined tank mesh and phantom surface mesh resolution until reaching that convergence point.

Lastly, in order to model the tank faster in Nastran, two computer scripts that are written in Matlab and are implemented eigenvalue analyses for rectangular and cylindrical tanks are created. With these scripts, the required time to model the tanks for eigenvalue analyses are decreased as it is proposed in the beginning of this study.

REFERENCES

1. Silverman, S. and S. Abramson, "The Dynamic Behavior of Liquid in Moving Containers", *NASA, Report No. SP-106*, pp. 13–78, 1966.

2. Housner, G. W., "Dynamic pressures on accelerated fluid containers", *Bulletin of the seismological society of America*, Vol. 47, No. 1, pp. 15–35, 1957.

3. Erginbas, C., "Bachelor's Degree Final Project", *Bogazici University*, 2008.

4. Robinson, M., *MSC Nastran The Virtual Mass Method Explained*, Tech. rep., 2009.

5. Cakiroglu, K., "Numerical Modelling of Sloshing Using the Radial Basis Function Collocation Method", *Bogazici University*, 2012.

6. Henzel, T., *Sloshing Motion in Rectangular Tank*, Tech. rep., Boğaziçi University, Civil Engineering Department, technical report.

7. Corporation, M. S., *Nastran Linear Static Analysis User's Guide*, MSC Software Corporation, 2009.

8. Ibrahim, R. A., *Liquid sloshing dynamics: theory and applications*, Cambridge University Press, 2005.

9. Faraday, M., *Philosophical Transactions*, The Royal Society Publishing, 1831.

10. Lamb, H., *Hydrodynamics*, Cambridge university press, 1993.

11. Westergaard, H. M., "Water pressures on dams during earthquakes", *Trans. ASCE*, Vol. 95, pp. 418–433, 1933.

12. Jacobsen, L. S., "Impulsive hydrodynamics of fluid inside a cylindrical tank and of fluid surrounding a cylindrical pier", *Bulletin of the Seismological Society of*

America, Vol. 39, No. 3, pp. 189–204, 1949.

13. Graham, E. and A. Rodriguez, "The Characteristics of Fuel Motion Which Affect Airplane Dynamics. Rep. No. SM-14212", *Douglas Aircraft Company*, 1951.

14. Group, S. F. E. W., *Saturn SA1 Flight Evaluation*, Tech. rep., 1961.

15. NASA, *NASA Space Vehicle Design Criteria (Structures)-Propellant Slosh Loads*, Tech. rep., 1968.

16. Abramson, H. N., "NASA Technical Report SP-8031, Slosh Suppression", *NASA Technical Reports Server (NTRS)*, 1969.

17. Harlow, F. H. and J. E. Welch, "Numerical calculation of time-dependent viscous incompressible flow of fluid with free surface", *The physics of fluids*, Vol. 8, No. 12, pp. 2182–2189, 1965.

18. Von Kerczek, C., "Numerical solution of naval free-surface hydrodynamics problems", *Proc. First Intl. Conf. on Numerical Ship Hydrodynamics*, pp. 11–47, 1975.

19. Faltinsen, O. M. *et al.*, "A numerical nonlinear method of sloshing in tanks with two-dimensional flow", *Journal of Ship Research*, Vol. 22, No. 03, pp. 193–202, 1978.

20. Nakayama, T. and K. Washizu, "Nonlinear analysis of liquid motion in a container subjected to forced pitching oscillation", *International Journal for Numerical Methods in Engineering*, Vol. 15, No. 8, pp. 1207–1220, 1980.

21. Hirt, C. W. and B. D. Nichols, "Volume of fluid (VOF) method for the dynamics of free boundaries", *Journal of computational physics*, Vol. 39, No. 1, pp. 201–225, 1981.

22. Chen, W., M. A. Haroun and F. Liu, "Large amplitude liquid sloshing in seismically excited tanks", *Earthquake engineering & structural dynamics*, Vol. 25, No. 7, pp.

653–669, 1996.

23. Cho, J. and H. Lee, "Non-linear finite element analysis of large amplitude sloshing flow in two-dimensional tank", *International Journal for Numerical Methods in Engineering*, Vol. 61, No. 4, pp. 514–531, 2004.

24. Liu, D. and P. Lin, "Three-dimensional liquid sloshing in a tank with baffles", *Ocean engineering*, Vol. 36, No. 2, pp. 202–212, 2009.

25. Kim, M. and S. Lee, "Hydroelastic analysis of rectangular tank", *The aerospace corporation El Segundo, California*, Vol. 90245, 1997.

26. Hatanaka, T. and J. Yoshida, "Dynamic stress analysis of fuel tank considering factors including vehicle body stiffness", *JSAE review*, Vol. 19, No. 4, pp. 337–341, 1998.

27. Wu, X., Y. Lei and D. Li, "Dynamic analysis of a large scale satellite structure with the liquid propellant consuming", *Journal of National University of Defense Technology*, Vol. 34, No. 4, pp. 38–42, 2012.

28. Yazici, G., S. A. Kilic and K. Cakiroglu, "Experimental and Numerical Study of the Sloshing Modes of Liquid Storage Tanks with the Virtual Mass Method.", *Acta Physica Polonica A*, Vol. 135, No. 5, pp. 1068–1071, 2019.

29. Corporation, T. M.-S., *Preliminary Design Document: The Implementation of Fluid Capability in Nastran*, Tech. rep., 1977.

30. Corporation, M. S., *Nastran Quick Reference Guide 2012*, MSC Software Corporation.

31. Corporation, M. S., *Sloshing with Virtual Mass: Sample Problem 1*, MSC Software Corporation.

32. Bostic, S. W., "Lanczos eigensolution method for high-performance computers",

NASA Technical Memorandum 104108, 1991.

33. Byeon, J. H., H. J. Cho, S. J. Baek, A. R. Prabowo, D. M. Bae and J. M. Sohn, "Numerical approaches in idealizing mass of fluid in tank for ship vibration analysis", *MATEC Web of Conferences*, Vol. 159, p. 02059, EDP Sciences, 2018.

34. Corporation, M. S., *Nastran Advanced Dynamic Analyses User's Guide Version 70*, MSC Software Corporation.

35. Blevins, R. D., *Formulas for natural frequency and mode shape*, RE Krieger, 1979.

36. Tu, J., G. H. Yeoh and C. Liu, *Computational fluid dynamics: a practical approach*, Butterworth-Heinemann, 2018.

37. Stokes, G. G., *On the effect of the internal friction of fluids on the motion of pendulums*, Vol. 9, Pitt Press Cambridge, 1851.

38. Rzhevkin, S., *Acourse of Lectures on the Theory of Sound*.

39. Arecchi, A. V., R. J. Koshel and T. Messadi, *Field guide to illumination*, Vol. FG11, SPIE Press, 2007.

40. Girard, A., "Tables des sinvs tangentes & secantes./By Albert Girard", *La Haye, J. Elzevir, 1626*, 2011.

41. Fox, R., *Thomas Harriot and his world: Mathematics, exploration, and natural philosophy in early modern England*, Routledge, 2016.

42. Katzoff, S., M. F. Faison and H. C. DuBose, *Determination of mean camber surfaces for wings having uniform chordwise loading and arbitrary spanwise loading in subsonic flow*, Tech. rep., NASA ADMIN LANGLEY Research Center Hampton VA, 1953.

43. Cohen, D., *A method for determining the camber and twist of a surface to support a*

given distribution of lift with applications to the load over a sweptback wing, 1945.

44. Miller, F., A. Vandome and J. McBrewster, *Biot-Savart Law*, Alphascript Publishing, 2009.

45. R.H., M., *Investigation of Digital Computer Techniques for Hydroelastic Analysis*, Tech. rep., MacNeal Corporation, 1968.

46. Strutt, J. W. and B. Rayleigh, *The theory of sound*, Dover, 1945.

APPENDIX A: MATHEMATICAL DERIVATION OF NATURAL FREQUENCY FROM HOUSNER'S ANALYTICAL METHOD STUDY

In 1957, Housner found an analytical method which calculated the natural frequencies of the fluid inside the containers that was subjected to horizontal accelerations. His study also contained the calculation of impulsive and convective fluid pressures.

In his study, it was declared that the pressures are able to be separated into two parts as impulsive and convective parts. Impulsive pressures are related to the inertia forces which are created by impulsive movements of the tank walls. These pressure are considered as directly proportional to acceleration of tank walls. On the other hand, convective pressure is the result of fluid oscillations. The fluid in his study was assumed as incompressible and the fluid displacements were considered as small whereas the tank was assumed as rigid.

A.1. Impulsive Pressures

Let's consider a tank with vertical side walls and horizontal bottom and let's consider this tank's walls are under the impulsive acceleration of $\dot{u}_0$ in x direction. As a result of this acceleration, the accelerations of $\dot{u}$, $\dot{v}$, and $\dot{w}$ in x, y and z directions are produced, respectively. For rectangular and cylindrical tanks $\dot{w}$ are neglected and considered as zero [2]. In physical point of view, this situation is equivalent to that the fluid motion is restrained by thin, vertical membranes, spaced dz apart, which causes fluid motion only in x and y plane. In his study, it was declared that it can be considered the impulsive pressures are generated in a lamina of fluid [2]. This lamina of fluid can be seen in the figure below

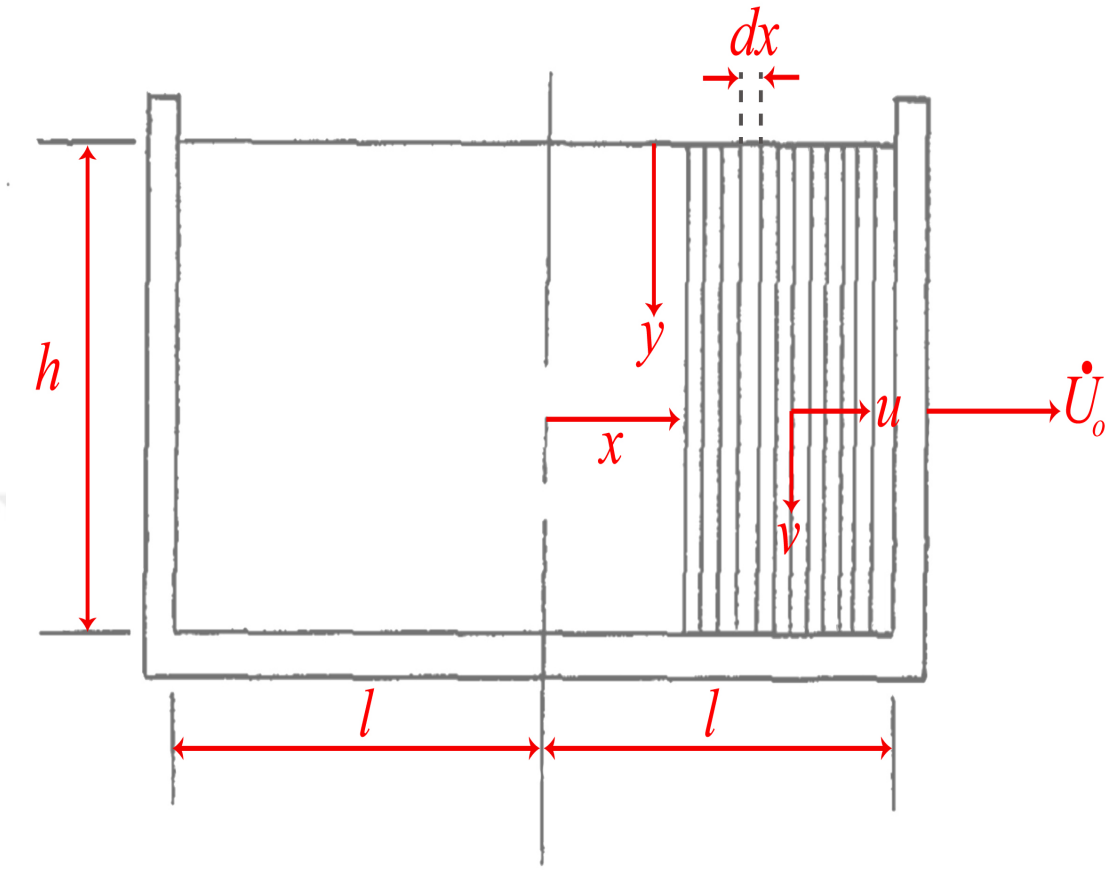

Figure A.1. Laminas of fluid with unit thickness in 2 dimensional tank. Adapted from [2]

The lamina of fluid from the figure above has unit thickness and its walls are horizontal to the acceleration of $\dot{u}_0$. As a result of this acceleration, the horizontal and vertical accelerations can be given to the fluid.

This fluid behaviour is similar to the situation that would be seen if the fluid velocity in horizontal direction, u, were not dependent on y coordinate, that is, consider the fluid that is constrained by thin, vertical, massless membranes that is free to move in x direction, and the distance between membranes are dx. When the tank is subjected to acceleration, the membranes will be accelerated with the fluid, and in addition, the fluid will also be squeezed vertically, with respect to membranes. As it is

demonstrated in Figure A.2 the fluid that is between two adjacent membranes has the following vertical velocity

$$v = (h - y)\frac{du}{dx} \tag{A.1}$$

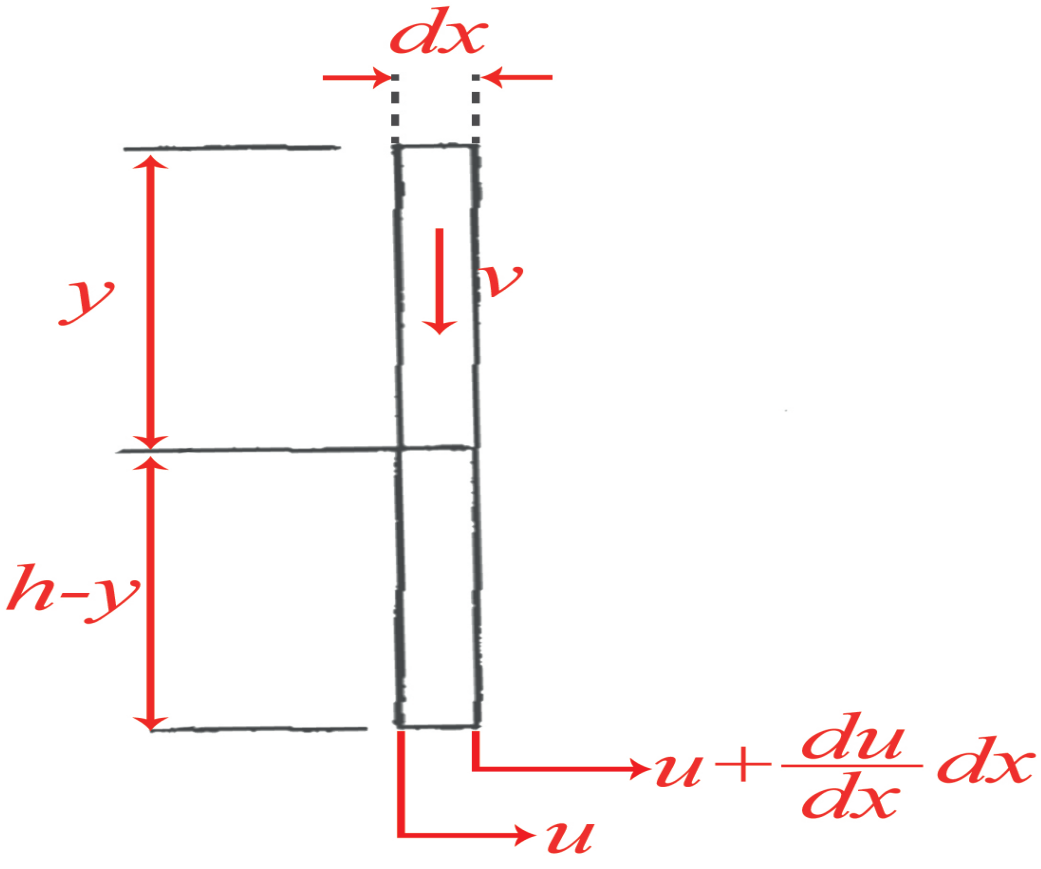

Figure A.2. Vertical velocity of fluid when it is constrained between two adjacent membranes. Adapted from [2]

Since the fluid is assumed as incompressible, the acceleration component is also fulfill the equation above

$$\dot{v} = (h - y)\frac{d\dot{u}}{dx} \tag{A.2}$$

Then the pressure in the field is

$$\frac{\partial p}{\partial y} = -\rho\dot{v} \tag{A.3}$$

where ρ is the fluid density. One membrane's total horizontal force then can be denoted as

$$P = \int_0^h p dy \tag{A.4}$$

The equations demonstrated above can be written as follows

$$\dot{v} = (h - y)\frac{d\dot{u}}{dx} \tag{A.5}$$

$$p = -\rho \int_0^y (h - y)\frac{d\dot{u}}{dx} dy = -\rho h^2 (y/h - \frac{1}{2}(y/h)^2)\frac{d\dot{u}}{dx} \tag{A.6}$$

$$P = -\rho h^2 \int_0^h (y/h - \frac{1}{2}(y/h)^2)\frac{d\dot{u}}{dx} dy = -\rho h^3/3\frac{d\dot{u}}{dx} \tag{A.7}$$

The acceleration $\dot{u}$ can be found from the horizontal motion of the fluid which are contained between two membranes. The fluid from A.2 can have acceleration in x axis when there is a difference between the faces of the slice of fluid. The equation of motion is

$$\frac{dP}{dx} dx = -\rho h dx \dot{u} \tag{A.8}$$

Applying P from Equation A.7 yields

$$\frac{d^2\dot{u}}{dx^2} - \frac{3}{h^2}\dot{u} = 0 \tag{A.9}$$

and the solution of the Equation A.9 becomes

$$\dot{u} = C_1 cosh\sqrt{3}\frac{x}{h} + C_2 sinh\sqrt{3}\frac{x}{h} \tag{A.10}$$

After finding Equation A.10, Equation A.6 can be used to define fluid pressures.

A.2. Convective Pressures

When the tank is stimulated with an acceleration, the fluid is excited and this behaviour of fluid causes pressure on the tank walls and at the bottom of the tank. In order to investigate the first mode of fluid motion inside the tank, it was considered firstly that the constraints of horizontal and rigid membranes which are free to rotate are maintained as it can be seen in the figure below

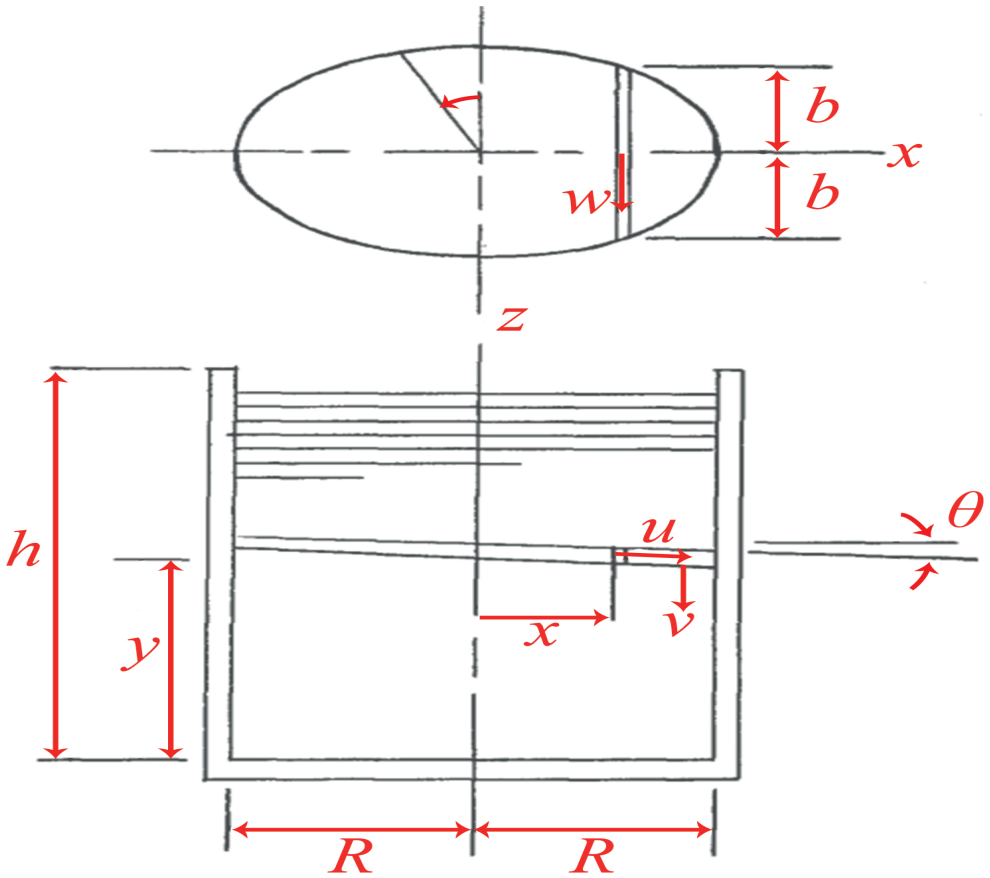

Figure A.3. 2 dimensional tank with horizontal, rigid membranes that are free to rotate. Adapted from [2]

If we consider that u, v, and w are the x, y, and z components of the fluid velocity, the constraints on the flow can be defined as follows

$$\frac{\partial(ub)}{\partial x} = -b\frac{\partial v}{\partial y} \tag{A.11}$$

$$v = x\dot{\theta} \tag{A.12}$$

$$\frac{\partial(w)}{\partial z} = -(\frac{\partial u}{\partial x} + \frac{\partial v}{\partial y}) \tag{A.13}$$

where b and θ are as they are demonstrated in Figure A.3

From the equations above it can be concluded that the fluid at given x, y coordinates has constant uniform velocity u where all the fluids at give x and y coordinates move with same v, and as a result the continuity of the flow is maintained. For the equation of motion for certain shape of containers filled with fluid the following steps are going to be employed.

$$u = -\frac{1}{b}\frac{\partial\dot{\theta}}{\partial y}\int_{-R}^{x} xbdx \tag{A.14}$$

$$w = z\frac{b'}{b^2}\frac{\partial\dot{\theta}}{\partial y}\int_{-R}^{X} xbdx \tag{A.15}$$

where $b' = \frac{db}{dx}$.

Therefore the total kinetic energy becomes

$$T = \frac{1}{2}\rho \int_0^h \int_{-R}^{+R} \int_{-b}^{+b} (x^2\dot{\theta}^2 + \frac{1}{b^2}(\frac{\partial\dot{\theta}}{\partial y})^2(\int_{-R}^{x} xbdx)^2(1 + z^2(\frac{b'}{b})^2))dxdydz \tag{A.16}$$

$$T = \frac{1}{2}\rho \int_0^h (I_z\dot{\theta}^2 + K(\frac{\partial\dot{\theta}}{\partial y})^2)dy \tag{A.17}$$

where

$$I_z = \int_A x^2 dA \tag{A.18}$$

$$K = 2\int_{-R}^{+R} \frac{1}{b}(\int_{-R}^{x} bxdx)^2(1 + \frac{b'^2}{3})dx \tag{A.19}$$

The potential energy of the fluid is

$$V = \frac{1}{2}\rho g{\theta_h}^2 \int x^2 dxdz = \frac{1}{2}\rho g{\theta_h}^2 I_z \tag{A.20}$$

By using Hamilton's Principle

$$\delta \int_{t_1}^{t_2} (T - V) dt = 0 \tag{A.21}$$

$$\delta \int_{t_1}^{t_2} \frac{1}{2} \rho (\int_0^h [I_z \dot{\theta}^2 + (\frac{\partial \dot{\theta}}{\partial y})^2) K] dy - g {\theta_h}^2 I_z) dt = 0 \tag{A.22}$$

From the equations above we reach

$$\frac{\partial^2 \dot{\theta}}{\partial y^2} - \frac{I_z}{K} \dot{\theta} = 0 \tag{A.23}$$

$$\frac{\partial^2}{\partial t^2} (\frac{\partial \theta}{\partial y})_h + g \frac{I_z}{K} \theta_h = 0 \tag{A.24}$$

Therefore, by integration the equations of free oscillation and the natural frequency of the first mode are obtained as follows

$$\theta = \theta_h \frac{sinh\sqrt{\frac{I_z}{K}}y}{sinh\sqrt{\frac{I_z}{K}}h} sin\omega t \tag{A.25}$$

$$f = \frac{1}{2\pi}\sqrt{g\sqrt{\frac{I_z}{K}}tanh\sqrt{\frac{I_z}{K}}h} \tag{A.26}$$

Natural frequencies of rectangular and cylindrical tanks, by using Equation A.26 with only calculating their specific I_z and K integrals, can be found.

The pressure in the fluid is found as

$$\frac{\partial p}{\partial z} = -\rho\dot{w} \tag{A.27}$$

$$\frac{\partial p}{\partial x} = -\rho\dot{u} \tag{A.28}$$

$$p = -\rho\frac{\partial\ddot{\theta}}{\partial y}(-\int\frac{Q}{b}dx + \frac{z^2}{2}\frac{b'}{b^2}Q) \tag{A.29}$$

$$Q = \int_{-R}^{x} xbdx \tag{A.30}$$

The natural frequency of rectangular tank with unit width are found by finding its rectangular tank specific I_z and K values as follows

$$I_z = \int_{-l}^{+l} x^2 dx = \frac{2}{3} l^2 \tag{A.31}$$

$$K = 2 \int_{-l}^{+l} 2(\int_{-l}^{+l} \frac{x}{2} dx)^2 = \frac{4}{15} l^5 \tag{A.32}$$

By substituting I_z and K for rectangular tank into Equation A.26, we will have first natural frequency as follows

$$\omega^2 = \sqrt{\frac{5}{2}} \frac{g}{l} tanh \sqrt{\frac{5}{2}} \frac{h}{l} \tag{A.33}$$

$$f = \frac{1}{2\pi} (\sqrt{\frac{5}{2}} \frac{g}{l} (tanh \sqrt{\frac{5}{2}} \frac{h}{l})) \tag{A.34}$$

For the cylindrical tank, I_z and K are found as

$$I_z = \frac{\pi R^4}{4} \tag{A.35}$$

$$K = \frac{2\pi}{27} R^6 \tag{A.36}$$

By putting I_z and K into Equation A.26, the first natural frequency of cylindrical tank can be found below

$$\omega^2 = \frac{g}{R}\sqrt{\frac{27}{8}} tanh \sqrt{\frac{27}{8}}\frac{h}{R} \tag{A.37}$$

$$f = \frac{1}{2\pi}(\frac{g}{R}\sqrt{\frac{27}{8}}(tanh\sqrt{\frac{27}{8}}\frac{h}{R})) \tag{A.38}$$

APPENDIX B: MATHEMATICAL DERIVATION OF SLOSHING MOTION FOR RECTANGULAR AND CYLINDRICAL TANKS

B.1. Sloshing Motion in Rectangular Tank

B.1.1. Governing equation

In this section, the sloshing motion in rectangular tank will be physically and mathematically explained and as a result the natural frequency that is obtained by Abramson in 1966 is going to be found [1]. For the mathematical derivation part, the quantity of "velocity potential" will be employed. The velocity potential can be basically denoted as

$$\vec{V} = \nabla\Phi \tag{B.1}$$

where V is the fluid velocity.

Ibrahim [8] declares that for reaching analytical solution of sloshing motion's function easily, the fluid can be assumed as inviscid, incompressible and irrotational. Also, he considers that the tank is rigid.

For physical explanation of sloshing motion, we will start by examining the volume of an infitesimal parallelpiped fluid particle as it is shown below.

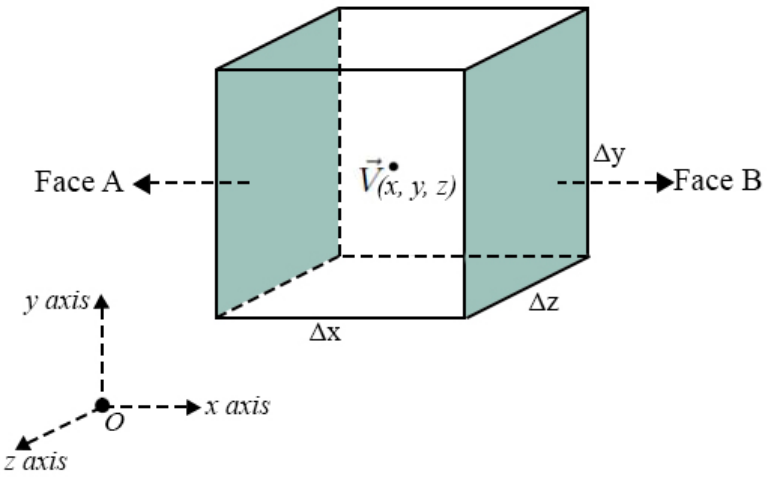

Figure B.1. Representation of infinitesimal parallelpiped fluid particle. Adapted from [6].

Since the fluid is incompressible, the volume of the fluid does not change. This means that the mass goes in and the mass goes out should be the same amount, in other words, the mass should be conserved and thus the density, ρ, should be constant. For reaching solution, another assumption should be made which is "the acceleration is constant". By this assumption, nonlinear terms in Taylor expansion series are ignored. Since the volume that is investigated is really small, it is a logical assumption.

As it can be seen from Figure B.1, the velocity in the middle of the parallelpiped volume is denoted as $\vec{V}(x, y, z)$ where it includes the fluid velocity in x,y and z directions as

$$\vec{V}(x, y, z) = u\hat{x} + v\hat{y} + w\hat{z} \tag{B.2}$$

At Face A and B, the velocities are

$\vec{V_A} : u - \frac{\partial u}{\partial x}\frac{\Delta x}{2}$ where $\frac{\partial u}{\partial x}$ is the rate of change of u with respect to x coordinate and $\frac{\Delta x}{2}$ is the distance from center to the Face A.
$\vec{V_B} : u + \frac{\partial u}{\partial x}\frac{\Delta x}{2}$ where $\frac{\partial u}{\partial x}$ is the rate of change of u with respect to x coordinate and $\frac{\Delta x}{2}$ is the distance from center to the Face B.

Mass flux on Face A: $\rho(u - \frac{\partial u}{\partial x}\frac{\Delta x}{2})$
Mass flux on Face B: $\rho(u + \frac{\partial u}{\partial x}\frac{\Delta x}{2})$

Since the net mass flux is the difference between fluxes which goes into the volume and leaves the volume, it can be denoted as

$$Netflux = \rho(u - \frac{\partial u}{\partial x}\frac{\Delta x}{2}) - \rho(u + \frac{\partial u}{\partial x}\frac{\Delta x}{2}) = -2\rho\frac{\partial u}{\partial x}\frac{\Delta x}{2} = -\rho\frac{\partial u}{\partial x}\Delta x \tag{B.3}$$

Equation B.3 represents the mass per unit area and time. To find the mass accumulation in x direction which is the mass per unit time, Equation B.3 is multiplied by area on Face A and B that both have the same area.

$$(Netflux)(Netarea) = (-\rho\frac{\partial u}{\partial x}.\Delta x)(\Delta y.\Delta z) \tag{B.4}$$

In order to find "total mass accumulation" in x, y, and z directions, the same steps are done in y and z directions and the results are summed

$$= (-\rho \cdot \frac{\partial u}{\partial x} \cdot \Delta x)(\Delta y \cdot \Delta z) + (-\rho \cdot \frac{\partial v}{\partial y} \cdot \Delta y)(\Delta x \cdot \Delta z) + (-\rho \cdot \frac{\partial w}{\partial z} \cdot \Delta z)(\Delta y \cdot \Delta x) = 0$$

$$= -\rho \cdot \Delta x \cdot \Delta y \cdot \Delta z \cdot (\frac{\partial u}{\partial x} + \frac{\partial v}{\partial y} + \frac{\partial w}{\partial z}) = 0$$

Thus

$$(\frac{\partial u}{\partial x} + \frac{\partial v}{\partial y} + \frac{\partial w}{\partial z}) = 0 \tag{B.5}$$

where $u = \frac{\partial \Phi}{\partial x}$, $v = \frac{\partial \Phi}{\partial y}$, $w = \frac{\partial \Phi}{\partial z}$

As a result, Equation B.5 can be written as

$$\frac{\partial^2\Phi}{\partial x^2} + \frac{\partial^2\Phi}{\partial y^2} + \frac{\partial^2\Phi}{\partial z^2} = 0 or \nabla^2\Phi = 0 \tag{B.6}$$

$$\nabla^2\Phi = 0 \tag{B.7}$$

which both Equation B.6 and Equation B.7 are the Laplace's equations.

The governing equation of fluid in rectangular tank is found as "Laplace's equation".

Since we pay attention to the modes of oscillation, we choose the form of function, Φ, as standing waves with pure sinusoidal time dependence

$$\Phi(x, y, z, t) = \Psi(x, y, z).cos(wt) \tag{B.8}$$

When we insert Ψ instead of Φ, we have

$$\frac{\partial^2 \Psi}{\partial x^2} + \frac{\partial^2 \Psi}{\partial y^2} + \frac{\partial^2 \Psi}{\partial z^2} = 0 \tag{B.9}$$

Equation B.9 is the final version of governing equation. By solving B.9, the general solution is found. For having a specific solution, the boundary conditions should be defined.

B.1.2. Boundary Conditions

The boundary conditions are defined on tank's boundaries and the free surface of the fluid. A simple representation of a rectangular tank can be seen below

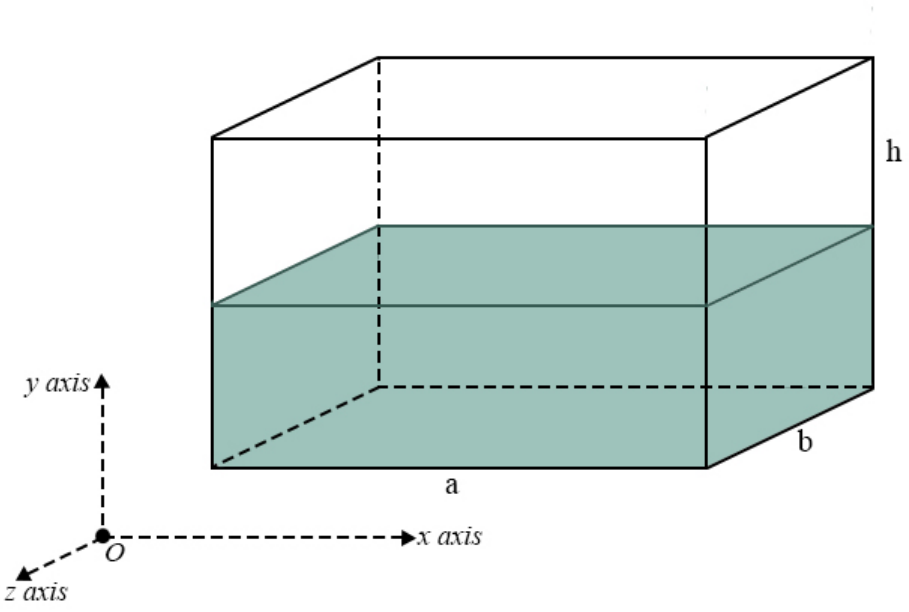

Figure B.2. Simple representation of a rectangular tank. Adapted from [6].

On tank's bottom, the fluid particles' velocity is zero on the directions normal to the bottom surface. The reason is that the fluid can not move into this rigid surface. Likewise, on tank's walls, the fluid particles' velocity on the directions normal to the tank wall surface is zero due to same reason. These boundary conditions are expressed as follows

$$\frac{\partial \Phi}{\partial z}(x, y, 0, t)\Big|_{z=0} = 0 \tag{B.10}$$

$$\frac{\partial \Phi}{\partial x}(0, y, z, t)\Big|_{x=0} = \frac{\partial \Phi}{\partial x}(a, y, z, t)\Big|_{x=a} = 0 \tag{B.11}$$

$$\frac{\partial \Phi}{\partial y}(x, 0, z, t)\Big|_{y=0} = \frac{\partial \Phi}{\partial y}(x, b, z, t)\Big|_{y=b} = 0 \tag{B.12}$$

The boundary conditions are valid for the situation of unforced sloshing of the free surface. If we would look for sloshing during ground is shaking, we would have different boundary conditions. Thus, in our case, the tank is not shaked at the moment, but the free surface is sloshing.

The boundary conditions that are related to the free surface of fluid are defined over a kinematical analysis. The velocity in the direction of z can be written as $\frac{\partial \eta}{\partial t}$ from the Figure B.3 below.

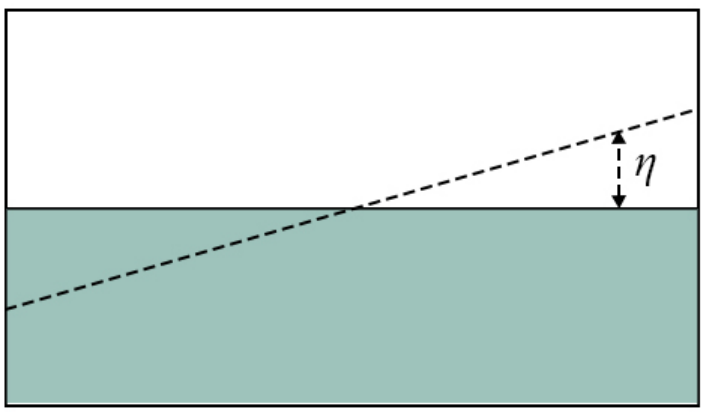

Figure B.3. Side view of the rectangular tank during sloshing. Adapted from [6].

In addition, as it can be seen from the boundary conditions above, the velocity of z component can also be written as $\frac{\partial \Phi}{\partial z}$. Thus, since these two expressions both denote the velocity in z direction, we can say that

$$-\frac{\partial \eta}{\partial t} + \frac{\partial \Phi}{\partial z} = 0 \tag{B.13}$$

Another equation that we can derive from the free surface comes from Bernoulli's principle. As it is known, time dependent Bernoulli's principle is

$$\frac{\partial \Phi}{\partial t} + \frac{1}{2}V^2 + \frac{p}{\rho} + gz = 0 \tag{B.14}$$

where V is the velocity, p is the gage pressure, ρ is density, and g is gravitational acceleration. Since the wave heights are considered as small, the square term of the velocity can be neglected, and as a result, we can use linear theory to define the motion. In addition, since we consider we have only ambient pressure (the other are neglected), the gage pressure is zero. After taken these two assumptions into account, Equation B.14 becomes

$$\frac{\partial \Phi}{\partial t} + gz = 0 \tag{B.15}$$

After reaching Equation B.15, we take the derivative of it with respect to time

$$\frac{\partial^2 \Phi}{\partial t^2} + \frac{\partial z}{\partial t}g = 0 \tag{B.16}$$

Also we multiply Equation B.13 with gravitational acceleration

$$-\frac{\partial \eta}{\partial t}g + \frac{\partial \Phi}{\partial z}g = 0 \tag{B.17}$$

Since both $\frac{\partial z}{\partial t}$ and $\frac{\partial \eta}{\partial t}$ give the velocity in z direction, in Equation B.16 we can write $\frac{\partial \eta}{\partial t}$ instead of $\frac{\partial z}{\partial t}$. After applying this substituion and sum Equation B.16 and B.17 with each other, we have

$$\frac{\partial^2 \Phi}{\partial t^2} + \frac{\partial \Phi}{\partial z} g = 0 \tag{B.18}$$

Equation B.18 is the boundary condition that comes from the surface of the fluid. Since we have both the governing equation and the boundary conditions, we can start solving the differential equation.

B.1.3. Solving the Differential Equation

We begin by assuming a solution as

$$\Psi(x, y, z) = X(x)Y(y)Z(z) \tag{B.19}$$

When Equation B.19 is put into the Laplace's equation

$$\frac{\partial^2 X(x)}{\partial x^2} Y(y)Z(z) + X(x)\frac{\partial^2 Y(y)}{\partial y^2} Z(z) + X(x)Y(y)\frac{\partial^2 Z(z)}{\partial z^2} = 0 \tag{B.20}$$

Dividing B.20 by X(x).Y(y).Z(z) gives us

$$\frac{\partial^2 X(x)}{\partial x^2}\frac{1}{X(x)} + \frac{\partial^2 Y(y)}{\partial y^2}\frac{1}{Y(y)} + \frac{\partial^2 Z(z)}{\partial z^2}\frac{1}{Z(z)} = 0 \tag{B.21}$$

$$\frac{\partial^2 X(x)}{\partial x^2}\frac{1}{X(x)} + \frac{\partial^2 Y(y)}{\partial y^2}\frac{1}{Y(y)} = -\frac{\partial^2 Z(z)}{\partial z^2}\frac{1}{Z(z)} \tag{B.22}$$

X(x), Y(y), and Z(z) are all independent variables and due to this fact both sides of the Equation B.22 should be a constant. If they are not constants, but variables, then X(x), Y(y), and Z(z) would be dependent on each other. As a result, we take both sides of Equation B.22 as constants.

Let's start with choosing right hand side of the Equation B.22 as constant. The constant can be zero, positive or negative. If the positive constant is the choice;

$$-\frac{\partial^2 Z(z)}{\partial z^2}\frac{1}{Z(z)} = k^2 \tag{B.23}$$

$$\frac{\partial^2 Z(z)}{\partial z^2} + k^2 Z(z) = 0 \tag{B.24}$$

Differential Equation B.24 has the solution in the form of

$$Z(z) = Acos(kz) + Bsin(kz) \tag{B.25}$$

where A and B are constants. This solution does not represent the fluid behaviour that we are expecting. In other words, we do not expect sloshing motion to be a pure trigonometric function, instead, the velocity of fluid should decay by the time passes.

In the case of negative constant;

$$-\frac{\partial^2 Z(z)}{\partial z^2}\frac{1}{Z(z)} = -k^2 \tag{B.26}$$

$$\frac{\partial^2 Z(z)}{\partial z^2}\frac{1}{Z(z)} = k^2 \tag{B.27}$$

$$\frac{\partial^2 Z(z)}{\partial z^2} - k^2 Z(z) = 0 \tag{B.28}$$

The solution Equation B.28 is

$$Z(z) = Ae^{kz} + Be^{-kz} \tag{B.29}$$

Equation B.29 is a solution that we expect for sloshing motion since the exponential term in the equation causes the decay of the fluid's velocity during sloshing.

In the case of "zero" as constant;

$$-\frac{\partial^2 Z(z)}{\partial z^2}\frac{1}{Z(z)} = 0 \tag{B.30}$$

$$\frac{\partial^2 Z(z)}{\partial z^2} = 0 \tag{B.31}$$

$$\frac{\partial Z(z)}{\partial z} = Cz \tag{B.32}$$

$$Z(z) = Cz + d \tag{B.33}$$

For Equation B.33, there are 2 cases. First one is the case that $C = 0$. In this situation, $Z(z) = d$ is our equation. This means the velocity potential, Φ, is constant along z, and there is no motion in z direction. Second one is the case that $C \neq 0$. This situation means that the velocity potential linearly changes with respect to z height.

As a result, we choose the case of negative constant where it is the expected scenario.

When we put negative constant into Equation B.22, we have

$$\frac{\partial^2 X(x)}{\partial x^2}\frac{1}{X(x)} + \frac{\partial^2 Y(y)}{\partial y^2}\frac{1}{Y(y)} = -k^2 \tag{B.34}$$

As it was mentioned previously, X(x) and Y(y) are indepedent variables, and that is why they should be constant in Equation B.34. Since we expect to have wave motion on the surface of fluid, we should have trigonometric form for X(x) and Y(y). In order to have these forms for X(x) and Y(y) variables, we will choose negative constants;

$$\frac{\partial^2 X(x)}{\partial x^2}\frac{1}{X(x)} = -v^2 \tag{B.35}$$

$$\frac{\partial^2 X(x)}{\partial x^2} + X(x)v^2 = 0 \tag{B.36}$$

The solution of differential equation B.36 is;

$$X(x) = Ccos(vx) + Dsin(vx) \tag{B.37}$$

where C and D are arbitrary constants.

For the variable of Y(y);

$$-k^2 - \frac{\partial^2 Y(y)}{\partial y^2}\frac{1}{Y(y)} = -v^2 \tag{B.38}$$

If we define that

$$l^2 = k^2 - v^2 \tag{B.39}$$

then

$$\frac{\partial^2 Y(y)}{\partial y^2}\frac{1}{Y(y)} = -l^2 \tag{B.40}$$

$$\frac{\partial^2 Y(y)}{\partial y^2}\frac{1}{Y(y)} + l^2 Y(y) = 0 \tag{B.41}$$

The solution of B.41 becomes

$$Y(y) = Ecos(ly) + Fsin(ly) \tag{B.42}$$

where E and F are arbitrary constants.

Since we have the form of general solution for X(x), Y(y) and Z(z), in the next step, we will apply defined boundary conditions.

We start by applying the first boundary condition, in other words the Equation B.10
$\frac{\partial \Phi}{\partial z}(x, y, 0, t) = 0$
$\frac{\partial \Phi}{\partial z}(x, y, 0, t) = \frac{\partial \Psi}{\partial z}(x, y, 0)cos(wt) = 0$

Thus
$\frac{\partial \Psi}{\partial z}(x, y, 0) = 0$
X(x)Y(y)$\frac{\partial \Psi}{\partial z}(z = 0)$;
$\frac{\partial \Psi}{\partial z}(z = 0) = 0$;
$\frac{\partial \Psi}{\partial z}(z) = Ake^{kz} - Bke^{-kz}$;

for $z = 0$
$Ak - Bk = 0$
$A = B$

Therefore
Z(z)=Acosh(kz)

We apply the second boundary condition; Equation B.11

$\frac{\partial \Phi}{\partial x}(0, y, z, t) = \frac{\partial \Phi}{\partial x}(a, y, z, t) = 0$

$\frac{\partial \Phi}{\partial x}(x, y, z, t) = Dvcos(vx) - Cvsin(vx);$

for $x = 0$

$Dvcos(0) - Cvsin(0) = 0;$

$Dv = 0,\ D = 0$

for $x = a$

$Dvcos(va) - Cvsin(va) = 0$

$Cvsin(va) = 0;$

$va = m\pi$ where $m = 0, 1, 2, 3...;$

$v = \frac{m\pi}{a}$

Thus

$X(x) = Ccos(\frac{m\pi}{a}x)$

Applying the third boundary condition; Equation B.12

$\frac{\partial \Phi}{\partial y}(x, 0, z, t) = \frac{\partial \Phi}{\partial y}(x, b, z, t) = 0$

Then

$\frac{\partial Y(y)}{\partial y}(y) = 0$ for $y = 0$ and $y = b;$

$\frac{\partial \Phi}{\partial y}(y) = Flcos(ly) - Elsin(ly)$

for $y = 0$

$Flcos(0) - Elsin(0) = 0$

$Fl = 0$, then $F = 0$

for $y = b$

$-Elsin(lb) = 0$

$lb = n\pi$ where $n = 0, 1, 2, 3...$

$l = \frac{n\pi}{b}$

Thus

$Y(y) = Ecos(\frac{n}{b})$

Since we already have X(x), Y(y), and Z(Z), we can write $\Psi(x, y, z)$ as follows

$\Psi(x, y, z) = X(x)Y(y)Z(z)$

$\Psi(x, y, z)_{m,n} = cos(\frac{m}{a})cos(\frac{n}{b})cosh(kz)$

We apply the fourth boundary condition; Equation B.18

$\frac{\partial^2\Phi}{\partial t^2}(x, y, z, t) + g\frac{\partial\Phi}{\partial z} = 0$

Let's put $\Phi(x, y, z, t) = \Psi(x, y, z)cos(wt)$ into the equation

$-w^2cos(wt)\Psi(x, y, z) + gcos(wt)\frac{\partial\Psi}{\partial z} = 0$

Dividing both sides by cos(wt)

$-w^2\Psi(x, y, z) + g\frac{\partial\Psi}{\partial z} = 0$

Putting $\Psi(x, y, z) = X(x)Y(y)Z(z)$ into the equation

$-w^2X(x)Y(y)Z(z) + gX(x)Y(y)\frac{\partial Z(z)}{\partial z} = 0$

Dividing both sides by X(x)Y(y)

$-w^2 Z(z) + g\frac{\partial Z(z)}{\partial z} = 0$

$\frac{\partial Z(z)}{\partial z} = Aksinh(kz)$

Putting Z(z) and $\frac{\partial Z(z)}{\partial z}$ into the equation

$-w^2 Acosh(kz) + gAksinh(kz) = 0$

$w^2 Acosh(kz) = gAksinh(kz)$

Cancelling A's out

$w^2 = gktanh(kz)$

$w = \sqrt{gktanh(kz)}$

In addition

$2 = w$

$f = \frac{w}{2\pi}$

Thus

$f = \sqrt{gktanh(kz)}\frac{1}{2\pi}$

where $k^2 = v^2 + l^2$ and $v = \frac{m\pi}{a}$, $l = \frac{n\pi}{b}$

Let's put k into the equation where $k = \pi\sqrt{\frac{m^2}{a^2} + \frac{n^2}{b^2}}$;

$f_{m,n} = \sqrt{gktanh(kz)}\frac{1}{2\pi}$

B.2. Sloshing Motion in Cylindrical Tank

B.2.1. Governing Equation

In this section, the sloshing motion in cylindrical tank is explained. Since the physical explanation part of sloshing motion in cylindrical tank is the same with rectangular one, it is skipped, but the mathematical derivation of it is completed.

For cylindrical tank, again, the governing equation is Laplace's equation. Since the tank is a cylinder, cylindrical coordinate is more useful to choose. Laplace's equation in cylindrical coordinates can be seen as follows

$$\frac{1}{r}\frac{\partial}{\partial r}(r\frac{\partial f}{\partial r}) + \frac{1}{r^2}\frac{\partial^2 f}{\partial^2 r} + \frac{\partial^2 f}{\partial^2 z} = 0 \tag{B.43}$$

With cylindrical coordinates, the form of velocity potential is chosen as

$$\Phi(r, \theta, z, t) = \Psi(r, \theta, z)cos(wt) \tag{B.44}$$

When we put Equation B.44 into Equation B.43, we have

$$\frac{1}{r}.\frac{\partial}{\partial r}(r\frac{\partial}{\partial r}(\Psi(r, \theta, z)cos(wt)) + \frac{1}{r^2}\frac{\partial^2}{\partial^2 r}(\Psi(r, \theta, z)cos(wt)) + \frac{\partial^2}{\partial^2 z}(\Psi(r, \theta, z)cos(wt)) = 0 \tag{B.45}$$

Equation B.45 is our general governing equation in cylindrical coordinates. By solving this equation, we can examine the fluid behaviour with respect to r, θ, and z values. To reach more specific solutions, we define the boundary conditions.

B.2.2. Boundary Conditions

For the bottom of the tank, due to same reasons, the boundary condition is the same with rectangular one;

$$\frac{\partial \Phi}{\partial z}(r, \theta, 0, t)\Big|_{z=0} = 0 \tag{B.46}$$

For the tank's wall, in the direction of surface's normal, the velocity is zero, since the fluid can not flow into the rigid surface. Thus, the boundary condition is

$$\frac{\partial \Phi}{\partial r}(a, \theta, z, t)\Big|_{r=a} = 0 \tag{B.47}$$

where a is the radius of the cylindrical tank's wall.

The boundary condition on the free surface is the same with rectangular tank except the fact that the velocity potential function is not in cartesian coordinates, but in cylindrical coordinates, as it can be seen below

$$\frac{\partial^2 \Phi(r, \theta, z)}{\partial t^2} + \frac{\partial \Phi(r, \theta, z)}{\partial z} g = 0 \tag{B.48}$$

In the next step, the boundary conditions will be applied to the general governing equation.

B.2.3. Solving the Differential Equation

We start solving the differential equation by assuming a form for the velocity potential function, Φ, as follows

$$\Phi(r,\theta,z) = \Psi(r,\theta,z)cos(wt) = R(r)\Theta(\theta)Z(z)cos(wt) \tag{B.49}$$

Since $cos(wt)$ does not change with respect to r, θ, and z, we focus on

$$\Psi(r,\theta,z) = R(r)\Theta(\theta).Z(z) \tag{B.50}$$

When we put Equation B.50 into Equation B.45, we have

$$\frac{1}{r}\frac{\partial}{\partial r}(r\frac{\partial R}{\partial r}) + \frac{1}{r^2}RZ\frac{\partial^2\Theta}{\partial^2\theta} + R\Theta.\frac{\partial^2 Z}{\partial^2 z} = 0 \tag{B.51}$$

After dividing both sides of B.51 to R(r)$\Theta(\theta)$Z(z), the equation becomes

$$\frac{1}{rR}\frac{\partial}{\partial r}(\frac{\partial R}{\partial r}) + \frac{1}{r^2\theta}\frac{\partial^2\Theta}{\partial^2\theta} + \frac{\partial^2 Z}{\partial^2 z}\frac{1}{Z} = 0 \tag{B.52}$$

$$\frac{1}{rR}.\frac{\partial}{\partial r}(\frac{\partial R}{\partial r}) + \frac{1}{r^2\theta}\frac{\partial^2\Theta}{\partial^2\theta} = -\frac{\partial^2 Z}{\partial^2 z}\frac{1}{Z} \tag{B.53}$$

Since we accept r, θ, and z as independent variables, both sides of Equation B.53 should be equal to a constant. If it would not, and equal to a variable, r, θ, and z would be dependent on each other. Like in the case of the rectangular tank, for choosing a constant, we have the options of positive, negative constants and zero.

In the case of positive constant

$$-\frac{\partial^2 Z}{\partial z^2}\frac{1}{Z} = l^2 \tag{B.54}$$

$$\frac{\partial^2 Z}{\partial z^2} + l^2 Z = 0 \tag{B.55}$$

The solution of differential equation of B.55 is

$$Z(z) = Acos(lz) + Bsin(lz) \tag{B.56}$$

where A and B are constants. Since we are not expecting a pure sinusoidal movement of fluid with constant magnitude, we will keep looking for a logical answer.

In the case of negative constant

$$-\frac{\partial^2 Z}{\partial z^2}\frac{1}{Z} = -l^2 \tag{B.57}$$

$$\frac{\partial^2 Z}{\partial z^2} - l^2 Z = 0 \tag{B.58}$$

The solution of Equation B.58 is in the form of

$$Z(z) = Ae^{lz} + Be^{-lz} \tag{B.59}$$

where A and B are constants. Since in z direction we expect decaying of fluid's velocity, Equation B.59 looks reasonable.

In the case of zero as constant

$$-\frac{\partial^2 Z}{\partial z^2}\frac{1}{Z} = 0 \tag{B.60}$$

$$\frac{\partial^2 Z}{\partial z^2} = 0 \tag{B.61}$$

$$\frac{\partial Z}{\partial z} = Cz \tag{B.62}$$

$$Z(z) = Cz + d \tag{B.63}$$

When we examine Equation B.63, we see that we have two options; $C = 0$ and $C \neq 0$. For $C = 0$, $Z(z) = d$, the velocity potential is constant and its derivative is zero. For $C \neq 0$, Z(z) has linear dependency on z. Both of these cases are not suitable to the behaviour of fluid in z direction.

As a result, among 3 options of constants where these are positive, negative constants and zero, the negative option is the most suitable choice for our case.
Since we decide to use negative constant, when we put it into Equation of B.53, we have

$$\frac{1}{rR}\frac{\partial}{\partial r}(r\frac{\partial R}{\partial r}) + \frac{1}{r^2\Theta}\frac{\partial^2\Theta}{\partial^2\theta} = -l^2 \tag{B.64}$$

$$\frac{r}{R}\frac{\partial}{\partial r}(r\frac{\partial R}{\partial r}) + \frac{1}{\Theta}\frac{\partial^2\Theta}{\partial^2\theta} = -l^2r^2 \tag{B.65}$$

$$\frac{r}{R}\frac{\partial}{\partial r}(r\frac{\partial R}{\partial r}) + l^2r^2 = -\frac{1}{\Theta}\frac{\partial^2\Theta}{\partial^2\theta} \tag{B.66}$$

Since r, θ, and z are independent variables, again, both sides of Equation B.66 should be chosen as constants.

In the direction of θ, instead of decaying of fluid's velocity, we expect to see a sinusoidal wave motion. Thus, for $\Theta(\theta)$, we choose negative constant;

$$\frac{1}{\Theta}\frac{\partial^2\Theta}{\partial^2\theta} = -n^2 \tag{B.67}$$

$$\frac{\partial^2\Theta}{\partial^2\theta} = -^2 \tag{B.68}$$

$$\frac{\partial^2\Theta}{\partial^2\theta} + ^2 = 0 \tag{B.69}$$

The solution of differential equation B.69 is as follows

$$\Theta(\theta) = Ccos(n\theta) + Dsin(n\theta) \tag{B.70}$$

where C and D are arbitrart constants.

Since there are not any boundary conditions in θ direction, Equation B.70 is the last point that we have reached for the function of $\Theta(\theta)$.

When we put the constant for θ, we have

$$\frac{r}{R}\frac{\partial}{\partial r}(r\frac{\partial R}{\partial r}) + l^2r^2 = n^2 \tag{B.71}$$

$$\frac{r}{R}\frac{\partial}{\partial r}(r\frac{\partial R}{\partial r}) = (n^2 - l^2r^2)R \tag{B.72}$$

$$\frac{r}{R}\frac{\partial}{\partial r}(r\frac{\partial R}{\partial r}) + R(l^2r^2 - n^2) = 0 \tag{B.73}$$

When we arrange Equation B.73, we see that it is very similar to the "Bessel Differential Equation" that we already know how to solve

$$r^2\frac{\partial^2 R}{\partial^2 r} + r\frac{\partial R}{\partial r} + R(l^2r^2 - n^2) = 0 \tag{B.74}$$

As it is known, Bessel Differential Equation has the form of

$$x^2\frac{\partial^2 y}{\partial^2 x} + x\frac{\partial y}{\partial x} + y(x^2 - a^2) = 0 \tag{B.75}$$

where a is a constant.

To make Equation B.74 in the form of Equation B.75, we denote that $x = rl$, and thus, $r = \frac{x}{l}$ and $dr = \frac{dx}{l}$. As a result, Equation B.74 will be as follows

$$x^2\frac{\partial^2 R}{\partial^2 x} + x\frac{\partial R}{\partial x} + R(x^2 - n^2) = 0 \tag{B.76}$$

Equation B.76 is a Bessel function that we can define as our governing differential equation for R. In order to solve it, we will employ "series solution" in the following form

$$R(x) = \sum_{m=0}^{\infty} a_m x^{k+m} = 0 \tag{B.77}$$

where $a_0 \neq 0$

$$\frac{\partial R(x)}{\partial r} = \sum_{m=0}^{\infty} a_m (k+m) x^{k+m-1} \tag{B.78}$$

$$\frac{\partial^2 R(x)}{\partial^2 r} = \sum_{m=0}^{\infty} a_m (k+m)(k+m-1) x^{k+m-2} \tag{B.79}$$

When we insert R(x) into Equation B.76, we have

$$\sum_{m=0}^{\infty} a_m(k+m)(k+m-1)x^{k+m}+\sum_{m=0}^{\infty} a_m(k+m)x^{k+m}+\sum_{m=0}^{\infty} a_m x^{k+m+2}-\sum_{m=0}^{\infty} a_m n^2 x^{k+m}=0 \tag{B.80}$$

The terms in Equation B.80 consist of x^{k+m} and x^{k+m+2}. To have all the terms in the same form, we change x^{k+m} and x^{k+m+2} by doing some changes in the series. We will do this by putting $m = 0$ and $m = 1$ into x^{k+m} terms, so we will be able to begin the series with $m = 2$. By doing this, we benefit from the fact that the series that starts with $m = 0$ and have the terms of $(k + m + 2)$ will be equal to the series that starts with $m = 2$ and have the terms of $(k + m)$. The mathematical representation of this explanation can be found below as

$$\sum_{m=2}^{\infty} a_m = \sum_{m=0}^{\infty} a_{m+2} \tag{B.81}$$

For $m = 0$;

$$a_0(k)(k-1)x^k + a_0kx^k - a_0n^2x^k = 0 \tag{B.82}$$

$$a_0x^k[k^2 - n^2] = 0 \tag{B.83}$$

where $a_0 \neq 0$

From Equation B.83, since $a_0 \neq 0$ and we need to satisfy the equation, we see that $k^2 = n^2$ can be a true assumption. Thus, from now on, we take $k = n$.

For $m = 1$;

$$a_0(k+1)(k)x^{k+1} + a_1(k+1)x^{k+1} - a_1n^2x^{k+1} = 0 \tag{B.84}$$

$$a_1x^{k+1}[(k+1)^2 - n^2] = 0 \tag{B.85}$$

To satisfy Equation B.85, $(k+1)^2$ should be equal to n^2 or a_1 should be zero. When the equation is examined it is seen that m should be a fractional number and since according to definition of Bessel equation m has to be an integer, $(k+1)^2 = n^2$ can not used. Another reason that this equation can not be used is that k is equal to n. Thus, since $(k+1)^2$ is not equal to n^2, a_1 should be equal to zero.

After these changes, the new form of Equation B.80 is

$$\sum_{m=0}^{\infty}[a_{m+2}(n+m+2)(n+m+1)+a_{m+2}(n+m+2)+a_m-a_{m+2}n^2]x^{n+m+2}=0 \quad \text{(B.86)}$$

Since $x=0$ will give us a trivial solution, we will equate the terms inside the brackets to the zero;

$[a_{m+2}(n+m+2)(n+m+1)+a_{m+2}(n+m+2)+a_m-a_{m+2}n^2]=0$

$a_{m+2}[(n+m+2)(n+m+1)+(n+m+2)-n^2]=-a_m$

$a_{m+2}[(m+2)(m+2+2n)]=-a_m$

In order to find the relationship between series' terms, we will find them in terms of a_0. In addition, since $a_1=0$, a_3, a_5, a_7,...a_{2m+1} are equal to zero. Thus, we look at the relationship between a_0 and a_2, a_4, a_6,...a_{2m} terms.

For $m=0$;

$a_2=\frac{-a_0}{2(2n+2)}$

For $m=2$;

$a_4=\frac{-a_2}{4(2n+4)}$

Then

$a_4=\frac{a_0}{2\cdot4(2n+2)(2n+4)}$

For $m=4$;

$a_6=\frac{-a_4}{6(2n+6)}$

Then

$a_6 = \frac{a_0}{2\cdot4\cdot6(2n+2)(2n+4)(2n+6)}$

Thus

$a_{2m} = \frac{(-1)^m a_0}{2\cdot4\cdot6\cdots(2m)(2n+2)(2n+4)(2n+2m)}$

$$a_{2m} = \frac{(-1)^m a_0}{1\cdot2\cdot3\cdots m2^m(n+1)(n+2)(n+3)...(n+m)2^m} \tag{B.87}$$

After the right hand side of Equation B.87 is rearranged, a_{2m} will be

$$a_{2m} = \frac{(-1)^m a_0 n!}{2^{2m}m!(m+n)!} \tag{B.88}$$

As a result,

$R(x) = \sum_{m=0}^{\infty} a_m x^{k+m}$ becomes

$R(x) = a_0 2^n n![\frac{1}{n!} + \frac{x^2}{2^2\cdot1!(n+1)!} + \frac{x^4}{2^4\cdot2!(n+2)!}....]$

$$R(x) = a_0 2^n n! \sum_{m=0}^{\infty} \frac{(-1)^m}{m!(n+m)!}(\frac{x}{2})^{2m+n} \tag{B.89}$$

Equation B.89 is the series expansion around $x = 0$ of the first order Bessel Equation and it is shown as $J_n(x)$. Thus, Equation B.89 can be shown as

$R(x) = a_0 2^n n! J_n(x)$

However, since we defined R in terms of r, we need to use $x = rl$ to solve this problem. We will do this by writing rl instead of x;

$R(r) = a_0 2^n n! J_n(rl)$

We apply the boundary condition of the tank's wall, Equation B.47;
$\frac{\partial \Phi}{\partial r}(a, \theta, z, t) = 0$

After cancelling cos(wt) terms, Equation B.47 becomes
$\frac{\partial \Psi}{\partial r}(a, \theta, z) = 0$
$\frac{\partial \Psi}{\partial r} = \frac{\partial R}{\partial r} = 0$

Then,
$\frac{\partial R}{\partial r}(a, \theta, z) = 0$
where $\frac{\partial R}{\partial r} = a_0 2^n n! \frac{\partial J_n}{\partial r}$

Thus,
$\frac{\partial (J_n(al))}{\partial r} = 0$

Since the derivative of Bessel functions that equal to zero can not be found analytically, we will find it by numerical analysis. We define a variable to represent these points and assign it to the symbol of $\alpha_m(n)$

$\alpha_m(n)$: m'th positive root of the equation $\frac{\partial(J_n(rl))}{\partial r} = 0$

From the equation $\frac{\partial(J_n(al))}{\partial r} = 0$, we reach that
$al = \alpha_m(n)$, $l = \frac{\alpha_m(n)}{a}$

Thus
$R(r) = GJ_n(\frac{r\alpha_m(n)}{a})$ where G is an arbitrary constant.

Also, we use equation of $l = \frac{\alpha_m(n)}{a}$ in the solution of Z(z), since it includes l, as well. As it was declared before, Z(z) is

$Z(z) = Acos(lz) + Bsin(lz)$
where A and B are constants.

When we insert $l = \frac{\alpha_m(n)}{a}$ into the solution of Z(z), it will become
$Z(z) = Acos(\frac{\alpha_m(n)}{a}z) + Bsin(\frac{\alpha_m(n)}{a}z)$

We apply the boundary condition of the tank's bottom surface, Equation B.46;

$\frac{\partial\Phi}{\partial z}(r, \theta, 0) = 0$
$\frac{\partial(R)}{\partial z} = 0$
$R.\Theta\frac{\partial Z}{\partial z} = 0$
$\frac{\partial Z}{\partial z}(r, \theta, 0) = 0$
$A.le^{lz} - Ble^{-lz} = 0$ for $z = 0$
$A - B = 0$, $A = B$

Thus
$Z(z) = Acos(lz)$ where $l = \frac{\alpha_m(n)}{a}$

$Acosh(\frac{\alpha_m(n)z}{a})$

As a result, the general governing equation will be as follows

$$\Psi(r,\theta,z) = R(r)\Theta(\theta)Z(z) \tag{B.90}$$

$$\Psi(r,\theta,z) = J_n(\frac{r\alpha_m(n)}{a})(Ccos(n\theta) + Dsin(n\theta))cosh(\frac{\alpha_m(n)z}{a})) \tag{B.91}$$

We apply the boundary condition that comes from the free surface, Equation B.48;

$\frac{\partial^2\Phi(r,\theta,z)}{\partial t^2} + \frac{\partial\Phi(r,\theta,z)}{\partial z}g = 0$
$-w^2\Psi(r,\theta,h) + g\frac{\partial\Psi}{\partial z}(r,\theta,h) = 0$
$w^2R(r)\Theta(\theta)Z(h) + gR(r)\Theta(\theta)\frac{\partial Z}{\partial z}(h) = 0$

After we cancel $R\Theta$ terms, we have
$w^2 = g\frac{1}{Z(h)}\frac{\partial Z(h)}{\partial z}(h)$
where $\frac{\partial Z(h)}{\partial z}(h) = sinh(\frac{\alpha_m(n)h}{a})\frac{\alpha_m(n)}{a}$
$w^2_{m,n} = gtanh(\frac{\alpha_m(n)h}{a})\frac{\alpha_m(n)}{a}$

In addition,
$f2\pi = w$
$f = \frac{w}{2\pi}$

As result, the equation for eigenfrequencies is

$$f_{m,n} = \frac{1}{2\pi}\sqrt{gtanh(\frac{\alpha_m(n)h}{a})(\frac{\alpha_m(n)}{a})} \tag{B.92}$$

APPENDIX C: MATHEMATICAL DERIVATION OF SLOSHING MOTION FOR MSC NASTRAN

In MSC Nastran, to model the fluid behaviour during sloshing motion, the virtual mass method is used with some assumptions which accompany to the method, such as irrotational fluid and inviscid flow [4]. In the next section, before explaining the virtual mass method in detail, these assumptions are going to be clarified. For all the assumptions that are explained below the study of Robinson [4] is utilized.

C.1. Assumptions

C.1.1. Incompressibility

When the velocity of the fluid much is lower than the sound's speed, the fluid can be considered as incompressible. In Nastran, since the velocity of the fluid that is used in the analyses is way lower than the speed of sound, the fluid is assumed as incompressible. In addition, incompressibility assumption can also be made for the fluids with uniform and constant density which means that there no layers of various fluids. Again, in Nastran, since the fluids have uniform and constant density, this assumption is made.

C.1.2. Small Displacements

The displacements of the fluid particles are considered as small compared to characteristic dimensions of the body analyzed, such as height and length of a tank. This assumption matches with the linear finite element theory and thus the nonlinear terms are able to be ignored during the calculations.

C.1.3. Inviscid Flow

The assumption of inviscid flow denotes that in fluid the viscosity effects are neglected. It is a fair assumption for the fluids which have low viscosity behaviours, such as water and petrol. In this study, the fluid that is contained in the tank is taken as water and since the thickness of the layer that viscosity effects are seen is small compared to the body's characteristic dimensions, such as its height and length, the viscosity effects of water are ignored with keeping in our mind that still a small amount of error will exist.

C.1.4. Irrotational Flow

The assumption of irrotational flow indicates that any fluid particle in the fluid domain is not rotating, and there is no any turbulence. Uniform density and irrotational flow assumptions help us to employ potential flow theory that is governing theory of the mathematical derivation of sloshing motion in Nastran.

C.1.5. Free surface

The pressure at the free surface of the fluid is assumed as zero.

C.1.6. Surface Waves and Gravitational Effects

With virtual mass method, the surface wave effects and the gravitational effects are ignored.

C.2. Mathematical Derivation of Virtual Mass Method

Before examining the "Virtual Mass Method in Nastran", it is good to give some information about the concept of "Virtual Mass".

C.2.1. The concept of Virtual Mass

The virtual mass concept is defined for the first time by Friedrich Bessel in order to define a pendulum's movement inside the fluid [37]. This study had the aim of comparing a moving body in a fluid with a moving body in a vacuum. For the case of a body in a vacuum, the body can move freely without experiencing an additional force that is caused by the fluid particles moving around the body whereas for a moving body in a fluid the body will experience this additional force. As a result, to move an object in a fluid more force is needed compare to move a body in a vacuum. By taking Newton's 2nd law, $F = ma$, into account, it can be said that for the case with vacuum since there is no any additional force, the situation can be represented with the equation of $F = ma$ whereas for the case with fluid there is an additional force and it can be seen in terms of the virtual mass of the body in the fluid as $(F + F_{additional}) = (m + m_{virtual})a$

To reach the virtual mass, the additional force -in other words the hydrodynamic force- can be employed through integrating the pressure over the body in the x-direction. For giving an instance, a figure of a cylinder inside the fluid under the effect of additional force and the derivation of virtual mass for a cylinder are shown below.

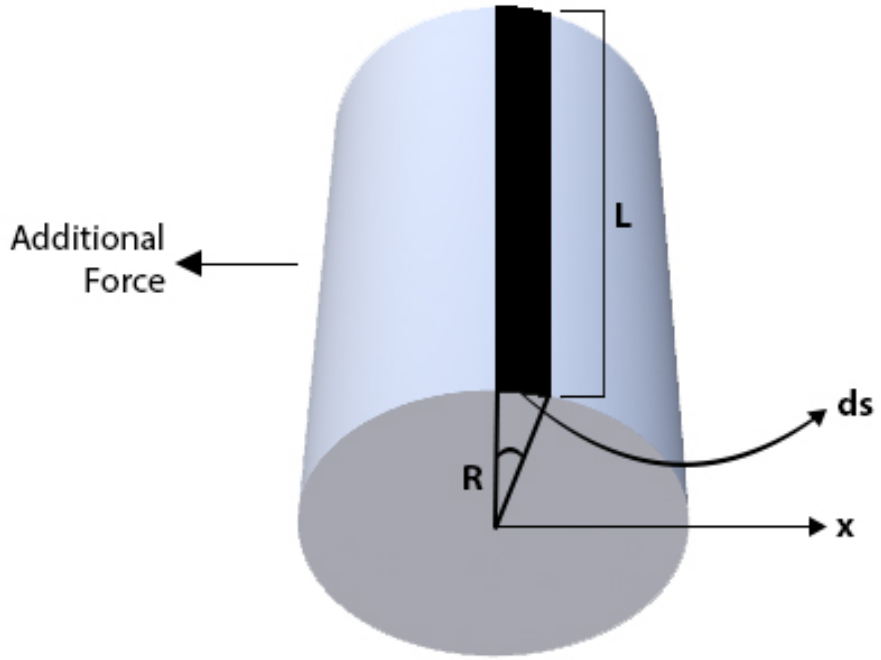

Figure C.1. An accelerated cylinder in a fluid under the effect of additional force

By referring to Figure C.1, for a cylinder of length L, and radius R which accelerates at $\dot{U}$, the hydrodynamic force in the x-direction is:

$$\vec{F}_x = \int P d\vec{A}_x$$

where

$d\vec{A}_x = cos\theta dA$

$dA = Lds$

$ds = Rd\theta$

For unsteady flow, unsteady Bernoulli equation will be used as

$P = -\rho[\frac{\partial \phi}{\partial t} + \frac{1}{2}|\vec{\nabla}\phi|^2]$

where

$\phi = U\frac{R^2}{r}cos\theta$ refers to potential flow for flow around the cylinder

$\frac{\partial \phi}{\partial t}\big|_{r=R} = \dot{U}\frac{R^2}{r}cos\theta = \dot{U}Rcos\theta$

$\frac{1}{2}|\nabla\phi|^2\big|_{r=R} = \frac{1}{2}|(-U\frac{R^2}{r^2}cos\theta), -U\frac{R^2}{r^2}sin\theta|^2 = \frac{1}{2}U^2$

From the equations above it can be concluded that

$F_x = \int_0^{2\pi}[-\rho[\frac{\partial \phi}{\partial t} + \frac{1}{2}|\vec{\nabla}\phi|^2]]cos\theta RLd\theta$

$F_x = \int_0^{2\pi}[-\rho[\dot{U}Rcos\theta + \frac{1}{2}U^2]]cos\theta RLd\theta$

$= -\rho(RL)(\dot{U}R)\int_0^{2\pi} cos^2\theta d\theta - \rho(RL)\frac{1}{2}U^2\int_0^{2\pi} cos\theta d\theta$

$= -\rho\pi R^2 L\dot{U}$

where $\dot{U}$ denotes acceleration of the object. In addition, opposite sign shows that the hydrodynamic force is in the opposite direction of the body's movement. This hydrodynamic force can be represented in terms of "virtual mass" as

$m_a = \rho\pi R^2 L$

After giving an information about the concept of virtual mass, the derivation of "Virtual Mass Method in Nastran" can now be explained. The derivation of this method starts with the law of "mass conversation".

C.2.2. Mass Conservation

Since it is assumed that we have incompressible fluid, the mass should be conserved. Let's consider a volume V that is surrounded by surface S as it can be seen in the figure below

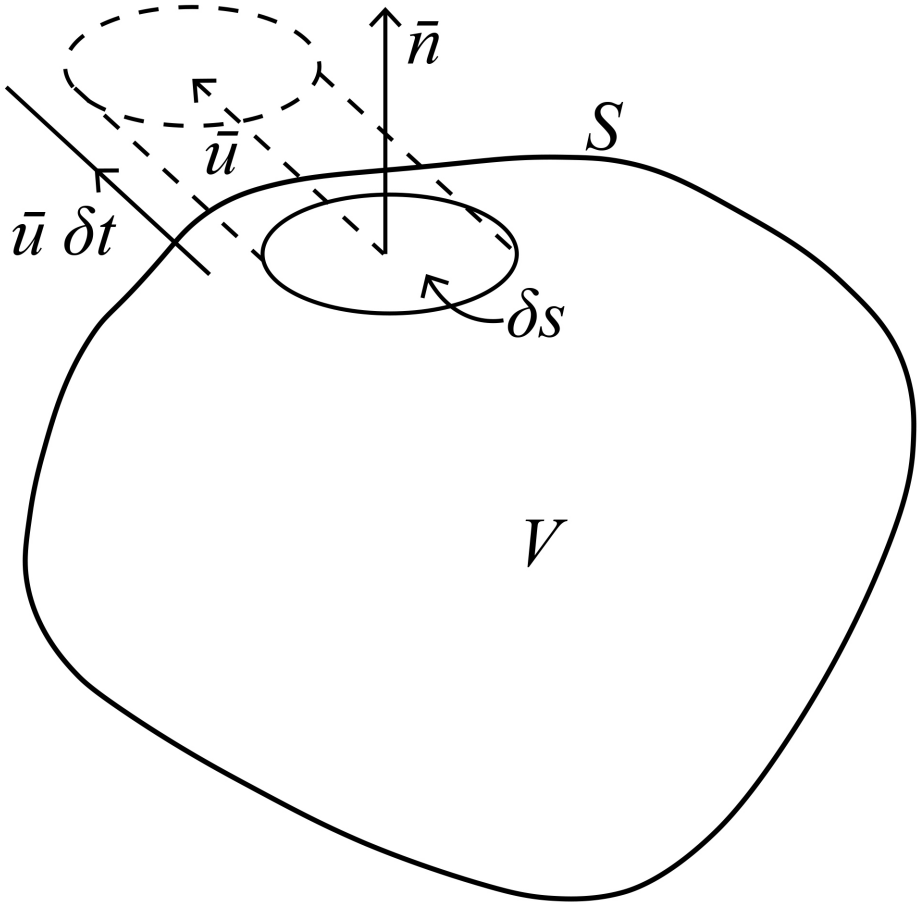

Figure C.2. Representation of the fluid volume V surrounded by surface S. Adapted from [4]

As it can be seen in Figure C.2, the surface S has the unit normal of $\bar{n}$. Due to conservation of mass law, the mass that goes into the volume and the mass goes out from that volume should be equal to each other. Let's consider the idea of having a fluid flowing through unit surface δs, in the direction of $\bar{u}$ with the density of ρ, in unit time δt. With these terms, the fluid particle's volume which passes through δs would be

$(\bar{n}\delta s).(\bar{u}\delta t)$

and the mass of that fluid particle is

$\rho.(\bar{n}\bar{u}).(\delta s\delta t)$

When the mass is divided by time, the mass passing through in unit time is found as $\rho.(\bar{n}\bar{u}).(\delta s)$

To find the mass flowrate for all over the surface S, we integrate the equation above over S as follows
$\int_S \rho.(\bar{n}\bar{u}).(\delta s)$

The mass can also be found by integrating the multiplication of density and unit volume over all volume V
$\int_V \rho.dV$

Since the mass is conserved, it can be said that flowrate and rate of change of mass are equal to each other

$$\int_V \frac{\partial \rho}{\partial t} dV = -\int_S \rho.(\bar{n}\bar{u}).ds \tag{C.1}$$

By using divergence theorem, we can change the surface integral of Equation C.1 to a volume integral

$$\int_V \frac{\partial \rho}{\partial t} dV = -\int_V \nabla(\rho \bar{u}) dV \tag{C.2}$$

If it is assumed that the integrands of the Equation C.2 are continuous

$$\frac{\partial \rho}{\partial t} + \nabla(\rho \bar{u}) = 0 \tag{C.3}$$

To examine the time rate of change of density, firstly the function of density will be shown as

$$\rho = \rho(x, y, z, t) \tag{C.4}$$

where the density is the function of position and time. During the change of unit time, δt, the position of the particle also changes (x, y, z) to $(x + \delta x, y + \delta y, z + \delta z)$ and unit density, $\delta \rho$, becomes

$$\delta \rho = \frac{\partial \rho}{\partial t}.\delta t + \frac{\partial x}{\partial t}.\delta x + \frac{\partial y}{\partial t}.\delta y + \frac{\partial z}{\partial t}.\delta z \tag{C.5}$$

However, when the fluid is tracked by an observer who has the same velocity of the fluid, Equation C.5 becomes

$$\frac{d\rho}{dt} = \frac{\partial \rho}{\partial t} + \frac{\partial x}{\partial t}\frac{dx}{dt} + \frac{\partial y}{\partial t}\frac{dy}{dt} + \frac{\partial z}{\partial t}\frac{dz}{dt} \tag{C.6}$$

It can be noticed that Equation C.6 involves the fluid velocity as

$$\bar{u}(u,v,w) = (\frac{dx}{dt}, \frac{dy}{dt}, \frac{dz}{dt}) \tag{C.7}$$

Putting Equation C.7 into Equation C.6 gives

$$\frac{d\rho}{dt} = \frac{\partial \rho}{\partial t} + u.\frac{\partial x}{\partial t} + v.\frac{\partial y}{\partial t} + w.\frac{\partial z}{\partial t} \tag{C.8}$$

From Equation C.8, it can be basically written as

$$u.\frac{\partial x}{\partial t} + v.\frac{\partial y}{\partial t} + w.\frac{\partial z}{\partial t} = \bar{u}.\nabla\rho \tag{C.9}$$

Then, Equation C.9 becomes

$$\frac{d\rho}{dt} = \frac{\partial \rho}{\partial t} + \bar{u}.\nabla\rho \tag{C.10}$$

Usually left hand side of Equation C.10 is written as $\frac{D\rho}{Dt}$ and it is called "Material derivative" or "Lagrangian derivative". From the differentiation rule of Leibniz, it can be denoted that

$$\nabla.(\rho\bar{u}) = \bar{u}.\nabla\rho + \rho\nabla.\bar{u} \tag{C.11}$$

When Equation C.11 is put into Equation C.3

$$\frac{\partial \rho}{\partial t} + \bar{u}.\nabla\rho + \rho\nabla.\bar{u} = 0 \tag{C.12}$$

Putting Equation C.11 into Equation C.12

$$\frac{D\rho}{Dt} + \rho\nabla.\bar{u} = 0 \tag{C.13}$$

When the assumptions of incompressible fluid and constant density are applied, the outcome is

$$\frac{D\rho}{Dt} = 0 \tag{C.14}$$

Thus, Equation C.13 gives

$$\nabla.\bar{u} = 0 \tag{C.15}$$

From Equation C.15, it can be understood that for incompressible fluid, the velocity field is not diverged and the mass is conserved.

In addition, when the assumption of irrotational flow is applied, the velocity potential can be expressed as

$$\bar{u} = \nabla\phi \tag{C.16}$$

Putting C.16 into C.15 gives

$$\nabla.\nabla\phi = 0 \tag{C.17}$$

The last equation above yields to Laplace's Eqaution which is the general governing equation for incompressible, inviscid and irrotational fluid

$$\nabla^2\phi = 0 \tag{C.18}$$

From the derivation above, it can be concluded that for a tank which contains fluid, Nastran uses the Laplace's Equation as a governing equation.

As it is known, the concept of virtual mass leans on the effects due to fluid-structure interaction [37]. In the parallel way, for Nastran, virtual mass method is created to model the fluid that has interaction with the boundary of the structure in dynamic analysis, and therefore, in Nastran, it is found a way that describes the fluid's movement by using its structural boundary [4].

Using the velocity potential function which comes from the potential flow theory gives the chance of knowing the possible movement of the fluid at any position of fluid volume if the fluid has a preconcert behaviour on the boundary. In Nastran, this idea is employed by locating a source at the centre of the structure's finite element meshes that has interaction with fluid and the response of this source is measured at the center of other finite element meshes which has interaction with the same fluid volume, in addition, the selected source type is located on a pulsating sphere's exterior surface [4]. Even though the structural elements are not spheres, in order to calculate the acoustic field of a pulsating source type which its wavelength is significantly bigger than the dimensions of source, it is a good estimation [38].

In Cartesian coordinates, the Laplace equation can be seen as

$$(\nabla.\nabla)\phi = \frac{\partial^2\phi}{\partial x^2} + \frac{\partial^2\phi}{\partial y^2} + \frac{\partial^2\phi}{\partial z^2} \tag{C.19}$$

In order to make things easier, by taking advantage of sphere's axisymmetric shape, spherical coordinates are used for solving Laplace equation. In Figure below, both cartesian and spherical coordinates are demonstrated

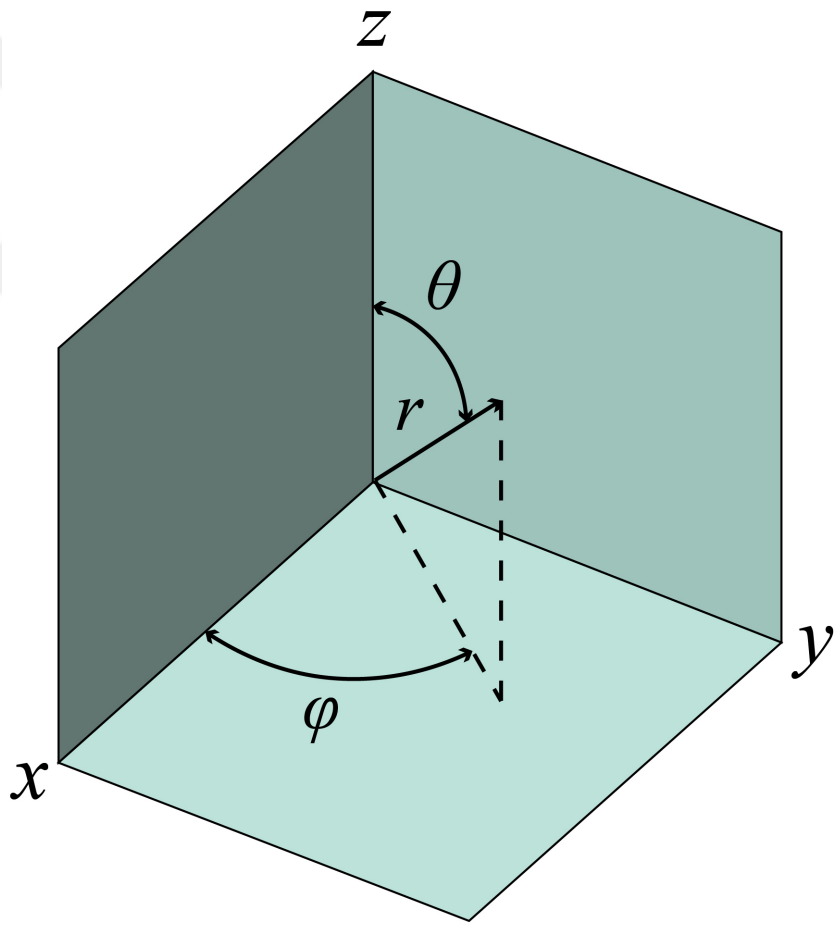

Figure C.3. Cartesian and Spherical Coordinates. Adapted from [4]

For transformation between cartesian and spherical coordinates, it can be used that

$x = rsin\vartheta cos\varphi$

$y = rsin\vartheta sin\varphi$

$z = rcos\vartheta$

Thus, the Laplace Equation in spherical coordinates is

$$(\nabla.\nabla)\phi = \frac{1}{r^2}\frac{\partial}{\partial r}(r^2\frac{\partial\phi}{\partial r}) + \frac{1}{r^2 sin\vartheta}\frac{\partial}{\partial\vartheta}(sin\vartheta\frac{\partial\phi}{\partial\vartheta}) + \frac{1}{r^2 sin^2\vartheta}\frac{\partial^2\phi}{\partial\varphi^2} \tag{C.20}$$

To solve the Laplace's equation, the separation of variables method is used. The velocity potential which is assumed as the function of independent variables, r, ϑ, and φ is written as

$$\Phi(r,\vartheta,\varphi) = R(r).P(\vartheta).Q(\varphi) \tag{C.21}$$

Putting Equation C.21 into Equation C.20 and multiplying it both sides with $\frac{r^2}{\phi}$ gives

$$(\nabla.\nabla)\phi = \frac{1}{R}\frac{\partial}{\partial r}(r^2\frac{\partial R}{\partial r}) + \frac{1}{Psin\vartheta}\frac{\partial}{\partial\vartheta}(sin\vartheta\frac{\partial P}{\partial\vartheta}) + \frac{1}{Qsin^2\vartheta}\frac{\partial^2 Q}{\partial\varphi^2} = 0 \tag{C.22}$$

As it can be noticed, Equation C.22 consists of 2 parts which are with only variable of r and only variables of ϑ and φ. In order to satisfy Laplace equation, these 2 parts should be equal to a constant, similar to the case that is done in for "mathematical derivation of sloshing motion for rectangular and cylindrical tanks". For the part that consists of r variable, the constant of $n(n+1)$ is chosen, for its easiness where n is chosen as zero or positive integer. Thus

$$\frac{1}{R}\frac{d}{dr}(r^2\frac{dR}{dr}) = n(n+1) \tag{C.23}$$

Inserting Equation C.23 into Equation C.22 and multiplying both sides of it with $sin^2\vartheta$ yields

$$n(n+1)sin^2\vartheta + \frac{sin\vartheta}{P}\frac{d}{d\vartheta}(sin\vartheta\frac{dP}{d\vartheta}) + \frac{1}{Q}\frac{d^2Q}{d\varphi^2} = 0 \tag{C.24}$$

Like the situation in the beginning, the equation that is reached above still consists of 2 parts; the distinct parts of ϑ and φ. Once more, these 2 parts should be equal to constants to satify Laplace's equation. Thus, for the part with variable ϑ, m^2 is chosen as constant.

$$n(n+1)sin^2\vartheta + \frac{sin\vartheta}{P}\frac{d}{d\vartheta}(sin\vartheta\frac{dP}{d\vartheta}) = m^2 \tag{C.25}$$

After reorganizing Equation to have polar dependence, C.25, the following equation is reached

$$[n(n+1)sin^2\vartheta - m^2]P + sin\vartheta\frac{d}{d\vartheta}(sin\vartheta\frac{dP}{d\vartheta}) = 0 \tag{C.26}$$

Solving Equation C.23 gives

$$R(r) = Ar^n + Br^{-(n+1)} \tag{C.27}$$

To have an easier problem, axisymmetric case of pulsating sphere is chosen and this choice leads to

$$\frac{\partial \phi}{\partial \varphi} = 0 \tag{C.28}$$

where it makes the constant $m = 0$. Thus, Equation C.26 becomes

$$n(n+1)sin^2\vartheta P + sin\vartheta \frac{d}{d\vartheta}(sin\vartheta \frac{dP}{d\vartheta}) = 0 \tag{C.29}$$

Putting $x = cos\varphi$ makes $f(\vartheta)$ as follows

$$\frac{df}{d\vartheta} = \frac{df}{dx}\frac{dx}{d\vartheta} = -sin\vartheta \frac{df}{dx} \tag{C.30}$$

In addition, it should be paid attention that

$$sin^2\vartheta = (1 - x^2) \tag{C.31}$$

Putting Equation C.31 and Equation C.30 into Equation C.29 yields

$$n(n+1)(1-x^2)P + (1-x^2)\frac{d}{dx}((1-x^2)\frac{dP}{dx}) = 0 \tag{C.32}$$

and after reorganizing Equation C.32

$$(1-x^2)\frac{d^2P}{dx^2} - 2x\frac{dP}{dx} + n(n+1)P = 0 \tag{C.33}$$

The equation above represents the Legendre's equation where there are polynomial solutions of order n for integral values of n. For $n = 0, 1, 2, 3$, Legendre polynomials, also acknowledged as $P_n(x)$ as well, are

$P_0(x) = 1$
$P_1(x) = x$
$P_2(x) = \frac{3x^2-1}{2}$
$P_3(x) = \frac{5x^3-3x}{2}$

After unifying the Legendre polynomials above with Equation C.28, solution to the Laplace for axisymmetric case is found as

$$\phi(r,\vartheta) = \sum_{n=0}^{\infty}[A_n.r^n + B_n r^{-(n+1)}]P_n(cos\vartheta) \tag{C.34}$$

A_n and B_n are the constants which change with respect to boundary conditions. Also, first few terms of these constants correspond to some physical meanings that A_n is associated with the solutions of sphere's inside whereas B_n is associated with the solutions external to the sphere.

For $n = 0$;

$$\phi(r, \vartheta) = A_0 r^0 + B_0 r^{-1} \tag{C.35}$$

where solutions for sphere's inside, A_0, is a constant as $r^0 = 1$, solutions external to the sphere, $\frac{B_0}{r}$, is a source or sink.

For $n = 1$;

$$\phi(r, \vartheta) = (A_1 r^1 + B_1 r^{-2}) cos\vartheta \tag{C.36}$$

where solutions for sphere's inside, $(A_1 r cos\vartheta)$, is a uniform stream solutions external to the sphere, $(\frac{B_1 cos\vartheta}{r^2})$, is a dipole at the origin.

In Nastran, approach of $n = 1$ is employed and B_1 used to represent a dipole at the finite element meshes' centre points. Also, since only the solutions exterior to the sphere are considered, A_n terms disappear. If B_1 is selected as the area of δs, then the displacement potential at the center of the element is

$$\phi_{\delta s} = \frac{cos\vartheta \delta s}{r^2} \tag{C.37}$$

The right hand side of Equation C.37 is known as “Solid Angle” [39]. To understand the solid angle method, starting point can be that thinking of a sphere which has a radius of r and onto this sphere the small area δs is projected as it can be seen in figure below

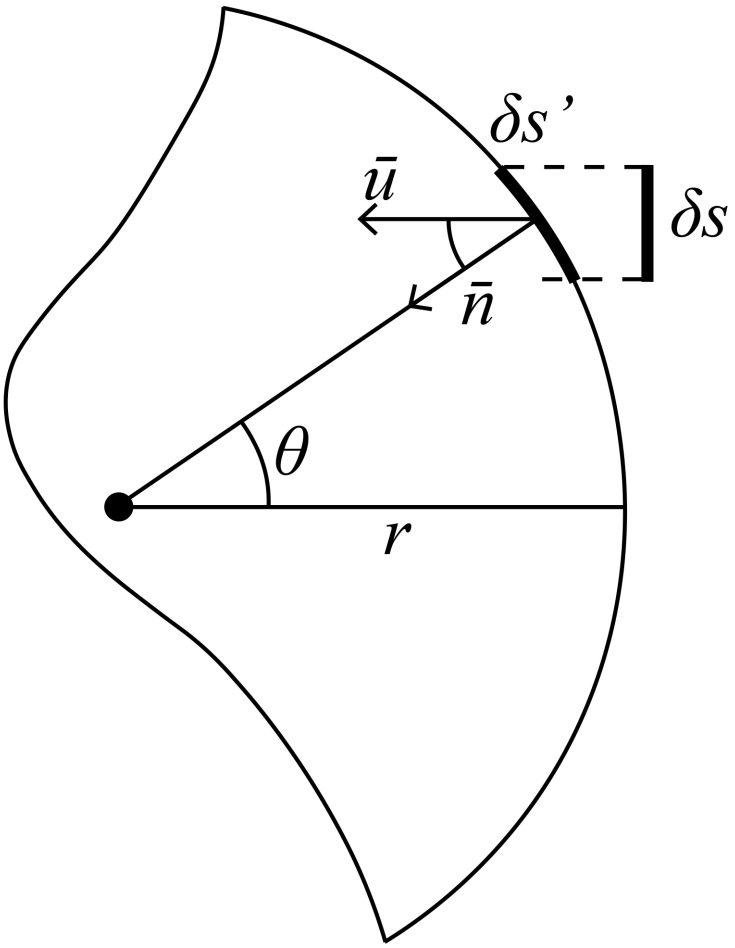

Figure C.4. Sphere of radius r for solid angle method. Adapted from [4]

The area of δs is inclined over the surface of the sphere with the angle of ϑ and the area of the inclined surface is named as $\delta s'$ where

$$\delta s' = cos\vartheta \delta s \tag{C.38}$$

Thus, the displacement potential becomes

$$\phi_{\delta s} = \frac{\delta s'}{r^2} \tag{C.39}$$

The quantity of $\frac{\delta s'}{r^2}$ can be calculated by using "spherical excess method". As it was demonstrated by Girard [40] that with this method the area of a triangle located on a sphere can be found. In Nastran, the shapes of the finite elements can be arbitrary but the edges of these elements should be straight [4]. Thus, in this case, the area of $\delta s'$ should have straight edges, as well. Since the smallest shape with straight edges is triangle, the explanation of the spherical excess method will start with a triangle and afterwards it will be extended to shapes with n vertices. First of all, the explanation of method begins with a triangle that can be seen in Figure C.5 below

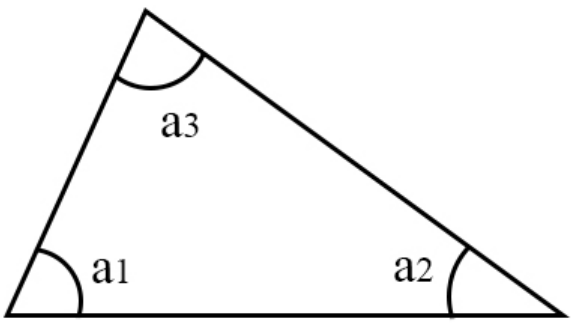

Figure C.5. A triangle with angles of a_1, a_2, a_3. Adapted from [4].

The summation of interior angle of the triangle that is seen in Figure C.5 is

$$\sum_{i=1}^{3} a_i = \pi \tag{C.40}$$

According to Thomas Harriot [41], if a triangle is projected onto a sphere's surface with the radius of r, as it can be seen in Figure C.6, the sum of interior angles is

$$\sum_i \alpha_i - \pi = \frac{A}{r^2} \tag{C.41}$$

where $i = 1, 2, 3$

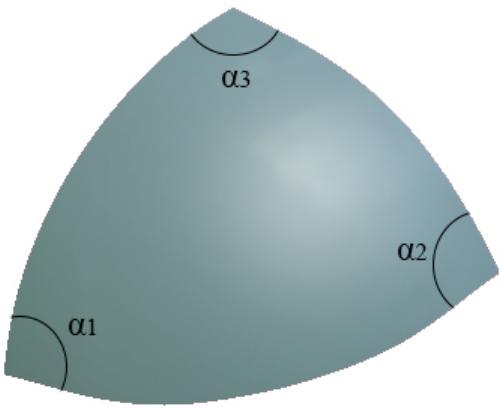

Figure C.6. A triangle projected onto a sphere with angles of $\alpha_1, \alpha_2, \alpha_3$. Adapted from [4].

Equation C.41 can be proved by using 3 great circles which crosses each other and creates the triangles on the sphere's surface as it is shown in Figure C.7

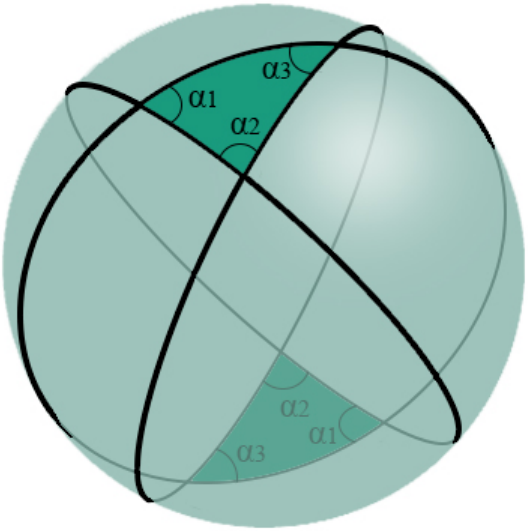

Figure C.7. A sphere crossed with 3 great circles which form 2 triangles on sphere's surface. Adapted from [4]

The sphere is separated into 6 pieces which have 2 sides for each. These shapes with 2 sides are called 2-gons. After separation by circles, 3 symmetrical pairs of 2-gons are formed. As it can be noticed from Figure C.7, 3 of the 2-gons go over the top spherical triangle whereas 3 of the 2-gons go over the bottom spherical triangle. This means, after dividing the sphere by 3 great circles, 2-gons go over the whole sphere for one time, but also go over each spherical triangle three times. The area of a sphere is $4\pi r^2$. In order to find the area of one of the 2-gons, this total area can be used. As it can be noticed from Figure C.8, the angle between 2 circles can be shown as α.

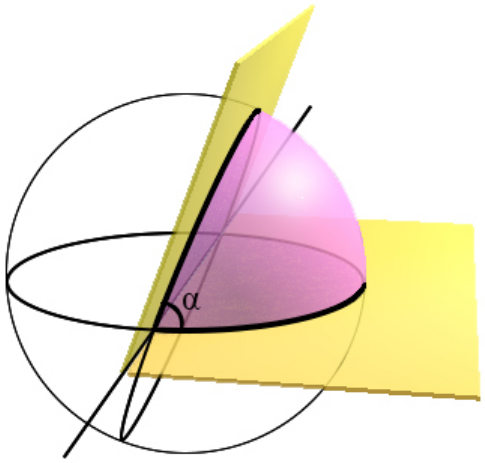

Figure C.8. The angle α between 2 great circles over the sphere. Adapted from [4].

To find the area of the 2-gon which has the angle of α between 2 circles, the equation below is used

$$\frac{\alpha}{2\pi}4\pi r^2 = 2\alpha r^2 \tag{C.42}$$

Since how to find a 2-gon's area is known, the area of 3 pairs of 2-gons can be found, as well. In Figure C.9, 2-gons with the angles of α_1, α_2, α_3 is shown as

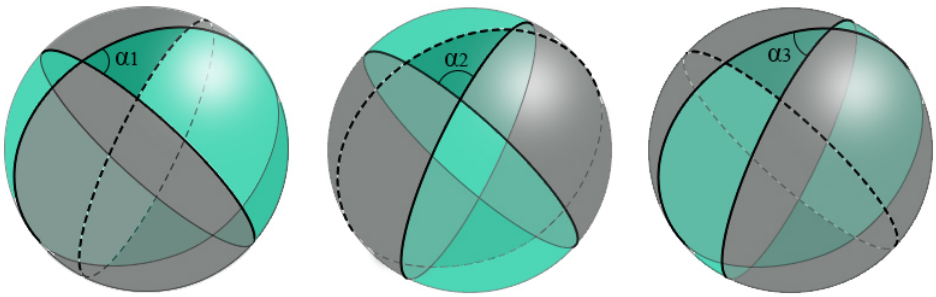

Figure C.9. 3 2-gons with the angles of α_1, α_2, and α_3. Adapted from [4].

The areas of these 2-gons are $2(2\alpha_1 r^2)$, $2(2\alpha_2 r^2)$, and $2(2\alpha_3 r^2)$, for 2-gons with angles of α_1, α_2, and α_3, respectively. These 3 pairs of 2-gons go all over the sphere's surface, and also go over each top and bottom triangles for 3 times. This means that top and bottom triangles are gone over for 6 times in total. However, since top and bottom triangles should be covered for twice in total, at the end, it is seen that these triangles are covered 4 times more than it should to be. Thus, the equation for the area calculation becomes

$$2(2\alpha_1 r^2) + 2(2\alpha_2 r^2) + 2(2\alpha_3 r^2) = 4\pi r^2 + 4A \tag{C.43}$$

Dividing Equation C.43 by $4r^2$ gives

$$\alpha_1 + \alpha_2 + \alpha_3 = \pi + \frac{A}{r^2} \tag{C.44}$$

and it yields to

$$\sum_i \alpha_i - \pi = \frac{A}{r^2} \tag{C.45}$$

where $i = 1, 2, 3$

Equation C.45 is reached for a triangle that is projected over a sphere. As it was declared before, this concept is extended to the shapes with n vertices.

$$\sum \alpha - (n-2)\pi = \frac{A}{r^2} \tag{C.46}$$

This equation is used for the partially immersed finite elements, as well [4]. In Figure C.10, the images of the wetted area of 2 triangle elements is shown

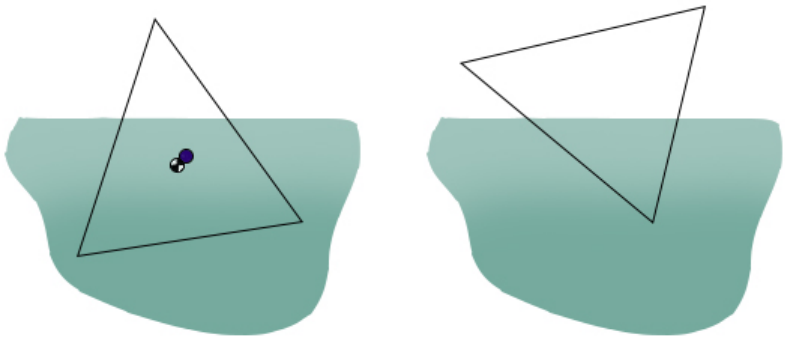

Figure C.10. 2 partially immersed triangle finite elements. Adapted from [4].

In Figure C.10, it is seen that the wetted part of the triangle on the left has 4 edges. In these situations, Nastran finds the centroid of the this part and its virtual mass effect only for the wetted surface on its calculations [4]. For quadrilateral ele-

ments in Nastran, 3 types of positioning of free surface are shown below

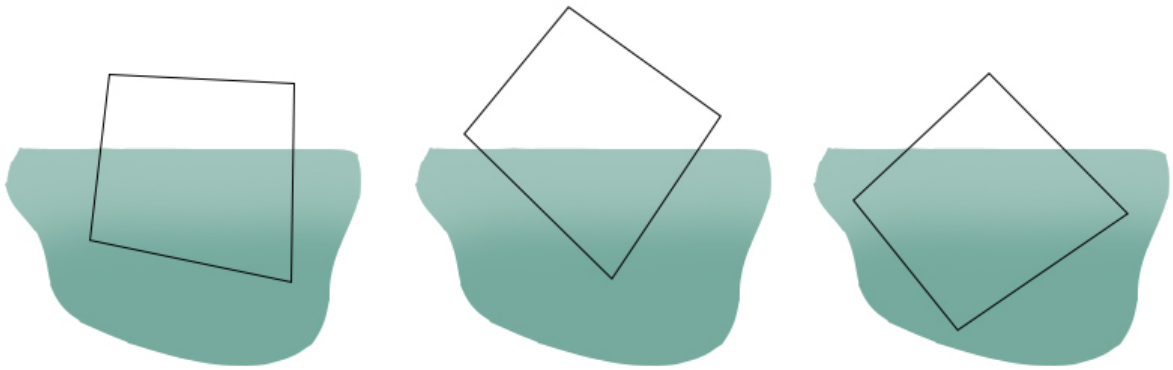

Figure C.11. 3 partially immersed quadrilateral finite elements. Adapted from [4]

From Figure C.11, it is seen that 3, 4, and 5 sides of wetted parts exist.

By examining the equations above for spherical excess, it can be denoted that the displacement potential can be found for the shapes with n vertices as

$$\phi = \sum \alpha - (n-2)\pi \tag{C.47}$$

The angle of α can be easily found by employing the vector algebra. Since the α is the angle between great circles which crosses the sphere, finding normals of circles' and finding the angle between normal vectors will give α.

C.2.3. Element Pressures

In Nastran, to calculate the element pressures, 2 integration methods which are exact and centre point integrations are in use and the choice of the method is provided by FMEXACT field of the MFLUID entry [30]. FMEXACT option is located in the

3rd field of MFLUID card and it is activated by putting the numbers inside the field. In Nastran Quick Reference Guide 2012 [30], how the required method is chosen by FMEXACT field is explained as "Exact integration is used if the distance between two elements is less than FMEXACT times the square root of the area of the larger element. Otherwise, center point integration is used by default. (Real; Default = 1.0E 15)".

The difference between exact and centre point integration in Nastran is that calculating virtual mass terms with exact integration is 5 times longer than the centre point integration, however, exact integration gives more accurate results than the centre point integration [4].

In Nastran, when the exact integration is used to obtain the element pressure, Equation C.16 is put into the momentum equation, $\rho\dot{\vec{u}} + \nabla p = 0$ and then it is integrated as

$$p = -\rho\dot{\phi} = -\rho\frac{\partial\phi}{\partial t} \tag{C.48}$$

where p is the pressure, ρ is the density, ϕ is the velocity potential, and t is the time [29]. When the centre point integration method is used, the following pressure formula is utilized

$$p_i = \int_{A_j} \frac{\rho\ddot{\sigma}_j}{|r_i - r_j|} dA_j \tag{C.49}$$

where $\ddot{\sigma}_j$ is the source at point j that is derived twice with respect to time [29]. To give a deeper understanding to Equation C.49, the background of the formula will be explained.

Nastran uses the approximate integral method which utilizes the superposition of fundamental solutions and these fundamental solutions are the sources and doublets which are distributed over the structural boundary [4]. Thus, the displacement potential can be written in terms of the sums of the sources' or doublets' strengths. In "Preliminary Design Document" of Nastran [29], by using displacement potential, the fluid displacement and pressure are found. The displacement potential of a 3D point source is be denoted as

$$\phi(\bar{r}_i) = -\frac{S_j}{|r_i - r_j|} \tag{C.50}$$

where S_j denotes the source strength at location of $\bar{r}_j$(with the unit of $volume/steradian$), and ϕ is calculated at $\bar{r}_i$. Also, $|r_i - r_j|$ defines the absolute distance value between point j and i. The strength for the sources distributed over the boundary per unit area, $\sigma(volume/area.steradian)$, is

$$\phi(\bar{r}_i) = -\int_{A_j} \frac{\sigma(\bar{r}_j) dA_j}{|\bar{r}_i - \bar{r}_j|} \tag{C.51}$$

The displacement of fluid becomes

$$u(\bar{r}_i) = \int_{A_j} \frac{\bar{e}_{ij}\sigma(\bar{r}_j)dA_j}{|\bar{r}_i - \bar{r}_j|^2} \tag{C.52}$$

where $\bar{e}_{ij}$ is a unit vector between j and i

$$\bar{e}_{ij} = \frac{(\bar{r}_i - \bar{r}_j)}{|\bar{r}_i - \bar{r}_j|} \tag{C.53}$$

Thus, Equation C.49 is reached below

$$p(\bar{r}_i) = \int_{A_j} \frac{\rho\ddot{\sigma}(\bar{r}_j)dA_j}{|\bar{r}_i - \bar{r}_j|} \tag{C.54}$$

As it can be noticed from the last equation that if $i = j$, the denominator of the equation becomes zero and it yields to singularity. To prevent this situation, a closed form solution of a circular disk is utilized. In this solution, for elements wetted on one side the pressure is taken as $\frac{16\rho}{3\sqrt{\pi}}A^{\frac{3}{2}}$ whereas for elements wetted on both sides the pressure is $4\pi\rho A$. However, instead of taking $\frac{16\rho}{3\sqrt{\pi}} = 3.009$, the value of 5.0 is taken in order to have better correlation.

C.2.4. Element Displacements

The application of FMEXACT for obtaining element displacements is very similar with the calculation of element pressures. For the distance between elements that is less than the FMEXACT times the square root of the element with the largest area, the method of Katzoff *et al.* [42] and Cohen [43] is used. This method leans on the Equation C.16. To solve this equation, a vortex's solution that is at the boundary of a closed surface is used. In the studies of Katzoff [42] and Cohen [43], it is shown that

total vortex through the surface's all boundary is equal to the velocity that is normal to the closed surface, and in Nastran, in order to calculate the velocity, vector algebra and Biot-Savart law are employed [4]. According to Biot-Savart law [44]

$$\bar{u} = \frac{\Gamma(d\vec{l} \times \vec{r})}{4\pi r^3} \tag{C.55}$$

where Γ is the strength of the vortex, and $d\vec{l}$ and $\vec{r}$ are unit vectors that are respectively in the direction of dl and r. The representation of vortex along boundary of the surface related to Biot-Savart law can be seen in figure below

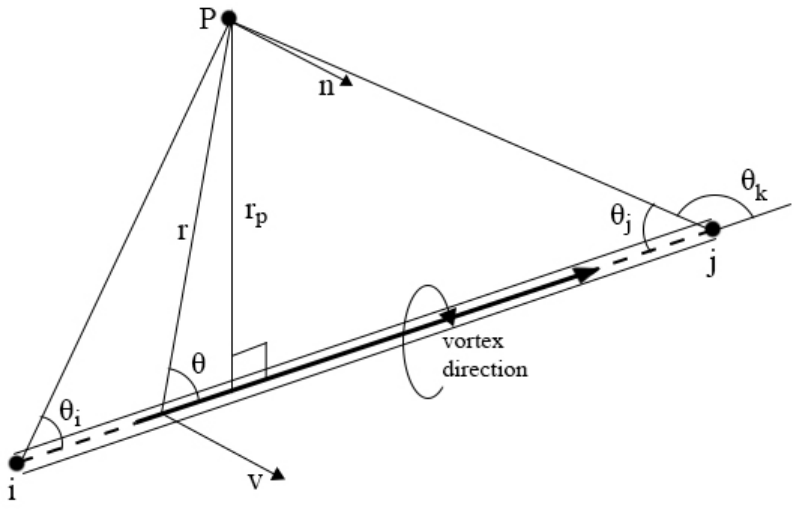

Figure C.12. Representation of vortex along boundary of the surface. Adapted from [4].

Thinking that there is fiber from i to j as it can be seen from Figure C.12, at the equation of $(d\vec{l} \times \vec{r})$, the vector v that is normal to the surface of (i,j,P) is reached

$$v = rsin\theta dl \tag{C.56}$$

Putting Equation C.56 into Equation C.55 gives the velocity at point P that has the direction of n normal to (i,j,P) surface.

$$\bar{u} = \frac{\Gamma r sin\theta dl}{4\pi r^3} = \frac{\Gamma sin\theta dl}{4\pi r^2} \tag{C.57}$$

Since the concern here is the velocity due to the potential, the constants are neglected

$$\bar{u} = \frac{sin\theta dl}{r^2} \tag{C.58}$$

From the geometry over (i,j,P) plane, it is seen that

$$r = \frac{r_p}{sin\theta} \tag{C.59}$$

and

$$r = \frac{dl}{cos\theta} \tag{C.60}$$

From Equation C.59 and C.60, it can be concluded that

$$\frac{dl}{cos\theta} = \frac{r_p}{sin\theta} \tag{C.61}$$

$$dl = r_p \frac{cos\theta}{sin\theta} = r_p cot\theta \tag{C.62}$$

When the derivative of dl with respect to angle θ is taken

$$\frac{dl}{d\theta} = \frac{d(r_p cot\theta)}{d\theta} \tag{C.63}$$

Then, it is reached

$$\frac{dl}{d\theta} = \frac{r_p d(cot\theta)}{d\theta} = -r_p csc^2\theta \tag{C.64}$$

$$dl = -r_p csc^2\theta d\theta \tag{C.65}$$

Inserting Equation C.59 and C.65 into Equation C.58 gives

$$\bar{u} = \frac{sin\theta(-r_p csc^2\theta d\theta)}{(\frac{r_p}{sin\theta})^2} = \frac{-r_p sin\theta(\frac{1}{sin^2\theta})d\theta}{(\frac{r_p^2}{sin^2\theta})} \tag{C.66}$$

Then,

$$\bar{u} = -\frac{sin\theta d\theta}{r_p} \tag{C.67}$$

After integrating Equation C.67 between θ_i and θ_k

$$\bar{u} = \frac{1}{r_p}\int_{\theta_i}^{\theta_k} -sin\theta d\theta = \frac{1}{r_p}(cos\theta_i - cos\theta_k) = \frac{1}{r_p}(cos\theta_i + cos\theta_j) \tag{C.68}$$

With the help of the vector algebra, the terms in Equation C.68 can be readily found.

For the distance between elements that is greater than the FMEXACT times the square root of the element with the largest area, the fluid displacement is found by using center point integration with the following Equation C.69 [29]. With this equation, the fluid displacement at a point source is measured by using the strength of source at another point

$$u(\bar{r}_i) = \int_{A_j} \frac{\bar{e}_{ij}\sigma(\bar{r}_j)dA_j}{|\bar{r}_i - \bar{r}_j|^2} \tag{C.69}$$

As it can be noticed from Equation C.69, when $i = j$, the denominator of the the equation yield to singularity. To prevent this situation, a closed form solution for a circular disk is utilized. According to MacNeal [45], the displacement can be taken for elements wetted on one side as 2π whereas for the elements wetted on both sides it

can be taken as $\frac{3\pi^{\frac{5}{2}}}{2\sqrt{A}}$. To have better correlation with $\frac{3\pi^{\frac{5}{2}}}{2\sqrt{A}} = 26.24$ is considered as it is equal to 16.0.

The requirement to have good results from closed form solutions for finding displacement and pressures is to keep the element aspect ratio under 2:1 where the element aspect ratio is the ratio between one finite element's longest dimension to its shortest dimension [30]. The reason of this situation is based on the studies of Rayleigh [46]. By using his studies, it is expressed in "Preliminary Design Document" of Nastran that the virtual mass of an elliptical disc which has equal area with a circular disc has almost the same virtual mass with circular disc, only with 3% error, if the elliptical disc's ratio between its principal axes is less than 2:1 [29]. This equal area principle of Rayleigh is adapted to triangular and quadrilateral elements in Nastran and the according to the testing results, it is seen that rectangular fields are more sensitive to the excess of 2:1 aspect ratio [29].

Since the displacements and the pressures are calculated for each of the finite elements, they are written in matrix form. Every structural element has a normal that is directed towards the fluid volume for the case of point sources and also the element displacement is denoted in terms of source strengths [4]. These source strengths are considered as constant for all the finite elements. Thus, the average normal element displacement for each element is

$$u_i = \frac{1}{A_i} \int_{A_i} (\bar{n}_i) \cdot \bar{u}(\bar{r}_i)) dA_i \tag{C.70}$$

where $\bar{u}(\bar{r}_i)$ comes from Equation C.69. Thus, Equation C.70 can be shown in matrix form as

$$\{u\} = [\lambda]\{\sigma\} \tag{C.71}$$

where σ means source strength and λ includes the terms of the rest of the Equation C.70.

Similar to the case of element displacements, forces on the finite elements can be demonstrated in matrix form, as well. Total force is reached by integrating the pressure term [29]

$$f_i = \int_{A_i} \bar{p}(\bar{r}_i))dA_i \tag{C.72}$$

Then, Equation C.72 can be shown in matrix form as

$$f = [\Lambda][\ddot{\sigma}] \tag{C.73}$$

where $\ddot{\sigma}$ denotes the source strength derivated with respect to time twice and Λ includes the rest of the terms of the Equation C.72.

C.2.5. Displacements, Forces and Virtual Mass Values at Grid Points

So far, the displacement and the pressure are considered as the elemental quantities. However, Nastran does its calculations by using displacement and pressures that is measured at grid points and that is why, a transformation matrix, $[G_{eg}]$ is established [29].

For the transformation from element displacements to grid ones, the following transformation matrix is used [29]

$$\{u_e\} = [G_{eg}]\{u_g\} \tag{C.74}$$

and for the forces at the grid point, the following equation is used [29]

$$\{f_g\} = -[G_{eg}]^T\{f_e\} \tag{C.75}$$

After deriving Equations C.71 and C.74 twice gives

$$\{\ddot{u}_e\} = [\lambda]\{\ddot{\sigma}_e\} \tag{C.76}$$

$$\{\ddot{u}_e\} = [G_{eg}]\{\ddot{u}_g\} \tag{C.77}$$

Inserting C.76 into Equation C.73 gives

$$\{f_e\} = [\Lambda][\lambda]^{-1}\{\ddot{u}_e\} \tag{C.78}$$

Then putting Equation C.78 into Equation C.75

$$\{f_g\} = -[G_{eg}]^T[\Lambda][\lambda]^{-1}\{\ddot{u}_e\} \tag{C.79}$$

Substituting Equation C.77 into Equation C.79

$$\{f_g\} = -[G_{eg}]^T[\Lambda][\lambda]^{-1}[G_{eg}]\{\ddot{u}_g\} \tag{C.80}$$

The right hand side of the Equation C.80, except $\{\ddot{u}_g\}$, gives us the virtual mass matrix [29]

$$[M^v_{gg}] = -[G_{eg}]^T[\Lambda][\lambda]^{-1}[G_{eg}] \tag{C.81}$$

C.2.6. Displacements, Forces and Virtual Mass Values in Analysis Set Coordinates

The equations so far are all in global coordinates, however, Nastran utilizes "the analysis set coordinates" [29]. The reason of this transformation is that the matrices with analysis set coordinates are symmetric and it helps to reduce the cost of calculation [29].

According to "Preliminary Design Document: The Implementation of Fluid Capability in Nastran" [29], the relationship between $\{u_a\}$ and $\{u_g\}$ is shown as

$$\{u_g\} = [G_{ga}]\{u_a\} \tag{C.82}$$

where $[G_{ga}]$ is the transformation matrix between global and analysis set coordinates, and in analysis set coordinates, the virtual mass matrix is

$$[M^v_{aa}] = -[G_{ea}]^T[\Lambda][\lambda]^{-1}[G_{ea}] \tag{C.83}$$

where

$$[G_{ea}] = [G_{eg}][G_{ga}] \tag{C.84}$$

From Equation C.77, the elemental displacement in terms of analysis set coordinates is found as

$$\{\ddot{u}_e\} = [G_{ea}]\{\ddot{u}_a\} \tag{C.85}$$

Equation C.85 can be put into Equation C.78 as

$$\{f_e\} = [\Lambda][\lambda]^{-1}[G_{ea}]\{\ddot{u}_a\} \tag{C.86}$$

Finally, the element pressure in analysis set coordinates is [29]

$$\{p_e\} = [A_e]^{-1}[f_e] = [A_e]^{-1}[\Lambda][\lambda]^{-1}[G_{ea}]\{\ddot{u}_a\} \tag{C.87}$$

APPENDIX D: COMPUTER SCRIPTS FOR CREATING RECTANGULAR AND CYLINDRICAL TANK MODELS AND IMPLEMENTING SOL 103 ANALYSES IN NASTRAN

The computer scripts below creates rectangular and cylindrical tanks and implements SOL 103 analyses by using these tanks in Nastran. These scripts are written in Matlab program. All the models that are mentioned in the chapter of "Numerical Analyses and Laboratory Experiments" are created with this model with the aim of reducing time of creating these models in Nastran. The description of these matlab files can be seen in the beginning of scripts. The scripts for the rectangular tank can be seen as follows

```
RECTANGULAR TANK

clear all
This matlab code (recttank_1.m,recttank_2.m, and recttank_3.m files together) creates the entries
for a SOL 103 analysis of a rectangular tank.

It works in 3 steps;

In first step, recttank_1.m creates case control
and bulk data entries of SOL 103 analysis.
Also it creates tank wall and merges
tank wall with tank bottom and phantom surface that
are given by the user.

In the second step, recttank_2.m does the static analysis of phantom surface, SOL 101,
for using the results as CELAS2 input in
SOL 1O3 analysis. It does this analysis
by creating case control and bulk
data entries of SOL 101 and
by merging them with
phantom surface bdf.

In the third step, recttank_3.m runs and
does data parsing over the results from sol 101
```

```
analysis' f06 file and use them
as CELAS2 input in SOL 103 analysis.
The control, bulk data, tank bottom,
tank wall and phantom surface entries
from recttank_1.m.
Therefore, it creates the final
version of SOL 103 bdf.

Note 1:
If it is required, for instance creating a tank for using in SOL 109/SOL 112
analysis, with this code, only the bdf of tank bottom, tank wall, phantom surface and
celas elements can be obtained by merging them and not including the case control and
bulk data bdfs of SOL 103.

Note 2: Phantom surface node and element numbers must be started from
100001 in order to prevent duplication of tank bottom and wall nodes and elements.

recttank_1 file

Variables of tank sizes, phantom surface height and mesh refinement

lt=150; length of the tank on x axis
wt=100; length of the tank on y axis
ht=500;  Height of the tank
psh=300; Phantom surface height
psmsnl=60; mesh seed number in length for phantom surface
pshmsnw=40; mesh seed number in width for phantom surface

If you want to mesh your tank with any number of elements you want, choose
the variables below, but the crucial part is that if you choose this way you
need to check aspect ratio of elements by checking the values of variables
arl(aspect ratio of tank wall elements on x axis), arw(aspect ratio of tank wall elements
on y axis), artb(aspect ratio of tank bottom elements).

msnl=24;    mesh number in x axis for tank bottom
msnw=16;    mesh number in y axis for tank bottom
nor=48;     Number of rows of elements at the tank's wall If you prefer to mesh your tank

If you want to mesh your tank
without concerning aspect ratio
(it will always be 1 if you use
this option), choose the variables below.
When you use them, your mesh number
will be the product of tank size times
"the multiplication factor, variable n"
```

```
that you want to use. For instance,
if you have lt= 20 m which is the
length of the tank on x axis, and n=2,
you will mesh your tank on x axis
with 40 elements.

n=;   the multiplication factor" for finding mesh numbers
msnl=lt*n;
msnw=wt*n;
nor=ht*n;

Creating edge nodes of bottom of
the tank (for creating elements
which are connected to tank bottom)

ueltb=lt/msnl; length of 1 element in x axis of tank bottom
uewtb=wt/msnw; length of 1 element in y axis of tank bottom
tb1e=1:msnl+1; tank bottom's 1st edge
tb2e=tb1e(1,end)+(msnl+1):(msnl+1):(msnl+1)*(msnw+1); tank bottom's 2nd edge
tb3e=tb2e(1,end)-1:-1:tb2e(1,end)-msnl; tank bottom's 3rd edge
tb4e=tb3e(1,end)-(msnl+1):-(msnl+1):msnl+2; tank bottom's 4th edge
tben=horzcat(tb1e,tb2e,tb3e,tb4e); tank bottom's edge node numbers
nf=(msnl+1)*(msnw+1); Total node number at tank bottom
nr=length(tben); Number of edge nodes in one row
el=ht/nor; Vertical element length of the tank's wall
e_nb=msnl*msnw; Total element number at the bottom of the tank
e_nt= e_nb+1:e_nb+1+(nr*nor-1); Element numbers of the tank's wall
arl=ueltb/el; aspect ratio of length of x axis/vertical
arw=uewtb/(ht/nor); aspect ratio of length of y axis/vertical
artb=ueltb/uewtb;   aspect ratio of length of x axis/length of y axis
zfstoll=0.01*sqrt(2*ueltb*el); tolerance value that is added to zfs in mfluid card
for length of the tank
zfstolw=0.01*sqrt(2*uewtb*el); tolerance value that is added to zfs in mfluid card
for width of the tank
zfstoltb=0.01*sqrt(2*ueltb*uewtb); tolerance value
that is added to zfs in mfluid card for
the tank bottom
zfs=psh+zfstoll;

Creating node numbers of the wall
for i=1:nr*(nor)
twnn(i)=[nf+i]; twnn stands for tank wall node numbers
end
first corner is left bottom one and next corners are described
counter clockwise
```

```
fcxc=-(lt/2); first corner x coordinate
scxc=lt/2; second corner x coordinate
tcxc=lt/2; third corner x coordinate
fthcxc=-(lt/2); fourth corner x coordinate
xc1e=fcxc:ueltb:scxc; x coordinates of first edge
xc2e=repelem(scxc,msnw); x coordinates of second edge
xc3e=(tcxc-ueltb):-ueltb:fcxc; x coordinates of third edge
xc4e=repelem(fthcxc,msnw-1); x coordinates of fourth edge
xce=horzcat(xc1e,xc2e,xc3e,xc4e);
xce=repmat(xce,1,nor);
fcyc=-(wt/2); first corner y coordinate
scyc=-wt/2; second corner y coordinate
tcyc=wt/2; third corner y coordinate
fthcyc=wt/2; fourth corner y coordinate
yc1e=repelem(fcyc,msnl); y coordinates of first edge
yc2e=scyc:uewtb:tcyc; y coordinates of second edge
yc3e=repelem(tcyc,msnl); y coordinates of third edge
yc4e=fthcyc-uewtb:-uewtb:fcyc+uewtb; y coordinates of fourth edge
yce=horzcat(yc1e,yc2e,yc3e,yc4e);
yce=repmat(yce,1,nor);
Creating z coordinate of the tank's nodes
for i=1:(nor)
    for k=1:nr
           z1(1:1:k,i)=el*i;
end
end
z=z1(:)'; Transposing of z1 in order to change it to vector that can be used in "pol2cart"

Creating the elements of the tank's wall
for i=1:nr:nr*(nor-1)+1
G1(1,i:i+nr-2) = twnn(1,nr*(nor-1)+2-(i-1):nr*(nor)-(i-1));
G2(1,i:i+nr-2) = twnn(1,nr*(nor-1)+1-(i-1):nr*(nor)-i);
end
for j = 1:nr:nr*(nor-2)+1
G3(1,j:j+nr-2) = twnn(1,nr*(nor-(2))+1-(j-1):nr*(nor-1)-j);
G4(1,j:j+nr-2) = twnn(1,nr*(nor-2)+2-(j-1):nr*(nor-1)-(j-1));
end

Phantom surface's node, element ve mesh seed numbers
tnnps=(psmsnl+1)*(pshmsnw+1);  Total number of nodes at the phantom surface
tenps=psmsnl*pshmsnw;  total element number at phantom surface
fenps=100001; first element number of phantom surface
lenps=fenps+tenps-1;  last element number of phantom surface
fnnps=100001;  first node number of phantom surface
lnnps=fnnps+tnnps-1; last node number of phantom surface
```

```
Creating elements that has grid points as first and last nodes
 for i=1:nr:nr*(nor)
G1(1,nr+(i-1)) = G2(1,i) ;
G2(1,nr+(i-1)) = G1(1,i+nr-2);
end
for j=1:nr:nr*(nor-2)+1
G3(1,nr+(j-1)) = G4(1,j+nr-2);
G4(1,nr+(j-1)) = G3(1,j);
end

Connection of bottom and wall
G3(1,nr*(nor-1)+1:nr*(nor)) = tben(1,1:nr);
G4(1,nr*(nor-1)+1:nr*(nor)-1) = tben(1,2:nr);
G4(1,nr*(nor))=tben(1,1);

Creating input file of the part between 'SOL 103' and CQUAD4s/GRIDs
fid= fopen('CaseControlBulkDataVariables.bdf','w');
fprintf(fid,'s\r\n','SOL 103');
fprintf(fid,'s\r\n','CEND');
fprintf(fid,'s\r\n','TITLE=Virtual mass sloshing');
fprintf(fid,'s\r\n','   SPC=1');
fprintf(fid,'s\r\n','   DISPLACEMENT=ALL');
fprintf(fid,'s\r\n','   SPCFORCES=ALL');
fprintf(fid,'s\r\n','   STRESS=ALL');
fprintf(fid,'s\r\n','method=10');
fprintf(fid,'s\r\n','mfluid=5');
fprintf(fid,'s\r\n','mpres=all');
fprintf(fid,'s\r\n','BEGIN BULK');
fprintf(fid,'s\r\n','PARAM,POST,0');
mfluid='mfluid, 5,1,f, 1000.e-12, 11,, n, n \r\n';
fprintf(fid,mfluid,zfs);
fprintf(fid,'s\r\n','cord2r,1,, 0.0, 0.0, 0.0, 0.0, 0.0, 1.0,+');
fprintf(fid,'s\r\n','+, 1.0, 0.0, 0.0 ');
elist1='elist,11,1,thru,d \r\n';
fprintf(fid,elist1,e_nb);
elist2='elist,11,d,thru,d \r\n';
fprintf(fid,elist2,-e_nt(1,1),-e_nt(1,end));
elist3='elist,11,d,thru,%d \r\n';
fprintf(fid,elist3,-fenps,-lenps);
fprintf(fid,'s\r\n','$');
fprintf(fid,'s\r\n','eigrl,10,,,30');
fprintf(fid,'s\r\n','$');
spc1a='SPC1,1,123456,1,thru,d \r\n';
fprintf(fid,spc1a,tb1e(1,end));
```

```
spc1b='SPC1,1,123456,d\r\n';
fprintf(fid,spc1b,tb2e);
spc1c='SPC1,1,123456,d,thru,d \r\n';
fprintf(fid,spc1c,tb3e(1,end),tb3e(1,1));
spc1d='SPC1,1,123456,d \r\n';
fprintf(fid,spc1d,tb4e);
spc1e='SPC1,1,12456,d,thru,d\r\n';
fprintf(fid,spc1e,fnnps,lnnps);
fprintf(fid,'s\r\n','$');
fprintf(fid,'s\r\n','$ tank');
fprintf(fid,'s\r\n','$');
fclose('all');

Creating input file(bulk data part) of tank wall's elements and grids
fid2 = fopen('tw.bdf','w');
fprintf(fid2,'s\r\n','$');
fprintf(fid2,'GRID,d,,f,f,f     \r\n',[twnn;xce;yce;z]);
fprintf(fid2,'CQUAD4,d,2,d,d,d,d\r\n',[e_nt;G1;G2;G3;G4]);
fclose('all');
status=dos('copy CaseControlBulkDataVariables.bdf +
rect_tank_bottom.bdf + tw.bdf + phantom_surface_6040.bdf tbw.bdf')

bdf descriptions:
tank_bottom: tank bottom's bdf
tw.bdf: tank wall's bdf
tbw.bdf: tank bottom and wall's bdf

recttank2.m

Static analysis of phantom surface for rectangular tank SOL 103 analysis

Do not change anything
Creating edge nodes of phantom surface
ps1e=fnnps:fnnps+psmsnl; phantom surface's 1st edge
ps2e=ps1e(1,end)+(psmsnl+1):(psmsnl+1):fnnps+(psmsnl+1)*(pshmsnw+1); phantom surface's 2nd edge
ps3e=ps2e(1,end)-1:-1:ps2e(1,end)-psmsnl; phantom surface's 3rd edge
ps4e=ps3e(1,end)-(psmsnl+1):-(psmsnl+1):fnnps+psmsnl+1; phantom surface's 4th edge
psen=horzcat(ps1e,ps2e,ps3e,ps4e); phantom surface's edge node numbers

Creating bulk data file of SOL 101
FID2 = fopen('BCsSOL101.bdf','w');Creating input file(The part between 'SOL 101' and CTRIA3s/GRIDs)
fprintf(FID2,'s\r\n','SOL 101');
fprintf(FID2,'s\r\n','CEND');
fprintf(FID2,'s\r\n','TITLE=Fake phantom surface analysis to calculate CELAS values');
fprintf(FID2,'s\r\n','   SPC=1');
```

```
fprintf(FID2,'s\r\n','   LOAD=1');
fprintf(FID2,'s\r\n','   SPCFORCES(SORT1,REAL)=ALL');
fprintf(FID2,'s\r\n','BEGIN BULK');
fprintf(FID2,'s','SPC1');
fprintf(FID2,',s','1');
fprintf(FID2,',s','123');
fprintf(FID2,',d', fnnps);
fprintf(FID2,',s','THRU');
fprintf(FID2,',d\r\n',lnnps);
pload4='PLOAD2,1,-9807.e-9,d,THRU,d \r\n';
fprintf(FID2,pload4,fenps,lenps);
fclose('all');

Creating "ENDDATA" entry for the bulkdata input file
FID = fopen('enddata.bdf','w');
fprintf(FID,'s\n','ENDDATA');
fclose('all');

Merging bdf files and running SOL 101 analysis
variable: put phantom surface bdf file name below
status1=dos('copy BCsSOL101.bdf +
phantom_surface_6040.bdf + enddata.bdf rectsol101.bdf'); Keeping kk.bdf and phantom_surface.bdf
together as SOL101.bdf by using dos command
status2=dos('rectsol101.bdf') Launching rectSOL101.bdf
Explanation of bdf files:
BCsSOL101.bdf: Creating input file(The part between 'SOL 101' and CTRIA3s/GRIDs)
enddata.bdf: bdf file that includes ENDDATA keyword
phantom_surface_file_name.bdf: phantom surface of the model
rectsol101.bdf: Final version of SOL 101 bdf

recttank_3.m

Importing "Forces of single point constraint" values and using them as CELAS element values
Do not change anything
fileID = fopen('rectsol101.f06','r'); Reading the file of sol101.f06 in order to import the required
values from it
Intro = textscan(fileID,'s','Delimiter','\n');
bb = Intro{1};

Creating the values that we want to find inside the f06 file by data parsing
expression1 = '[0123456789]+[0123456789]+[0123456789]      G';
[match1,noMatch1] = regexp(bb,expression1,'match','split','forceCellOutput');
hhh1=match1(~cellfun('isempty',match1));
hhh11 = string(hhh1);
hhh55=vertcat(hhh11);
```

```
hhh66 = string(hhh55);
hhh77 = length(hhh66);
Importing the column that we need that
has the values of forces of single point constraint
for i=1:hhh77
jjj(i,1)= strmatch(hhh66{i,1},bb);
ppp(i,1) = bb(jjj(i,1),1);
end

Importing the values that we need
by dividing "ppp" variable into columns
and taking the one that we need
spcf = regexp(ppp,'\S+','match');
spcf = vertcat(spcf{:});
celas = spcf(:,5);
c_e=lenps+1:lenps+1+tnnps-1; Creating the element numbers of celas elements

Variable: Put phantom surface bdf name below
fileid = fopen('phantom_surface_6040.bdf','r');

Intro2 = textscan(fileid,'s','Delimiter','\n');
cg= Intro2{1};
FILEID=fopen('rect_celas_elements.bdf','w'); Writing the input file of celas element's values
and its grids
celas2 = str2double(celas); Conversion of cell array "celas" to double "celas"
celas3 = celas2.'; Taking transpose of celas2
nnn= strmatch('GRID',cg); Finding the indices of "GRID" inside cc.bdf file
cg2 = string(cg);
cg2(6,1)=('$'); Inserting '$' to cg5(6,1) in order to get rid off "PSHELL" row which causes
the problem of having 2 "PSHELL" entry in bulk data file
cg3=cellstr(cg2);
nnn2=cg3(nnn,1); Creating the rows of "GRID" values that we need
nnn3 = regexp(ppp,'\S+','match');
nnn3 = vertcat(nnn3{:});
nnn4 = nnn3(:,1);
nnn5=string(nnn4);
nnn6 = str2double(nnn5);
nnn7 = nnn6.';

Printing CELAS2 elements
fprintf(FILEID,'CELAS2,d,f,d,3\r\n',[c_e;celas3;nnn7]);
fclose('all');

Creating the input file that we will use for having SOL103 analysis
status3=dos('copy tbw.bdf+rect_celas_elements.bdf+enddata.bdf rect_tank_rigid_6040.bdf' );
```

```
status3=dos('rect_tank_rigid_6040.bdf') Launching rect_tank_rigid_6040.bdf

Explanation of input files
rect_celas_elements.bdf: celas element values that comes from sol 101 analysis and
will be used in sol 103 in CELAS2 card.
rect_tank_rigid_6040: final bdf version of SOL 103 analysis
```

The matlab script for cylindrical tank is as follows

```
clear all
This matlab script works in 3 steps;

1)c_tank_1.m script  creates case control and bulk file entries of SOL 103 analysis.
Afterwards, it creates cylindrical tank's wall(elements and grid points) and merging
it with the bottom of the tank and phantom surface.
2)c_tank_2.m script creates input file of phantom surface's SOL 101
analysis in order to use those results in SOL 103 analysis as CELAS2
input.
3)c_tank_3.m script does data parsing from sol 101 analysis f06 file and
use those values as CELAS2 entries of sol 103 analysis. Finally, this
script brings the case control and bulk data entries, tank bottom, tank
wall, phantom surface and CELAS2 elements together and creates the final
version of the SOL 103 bdf.

Note 1:
If it is required, for instance creating a tank for using in SOL 109/SOL 112
analysis, with this code, only the bdf of tank bottom, tank wall, phantom surface and
celas elements can be obtained by merging them and not including the case control and
bulk data bdfs of SOL 103.

Note 2: Phantom surface node and element numbers must be started from
100001 in order to prevent duplication of tank bottom and wall nodes and elements.


c_tank_1.m

Tank sizes
Radius=100; radius of the tank bottom
ht=500;  Height of the tank
psh=300; Phantom surface height

Tank bottom properties
```

```
e_nb=150; Total element number at the bottom of the tank
nf=91; Total node of the tank bottom
nr=30; Number of edge nodes in one row

Tank wall and phantom surface properties
h=30;   Number of rows of elements at the tank's wall
psen=511; Phantom surface element number
nn_p=523; phantom surface node number

Do not change anything
b_n=1:nr; Creating edge nodes of bottom of the tank
el=(ht/h); Vertical length of the element  the aspect ratio of QUAD4 elements
should not kept below 2:1 to reduce
the errors in the virtual mass calculation
ar=(ht/h)/((2*pi*Radius)/(nr)); aspect ratio of tank wall elements
e_nt= e_nb+1:e_nb+1+(nr*h-1); Element numbers of the tank's wall
fen_p=100001; First element number at the phantom surface
fnn_p=100001; First node number at the phantom surface
len_p=fen_p+psen-1; Last element number at the phantom surface
lnn_p=fen_p+nn_p-1; Last node number

for i=1:nr*(h)
All_node_numbers(i)=[nf+i];
end

rho(1,1:nr*(h)) = Radius; Rho coordinate of the tank

Creating z coordinate of the tank's nodes
for i=1:(h)
    for k=1:nr
           z1(1:1:k,i)=el*i;
end
end

z=z1(:)'; Transposing of z1 in order to change it to vector that can be used in "pol2cart"
theta4=0:(2*pi/nr):(2*pi-(2*pi/nr));
theta5=repmat(theta4,1,h);
[All_node_xval1,All_node_yval1,All_node_zval] = pol2cart(theta5,rho,z);
Converting cylindrical coordinate values
to cartesian ones
All_node_xval=-All_node_xval1; Multiplying All_node_xval1 with -1 in order to have correct
coordinates that matches with bottom
tank's coordinates
All_node_yval=-All_node_yval1; Multiplying All_node_yval1 with -1 in order to have correct
coordinates that matches with
```

```
bottom tank's coordinates

Creating the elements of the tank's wall
for i=1:nr:nr*(h-1)+1
G1(1,i:i+nr-2) = All_node_numbers(1,nr*(h-1)+2-(i-1):nr*(h)-(i-1));
G2(1,i:i+nr-2) = All_node_numbers(1,nr*(h-1)+1-(i-1):nr*(h)-i);
end

for j = 1:nr:nr*(h-2)+1
G3(1,j:j+nr-2) = All_node_numbers(1,nr*(h-(2))+1-(j-1):nr*(h-1)-j);
G4(1,j:j+nr-2) = All_node_numbers(1,nr*(h-2)+2-(j-1):nr*(h-1)-(j-1));
end

Creating elements that has grid points as first and last nodes
 for i=1:nr:nr*(h)
G1(1,nr+(i-1)) = G2(1,i) ;
G2(1,nr+(i-1)) = G1(1,i+nr-2);
end

for j=1:nr:nr*(h-2)+1
G3(1,nr+(j-1)) = G4(1,j+nr-2);
G4(1,nr+(j-1)) = G3(1,j);
end

tol=1.5*(0.01*sqrt(2*(Radius/(nr-1))*el)); Tolerance value for using in "mfluid"
zfs=psh+tol; zfs value for using in "mfluid"

Connection of bottom and wall
G3(1,nr*(h-1)+1:nr*(h)) = b_n(1,1:nr);
G4(1,nr*(h-1)+1:nr*(h)-1) = b_n(1,2:nr);
G4(1,nr*(h))=b_n(1,1);

Creating input file of the part between 'SOL 103' and CQUAD4s/GRIDs
fid= fopen('delimiters.bdf','w');
fprintf(fid,'s\r\n','SOL 103');
fprintf(fid,'s\r\n','CEND');
fprintf(fid,'s\r\n','TITLE=Virtual mass sloshing');
fprintf(fid,'s\r\n','   SPC=1');
fprintf(fid,'s\r\n','method=10');
fprintf(fid,'s\r\n','mfluid=5');
fprintf(fid,'s\r\n','mpres=all');
fprintf(fid,'s\r\n','BEGIN BULK');
fprintf(fid,'s\r\n','PARAM,POST,0');
fprintf(fid,'s\r\n','cord2r,1,, 0, 0, 0, 0, 0, 1.0,+');
fprintf(fid,'s\r\n','+, 1.0, 0, 0 ');
```

```
mfluid='mfluid,5,1,f,1000.e-12,11,,n,n \r\n';
fprintf(fid,mfluid,zfs);
elist1='elist,11,1,thru,d \r\n';
fprintf(fid,elist1,e_nb);
elist2='elist,11,d,thru,d \r\n';
fprintf(fid,elist2,-e_nt(1,1),-e_nt(1,end));
elist3='elist,11,d,thru,%d \r\n';
fprintf(fid,elist3,-fen_p,-len_p);
fprintf(fid,'s\r\n','eigrl,10,,,30');
spc1_1='SPC1,1,123456,d,THRU,d \r\n';
fprintf(fid,spc1_1,1,nr);
spc1_2='SPC1,1,12456,d,THRU,d \r\n';
fprintf(fid,spc1_2,fnn_p,lnn_p);
fclose('all');

Creating input file(bulk data part) of tank wall's elements and grids
fid2 = fopen('tank_wall.bdf','w');
print all GRIDs
fprintf(fid2,'GRID,d,2,f,f,f     \r\n',
[All_node_numbers;All_node_xval;
All_node_yval;All_node_zval]);
fprintf(fid2,'CQUAD4,d,2,d,d,d,d\r\n',[e_nt;G1;G2;G3;G4]);
fclose('all');


Creating phantom surface with unstructured mesh
status=dos('copy delimiters.bdf+
unstr_tank_bottom_30.bdf+
tank_wall.bdf+
phantom_unstructured.bdf zz2.bdf' );


c_tank_2.m

Static analysis of phantom surface
FID2 = fopen('kk.bdf','w'); Creating input file(The part between 'SOL 101' and CTRIA3s/GRIDs)
fprintf(FID2,'s\r\n','SOL 101');
fprintf(FID2,'s\r\n','CEND');
fprintf(FID2,'s\r\n','TITLE=Fake phantom surface analysis to calculate CELAS values');
fprintf(FID2,'s\r\n','   SPC=1');
fprintf(FID2,'s\r\n','   LOAD=1');
fprintf(FID2,'s\r\n','   SPCFORCES(SORT1,REAL)=ALL');
fprintf(FID2,'s\r\n','BEGIN BULK');
SPC1p1='SPC1,1,123,d,thru,d \r\n'
fprintf(FID2,SPC1p1,fnn_p,lnn_p);
```

```
pload2='PLOAD2,1,-9807.e-9,d,thru,d \r\n'
fprintf(FID2,pload2,fen_p,len_p);
fclose('all');


Creating "ENDDATA" entry for the bulkdata input file
FID = fopen('enddata.bdf','w');
fprintf(FID,'s\n','ENDDATA');
fclose('all');

Creating and launching SOL101.bdf
status1=dos('copy kk.bdf+phantom_unstructured.bdf+enddata.bdf sol101.bdf'); Keeping kk.bdf
and phantom_surface.bdf together
as SOL101.bdf by using dos command
status2=dos('sol101.bdf') Launching sol101.bdf



c_tank_3.m


Importing "Forces of single point constraint" values and using them as CELAS element values
fileID = fopen('sol101.f06','r'); Reading the file of sol101.f06 in order to import the required values
Intro = textscan(fileID,'s','Delimiter','\n');
bb = Intro{1};

Creating the values that we want to find inside the f06 file
expression1 = '[0123456789]+[0123456789]+[0123456789]      G';
[match1,noMatch1] = regexp(bb,expression1,'match','split','forceCellOutput');
hhh1=match1(~cellfun('isempty',match1));
hhh11 = string(hhh1);
hhh55=vertcat(hhh11);
hhh66 = string(hhh55);
hhh77 = length(hhh66);

Importing the column that we need that
has the values of forces of
single point constraint
for i=1:hhh77
jjj(i,1)= strmatch(hhh66{i,1},bb);
ppp(i,1) = bb(jjj(i,1),1);
end

Importing the values that we need by dividing "ppp" variable into columns
and taking the one that we need
```

```
spcf = regexp(ppp,'\S+','match');
spcf = vertcat(spcf{:});
celas = spcf(:,5);
c_e=200001:100000+lnn_p; Creating the element numbers of celas elements
fileid = fopen('sol101.bdf','r');
Intro2 = textscan(fileid,'s','Delimiter','\n');
cg= Intro2{1};
FILEID=fopen('celas_circular_unstructured_phantom.bdf','w'); Writing the input file of celas element's
values and its grids
celas2 = str2double(celas); Conversion of cell array "celas" to double "celas"
celas3 = celas2.'; Taking transpose of celas2
nnn= strmatch('GRID',cg); Finding the indices of "GRID" inside cc.bdf file
cg2 = string(cg);
cg2(6,1)=('$');nInserting '$' to cg5(6,1)
in order to get rid off "PSHELL" row
which causes the problem of having 2
"PSHELL" entry in bulk data file
cg3=cellstr(cg2);
nnn2=cg3(nnn,1); Creating the rows of "GRID" values that we need
nnn3 = regexp(ppp,'\S+','match');
nnn3 = vertcat(nnn3{:});
nnn4 = nnn3(:,1);
nnn5=string(nnn4);
nnn6 = str2double(nnn5);
nnn7 = nnn6.';

Printing CELAS2 elements
fprintf(FILEID,'CELAS2,d,f,d,3\r\n',[c_e;celas3;nnn7]);
fclose('all');

Creating the input file that we will use for having SOL103 analysis
status3=dos('copy zz2.bdf+celas_circular_unstructured_phantom.bdf+enddata.bdf rigid_cylin_tank_unstr.bdf
status4=dos('rigid_cylin_tank_unstr.bdf');
```